

Observing the Unobservable

Identification and Characterization of Stealth Coronal Mass Ejections

Elke D’Huys

Supervisor:
Prof. dr. S. Poedts
Dr. D.B. Seaton, co-supervisor
(ROB/CU)

Dissertation presented in partial
fulfillment of the requirements for the
degree of PhD in Science

January 2016

Observing the Unobservable

Identification and Characterization of Stealth Coronal Mass Ejections

Elke D'HUYS

Examination committee:

Prof. dr. G. Lapenta, chair

Prof. dr. S. Poedts, supervisor

Dr. D.B. Seaton, co-supervisor (ROB/CU)

Prof. dr. L. Decin

Dr. D. Berghmans (ROB)

Prof. dr. P. Rochus (CSL)

Prof. dr. C. Parnell (St And)

Dissertation presented in partial
fulfillment of the requirements for
the degree of PhD in Science

January 2016

© 2016 KU Leuven – Faculty of Science
Uitgegeven in eigen beheer, Elke D'Huys, Koninklijke Sterrenwacht van België, Ringlaan 3, 1180 Brussel (Ukkel),
Belgium

Alle rechten voorbehouden. Niets uit deze uitgave mag worden vermenigvuldigd en/of openbaar gemaakt worden door middel van druk, fotokopie, microfilm, elektronisch of op welke andere wijze ook zonder voorafgaande schriftelijke toestemming van de uitgever.

All rights reserved. No part of the publication may be reproduced in any form by print, photoprint, microfilm, electronic or any other means without written permission from the publisher.

Acknowledgements

First of all, I am tremendously grateful to my supervisors for their enthusiastic guidance. It was a pleasure to work with the both of you.

Stefaan, you never even hesitated to take me on as a PhD student, although I was not working at the CmPA and you barely knew me. Thank you for the trust and your support throughout the years.

Dan, you had the harder job, having to deal with me on a daily basis. You needed a little convincing to become my supervisor at first, but you have lived up to all my expectations. I can only hope that I have met yours. Thanks for all the encouragement and good ideas. I'll miss our little coffee breaks and science discussions now that you've left ROB.

I am indebted to David, who immediately jumped on board when I asked to start a PhD, and who was an enthusiastic 'stealth' supervisor throughout the years. You were always full of good suggestions.

I also thank Leen, the fourth member of my little PhD advisory team. Coming from another department, you looked at my work with fresh eyes and your questions allowed me to progress further.

The comments and suggestions from the members of the examination committee were much appreciated as well. They helped me to improve and refine this manuscript. Thank you.

I am grateful for the support from my colleagues both at CmPA and at ROB. If it wasn't for the fun and inspirational atmosphere at ROB, I wouldn't have started this work in the hope to be allowed to stay there a little while longer.

Finally, I would like to thank my family, my friends, and Ruben, who have supported me throughout this journey. Their love and belief in me has helped me pull through the difficult moments. And I am sure Moeke would have danced around the table with me once more to celebrate today.

Abbreviations

ACE	Advanced Composition Explorer
ADP	Ancillary Data Processor
AIA	Atmospheric Imaging Assembly
AR	Active Region
AVL	Academisch Vormingscentrum voor Leraren
BELSPO	Belgian Science Policy Office
CACTus	Computer Aided CME Tracking
CCD	Charge-Coupled Device
CDAW	Coordinated Data Analysis Workshops
CDF	Cumulative Distribution Function
CDS	Correlated Double Sampling
CIR	Co-rotating Interaction Region
CME	Coronal Mass Ejection
CMOS-APS	Complementary Metal-Oxide-semiconductor Active-Pixel System
CmPA	Centre for mathematical Plasma-Astrophysics
CSL	Centre Spatial de Liège
DN	Data Numbers
EIT	Extreme-Ultraviolet Imaging Telescope
ESA	European Space Agency
ESAC	European Space Astronomy Centre
ESWW	European Space Weather Week
EUI	Extreme Ultraviolet Imager
EUV	Extreme UltraViolet
EUVI	Extreme UltraViolet Imager
EVE	Extreme Ultraviolet Variability Experiment

FITS	Flexible Image Transport System
FOV	Field-Of-View
FSI	Full-Sun Imager
GOES	Geostationary Operational Environmental Satellite
HAS	High Accuracy Star-tracker
HF	High Frequency
HMI	Helioseismic and Magnetic Imager
HRI	High-Resolution Imager
ICME	Interplanetary Coronal Mass Ejection
IMF	Interplanetary Magnetic Field
IOS	Instrument Operations Sheet
LASCO	Large Angle and Spectrometric COronagraph
LCS	Low-Coronal Signatures
LYBSDG	LYRA Base Science Data Generator
LYEDG	LYRA Engineering Data Processor
LYRAFF	LYRA Flare Finder
LYTMR	LYRA Telemetry Reformatter
MHD	Magnetohydrodynamics
MLE	Maximum Likelihood Estimator
MOC	Mission Operations Center
NASA	National Aeronautics and Space Administration
NOAA	National Oceanic and Atmospheric Administration
P2SC	PROBA2 Science Center
PFSS	Potential Field Source Surface model
PI	Principal Investigator
PMOD/WRC	Physikalisch-Meteorologisches Observatorium / World Radiation Center
PROBA	Project for On-board Autonomy
PSF	Point-Spread-Function
QPP	Quasi-Periodic Pulsations

ROB	Royal Observatory of Belgium
SCSL	Science Consortium for SWAP and LYRA
SDO	Solar Dynamics Observatory
SECCHI	Sun Earth Connection Coronal and Heliospheric Investigation
SEPs	Solar Energetic Particles
SIDC	Solar Influences Data analysis Center
SILSO	Sunspot Index and Long-term Solar Observations
SMOS	Soil Moisture and Ocean Salinity satellite
SOC	Self-Organized Criticality
SoFAST	Solar Flare Automated Search Tool
SOHO	Solar and Heliospheric Observatory
SSN	SunSpot Number
STEREO	Solar TERrestrial RELations Observatory
SWAP	Sun Watcher using Active Pixel System detector and Image Processing
SWAVINT	SWAP Integrated Intensity
SWBSDG	SWAP Base Science Data Generator
SWEDG	SWAP Engineering Data Processor
SWPC	Space Weather Prediction Center
SWTMR	SWAP Telemetry Reformatter
SXT	Soft X-Ray Telescope
TC	Telecommand
TM	Telemetry
TRACE	Transition Region And Coronal Explorer
USET	Uccle Solar Equatorial Table
UV	UltraViolet
VEX	Venus EXpress
WAVES	Radio and Plasma Wave Investigation on-board the WIND spacecraft
WDC	World Data Center
XRS	X-Ray Sensor

List of Symbols

\AA	ångström, unit of length corresponding to 10^{-10} m
α	power-law scaling parameter, scaling factor or exponent
β	plasma β , ratio of the plasma pressure to the magnetic pressure
$\hat{\alpha}$	power-law scaling parameter estimate
σ	error on the power-law scaling parameter estimate
B_0	heliographic latitude of the central point of the solar disk (angle correcting for the tilt of the ecliptic with respect to the solar equatorial plane)
<i>erg</i>	unit of energy, $1 \text{ J} = 10^7 \text{ erg}$
J	Joule, unit of energy
K_p	planetary K-index, measure for the disturbance of the Earth's magnetic field
M_\odot	solar mass (2×10^{30} kg)
n	sample size
R_\odot	solar radius (6.955×10^5 km)
R_m	magnetic Reynolds number, ratio of the convective to the diffusive term in the induction equation
x_{max}	highest x -value for which power-law properties hold
x_{min}	lowest x -value for which power-law properties hold
G	gauss, cgs unit of magnetic field strength, $1 \text{ G} = 10^{-4} \text{ T}$

G	gravitational constant, $6.67 \times 10^{-11} \text{ m}^3 \text{ kg}^{-1} \text{ s}^{-2}$
MeV	unit of energy, $1 \text{ MeV} = 1.602 \times 10^{-13} \text{ J}$
Sv	Sievert, unit for equivalent dose of ionizing radiation
T	Tesla, SI unit of magnetic field strength

Contents

Acknowledgements	i
Abbreviations	v
List of Symbols	viii
Contents	ix
Preface	1
1 Introduction	5
1.1 The Sun	5
1.2 The Solar Corona	9
1.3 Solar Activity and Space Weather	14
1.4 Coronal Mass Ejections	18
1.4.1 Definition and Properties	18
1.4.2 CME Observations	19
1.4.3 Models for CME Initiation	21
1.4.4 Signatures of CME Origin	28
1.5 Coronal Mass Ejections without Low-Coronal Signatures	32
1.6 Power Laws in Solar Physics	35

1.6.1	Power Laws for CMEs	37
2	Observational Tools to Study Solar Eruptions: the SWAP EUV Imager on-board the PROBA2 Spacecraft	39
2.1	The PROBA family	40
2.2	PROBA2	41
2.3	PROBA2 Science Center	43
2.4	Scientific Instruments on-board PROBA2	46
2.4.1	LYRA	46
2.4.2	SWAP	48
2.5	Personal Contribution	56
2.6	Conclusions	57
3	The 2010 August 14 Rotating CME: a Forecasting Case Study	59
3.1	Introduction	59
3.2	Observations	62
3.2.1	Filament Eruption	62
3.2.2	Flare	64
3.2.3	EIT Wave and Coronal Dimming	65
3.2.4	Coronal Mass Ejection	66
3.2.5	Radio Signatures and Solar Energetic Particles	68
3.2.6	Effects on Interplanetary Space	72
3.3	Three-dimensional Reconstructions	75
3.4	Initiation Mechanism	80
3.4.1	Flux Emergence versus Flux Cancellation	80
3.4.2	MHD Instability	82
3.5	Discussion	82

4	Observational Characteristics of CMEs without Low-Coronal Signatures	85
4.1	Introduction	85
4.2	Searching for CMEs without LCS	87
4.3	Observational Properties of CMEs without Low-Coronal Signatures	92
4.3.1	Appearance in Coronagraph Images	93
4.3.2	Position Angle	94
4.3.3	CME Speed and Velocity Profiles	96
4.3.4	Angular Width	103
4.3.5	Scale Invariance	105
4.4	Initiation Mechanisms for Stealth CMEs	108
4.5	Conclusions	110
4.6	A New Focus	111
5	The Effect of Limited Sample Sizes on the Accuracy of the Estimated Scaling Parameter for Power-Law-Distributed Solar Data	113
5.1	Introduction	114
5.2	Estimation Methods for the Power-Law Exponent	116
5.2.1	Graphical Methods	117
5.2.2	Maximum Likelihood Estimation	118
5.2.3	Alternative Methods	120
5.3	Sample Size Influence	121
5.3.1	Graphical Methods	124
5.3.2	Maximum Likelihood Estimator	128
5.3.3	Method Performance	128
5.3.4	Improvements to the Graphical Methods	131
5.4	Conclusions	132

6 Power Laws in Solar Data Re-Examined	135
6.1 Introduction	135
6.2 CMEs without Low Coronal Signatures	136
6.3 Quiet-Sun EUV Brightenings	143
6.4 Conclusions	148
Summary and Future Prospects	151
Beknopte Samenvatting	159
A PROBA2 Outreach	169
A.1 Scientific Outreach	169
A.2 Reaching Out to the General Public	170
A.2.1 Proba2@School	170
A.2.2 Junior College	172
B Table of CMEs Without Low-Coronal Signatures of Eruption	175
Project, Image and Data Acknowledgements	179
References	181
Curriculum Vitae	195

Preface

December 14, 2009: first light for the SWAP telescope on-board ESA's PROBA2 satellite. I was privileged to be at the ground station in Redu (Belgium) when the first solar image made by this new EUV instrument reached the ground late in the evening. The excitement among the members of our team was enormous, although, because the spacecraft pointing was still unrefined, we saw only a small part of the Sun in the corner of this first image (Figure 1). That day, I decide to become a solar physicist.



Figure 1 *First (uncalibrated) solar observation by the SWAP EUV imager after the opening of the telescope's door. The Sun is visible in the bottom right corner.*

One year before, I had been hired to reinforce the team working on the PROBA2 satellite in the Solar Physics and Space Weather department at the Royal Observatory of Belgium. During that first year before the satellite was launched, I contributed to the development and testing of the software that is used to process and distribute the scientific data from the solar instruments on-board the satellite. When we received that first image from SWAP, I realized that a new phase in the project would start. Up until that moment, we had focused on how we would get the data from the satellite to the scientists. Now, the team could finally start analyzing the images and gather new knowledge about the Sun and its activity. In pursuing a PhD in solar physics, I aspired to make that same transition.

With the support of the ROB and the CmPA (Centre for mathematical Plasma-Astrophysics), I registered as a doctoral student at the KU Leuven. The goal of the proposed research project was to study the initiation and driving mechanisms of solar eruptions through the combination of observational data (in particular the SWAP images provided by ROB) and (numerical) modeling, which is the speciality of the CmPA. My experience as a space weather forecaster at the SIDC (Solar Influences Data analysis Center, located at ROB) taught me the importance of a thorough understanding of solar eruptions, as they can cause severe geomagnetic storms during which our technological resources on Earth and in space may be strongly disturbed.

While it is generally accepted that a process called magnetic reconnection plays an important role in solar eruptions, many questions remain unanswered. The first goal of this PhD project was to understand what conditions in the corona are required to precipitate the onset of reconnection and trigger eruptions.

In order to distinguish between different candidate initiation mechanisms, we planned to compare eruption observations from various instruments to theoretical models and numerical simulations. In fact, each eruption mechanism results in a specific magnetic topology and thus has its own observational signatures. By examining various physical properties of eruptions in observations and comparing them to the output of different simulations and models, we envisioned to evaluate the models and decide which of the proposed eruption initiation processes is/are actually at work.

As is often the case in solar physics research, it was a fast and energetic eruption that first drew our attention. It had all the characteristics that one can expect from in a powerful solar eruption: a solar flare, a large filament that was unwinding as it erupted, a clear EUV dimming and EIT wave, and a fast coronal mass ejection (CME) followed by interplanetary and geomagnetic effects. However, the flare that accompanied this event was quite weak, which is unexpected for such as strong CME. We therefore asked the question what

was different in this event compared to eruptions where fast CMEs and strong flares do go hand in hand. Moreover, we thought it instructive to study the far end of the energetic spectrum more closely as well: eruptions for which only one of these observational signs was detected, the CME. This motivated us to turn our attention to an obscure class of solar eruptions: coronal mass ejections that are not associated with any kind of low-coronal or on-disk signature of eruption, the so-called *stealth* CMEs.

Because they lack most of the typical signs of solar eruptions, these events are hard to identify. After a challenging search through the solar observations made in 2012, we identified 40 stealth events. We studied their observational characteristics and compared them to more typical eruptions that occurred during that year. We especially focused on those properties that could reveal information on the initiation mechanism for these stealth events, such as their kinematic evolution and the power law for the CME angular width. This last property was particularly hard to study with our small sample of CMEs without low-coronal signatures.

Moreover, the difficulties we experienced when attempting to draw conclusions based on such a small sample of stealth CMEs made us wonder what the exact influence is of a low number of data points on power-law results in general. We therefore shifted focus and examined various methods to determine power-law parameters as well as the influence of the size of the sample on the accuracy of these estimations. With this knowledge we returned to our study of stealth CMEs and re-examined the power law for CMEs with and without low-coronal signatures.

This departure from our initial focus on the initiation mechanisms of CMEs towards methods to analyze power-law parameters may seem a more significant change of subject than it is. Power laws are ubiquitous in solar physics and much theoretical modeling results in power laws, especially when studying flare and CME properties. Once the theory is formulated, the methodology is much like what we set out to do in this thesis: compare the theoretical result to the observations. In order for that to work, it is of course crucial that the proper methods are applied to the observations in order to correctly estimate the power-law parameter.

Overall, we have conducted observational and statistical studies of unusual solar eruptions. We composed the largest sample of stealth coronal mass ejections thus far. We have deduced their general properties and compared them to those of regular coronal mass ejections. Throughout this research our focus has been on the initiation mechanisms of solar eruptions, questioning how the events studied in this manuscript differ from more typical solar eruptions.

Outline. This manuscript starts with an introduction to solar physics: the main characteristics of the Sun and the most important ingredients of space weather are explained. Next, in Chapter 2, we introduce the spacecraft that sparked my interest in solar research: PROBA2 and its EUV imager SWAP. Still early in the mission, eye-catching SWAP observations of the solar eruption on 2010 August 14 led to an in-depth analysis of this unusual event, which is described in Chapter 3. The contrast between this remarkable eruption and typical solar outbursts prompted us to focus on other inconspicuous solar events, that is to say eruptions without the usual observational signatures. Thus stealth CMEs became our next main research interest. In Chapter 4, we report on how we identified these events, what their main observational characteristics are and what the possibilities are for their initiation mechanism(s). We then change focus somewhat and turn our attention to power laws in solar physics. Good and bad practices to determine the parameters for these power laws are discussed, with a focus on the required sample size to do this estimation properly (Chapter 5). This theoretical approach is followed by the application of the preferred method to two solar data sets in Chapter 6. In the concluding chapter, the main results of our research are summarized.

Chapter 1

Introduction¹

1.1 The Sun

Our Sun is an ordinary G2V-type star that would be living its life on the main sequence relatively inconspicuously, were it not for its presence close to our planet Earth. Due to this proximity (the Sun-Earth distance is about 150×10^9 m), the Sun appears to be the brightest object in our sky, with an apparent magnitude of -26.7 (absolute magnitude 4.8). The Sun is roughly halfway through its lifetime and will continue to burn hydrogen into helium in its core as its main source of energy for approximately another 4 billion years. The Sun is the main driver of Earth's climate and of space weather, which is why it is vital to study this star and understand its activity. This knowledge also improves our understanding of other stars and plasma physics in general.

Compared to the Earth, the Sun is enormous: it has a mass $M_{\odot} = 2 \times 10^{30}$ kg and radius $R_{\odot} = 7 \times 10^8$ m, which corresponds to about 333 000 times the weight of Earth and 109 times its radius². The solar magnetic field strength varies from a few gauss at the poles ($1 \text{ G} = 10^{-4} \text{ T}$), to a few thousand gauss inside sunspots. The Sun exhibits a differential rotation, which means that the rotation rate decreases with increasing latitude: a feature at the solar equator (e.g. a sunspot) will take about 25 days to complete a full rotation, while in the polar regions this may take up to 10 days longer.

¹This overview is inspired by books and reviews from Priest (2014), Aschwanden (2004), Klimchuk (2001), Schrijver and Siscoe (2009), Webb and Howard (2012), Goedbloed and Poedts (2004), Chen (2011), Schwenn (2006) and Pulkkinen (2007)

²<http://solarsystem.nasa.gov/planets/sun/facts>

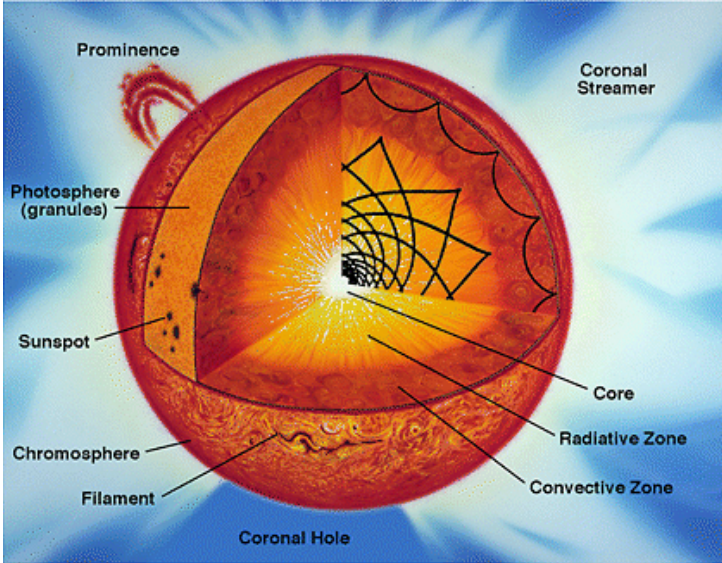


Figure 1.1 *Global model of the Sun. Gravity waves (g -modes) and pressure waves (p -modes) propagate through the solar interior which is divided into the core, the radiative and the convective zone. The lower solar atmosphere is depicted by the photosphere with sunspots and the chromosphere with filaments and prominences. The solar corona shows features such as coronal holes and coronal streamers and extends into the solar wind. (Image source: the SOHO consortium, reproduced with permission from <http://sohowww.nascom.nasa.gov/explore/img/mdigraphic.gif>)*

The solar interior is shielded from our view and thus the solar atmosphere is the only solar region we can observe directly. This means we have to resort to other techniques — such as helioseismology and modeling — to study the Sun’s core as well as its radiative and convective layer (see Figure 1.1). The *core* has a temperature around 15 million K and is the Sun’s source of energy: here hydrogen, which, at 92% of the solar mass, is the most abundant element in the Sun, is transformed into helium through nuclear fusion reactions, releasing enormous amounts of energy in the form of radiation. This radiation propagates outward through the *radiative zone*, which stretches from $0.25 R_{\odot}$ to $0.7 R_{\odot}$. Due to the high density in this region, photons travelling through this radiative zone are absorbed and re-emitted many times, thereby gradually shifting from gamma radiation to longer wavelengths as they lose energy. It takes an average of 1 million years for gamma rays to travel from the solar core into space and

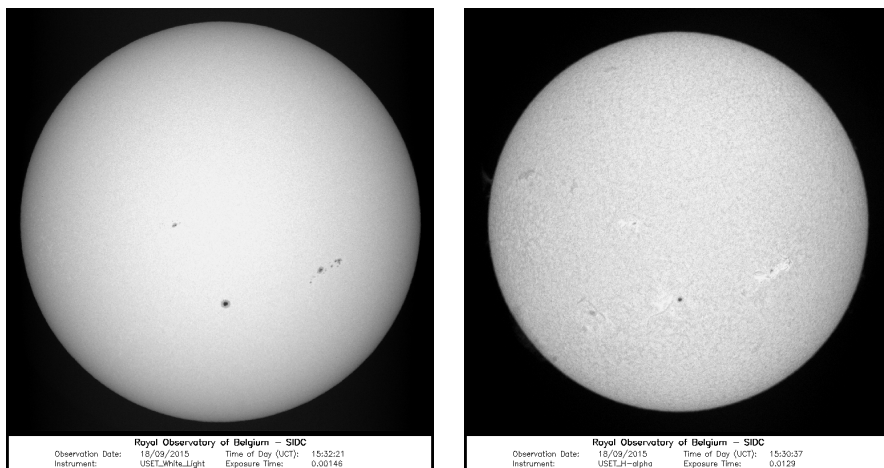


Figure 1.2 *Left Panel:* White light observation made by the Uccle Solar Equatorial Table (USET) on 2015 September 18 showing sunspots in the solar photosphere. *Right Panel:* $H\alpha$ (chromospheric) observation for the same day with active regions and filaments near the locations of the sunspots. (USET images provided by the Royal Observatory of Belgium, used with permission.)

in the process the radiation wavelength is increased to the visible light range (Elkins-Tanton, 2006).

The boundary between the radiative and the convective zone is called the *tachocline* and is thought to be the interface layer in which the magnetic field of the Sun is generated. In the *convective zone*, the energy transport occurs through convective motions (as opposed to radiation) due to the high temperature gradient. Indeed, in this zone the temperature decreases from some millions of degrees at the base of the convective layer to 6000 K at the solar surface. The convective motions in this layer are the source of the granulation pattern that is observed on the solar surface.

The solar atmosphere is the region in which energy (in the form of radiation) can finally escape from the Sun. In addition to the photosphere, this atmosphere consists of three other layers: the chromosphere, transition region and corona. Most of the Sun's radiation is emitted by the *photosphere*, predominantly in white light (that is, visible wavelengths; see Figure 1.2, left panel). Because the Earth's atmosphere largely shields us from the other types of solar radiation, we most often observe the photosphere when we point a telescope on ground towards the Sun. The photospheric layer also defines the surface of the Sun, even though the Sun is actually comprised of plasma and is not a solid sphere.

The photosphere is seen as the solar surface because it is a relatively dense, opaque layer that shields the solar interior from our direct view.

The bottom of the photosphere has an approximate temperature of 6600 K and the layer is a few hundreds of kilometers thick. The photosphere is governed by granular cells, as a result of the convective motions occurring in the convection layer just below. It is also the place where *sunspots* are formed. These sunspots appear as dark regions in the photosphere due to their increased magnetic field (strengths of a few thousand gauss) and lower temperature (~ 4500 K). They have been observed routinely for centuries and their occurrence maps the solar activity cycle (see, for example, Figure 4.4).

The *chromosphere* was first observed as a red glow around the solar disk during a solar eclipse, when the light from the much brighter photosphere is blocked by the moon. The chromosphere extends to about 2000 km above the solar surface and is much less dense than the photosphere. A chromospheric image shows *active regions* on the solar disk, which coincide with the locations of the sunspots in photospheric observations (Figure 1.2, right panel). A narrow *transition region* leads from the chromosphere to the *corona*, the outermost layer of the solar atmosphere. The transition region is in fact not a narrow, static layer on top of the chromosphere: it is the collection of all plasma that is cooling down from or heating up to the much higher coronal temperatures.

Due to the fact that the outer solar corona is not in hydrostatic equilibrium, it is continuously expanding and we thus observe a nearly radial outflow of charged particles, which is called the *solar wind*. The solar wind has a fast (~ 750 km s⁻¹), but relatively uniform component originating from coronal holes and a slow (~ 400 km s⁻¹), more dense and structured component originating from the streamer belt. Measured at the orbit of the Earth, the solar wind density is on average ~ 4 cm⁻³ and the mean magnitude of the interplanetary magnetic field (IMF) is 5 nT (Pulkkinen, 2007). The normal propagation of the solar wind can be disturbed by passing plasma clouds that erupted from the solar corona (coronal mass ejections). Due to the solar rotation, the interplanetary magnetic field follows a spiral pattern, called the *Parker spiral*. As a result the average direction of the IMF in the ecliptic plane is at an angle of about 45° from the radial direction (Hundhausen, 1972).

The solar wind flow of particles permeates space between the planets and continues past the orbits of the most distant solar system objects, filling a region called the *heliosphere*, until it collides with the interstellar medium. As such, it also envelopes our planet and is an important factor in the space weather (see below) affecting Earth. For example, when high speed solar wind overtakes slow speed wind, it creates a *Co-rotating Interaction Region* (CIR). CIRs consist of

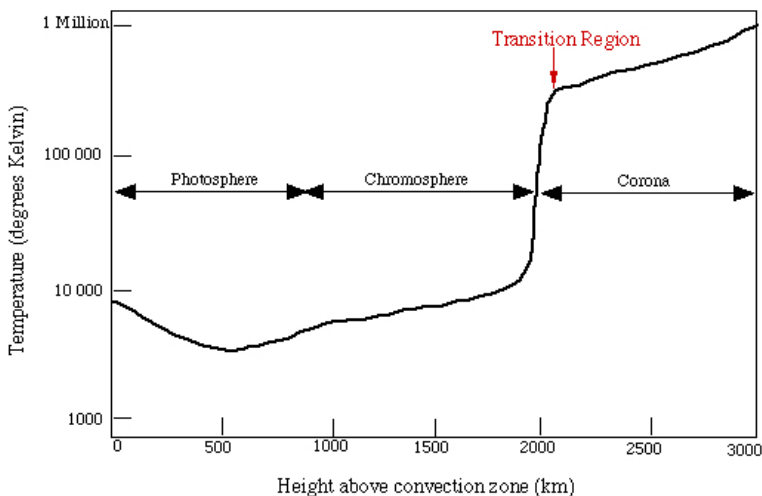


Figure 1.3 *Evolution of the temperature in the solar atmosphere as a function of height. The sharp increase in temperature in the transition region is the subject of the coronal heating debate. (Figure taken from <http://folk.uio.no/gardini/transgraph.gif>)*

solar wind with very high densities and strong magnetic fields and can cause geomagnetic disturbances when they interact with the Earth's magnetosphere.

1.2 The Solar Corona

From ground, the corona has been observed for centuries whenever a solar eclipse occurred: it is then visible as a tenuous halo, a crown (*corona* in Latin), around the occulted solar disk. The coronal light observed during an eclipse is mainly the result of scattering of photospheric light off electrons (K-corona) and dust particles (F-corona). Within 2.3 solar radii, the K-corona is dominant, while the F-corona dominates at larger distances. The intensity of the K-corona is proportional to the electron density, so the corona is brighter where there is denser plasma (Priest, 2014). The E-corona (E for emission) is the result of emission from high-temperature coronal ions that emit in isolated spectral lines in EUV and X-ray wavelengths.

Counterintuitively, the corona is much hotter than the layers below (Figure 1.3): the temperatures in the corona reach a few million degrees compared to a

few thousand in the photosphere, even though the latter is closer to the heat source (the solar core). This puzzling observation is referred to as the *coronal heating problem* and is not yet completely understood. The dominant theories explaining the high coronal temperatures are that it is heated either by magnetic reconnection or by dissipation of magnetohydrodynamical (MHD) waves in the corona. The first mechanism is based on the observation of small-scale flares all over the solar surface. If there are a sufficient number of these nanoflares present at all times, the cumulative energy released during these small-scale reconnection events would suffice to heat the corona. The second mechanism refers to MHD waves that are generated in the convection zone. These waves propagate outwards and carry energy through the solar atmosphere. In the corona they interact with the surrounding material and dissipate their energy as heat.

Due to its high temperature, the solar corona emits X-ray and EUV radiation, and is thus best imaged using satellites in space (outside of Earth's atmosphere which filters out these wavelengths). Eclipse images from ground only show the coronal structure at large heights, the lower corona is obscured by the occulting disk. Extreme ultraviolet (EUV) and X-ray images from space provide a complementary view of the small-scale configuration of the lower corona and of its bubbling activity as well.

Some of the most important coronal features are active regions (AR, see below), coronal loops, coronal streamers, and coronal holes. *Coronal loops* are magnetic loops that connect regions of opposite magnetic polarity. They can occur within one active region and may also connect different active regions. The lifetime of a single loop connecting active regions is around 1 day, however, an entire loop system may persist for several solar rotations. Single strands in active region loops have lifetimes of a few hundred seconds. *X-ray bright points* are tiny bipolar systems, manifesting themselves as a bundle of small-scale loops. They are scattered across the solar disk and have a mean lifetime of 8 hours (Priest, 2014).

Coronal streamers (also called helmet streamers) are the bright, large-scale, cusp-shaped structures that we observe above the solar limb in eclipse images (Figure 1.11, right panel). They correspond to the top of coronal loop systems, where the magnetic field is dragged outwards by the solar wind, hence the cusp-shape. During solar minimum, coronal streamers are observed mainly in the equatorial region, while in the maximum period they are spread over the entire solar limb. As these coronal streamers overlie active regions on the solar disk, this difference in streamer location mimics the location of active regions throughout the solar cycle. As a consequence of the dynamo that generates the solar magnetic field, active regions form at high latitudes (around 40°) during

maximum periods and migrate towards the equator as the solar cycle progresses to minimum conditions.

Coronal holes are dark features on the solar disk, observed in EUV wavelengths, that are linked to the fast solar wind. At these locations plasma is allowed to escape from the solar atmosphere through open magnetic field lines. Due to this plasma evacuation, coronal holes are cooler and less dense than the surrounding regions, which is why they appear dark in images of the corona. The temperature of coronal holes reaches 800 000 K at $1.1 R_{\odot}$ (Murdin, 2001). At solar minimum, two large, and long-living, coronal holes are observed at the solar poles. At solar maximum, they can form at all latitudes but persist for only a few months.

In the corona the magnetic field lines behave as if they move with the plasma. Therefore, we can image the coronal magnetic field in EUV wavelengths, for example in the form of coronal loops that are made visible by the coronal plasma which is trapped inside and emits radiation in EUV wavelengths. This glueing of the plasma to the field lines follows from the induction equation:

$$\frac{\partial \mathbf{B}}{\partial t} = \nabla \times (\mathbf{v} \times \mathbf{B}) + \eta \nabla^2 \mathbf{B}.$$

Here \mathbf{B} is the magnetic field, \mathbf{v} is the plasma velocity and η the magnetic diffusivity. This equation couples the dynamics of the magnetic field to that of the plasma through the velocity term.

One can then define the dimensionless magnetic Reynolds number R_m which decides whether the convective term in the equation (left term on the right hand side) dominates over the diffusive term (right term on the right hand side). If the plasma moves at a characteristic velocity v_0 and length scale l_0 , then the size of both terms can be written as

$$\nabla \times (\mathbf{v} \times \mathbf{B}) \sim \frac{v_0 B}{l_0}, \text{ and } \eta \nabla^2 \mathbf{B} \sim \frac{\eta B}{l_0^2}.$$

Their ratio defines the magnetic Reynolds number:

$$R_m = \frac{v_0 l_0}{\eta}$$

This parameter thus expresses whether diffusion (in case $R_m \ll 1$) or convection (when $R_m \gg 1$) of the magnetic field is dominant in the induction equation.

When $R_m \gg 1$, the induction equation reduces to

$$\frac{\partial \mathbf{B}}{\partial t} = \nabla \times (\mathbf{v} \times \mathbf{B}).$$

With this reduced induction equation, one can prove Alfvén’s frozen-flux theorem, which states that *in a perfectly conducting plasma, the magnetic flux is conserved, so that the magnetic field behaves as if it moves with the plasma*. This theorem follows from the calculation of the rate of change of the magnetic flux through a contour C which is moving with the plasma (Priest, 2014; Goedbloed and Poedts, 2004).

Consider that in a time dt an element $d\mathbf{l}$ of C sweeps out an element of area $\mathbf{v} \times d\mathbf{l} dt$. The rate of change of magnetic flux through C can then be written as:

$$\frac{d}{dt} \iint_S \mathbf{B} \cdot d\mathbf{S} = \iint_S \frac{\partial \mathbf{B}}{\partial t} \cdot d\mathbf{S} + \oint_C \mathbf{B} \cdot \mathbf{v} \times d\mathbf{l},$$

with S the surface defined by C . So the magnetic flux may change due to a variation of the magnetic field in time (first term on the right hand side) or because the boundary moves in space (second term). By setting $\mathbf{B} \cdot \mathbf{v} \times d\mathbf{l} = -\mathbf{v} \times \mathbf{B} \cdot d\mathbf{l}$ and applying Stokes’ theorem to the second term on the right, we obtain:

$$\frac{d}{dt} \iint_S \mathbf{B} \cdot d\mathbf{S} = \iint_S \left(\frac{\partial \mathbf{B}}{\partial t} - \nabla \times (\mathbf{v} \times \mathbf{B}) \right) \cdot d\mathbf{S}.$$

In the perfectly conducting limit, when $R_m \gg 1$, the right hand side of this equation corresponds to the induction equation and thus the term vanishes to zero. The total magnetic flux through the surface S therefore remains constant in time as it moves with the plasma. Thus magnetic flux is conserved and plasma elements that initially form a flux tube continue to do so at later times. This implies that magnetic field lines must move with the plasma. In other words, the field lines are frozen into the plasma. The plasma can move freely along the field lines. However, in case of a motion perpendicular to the field lines, the field lines are dragged with the plasma or the field lines push the plasma.

Because many coronal phenomena, like coronal loops, active regions and prominences, are observed to remain in a quasi-steady or slowly-evolving state for long periods of time relative to the local characteristic time scales — defined by the sound speed, gravitational free-fall speed and Alfvén speed — we can typically simplify the general MHD equations to those of a magnetohydrostatic equilibrium, ignoring flows and time variation. The momentum equation describing the state of the coronal field then reduces to the force balance:

$$0 = -\nabla p + \mathbf{j} \times \mathbf{B} + \rho \mathbf{g},$$

where p is the plasma pressure, \mathbf{j} the current density, \mathbf{B} the magnetic field, ρ the density and \mathbf{g} the gravity.

Each term refers to a force at play in the coronal plasma that this equation describes: the plasma pressure, the magnetic field and gravity. Even though

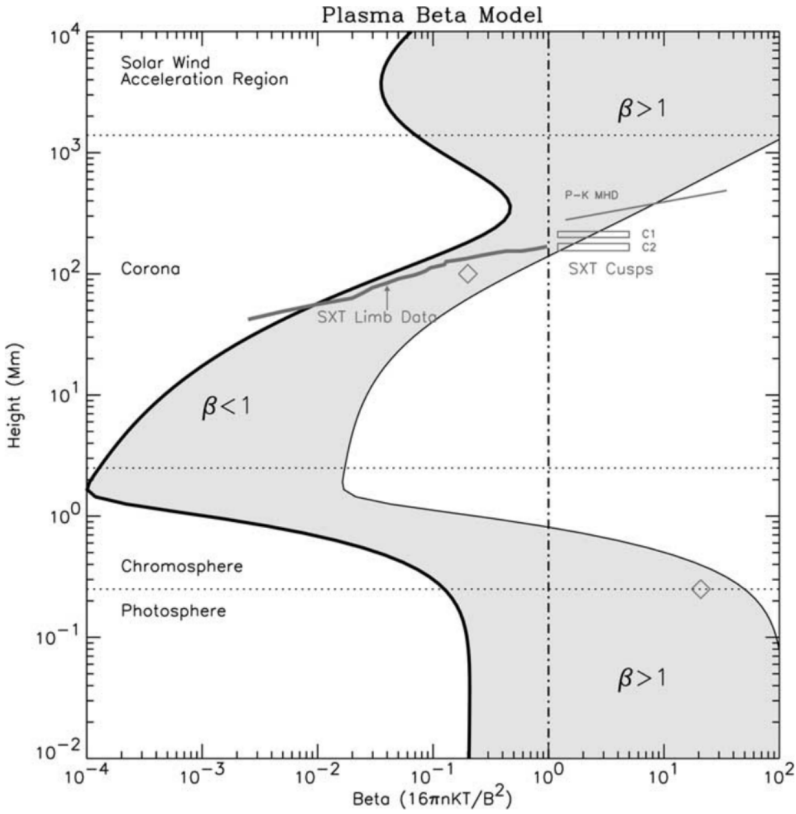


Figure 1.4 Model for the value of the plasma beta over an active region. The plasma beta as a function of height is shown as the shaded region for open and closed field lines originating between a sunspot of 2500 G (thick boundary) and a plage region of 150 G (thin boundary). The vertical dot-dashed line indicates where $\beta = 1$. (Image reprinted from Gary (2001), reproduced with permission.)

gravity is important in the case of, for example, erupting CMEs, it can be ignored in the steady-state approximation. We can then define a quantity called the *plasma* β that describes which of the two remaining forces is dominant. β is defined as the ratio of the plasma pressure to the magnetic pressure (with μ the magnetic permeability):

$$\beta = \frac{2\mu p}{B^2}.$$

Figure 1.4 illustrates the full range of the plasma β at different heights in the solar corona (Gary, 2001). This figure illustrates that in the higher corona, the plasma conditions may result in a high β -value, allowing the solar plasma to escape into the solar wind. Also in the photosphere, high β values are observed and thus the plasma pressure is important in this region. However, in the low solar corona $\beta \ll 1$, which implies that the structure and dynamics in this region are dominated by magnetic forces. In this case, and while still neglecting gravity, this force balance further simplifies to:

$$\mathbf{j} \times \mathbf{B} = 0.$$

This equation defines the force-free approximation for magnetic fields (force-free because under these conditions the Lorentz force vanishes). It also implies that the current density is either zero (current-free or potential magnetic field) or that it is parallel to the magnetic field. (Wiegmann and Sakurai, 2012; Priest, 2014; Parnell, 2010)

If the current density \mathbf{j} is zero, the magnetic field is potential and can be written as $\mathbf{B} = \nabla\phi$. The divergence constraint on the magnetic field $\nabla \cdot \mathbf{B} = 0$ then leads to the Laplace equation $\nabla^2\phi = 0$. Photospheric magnetogram data can be used as boundary conditions to solve this equation, yielding a potential field source surface (PFSS) model of the coronal magnetic field. However, potential fields do not have the electric currents that are necessary for plasma heating and impulsive energy releases, which occur in flares and CMEs for example. Thus, this PFSS extrapolation provides us with only a very approximate geometry of the magnetic field. However, the potential field does yield the minimal energy state for a given boundary condition.

1.3 Solar Activity and Space Weather

Where the Sun may seem to be a quiet orb in our sky —fortunately providing us with the warmth and light that are vital for life on our planet— it is actually a highly-dynamic, bubbling sphere of plasma that exhibits various forms of activity. This activity follows a pattern, known as the solar cycle, during which the Sun’s activity level increases to a maximum and then decreases again. This cycle takes on average 11 years to complete (varying from 7 up to 17 years) and is most clearly, and over a long time range, observed in sunspot observations (see, for example, Figure 4.4). Even though some very large sunspots have been reported on centuries ago, these black dots on the Sun were only observed routinely in white light wavelengths after the first telescopes were pointed at the solar disk. The solar cycle, in turn, was readily discovered once these systematical observations of sunspots started.

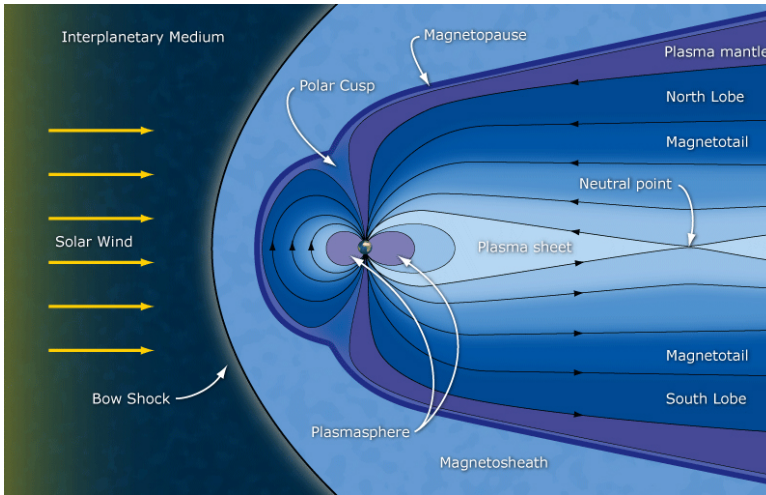


Figure 1.5 *The shape of the Earth's magnetosphere is continuously changing under the influence of the variable solar wind: the dayside magnetic field is compressed, while the nightside field is stretched into a long magnetotail. (Image reproduced with permission from NASA, http://www.nasa.gov/images/content/517890main_Earth-Magnetosphere.jpg)*

We now know that the locations of sunspot observations in white light correspond to the *active regions* we observe in chromospheric $H\alpha$ and coronal EUV wavelengths. These ARs have a much higher temperature and stronger magnetic field (strength of a few hundred gauss) than the surrounding regions, and appear as bright patches in EUV images. Active regions harbor most of the solar activity, even though they make up only a small fraction of the solar surface. These regions are usually confined within latitudes of $\pm 40^\circ$ from the solar equator and may persist for several rotations.

Next to active regions, the solar surface area can be classified into quiet-sun regions and coronal holes. *Quiet-sun* areas may seem undisturbed with respect to the bustling active regions, nevertheless they house many dynamical phenomena, from small-scale nanoflaring and soft X-ray jets to large-scale loop arcades such as filaments. As mentioned before, *coronal holes* are regions of open magnetic field lines that vacate the solar plasma. As such, coronal holes are important contributors to the fast solar wind and may disturb its nominal propagation.

The Sun and its activity play a central role in driving *space weather*. This term refers to the conditions in the interplanetary and near-Earth space environment

that can influence the performance and reliability of space-borne and ground-based technological systems and can endanger human life or health (Pulkkinen, 2007). Our planet is frequently subjected to bursts and flows of high-energy radiation, magnetized plasma, and energetic particles originating from the Sun. As our society's dependence on technology grows, we become increasingly vulnerable to the negative effects of space weather.

Fortunately, the Earth is mostly shielded from space weather hazards by its atmosphere and magnetic field. Where the magnetic field of the Earth is often depicted as a simple dipole, it is actually strongly deformed by the varying solar wind, as is shown in Figure 1.5. The solar wind pressure compresses the Earth's magnetic field on the dayside and stretches the field into a long magnetotail on the nightside, creating a shape similar to that of a comet's tail. Depending on its polarity, the magnetic field that is carried by the solar wind may reconnect with the Earth's magnetic field on the dayside. This reconnection then opens up the magnetic field lines of the Earth, which are transported by the solar wind towards the magnetotail. There, in turn, reconnection is observed between the anti-parallel magnetic field in the magnetotail. This tail reconnection releases two plasma jets of which one is directed towards the Earth, and the other one away from it.

Reconnection with the Earth's magnetic field thus allows the solar wind plasma and particles to travel along the magnetic field lines of the Earth and so they can penetrate deep into the Earth's magnetosphere. This results in intense currents in the magnetosphere, as well as changes in the radiation belts and heating of the ionosphere. These currents, in turn, increase the magnetic field strength and cause a *geomagnetic storm*. Similarly, magnetic *substorms* can occur, which differ from geomagnetic storms in the fact that they occur more frequently and have a shorter duration (timescale of hours instead of days). A geomagnetic storm is observed worldwide, where a substorm primarily impacts the polar regions, leading to more intense aurora. Geomagnetic storms also inject many more particles into the Earth's outer radiation belt than substorms do, resulting in a growth of the ring current surrounding our planet.

Interactions between Earth's magnetosphere and atmosphere on one side, and the solar wind, solar radiation and solar energetic particles on the other, are the main causes for space weather effects. For example, solar flares, which are strong outbursts of electromagnetic radiation emitted by the Sun, may heat up the Earth's atmosphere so that satellites experience increased drag, slow down and descend into a lower orbit. Other important contributors are coronal mass ejections (CMEs): clouds of magnetized plasma that are hurled from the solar corona into interplanetary space and that travel on the background solar wind. In case they arrive at Earth, have a large speed and a properly (southward) oriented magnetic field, they can cause strong geomagnetic storms. Similarly,

high speed solar winds streams originating from coronal holes can cause space weather disturbances, although their effects are usually mild compared to the much more energetic CMEs.

Solar energetic particles (SEPs) can be accelerated to relativistic speeds by shocks in the solar corona. Particles with energies above tens of MeV ($1 \text{ MeV} = 1.602 \times 10^{-13} \text{ J}$) may penetrate deep into the Earth's magnetic field to altitudes of low-Earth-orbiting satellites (~ 300 to 1000 km altitude) and cause damage to their electronic circuits, causing disruptions or failures. Energetic particles are also hazardous to the health of astronauts that travel in space outside of our protective magnetosphere. As the atmospheric shielding is significantly reduced above 10 km altitude, polar airline crews and passengers may also be exposed to increased doses of radiation in case of a severe particle storm. The UK Royal Academy of Engineering estimates that in case of such an extreme event, airline passengers and crew would be exposed to an additional dose of radiation up to 20 mSv , which is comparable to the dose received from 3 CT scans³. This dose exceeds the annual limit for members of the public which is set at 1 mSv . The occupational annual dose is limited to 50 mSv . This upper boundary is maintained by limiting the flight time for crew members on transpolar routes.

Space weather influences other applications as well. The ionosphere, for example, is technologically important because this atmospheric layer reflects radio waves which are used for communication and navigation. Solar flares and geomagnetic storms may influence the charging of this layer and as a result cause disruptions in radio communication, navigation and satellite communication. Aircraft depend on high-frequency (HF) radio waves for their long-distance communications. In case of a strong storm, HF communication may be disturbed or interrupted due to the increased ionisation of the ionosphere (which causes an increase in radiowave absorption). At those occasions, (polar) flights may have to be rerouted or rescheduled, resulting in a high cost for the airline companies (up to $\$ 100\,000$ per flight; National Research Council, 2008).

Space weather effects are even observed on ground, as strong currents in the ionosphere can induce currents in long-baseline conductor systems on ground. Systems that are affected by this include power networks, oil and gas pipelines, telecommunication cables and railway systems (Pulkkinen, 2007). One of the most beautiful consequences of solar activity, however, is the aurora. These polar lights are caused by accelerated electrons that follow the terrestrial magnetic field lines towards the polar regions where they collide with oxygen and nitrogen atoms in the upper layers of Earth's atmosphere. When, afterwards, the excited atoms fall back to a lower energy state, they emit the photons that are observed as the colorful polar lights.

³<http://www.raeng.org.uk/publications/reports/space-weather-summary-report>

Clearly, space weather has a large impact on our technology on Earth and in space. Space weather forecasters therefore attempt to predict severe space weather events so that their impact may be mitigated. This is a difficult task however, and for now the forecasting is limited to the observation of solar eruptions and the assessment of their influence on the Earth's environment. Predicting exactly when an eruption on the Sun will occur, is beyond our capabilities at this point. In order to improve our ability to predict strong space weather events, we thus need a better understanding of what triggers and drives solar eruptions such as coronal mass ejections, which are the main object of study for this thesis.

1.4 Coronal Mass Ejections

1.4.1 Definition and Properties

Coronal mass ejections are large magnetic structures, filled with coronal plasma, that are expelled forcefully from the solar atmosphere and expand into interplanetary space. CMEs are of great importance due to their strong space weather impact on our technologies. Scientifically they are of interest as they remove built-up energy and plasma from the solar corona (Low, 1996) and push it out into interplanetary space.

CME occurrence rates vary from about 2 to 8 per day (Robbrecht et al., 2009a), depending on the phase of the solar cycle. Following the changes in the solar dynamo throughout the solar cycle, CME source regions are clustered around the equator at solar minimum, spreading towards the poles as the corona evolves to solar maximum conditions. The average CME mass is 3×10^{12} kg, while CME kinetic energy ranges between 10^{22} and 10^{25} J (Priest, 2014). Depending on the phase in the solar cycle, their median angular widths range between 47° and 61° (Yashiro et al., 2004), where the angular width distribution shows a significant fraction at the low end ($< 20^\circ$) and a small fraction at the high end ($> 120^\circ$) (Chen, 2011).

Using observations from LASCO, the Large Angle Spectroscopic Coronagraph on the Solar and Heliospheric Observatory (SOHO/LASCO; Brueckner et al., 1995), the mean speed of CMEs was determined to be 300 km s^{-1} at solar minimum, rising to about 500 km s^{-1} at solar maximum. However, this mean value hides a wide range of possible velocities for coronal mass ejections, from less than 20 km s^{-1} to over 3000 km s^{-1} . Above a height of $2 R_\odot$, the CME speeds remain relatively constant in the field-of-view of the coronagraphs although the slowest CMEs tend to show acceleration, while the fastest ones are decelerating.

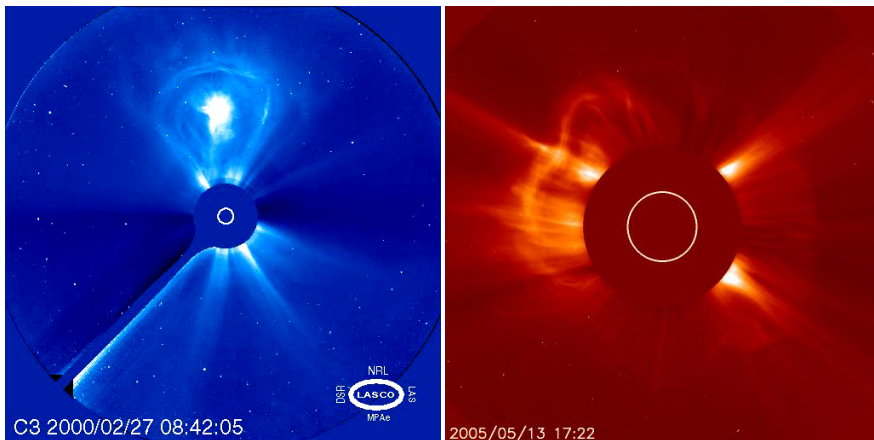


Figure 1.6 *Left Panel:* CME observed by SOHO/LASCO C3 on 2000 February 27, showing the typical 3-part structure: a bright front, followed by a dark cavity and then a bright core. *Right Panel:* Full halo CME observed by SOHO/LASCO C2 on 2005 May 13.

This behaviour is explained by the interaction of the plasma cloud with the surrounding solar wind, which has an average velocity around 400 km s^{-1} in the outer corona (Webb and Howard, 2012).

Attempts have been made to classify CMEs according to their observational characteristics. For example, Sheeley et al. (1999) distinguished two categories according to the kinematic evolution of CMEs: *gradual CMEs*, which start off relatively slowly and accelerate in the field-of-view of coronagraphs, and *impulsive CMEs* that are fast events showing deceleration as they propagate into interplanetary space. These authors associated gradual CMEs with the eruption of prominences and their cavities, and linked impulsive CMEs to solar flares and EIT waves. Vrřnak et al. (2005) challenged this idea of two distinct CME categories and found indications for a continuum of CME properties as opposed to different classes of events.

1.4.2 CME Observations

CMEs are mainly observed using coronagraphs, instruments that create an artificial solar eclipse by using an occulter to block the overpowering visible light from the solar disk and thus making the tenuous outer corona observable. These instruments make use of the Thomson scattering principle, where solar radiation is scattered by free solar electrons. The emission measured by the coronagraph

has an angular dependence which must be accounted for when interpreting the measured brightness, for example in mass calculations (Webb and Howard, 2012). This dependency on the scattering angle also means that CMEs near the plane of the sky are more easily observed. To derive the properties mentioned in the previous section, many of the study authors assumed that the CME was in the plane of the sky. This implies that, unless the CME originated exactly at the solar limb, its derived properties, like velocity, are underestimated while its width is overestimated (Webb and Howard, 2012).

The shape of coronal mass ejections can vary between a narrow jet, probably along open magnetic field lines, and a wide-scale, complex geometry with a closed frontal loop. About 30% of CMEs exhibit a typical 3-part structure in the coronagraph observations: a bright outer loop followed by a dark cavity and then a bright core (Priest, 2014, Figure 1.6, left panel). These 3-part CMEs are often associated with the blow-out of a coronal streamer, which has a prominence lying in its core.

When a CME is directed towards the observing instrument, it is perceived as a halo around the solar disk, and hence these events are called *halo* CMEs (Figure 1.6, right panel). Halo CMEs are especially important when they are directed towards the Earth as these events hold large potential for strong space weather storms. To make matters worse, the influence of these events is hard to predict: these eruptions are observed head-on, which means the observations suffer strongly from projection effects and the true dimensions, speed and direction of the CME are hard to derive. Partial and full halo CMEs comprise about 10% of all CMEs (Priest, 2014). Halo CMEs appear to be faster and more energetic than non-halo events (Gopalswamy et al., 2010). This is most likely not a physical difference, but an observational one caused by the inability of the coronagraphs to detect faint CMEs that originate near Sun center (Webb and Howard, 2012).

Projection effects must always be taken into account when interpreting observations of coronal mass ejections. While these effects are especially strong for halo CMEs, all CME observations are essentially the projection of a three-dimensional structure on a two-dimensional image. The STEREO mission (Solar TERrestrial RELations Observatory; Kaiser et al., 2008) attempts to overcome this problem by having two additional coronagraphs in orbit around the Sun (STEREO/COR, part of SECCHI, the Sun Earth Connection Coronal and Heliospheric Investigation suite; Howard et al., 2008a), providing a side view of any CME headed towards Earth. Both STEREO spacecraft have an orbit similar to that of Earth, with STEREO-A moving ahead in a slightly smaller orbit and STEREO-B lagging behind in a bigger one (see e.g. Figure 3.5 for the position of both spacecraft in August 2010). Figure 1.7 clearly shows how

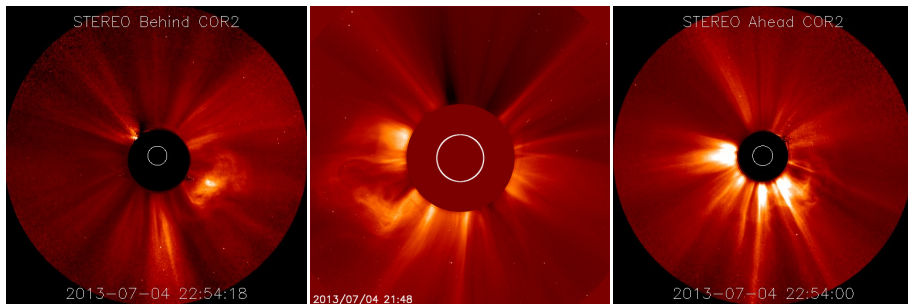


Figure 1.7 *Observations of a CME occurring on 2013 July 4, made by STEREO-B/COR2, SOHO/LASCO C2, and STEREO-A/COR2 (from left to right, respectively). These images illustrate how projection effects can make CMEs appear very different when they are observed from distinct vantage points.*

different the observations of one CME from these 3 distinct vantage points can be.

STEREO-A and -B were launched in 2006, and because of their smaller (respectively larger) orbit, the separation angle between Earth and both spacecraft has been increasing ever since. A crucial phase for the mission started in 2015 when the spacecraft were turning behind the Sun as seen from Earth's point-of-view. This phase was scientifically still very interesting because the spacecraft could provide us with a view of the far side of the Sun, which is normally not observed. However, for the period during which the spacecraft were traversing behind the Sun, it was impossible for them to communicate with the ground station due to the solar radio interference. Towards the end of March 2015, the STEREO-A spacecraft was therefore put into safe mode for a period of 3 months during which no data could be received. On July 11, 2015, the first new images from STEREO-A were transmitted. Communications with the STEREO-B spacecraft were already interrupted earlier as the unexpected result of a planned spacecraft reset on October 1, 2014. Attempts to re-establish communication with STEREO-B are still ongoing at the time of writing⁴.

1.4.3 Models for CME Initiation

It is clear that the required energy to power a strong CME can only come from the coronal magnetic field, which must be in an equilibrium state before it erupts (Chen, 2011). Due to the gradual evolution of the photospheric field,

⁴<http://stereo.gsfc.nasa.gov/news/news.shtml>

currents accumulate slowly in the corona and therefore the corona evolves quasi-statically, as in a sequence of force-free equilibria (Aulanier, 2014). The exact physical mechanism that triggers coronal mass ejections is not yet fully understood, however, the crucial ingredient is a restructuring of the magnetic field that results in a loss-of-equilibrium and an eruption.

Flux ropes (twisted bundles of magnetic field lines) in the solar corona are held in equilibrium by a balance of the outward forces inside the flux rope that tend to push it to expand (magnetic pressure) and the inward and downward forces from the surrounding magnetic field that restrain the flux rope (magnetic tension). Once the equilibrium between these two forces is lost, the flux rope is allowed to rise until a new equilibrium is reached or the flux rope erupts catastrophically.

Several physical processes may facilitate an eruption by eroding the equilibrium of the flux rope until it reaches a new meta-stable state or a state close to eruption. In case a new meta-stable state is reached, the flux rope can resist small perturbations and a strong trigger with significant observable features is needed to initiate an eruption. If the flux rope is close to a loss-of-equilibrium, however, even a minimal change in the magnetic field parameters — for example the magnetic twist — can directly trigger an eruption. (Chen, 2011)

Forbes et al. (2006) discussed a number of different mechanisms that may facilitate and trigger the loss-of-equilibrium that causes previously stable structures in the corona to erupt. Possibilities range from increases (Chen, 1989) or decreases (Lin and Forbes, 2000) in the overall background magnetic field strength in the corona (flux emergence or cancellation) and reconfigurations of the topology of field lines that hold the pre-eruption flux rope in place (referred to as ‘breakout’ by Antiochos et al., 1999), to mass flows that change the net buoyancy of these structures (mass-loading or drainage; see for example Seaton et al., 2011). Given the complexity of the solar corona, it is likely that different eruptions can be triggered by (a combination of) different mechanisms, a few of which are discussed in more detail below.

Aulanier (2014) argues that there are only two mechanisms that can actually initiate a solar eruption: magnetic breakout and the torus instability, or a combination of both. In his view other processes, such as flux emergence or cancellation, are pre-eruptive facilitators, bringing the system to the critical threshold for one or both trigger mechanisms. Once the eruption is triggered, tether-cutting reconnection accelerates the erupted CME, releases stored magnetic energy and produces the flare that develops in the wake of the CME.

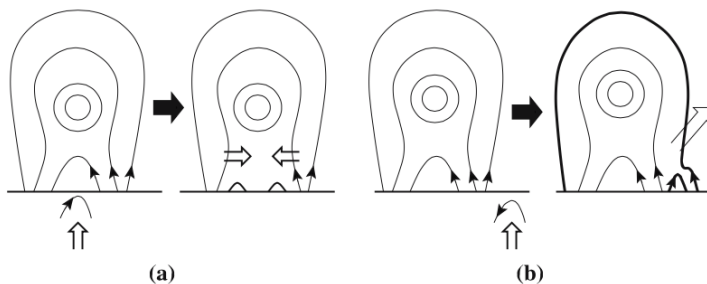


Figure 1.8 *Emerging flux mechanisms for coronal mass ejections, where the magnetic flux emerges inside (panel a) or outside (panel b) the filament channel. (Figure reprinted from Chen (2008), used with permission.)*

CME Facilitators

CME facilitators are slow processes, driven by changes in the photosphere, that gradually modify the configuration of the surrounding magnetic fields, thereby eroding the equilibrium in which the flux rope sits.

Flux emergence. Emerging flux with a favorable polarity may reconnect with the pre-existing coronal field either inside or outside a filament channel, as is illustrated in Figure 1.8. When the reconnection occurs inside the filament channel (panel a), the small magnetic loops below the flux rope are cancelled, thereby decreasing the magnetic pressure locally. This drives plasma inflows which form a current sheet underneath the flux rope and move the flux rope up. Panel b illustrates how emerging flux outside the filament channel may reconnect with the large-scale restraining field lines. This results in an expansion of the outer loop. The flux rope below is allowed to rise and a current sheet forms underneath it. In both cases the change in magnetic configuration forces the core magnetic field to move up and a current sheet to form underneath, hereby creating a new magnetic configuration favorable to eruption.

Flux cancellation. The term *flux cancellation* refers to the disappearance of magnetic flux at the coronal level due to photospheric motions that make the footpoints converge towards the polarity inversion line. During the flux cancellation process, the magnetic field becomes submerged below the photosphere. The converging footpoints may also bring oppositely directed magnetic field close together, allowing reconnection to set in. In that case, part of the restraining magnetic field is converted into flux rope field, thus increasing

the magnetic pressure in the flux rope. At the same time this tether cutting decreases the downward tension of the overlying field.

Shearing motions. Shearing motions in the photosphere are a mechanism by which free magnetic energy can build up in the solar corona, energy which is needed to power a solar eruption. A highly sheared flux rope is also an ideal configuration for tether cutting to take place. Additionally, a magnetic arcade will inflate when it is subjected to shearing motions, leading to a rise of the loop system and the formation of a current sheet underneath, paving the way for a potential eruption of the entire arcade.

Jacobs et al. (2006) investigated how the shearing velocity affects different CME initiation parameters and in addition the possible relation between the magnetic helicity injection rate and the occurrence of eruptive events. Priest (2014) describes *magnetic helicity* as a measure of the twisting and kinking of a flux rope (*self-helicity*) as well as the linkage between different flux tubes (*mutual helicity*). Magnetic helicity is built up by footpoint motions at the coronal boundary. Because it dissipates very slowly in the corona, helicity accumulates as a result of these footpoint motions and can only be expelled by magnetic eruptions. Even during magnetic reconnection, this topological quantity is conserved to a high degree of approximation (Priest, 2014). Thus it cannot be destroyed, simply converted from one form to another. This implies that reconnection can only redistribute the magnetic helicity within a configuration. It often tends to distribute the helicity from small to large scales, so that it approaches the minimal energy state with the same total helicity. Thus injection of small scale magnetic helicity (footpoint motions) drives instabilities that facilitate the relaxation of the system and the transfer of magnetic helicity to larger scales. The total amount of helicity in a system may be an important criterion for the onset of an instability (Jacobs et al., 2006).

CME Triggers

Once the eruption facilitators have put the flux rope in a state close to eruption, it needs a final trigger to lift off. The balance between the outward magnetic pressure and the inward magnetic tension force may be disrupted by changes in the surrounding magnetic field or the internal flux rope field by, respectively, the breakout mechanism or an MHD instability.

MHD Instabilities. Kliem and Török (2006) describe a current ring which experiences an outward hoop (or curvature) force that is balanced by an external potential magnetic field. When this current ring expands, it becomes unstable in case the external field decays sufficiently fast. This MHD instability is called the *torus instability*. Translated to flux ropes, this means that even a weakly

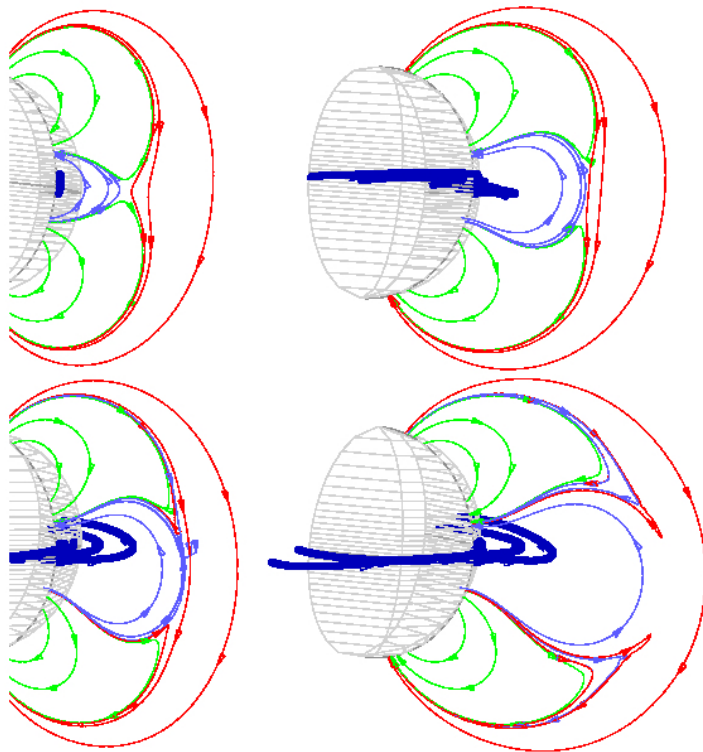


Figure 1.9 *Schematic illustration of the breakout mechanism described by Antiochos et al. (1999). The top left panel shows the initial quadrupolar configuration. In the following panels, the central blue arcade rises due to shearing footpoint motions imposed near the equator that increase the magnetic pressure. The blue field lines then reconnect with the red field lines that belong to the overlying field and have an opposite polarity. They form new field lines that pull away from the magnetic X-point towards the green side arcades. This process diminishes the tension of the restraining field and allows the blue field lines of the central arcade to rise even more and eventually erupt, at least in case of sufficient driving from below. (Figure reprinted from Klimchuk, 2001, used with permission.)*

twisted flux rope may erupt on the condition that the magnetic field strength of the overlying arcades decreases faster with height than the magnetic pressure which pushes the flux rope upwards. Note that this magnetic pressure, in turn, also decreases with time during the rise of the flux rope (Aulanier, 2014).

Another MHD instability, named *kink instability*, refers to a critical twist above which a flux tube is unstable. Török and Kliem (2005) studied a twisted core field that is stabilized by an overlying magnetic field. They found that in case the core field reaches this critical twist and the overlying field decays sufficiently rapid with height, the kink instability is able to produce a coronal mass ejection. On the other hand, in case the decay in strength of the overlying magnetic arcade is too gradual, the result is a failed eruption. However, Schmieder et al. (2013) claim that the kink instability alone only leads to confined eruptions, unless a loss-of-equilibrium height is reached and the torus instability sets in.

Breakout. In the breakout model the loss of equilibrium is caused by reconnection between the overlying magnetic fields and the neighbouring flux systems. This reconnection removes some of the arcades that overlie and confine the flux rope, thereby decreasing the downward tension force. This external tether cutting allows the flux rope to rise, form a current sheet underneath and eventually possibly erupt due to the reconnection in this current sheet below. Prerequisites for this model are the presence of a multipolar flux configuration and at least one null point where the reconnection can occur. This model may also require a relatively strong flare reconnection to produce a fast eruption (Karpen et al., 2012). An illustration of the magnetic field configuration for this model is shown in Figure 1.9.

CME Driving

Generally speaking, the different stages of a solar eruption can be described as follows (Forbes, 2000; Chen, 2011, and Figure 1.10): a flux rope, which may or may not hold a prominence, is held in place by overlying magnetic field lines that are tied to the solar surface. Due to a magnetic reconfiguration or an instability, the flux rope is allowed to rise, stretching the restraining field and forming antiparallel magnetic field lines in its wake. As the flux rope rises further, and because of the line-tying of the flux rope to the photosphere, the antiparallel field below forms a current sheet in which reconnection may take place. This tether-cutting reconnection gradually removes the magnetic tension force of the overlying field lines and facilitates the rapid eruption of the core field into interplanetary space.

The reconnection underneath the flux rope drives the eruption by converting stored magnetic energy into heat and kinetic energy, producing a CME and,

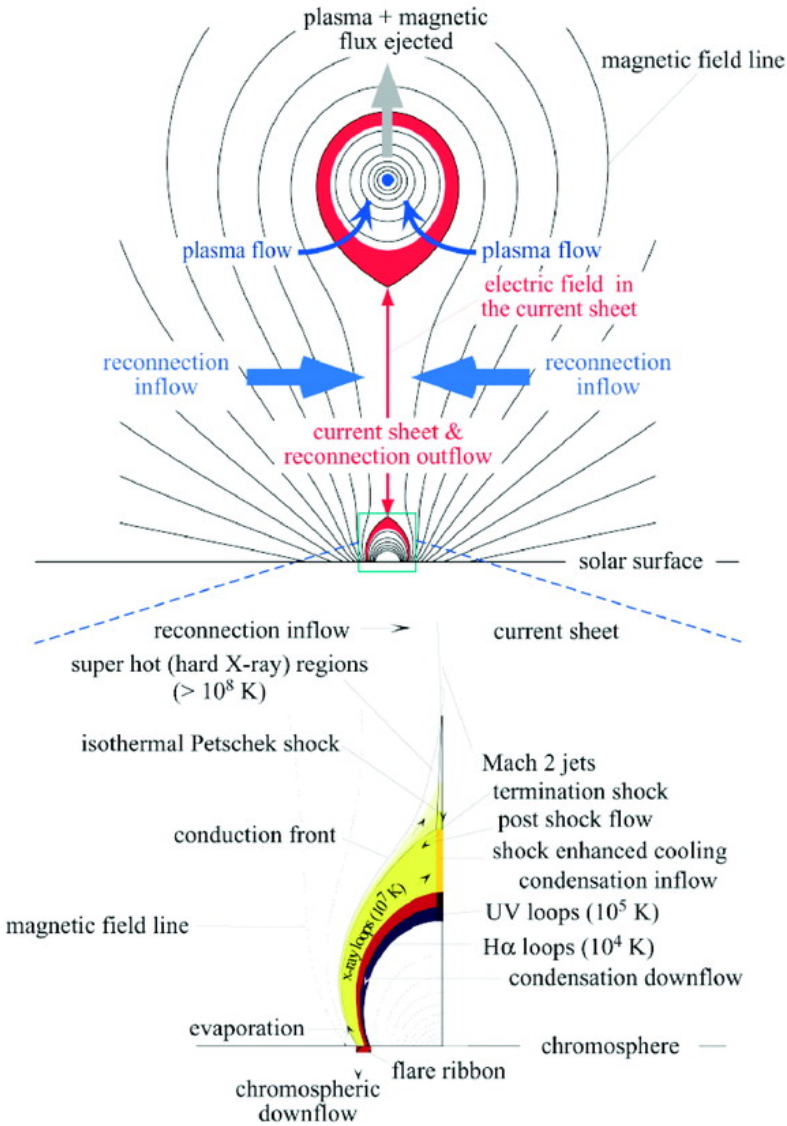


Figure 1.10 Schematic diagram of the various physical processes taking place during a solar eruption. The bottom panel shows the post-eruptive arcade in more detail. (Reproduced with permission from Lin et al., 2005, figure © AAS.)

possibly, a flare. In case no fast reconnection is allowed to take place in the current sheet, the driving is weak. However, even in that case, the flux rope may still erupt due to a loss-of-equilibrium or an ideal MHD instability and no flare, brightening or post-eruptive arcade need necessarily be observed as signatures of the eruption.

1.4.4 Signatures of CME Origin

The onset of CMEs has been associated with various solar disk signatures such as solar flares, eruptive prominences, and post-flare arcades. Other low-coronal signatures that are thought to be related to CMEs are radio bursts and EIT waves. Depending on the nature of a specific coronal mass ejection, all, some or none of these near-solar-surface signatures may be observed. Solar disk phenomena help forecasters to determine the source region of the eruption, which, in turn, allows them to better estimate the trajectory of the CME and forecast the possible space weather effects for a specific event. When these signatures are absent, as is the case for stealth CMEs (see below), it is extremely challenging for space weather forecasters to analyze the eruption.

We describe some of the most common on-disk and low-coronal signatures associated with the eruption of a CME. A remarkable example of a coronal mass ejection, that exhibited many of these associated phenomena, is discussed in detail in Chapter 3.

Solar Flare

A solar flare is a sudden, rapid and intense increase in brightness observed on the solar surface (Figure 1.11, left panel). Most often, X-rays or EUV wavelengths are used to identify these strong increases in solar emission, but the very energetic ones can also be observed in white light. Large flares release up to 10^{25} J (10^{32} erg) of energy. There is no one-to-one relation between flares and CMEs, but both phenomena often come in pairs, originating from the same magnetic instability in the solar atmosphere. Yashiro et al. (2005) found that the flare-CME association depends on the flare strength: while only 20% of the C3 to C9 class flares in their sample was related to a CME, this number increased up to 100% for flares above class X3. (Recent observations of a confined X3.1 flare on 2014 October 24 — discussed by Jing et al. (2015), Chen et al. (2015), and Sun et al. (2015) — contradict this statement. Even so, confined X-flares are extremely rare.) Moreover, brighter flares are most often related to faster and wider CMEs (Schrijver and Siscoe, 2009).

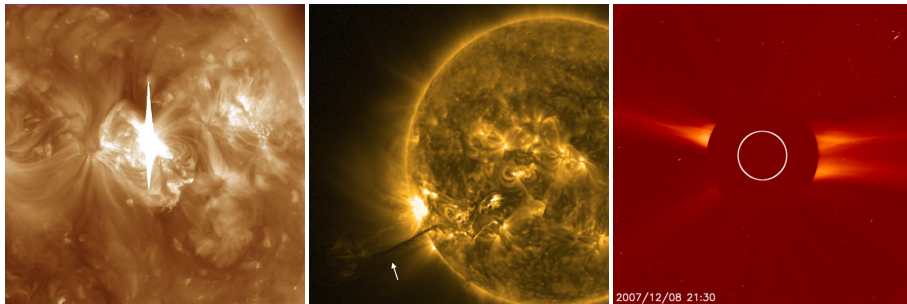


Figure 1.11 *Left Panel:* M6 solar flare observed by the SDO/AIA 193 Å channel on 2011 August 3. The pixels in the detector are saturated due to the sudden increase in radiation. *Middle Panel:* Spectacular eruption of a dark filament (indicated by the white arrow) observed by PROBA2/SWAP on 2012 August 31. *Right Panel:* Coronal streamers observed by the SOHO/LASCO C2 instrument.

When a flare is associated with a CME, the CME usually precedes the flare and contains more energy. When a flare occurs without a related CME it is called a confined flare (see, for example, Thalmann et al., 2015). Flare-less CMEs are actually quite common in the form of filament eruptions (discussed below). When quiescent filaments become unstable, the coronal material can be ejected as a CME without a (strong) flare being observed. Indeed, the destabilization of a filament may be very gradual, therefore no sudden reconnection need necessarily take place and no flares, which are a sure sign of violent magnetic reconnection and heating occurring, need be observed. Most models of solar eruptions now incorporate flares and CMEs as equally important parts of the same magnetically driven event where, depending on the configuration and the available energy, one or the other signature may be more powerful.

Prominence or Filament

A filament is a twisted magnetic structure at the bottom of which cooler and denser chromospheric material can remain suspended above the solar surface for large periods of time. They are typically around 200 000 km long, 6 000 km wide and 50 000 km high (Goedbloed and Poedts, 2004). When observed as bright emissive structures on the solar limb, these arc-like structures are called prominences (Figure 1.11, middle panel). On the solar disk, they are seen as dark absorption fibrils and referred to as filaments. Quiescent prominences may last up to 200 days before they dissipate or activate and are expelled. In an eruptive prominence, (a part of) the filament may form the core of the associated

CME, although dark chromospheric prominence material is sometimes seen to flow back towards the solar surface as well.

Helmet Streamer

A coronal streamer is a dense, bright, quasi-stationary and long-lived magnetic structure observed on the solar limb in coronagraph images. Streamers extend from the base of the corona out to several solar radii and frequently overarch active regions and/or filaments (Figure 1.11, right panel). Their cusp shape allows coronal material to flow into the solar wind. When such a structure is disrupted, it may be seen to increase in size and brightness for days, before erupting into a *blow-out CME*, which often exhibits the typical 3-part CME morphology.

Radio Burst and Solar Energetic Particles

In case the velocity of the CME exceeds the local Alfvén speed in the corona and interplanetary medium, a forward shock may form. This results in various types of radio bursts that are observed in association with the CME. The shock may also accelerate electrons and ions resulting in a solar energetic particle event. SEP events are usually only associated with the fastest CMEs. In case the source region is in the western hemisphere, it may be magnetically connected with Earth through the Parker spiral, allowing the particles to travel along these magnetic field lines and reach our planet. Solar energetic particles take only minutes to hours to cross the Sun-Earth distance and may disturb or damage the electronics of the satellites they encounter on their path. Observations made by EUV imagers or coronagraphs, for example, may show saturated pixels ('snow' or 'streaks') where the particles hit the detector, as is illustrated in the left panel of Figure 1.12.

Coronal Dimming

When a CME erupts, EUV and X-ray images may show a reduction of intensity across a large area of the solar disk, called a coronal dimming. This darkening is interpreted as the evacuation of mass in the low corona. This feature is often referred to as a *transient coronal hole* as well.



Figure 1.12 *Left Panel:* The energetic particles associated with the eruption on 2010 August 14 cause artefacts in the form of white streaks in the SOHO/LASCO C3 images. *Middle Panel:* PROBA2/SWAP difference images show an EIT wave (indicated by white arrows) on 2011 February 15. *Right Panel:* Post-flare loops are observed by SDO/AIA 171 Å on 2012 January 15 in the aftermath of a C1 flare.

EIT Wave

EIT waves are observed in EUV wavelengths as bright, propagating disturbances after the onset of a coronal mass ejection with a typical speed of 200 to 400 km s⁻¹. They were first observed by the Extreme-Ultraviolet Imaging Telescope on-board the Solar and Heliospheric Observatory (SOHO/EIT; Delaboudinière et al., 1995), and were therefore named EIT waves (they are sometimes called EUV waves, coronal waves or coronal bright fronts (CBF) as well). Although Biesecker et al. (2002) found a CME related to nearly every wave observed by EIT, the reverse is not true: not all CMEs are associated with waves. EIT waves are best observed on running difference images, where the difference between two subsequent images is shown (see, for example, Figure 1.12, middle panel).

The exact nature of EIT waves is still under intense debate. Possible explanations include fast-mode MHD waves, slow-mode MHD waves and pseudo-waves due to the restructuring of field lines at the CME front.

Post-eruptive Arcade

Post-eruptive loops are primarily observed in soft X-ray and EUV wavelengths and are the most direct indicators of the source region of a solar eruption. As a result of the magnetic reconnection occurring during a solar eruption, the magnetic loops rise and fill up with heated chromospheric plasma. The

following cooling and magnetic relaxation process is observed as a bright arcade of shrinking loops. An observation of post-eruptive loops is shown in Figure 1.12 (right panel). A schematic diagram of the loops as the result of reconnection in a current sheet below a flux rope is shown in the bottom panel of Figure 1.10.

1.5 Coronal Mass Ejections without Low-Coronal Signatures⁵

CMEs are frequently associated with a variety of phenomena occurring in the low corona before, during, and after onset of eruption. Solar flares, flows, magnetic reconfiguration, EIT waves, jets, coronal dimmings, coronal brightenings, filament eruptions, and the formation of post-flare loop arcades are some of the eruptive or dynamical phenomena in the low corona that often accompany coronal mass ejections. However, CMEs that cannot be associated with any of these low-coronal signatures (LCS) of eruption have been observed as well.

Initially, there were many reports of so-called ‘*problem storms*’: geomagnetic disturbances for which no obvious related solar activity was observed. Indeed, before the STEREO era, CMEs without any clear surface association would be assumed to be *back-sided* events (CMEs occurring at a location on the Sun that is facing away from Earth at the time of eruption). For non-halo CMEs near the solar limb without surface signatures, the assumption was often made that the source region was just behind the limb. Since then, several studies have shown (by taking advantage of the different vantage points of both STEREO spacecraft) that there are indeed *front-sided* coronal mass ejections (thus directed towards Earth) that, even though they are easily visible in coronagraph observations, show little to no signs of eruption close to the solar surface. These coronal mass ejections without low-coronal signatures (LCS) of eruption are the subject of much of the research presented in this manuscript.

We have investigated how the presence or absence of distinct low-coronal signatures can be linked to different theoretical models to establish the mechanisms by which the eruption is initiated and driven. Solar eruptions without clear on-disk or low-coronal signatures can lead to unexpected space weather impacts, since many early warning signs for significant space weather activity are not present in these events. Their lack of surface association indeed makes it hard to determine the solar source region for these CMEs, which, in turn, makes them difficult for space weather forecasters to assess and has

⁵Paragraphs of this section were previously published in D’Huys et al. (2014), © AAS, reproduced with permission.

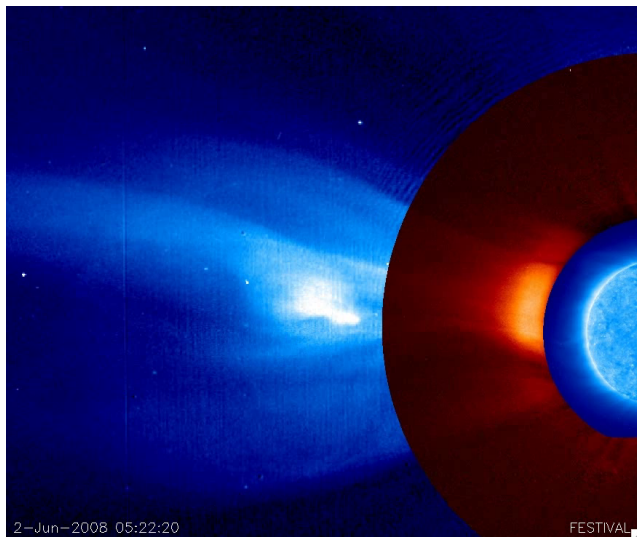


Figure 1.13 *CME observed on 2008 June 2 for which no clear on-disk signatures could be identified by Robbrecht et al. (2009b). This composite picture is an overlay of a STEREO-A/EUVI 171 Å image of the solar disk displaying no low-coronal signatures, an inner coronagraph snapshot from STEREO-A/COR1 depicting the helmet streamer and an outer coronagraph image from STEREO-A/COR2 showing the erupting CME. (Still taken from supplementary movie from Robbrecht et al., 2009b, © AAS, reproduced with permission)*

earned them the title *stealth* CMEs. A better understanding of their initiation mechanism(s) will considerably improve our ability to predict such space weather events.

A seminal case-study of a stealth CME was published by Robbrecht et al. (2009b). This publication described a slowly-evolving, streamer blow-out CME without obvious EUV and H α signatures. 171 Å images from the Extreme Ultraviolet Imager on-board STEREO-A (STEREO-A/EUVI; Howard et al., 2008a) revealed a concave structure above the solar limb, reminding the authors of a flux rope that has not mass-loaded, which explains why there is barely any filamentary material visible in the STEREO-A/EUVI 304 Å data. Once the flux rope destabilizes, it starts to rise and evolves into the core of the CME. Thus, the coronal mass ejection apparently originated unusually high in the solar corona, which clarifies the lack of on-disk signatures. Figure 1.13 shows STEREO-A observations of this event.

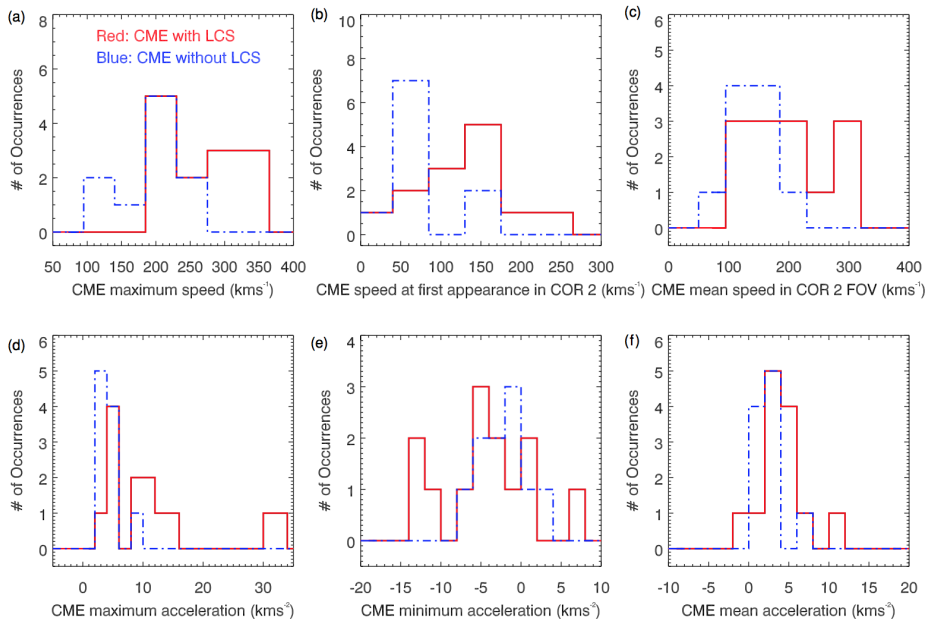


Figure 1.14 Velocity and acceleration distributions for 24 front-side CMEs observed in STEREO/COR2 images that were selected by Ma et al. (2010). The red distributions are for CMEs with distinct low-coronal signatures, the blue ones for stealth CMEs. (Reproduced with permission from Ma et al., 2010, figure © AAS.)

Howard and Harrison (2013) pointed out once more that while the paper by Robbrecht et al. (2009b) gave rise to the term *stealth CME* in several subsequent publications, the concept of so-called *problem storms* is found much earlier in the literature, referring to geomagnetic storms without an obvious solar counterpart. As a result, the terms *problem storms* and *stealth CMEs* are now sometimes used interchangeably. We advise careful wording, however, since the former applies to geomagnetic effects observed near Earth, while the latter refers to the solar origin of these space weather effects. Moreover, many stealth CMEs are not Earth-directed and thus do not cause a problem storm.

Additionally, there is no agreement on the definition of a stealth CME. In Chapter 4 we define a stealth CME as a CME without any signature of eruption, not only on the solar disk but also higher up in the corona. The CME discussed by Robbrecht et al. (2009b) was associated with an erupting flux rope above the solar limb and would thus in our definition not be a true stealth event.

Ma et al. (2010) presented a statistical study of CMEs with and without low-coronal signatures that were observed between 2009 January 1 and August 31 of the same year. They found that during this solar minimum period about 1 out of 3 coronal mass ejections was a stealth-type CME. Their source regions were assumed to be located in quiet-sun areas as opposed to active regions. These authors also investigated the statistical properties of CMEs without low-coronal signatures and found that their velocity is typically lower than 300 km s^{-1} and their angular width smaller than 40° . Figure 1.14 shows the histograms distributions for the velocity (top) and acceleration (bottom) of 24 front-sided CMEs that were identified during this study. The top panels show a shift to the left for stealth CMEs, indicating that they start off slowly and do not reach high speeds. The distributions of the acceleration for both classes, on the other hand, are not clearly separated (lower panels in Figure 1.14).

Interestingly, for 8 out of 11 stealth CMEs, Ma et al. (2010) found off-limb structures, resembling flux ropes that are suspended high in the corona, as was the case for the stealth CME reported on by Robbrecht et al. (2009b). Again, in our study we would not count these events as stealth eruptions.

The number of CMEs studied by Ma et al. (2010) is very low, owing to the deep solar minimum period during which they were observed. This means, however, that their sample size was insufficiently large to obtain statistically significant results and decide whether the nature of stealth CMEs is in fact different from that of CMEs with LCS. Therefore we decided to build on this study and perform a statistical analysis of stealth CMEs during a period of stronger solar activity, in which we hoped to find a statistically relevant sample of CMEs without low-coronal signatures. Apart from studying the observational properties of these stealth CMEs and comparing them to the characteristics of normal CMEs, we were also interested in the — possibly different — initiation mechanism(s) for both classes of events. The results of this investigation are described in Chapter 4.

1.6 Power Laws in Solar Physics⁶

Mathematically, a frequency distribution $N(x)$ of a quantity x can be described by a power law if

$$N(x) \sim x^{-\alpha},$$

where α is called the exponent or scaling parameter. The scaling parameter typically lies in the range $2 < \alpha < 3$, although there are occasional exceptions

⁶Paragraphs of this section are included in a submission to *Solar Physics* (DHuys et al., 2015).

(Clauset et al., 2007, v2). Often only the tail of the distribution follows a power law.

Power law distributions thus describe a relationship between the size and the frequency of a variable, where the frequency decreases faster than the increase in size. Think, for example, of earthquakes: strong earthquakes occur less frequently than weak ones. If the power law holds for all sizes, it is said to 'scale'. This means that there is no typical size of the variable that is representable for the whole class. This is in contrast with normal distributions, where the distribution reveals a central peak and the population can be well described by a mean and a standard deviation. In that case, this mean value is representative for most of the observations (Clauset et al., 2007, v2). In the world of power-law distributions, extreme events are much more prominent. These events in the tail of the distribution are far more likely to occur and have a larger magnitude, in contrast to normal distributions where they can be safely ignored.

Power laws are found in a wide range of scientific domains. Amongst other applications, these distributions are used to describe the intensity of earthquakes, the populations of cities, the distribution of wealth (yielding to 80/20 rule that describes how 80% of the wealth is in the hands of the richest 20% of the population), the frequencies of words in languages, the distribution of internet traffic, and the number of citations received by papers.

Many power laws are reported on in solar physics as well. For example, Vourlidis et al. (2010) found a scaling parameter with value 1 for the power law describing the kinetic energy distribution for coronal mass ejections. This index differs from the values around 2 that were derived for solar flares by several authors (e.g. Berghmans et al., 1998; Hudson, 1991). Indeed, the energy distributions of solar flares also exhibit a power-law behavior over a large range of energies (from major flares down to microflares). Additionally, a wide range of parameters associated with solar flares can be well described using a power law.

Power laws are important because they suggest scale invariance: small and large events have the same properties as they are initiated by the same underlying physical process. For instance, as noted before, a strong correspondence is found between the power-law behavior of the X-ray radiation received from solar microflares and from major flares — even though these events are observed with separate instruments and on widely different physical scales — and indeed most solar physicists believe all flares are powered by one and the same process, called magnetic reconnection.

The fact that the frequency distributions of different solar parameters exhibit a power-law behavior is often attributed to self-organized criticality (SOC; Bak et al., 1987). SOC describes how dissipative dynamical systems naturally evolve

into a minimally stable state through driving by weak external perturbations. These systems are therefore said to ‘self-organize’ to the critical point. A subsequent minor event can then start a chain reaction by which any number of elements in the system may be affected. An analogy that is often used to explain the SOC concept is that of a sandpile with a critical slope on which grains of sand are slowly sprinkled. When the critical slope is reached, an avalanche suddenly occurs. The size distribution for these avalanches takes the form of a power law.

Lu and Hamilton (1991) argued that a solar flare can be interpreted as an avalanche of many small reconnection events, resulting in a power-law distribution for the flare occurrence. This power law suggests that flares are scale-invariant: flares of all sizes are the result of the same physical process and their strength is determined by the number of elementary reconnection events involved. This reasoning can arguably be extended to all solar parameters for which a power law can be derived.

Besides critical phenomena such as SOC, other processes are known to produce power laws, such as network theory, the combination of exponential functions, random walks, multiplication of random numbers, and the Yule process, which is a stochastic process describing how a variable increases proportional to its current size (Newman, 2005). In the case of solar flare waiting times (the time between two consecutive flares), for example, Boffetta et al. (1999) claim SOC cannot reproduce the observed power-law behavior, while MHD turbulence models can.

1.6.1 Power Laws for CMEs

Complementary to carefully selected case studies, statistical studies are an important tool to determine CME properties, and we will apply both approaches in this work. To facilitate the statistical studies, several databases of the observations of CMEs and their kinematic properties have been compiled, both manually and in automated ways. One such catalog is based on the CACTus tool (Computer Aided CME Tracking; Robbrecht et al., 2009a), and we used this database to identify stealth CMEs.

Robbrecht et al. (2009a) describe the general properties of the CMEs in the CACTus catalog and compare the output of the automated CACTus detections to the manually-compiled CDAW (Coordinated Data Analysis Workshops) catalog⁷. Of particular interest to us is the difference between both catalogs

⁷http://cdaw.gsfc.nasa.gov/CME_list/

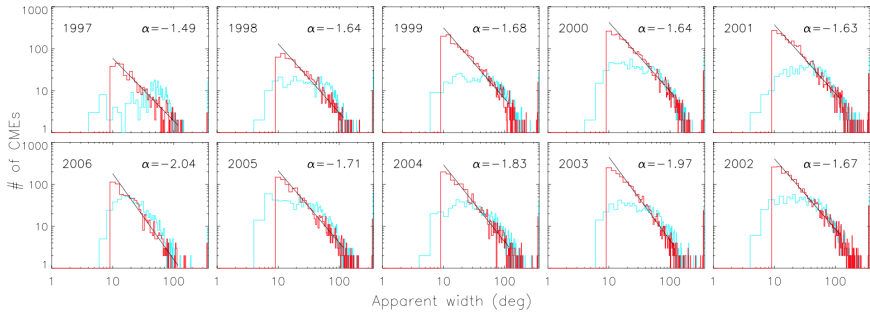


Figure 1.15 *Apparent CME width distributions, displayed per year in log-log scale. The CACTus distribution corresponds to the red curve; the CDAW distribution is represented by the light blue curve. A power-law behavior (straight line on a logarithmic scale) is found within the range $20^\circ - 120^\circ$. (Reproduced with permission from Robbrecht et al., 2009a, figure © AAS.)*

in the CME angular width distributions, which is especially clear for the most narrow events.

This difference is related to the definition of a CME. It is not straightforward to decide whether narrow events such as jets and outflows are to be counted as separate CMEs or should be explained as observations of the turbulent solar wind or bursty outflow related to large-scale CMEs. These events are treated differently by human operators compared to detection software, which explains the difference between both catalogs for narrow events.

In the framework of this discussion, Robbrecht et al. (2009a) studied the angular widths of CMEs that were automatically calculated by the CACTus CME detection tool. They found evidence for the scale invariance of the CME angular span within the range of 20° to 120° : this power law is illustrated in Figure 1.15. This suggests that no typical CME size exists and that a wide-scale coronal mass ejection is not physically different from a narrow transient.

This observation led us to wonder whether the same power law would also be valid for CMEs without low-coronal signatures, or whether a different scaling parameter α would apply. This is an important point as it can shed some light on the intrinsic nature of stealth CMEs and whether they differ from normal CMEs or not. The power law for the angular span of CMEs without low-coronal signatures is investigated in Chapter 4 and Chapter 6.

Chapter 2

Observational Tools to Study Solar Eruptions: the SWAP EUV Imager on-board the PROBA2 Spacecraft

At the Royal Observatory of Belgium one of the primary sources of observational data to monitor the current solar activity and space weather is the *Project for On-board Autonomy* satellite PROBA2, with the *Sun Watcher using APS detectors and Image Processing* (SWAP) and the Large-Yield Radiometer (LYRA) as its main scientific instruments. Both instruments are commanded from the PROBA2 Science Center (P2SC), located at ROB. The SWAP EUV images of solar eruptions were the basis for the observational studies on CMEs, with and without coronal signatures, that are presented in Chapters 3 and 4.

Clearly, much work needs to be done before scientific data from an instrument on-board a spacecraft can reach the users and be exploited in research. The P2SC team developed and tested a complete data processing pipeline for SWAP and LYRA, and maintains it at ROB. The data from the scientific instruments was calibrated and the P2SC team initiated various outreach projects to advertise the satellite, not only aiming at scientists, but also at the general public.

I was involved in the PROBA2 Science Center (P2SC) throughout this PHD. I participated in the final phase development and testing of the SWAP and LYRA data pipelines and the software used to carry out P2SC and spacecraft

operations; and contributed to the maintenance of the P2SC servers as well. I then turned to the scientific exploitation of the data gathered by the PROBA2 satellite: especially the SWAP images have served as a prime resource for the research presented in this manuscript. I also shared my knowledge of the PROBA2 satellite and the inner workings of the P2SC in several outreach projects, aimed mainly at high school students and organized in collaboration with KU Leuven.

The P2SC team indeed supports several outreach projects to make the PROBA2 satellite known to both the scientific community and the general public. In Appendix A, we discuss in more detail two long-term outreach projects that were specifically inspired by the PROBA2 mission and that have been a huge success, reaching out to thousands of high school students over the last six years.

Much of the content of this chapter and in Appendix A was previously published in Seaton et al. (2013a), Dominique et al. (2013), Zender et al. (2013) and Vanlommel et al. (2014). Text excerpts and images are reproduced with permission.

2.1 The PROBA family

The *Project for On-board Autonomy* (PROBA) spacecraft are part of the in-orbit Technology Demonstration Programme of the European Space Agency (ESA). The PROBA missions are a series of low-cost micro-satellites developed as a platform for in-orbit testing of new technologies. These satellites are designed with a high degree of on-board autonomy. Together with ground station automation, this property considerably reduces the complexity of operations and commanding compared to other spacecraft.

The first PROBA satellite, now known as PROBA1, was launched in 2001 and carried Earth-observing instruments as well as instruments measuring the space environment. Although it was originally designed as a two-year mission, PROBA1 remains operational today.

The most important scientific instruments on-board PROBA2, the second satellite in the series, are pointed towards the Sun instead of the Earth (Figure 2.1, left panel). PROBA2 also carries two instruments that monitor the space environment. The third PROBA satellite to be deployed was PROBA V, launched in 2013. The aim of this mission is to map land cover and vegetation growth across the entire planet every two days.



Figure 2.1 *Left Panel:* Artist's view of PROBA2 showing its front side continuously oriented toward the Sun, displaying the instruments used for solar observation. LYRA can be seen as the three vertically-arranged circles on the right. Just below it is SWAP, the grey surface in the bottom right corner. **Right Panel:** The paired PROBA3 satellites will have a highly elliptical orbit with an apogee (or top of orbit) of 60 524 km and perigee of 800 km. An artificial eclipse is formed between the two satellites, allowing for coronagraph observations. These observations and also the active formation flying experiments will be performed towards apogee. Passive formation flying will take place as the satellites circle closer to Earth. (Images courtesy of ESA, reproduced with permission.)

The next PROBA spacecraft will be PROBA3, ESA's first mission in precision formation flying, expected to launch in 2019 (Figure 2.1, right panel). PROBA3 is again a solar mission: a pair of satellites will fly together maintaining a fixed configuration to form a 150 m long solar coronagraph. With these satellites we will be able to study the Sun's faint corona closer to the solar limb than any current coronagraph in space can. Beside its scientific mission, this experiment will be an opportunity to measure the accuracy of the precise positioning of the two spacecraft and to evaluate ESA's formation flying technologies.

2.2 PROBA2

PROBA2 is a micro-satellite with dimensions $600 \times 700 \times 850$ mm and a mass < 130 kg. The PROBA2 satellite was launched on 2009 November 2 together with ESA's Soil Moisture and Ocean Salinity spacecraft (SMOS; Barré et al., 2008). PROBA2's nominal 2-year mission started with the launch of the satellite at the end of 2009 and was extended several times.

PROBA2 was injected into a sun-synchronous polar orbit at a height of approximately 725 km. PROBA2's orbital period is around 98 min. This orbit allows the satellite to perform uninterrupted solar observations throughout most of the year. The nearly constant view of the Sun also ensures the satellite's power supply through its solar panels. Because its orbital plane is slightly tilted away from Earth's rotational axis, PROBA2 nevertheless has an eclipse season. During these eclipse periods solar observations are impossible for part of the orbit, that is, when the spacecraft is orbiting behind Earth. The eclipse periods are further extended as solar EUV imaging is impossible while the SWAP telescope is observing through the atmosphere of the Earth. This is because this layer blocks most of the incoming EUV irradiance from the Sun to which SWAP is sensitive. However, LYRA (the radiometer on-board the spacecraft) makes use of these occultation periods to study the Earth's atmosphere (see below). The maximum eclipse period is less than 20 minutes, and thus the effect of the eclipses on continuous solar observations is minimal.

The scientific interests of PROBA2 are focused on the Sun and space weather. On-board the satellite are two instruments for solar observation: SWAP and LYRA (see below), both operated at ROB. This scientific payload is complemented by two instruments intended to measure the in-situ properties of the magnetosphere: the Thermal Plasma Measurement Unit for Micro-satellites (TPMU) and the Dual Segmented Langmuir Probe (DSLPP). Both instruments are contributions from and operated by the Academy of Science of the Czech Republic (Hercik et al., 2008).

In addition to the 4 scientific instruments on-board PROBA2, the satellite also carries 17 technology demonstrators, divided into two groups: platform technologies which are part of the infrastructure and are mission critical, and passenger technologies meant to gain flight heritage and experience before committing them to the infrastructure of other missions (Gantois et al., 2006; Santandrea et al., 2013). These new technologies include a battery, reaction wheels, a digital sun-sensor, a GPS receiver, a star-tracker, solar panels and a micro-camera.

Because PROBA2's small size restricted the options for on-board control systems, all of the star-trackers necessary for maintaining attitude control are mounted on the top panel of the spacecraft platform. Thus, in order to keep the star field observed by these trackers from being obstructed by the Earth, PROBA2 performs four Large Angle Rotations (LARs) over the course of every orbit. These maneuvers rotate the spacecraft 90 degrees at regular intervals during PROBA2's 98 minute orbit (Figure 2.2). The spacecraft's capability to calculate and perform these LAR maneuvers autonomously is one of the technological advances tested by ESA during the PROBA2 mission.

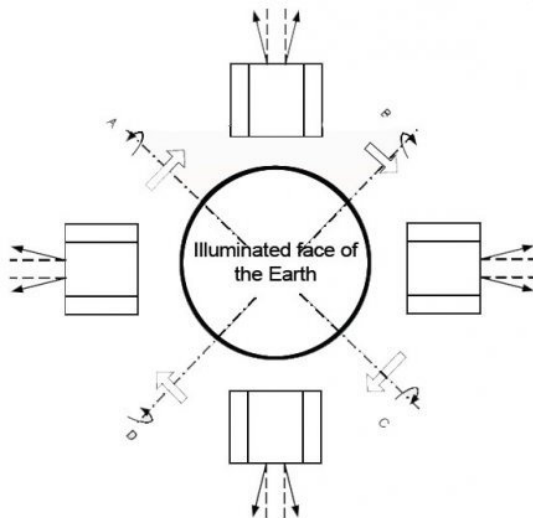


Figure 2.2 *Schematic overview of PROBA2’s Large Angle Rotation manoeuvres. The arrows on top of the spacecraft indicate the position of the star trackers as well as their viewing direction. (Image adapted from Santandrea et al., 2013, used with permission.)*

PROBA2 is unique among current solar-observing spacecraft because of its highly flexible off-pointing capability. The imager can off-point up to 5 degrees away from sun-center in two axes to map the corona far off the solar disk and follow solar eruptions farther into space than any EUV imager has done before. Large off-points are only used for calibration purposes, whereas smaller off-points are commanded in order to make SWAP mosaic images. In these mosaics multiple off-pointed exposures are combined to one image of the Sun and its outer corona. Such observation campaigns are useful to fill in the gaps between the low corona, visible in EUV images, and the more extended, and fainter, corona observed in coronagraph images (Seaton et al., 2013a).

2.3 PROBA2 Science Center¹

The PROBA2 Science Center (P2SC) is a small-scale science operations center supporting the solar observation instruments on-board PROBA2: SWAP and

¹This section is largely based on Zender and 20 co-authors, including D’Huys (2013). Text reproduced with permission.

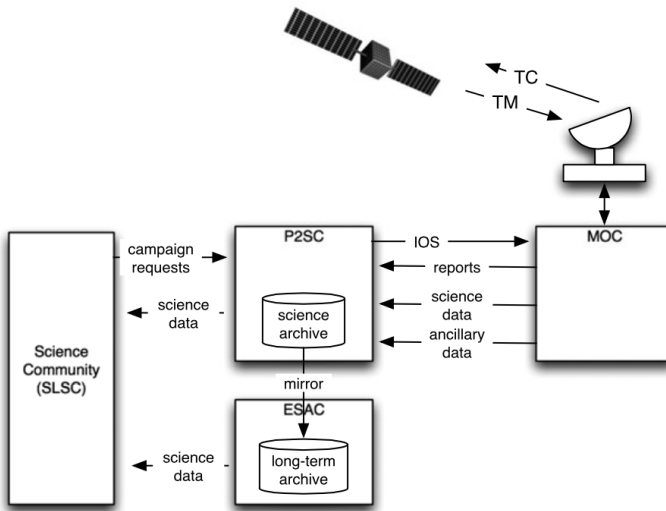


Figure 2.3 Schematic overview of the ground segments for PROBA2. Image taken from Zender et al. (2013), see text for explanation on the acronyms. (Image used with permission.)

LYRA. The P2SC is hosted at the Royal Observatory of Belgium, where it is co-located with the Principal Investigator (PI) teams of both instruments. The P2SC tasks cover instrument commanding and monitoring, science planning, data processing, supporting outreach activities and the distribution of the scientific data products.

PROBA2 Ground Segments

The main building blocks of the PROBA2 ground segment are depicted in Figure 2.3. The spacecraft sends telemetry (TM) to and receives telecommands (TC) from the Mission Operation Center (MOC) in Redu, Belgium. From there, the scientific and ancillary data are forwarded to the P2SC in Brussels, where they are processed to produce calibrated measurements that can be used by the scientific community. ESA’s European Space Astronomy Centre (ESAC) maintains the long-term archive of these scientific data. The high-level commands for the solar observations are sent by the P2SC to the MOC in an Instrument Operations Sheet (IOS) over a secure connection. The Science Consortium for SWAP and LYRA (SCSL) may request specific observation campaigns for the solar instruments to the P2SC.

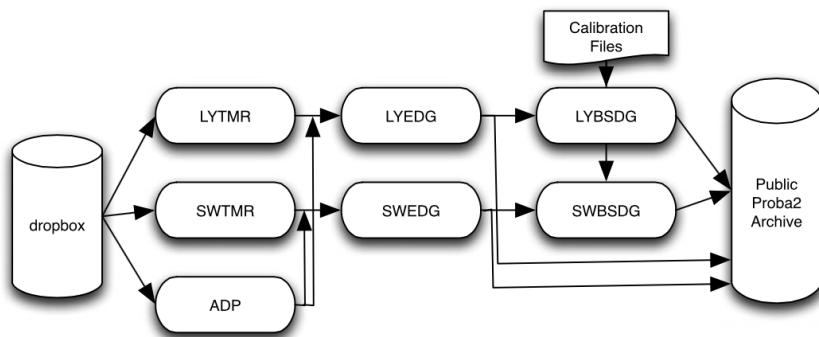


Figure 2.4 *Architectural overview of the P2SC data processing. Image taken from Zender et al. (2013), see text for explanation on the acronyms. (Image used with permission.)*

Data Pipeline Architecture

The P2SC data pipeline processes all raw data files that are transferred by the MOC into intermediate files and databases, and finally into scientific data products. The data flow passes through 30 modules, written in various programming languages. A graphical interface allows the operator on duty to monitor the data pipeline, as well as several instrument and spacecraft housekeeping parameters. As such the operator can easily assess the health and nominal operations of the solar instruments on-board PROBA2.

Figure 2.4 illustrates the general architecture of the P2SC data pipeline. Incoming data arrive in one of three formats: SWAP images, LYRA measurements and ancillary data; and is received from the MOC over a secure ftp connection. The processing is carried out by three chains that can be run in parallel. The housekeeping data are directly processed and stored into databases by the Ancillary Data Processor (ADP). SWAP and LYRA data are first reformatted from raw telemetry by the SWAP and LYRA Telemetry Reformatters (SWTMR and LYTMR). Next, they are combined with the auxiliary data into level-0 data files (by the Engineering Data Processors, SWEDG and LYEDG). Finally, calibration is applied by the Base Science Data Generators, SWBSDG and LYBSDG, to turn these files into scientific level-1 data files. Each of the tools in Figure 2.4 was formally tested and validated with respect to the predefined software specifications (test reports on internal wiki page; D’Huys, 2009-2010) both before the launch and during the commissioning phase (December 2009 to March 2010).

Several additional SWAP and LYRA data products are available. Besides the nominal level-1 data files, LYRA measurements are also distributed averaged over one minute, and in the format of PNG images containing 1-day and 3-day quick-look overviews of the LYRA curves. Additionally, the LYRA team composes a list of flares that are observed in the LYRA data, which is updated semi-automatically. In 2014, the LYRAFF (LYRA Flare Finder) tool was introduced in the LYRA pipeline to automatically search for flares in the LYRA measurements (Ryan et al., 2016, in preparation).

SWAP data are provided in the form of quick-look images in JPEG format, daily movies, and time-series files containing mean integrated flux which are referred to as SWAVINT (for SWAP Integrated Intensity) files. Deep exposure SWAP-movies, running over an entire Carrington rotation, are generated by stacking many individual images to improve the image signal-to-noise ratio (especially high up in the corona) and are distributed through the P2SC website. Additionally, an automated flare detection tool was developed based on the SWAP images. SoFAST (the Solar Flare Automated Search Tool; Bonte et al., 2013) automatically processes the SWAP images and localises and identifies solar EUV flares by thresholding macro-pixelled image sequences. This tool will be an important instrument in the identification of the stealth CME events that are studied in Chapter 4.

2.4 Scientific Instruments on-board PROBA2

LYRA and SWAP, the two main scientific instruments on-board the PROBA2 spacecraft observe the Sun continuously, only interrupted by calibration or other dedicated scientific campaigns and eclipses.

2.4.1 LYRA²

LYRA, the *Large-Yield Radiometer* on-board PROBA2 (Figure 2.5, panel a), is a compact solar X-ray and UV radiometer, manufactured by a Belgian-Swiss consortium including ROB, the Centre Spatial de Liège (CSL, Belgium) and the Physikalisch-Meteorologisches Observatorium/World Radiation Center (PMOD/WRC, Switzerland). LYRA monitors the variability of the solar irradiance in four different passbands, selected for their relevance to aeronomy, space weather and solar physics (Zender et al., 2013).

²This section is based on Dominique et al. (2013). Text reproduced with permission.

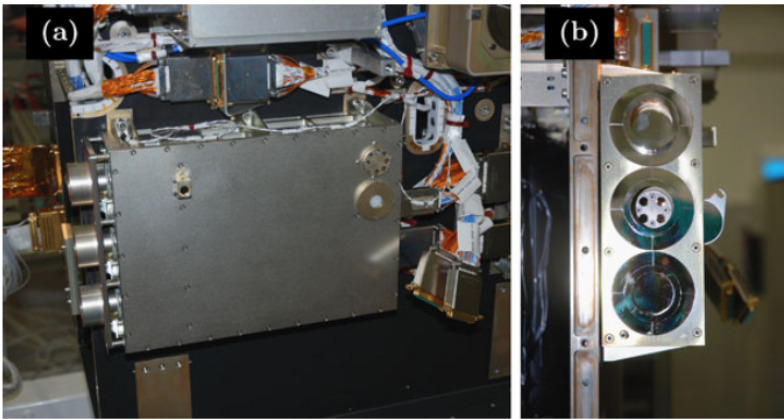


Figure 2.5 *Panel a:* The LYRA radiometer mounted on the PROBA2 spacecraft. *Panel b:* The open cover of the nominal unit 2 reveals the four observation channels. (Image taken from Dominique et al., 2013, used with permission.)

Instrument Overview

LYRA is equipped with newly developed diamond detectors that have a high bandgap energy that makes them insensitive to visible light (Hochedez et al., 2006; Dominique et al., 2013). Therefore, visible light blocking filters, which considerably attenuate the desired ultraviolet (UV) signal, are not needed. The absence of these filters, in turn, improves the signal-to-noise ratio and thus the precision of the instrument.

LYRA observes the solar irradiance with three units, which each make measurements in the same four UV passbands: the Lyman- α channel (120 to 123 nm), the Herzberg continuum (190 to 222 nm), the Aluminium channel (17 to 80 nm) and the Zirconium channel (6 to 20 nm). The difference between these units lies in the combination of filters and detectors that have been chosen to achieve these bandpasses. The nominal unit (unit 2) is fully equipped with pioneering diamond detectors and is used continuously (Figure 2.5, panel b). The two other units are a mix of diamond and classical silicon detectors to allow a comparison of both technologies. The use of these last units is mostly restricted to calibration campaigns, during which, for example, the aging effects on diamond detectors are monitored.

Scientific Opportunities

LYRA adds sub-second cadence (nominally 20 measurements per second, high-cadence up to 100 measurements per second) to the ensemble of solar irradiance experiments that are in orbit already. The time series recorded by LYRA are ideally suited for the high-cadence study of solar flares. Comparing the flare profiles in LYRA channels with observations of instruments acquiring at other wavelengths —such as the X-Ray Sensor on-board the Geostationary Operational Environmental Satellite (GOES/XRS; Hanser and Sellers, 1996) and SDO/EVE, the Extreme Ultraviolet Variability Experiment on the Solar Dynamics Observatory (Woods et al., 2012)— allows to determine a chronology of the temperature evolution in the flare and to confront it with the theoretical scenarios for energy release.

In addition, LYRA’s exceptionally high sampling rate enables to detect short-timescale phenomena, such as quasi-periodic pulsations (QPP), and to study them in more detail. QPPs are oscillations in intensity that are observed in various wavelengths during solar flares and that have periods from fractions of a second to a few minutes (Van Doorselaere et al., 2011; Dolla et al., 2012).

While the eclipse periods disrupt normal observations by SWAP, at the same time they provide LYRA with the scientific opportunity to study the composition of Earth’s upper atmosphere. Depending on the chemical nature of the atmospheric layers, part of the solar radiation is absorbed. Analyzing the extinction curve of the LYRA (and SWAVINT) channels as the PROBA2 satellite drops into the shadow of the Earth can therefore provide information about the atmospheric constituents as a function of altitude.

2.4.2 SWAP³

The *Sun Watcher using APS detectors and Image Processing* (SWAP; Berghmans et al., 2006; Seaton et al., 2013a; Halain et al., 2013) is an EUV imager designed for space weather monitoring and includes various innovative technologies such as its CMOS-APS detector (see below). SWAP is a follow-up of the successful EIT imager on-board the SOHO spacecraft. SWAP’s image cadence is an order of magnitude better than that of EIT, but has now been surpassed by that of the Atmospheric Imaging Assembly on-board SDO (AIA, Lemen et al., 2012). SWAP can track the evolution of many events in the solar corona that are relevant for space weather, including flares, CMEs, EIT waves, and EUV dimmings. In addition, SWAP continuously images solar features such as

³This section is largely based on Seaton and 19 co-authors, including D’Huys (2013a). Text reproduced with permission.

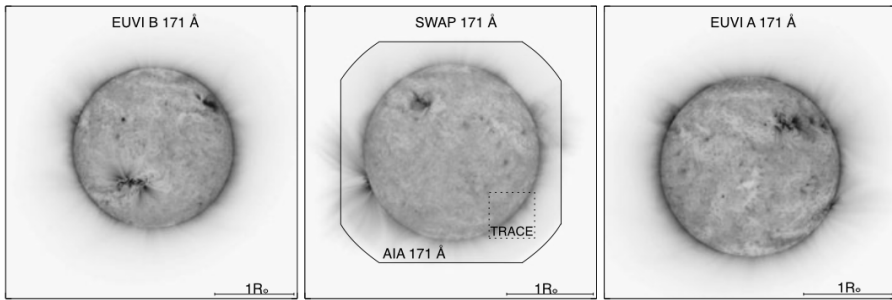


Figure 2.6 Comparison between the SWAP field-of-view (center, large frame) and those of AIA (center, polygon), TRACE (center, dotted square), EUVI-A (right), and EUVI-B (left). (Image taken from Raftery et al., 2013, used with permission.)

coronal holes and active regions, the locations of which are essential information for space weather forecasters.

Over the last decades, multiple EUV imagers were launched, each with their own strengths and capabilities. The first EUV imager of the modern era was EIT, which was a groundbreaking instrument for solar physics in revealing the turbulent dynamics of the solar corona. It was followed by TRACE, the *Transition Region And Coronal Explorer* (Handy et al., 1999). This spacecraft provided coronal images at an unprecedented spatial resolution (1 arcsec) and temporal cadence (less than 1 min). However, this came at the cost of losing the full view of the solar disk: the field-of-view of TRACE is only 3.5% of the area of EIT’s field-of-view (Figure 2.6; Raftery et al., 2013).

Compared to more resource-rich contemporary EUV imagers such as EUVI on-board STEREO and AIA on SDO, SWAP offers only modest temporal and spatial resolution. For example, SWAP’s nominal cadence is about 2 minutes and its spatial resolution is 3.2 arcsec, while SDO/AIA observes in 10 different wavelengths with 4 telescopes at an image cadence of about 10 seconds and with a resolution of 1 arcsec.

However, SWAP’s design and operational strategy result in some unique capabilities compared to other solar EUV imagers. In particular, SWAP images are useful because they provide the largest EUV field-of-view available from Earth orbit (out to $1.8 R_{\odot}$ and even $2.5 R_{\odot}$ on the diagonals, Figure 2.6) and SWAP’s complementary metal-oxide-semiconductor active-pixel system (CMOS-APS) detector does not bloom significantly during bright flares, when nearly all other detectors do so (see, for example, the left panel of Figure 1.11). In addition,

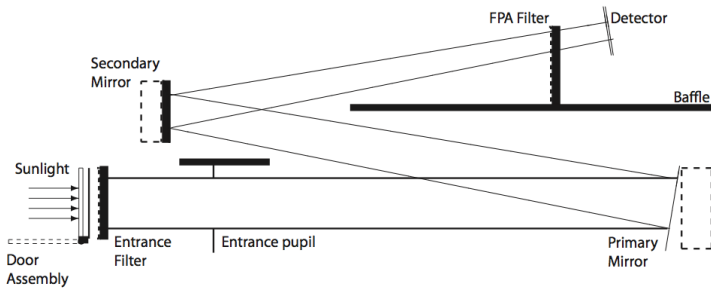


Figure 2.7 *Schematic overview of the SWAP optical path, which is folded into SWAP’s 565 × 150 × 125 mm case. (Image taken from Seaton et al., 2013a, used with permission.)*

the agility feature of PROBA2 permits SWAP to off-point, allowing imaging of extended coronal features. In nominal operations, the off-point for SWAP is at most one degree, because a stronger off-point would prevent sufficient solar signal to reach the detector. Larger off-points are only commanded during calibration maneuvers, when a dark field-of-view for SWAP is required (see below).

Instrument Overview

The EUV solar telescope SWAP was developed and tested by CSL. The instrument has a spectral bandpass centered over 17.4 nm and provides images of the low solar corona over a 54×54 arcmin field-of-view. The dimensions of the SWAP telescope are $565 \times 150 \times 125$ mm. Its mass is approximately 11 kg for the telescope, the power unit and the data-processing unit combined. SWAP’s peak power consumption is just 2.6 W.

The optical layout of the SWAP instrument is illustrated in Figure 2.7. The spectral selection is achieved with a set of aluminium foil filters, together with EUV reflective multilayer coatings deposited on the two mirrors of the Ritchey-Chrétien off-axis telescope. This design minimizes the telescope length while retaining good optical quality and allows for a simple and efficient internal baffling system. One filter is located at the instrument entrance to avoid excessive heating of the primary mirrors, and the secondary one is inserted near the focal plane to eliminate any residual visible stray light from potential light leaks in the front housing or the entrance filter itself. The compact design of the SWAP telescope allows for reduced filter diameters resulting in a lower risk of damage during launch. The multilayer coatings of the mirrors play a dual

role: they provide EUV reflectivity in nearly normal incidence and they also ensure the fine spectral tuning of the instrument.

SWAP is the first solar instrument in orbit to be equipped with a CMOS-APS detector (De Groof et al., 2008). More specifically, SWAP is equipped with the High Accuracy Star-tracker (HAS) detector, developed for ESA by Fillfactory (now part of Cypress). In contrast to a CCD, a CMOS detector does not transport the charges from pixel to pixel during the readout. Therefore, SWAP has no need for a shutter, leaving the door as the only mechanism on the telescope (Berghmans et al., 2006). SWAP's CMOS-APS detector is sensitive to visible light, so the sensor surface is covered by a scintillator coating that absorbs incoming EUV radiation and re-emits it as visible light (at 545 nm).

In the typical ten-second integration time used in nominal SWAP observations, bright features in the corona do occasionally become saturated, and thus clipped by the instrument electronics. However, despite the fact that the detector is operated with its anti-blooming protection switched off, in SWAP images signal from saturated pixels rarely overflows into pixels beyond their immediate neighbors as often occurs in CCD (Charge-Coupled Device) images, creating large areas of blooming (see, for example, the left panel of Figure 1.11). So saturation in SWAP images is not as much of a concern as it is for CCD-based instruments.

As a result of the spacecraft's Large Angle Rotations, which occur approximately every 25 minutes, the orientation of images from SWAP changes correspondingly. It takes PROBA2 several minutes to carry out the LAR maneuver and restabilize itself afterwards, and any images obtained during one of these maneuvers will be blurred by the motion of the spacecraft. For simplicity, observations on-board PROBA2 were originally not suspended during a LAR; instead, LAR-blurred images were detected on the ground and removed from the SWAP data archive during calibration. Since 2015, however, the spacecraft calculates the LAR window and flags blurred images on-board, so telemetry is no longer wasted on the download of the scientifically useless LAR images.

SWAP images are compressed by the platform computer on the PROBA2 satellite. To improve this image compression, malfunctioning pixels are first replaced by the median of their local neighbors by on-board software. Discontinuities, which are typically caused by cosmic rays, are removed from the image before compression as well. In addition to the image compression, a novel image prioritization scheme also contributes to making efficient use of the limited spacecraft telemetry by first downloading the most interesting scientific data. The operator on-ground has the ability to specify a priority for each commanded image as well, which may, for example, be used during special scientific campaigns.

Calibration⁴

SWAP images must be calibrated to transform the raw data that the spacecraft delivers into useful scientific data. There are various effects that influence the quality of an image, which can be divided into three groups: platform effects, optical effects and detector effects. An ideal calibration process would remove all instrumental effects and yield an image in which all correctable noise has been removed. Shot noise and read noise cannot be removed from images, meaning that no calibrated image is perfectly noiseless.

Platform effects are caused by the behavior of the PROBA2 spacecraft. For example, the spacecraft pointing may be inaccurate, placing the Sun off-center in the image. Due to its roll, the spacecraft is also not oriented in the same way as the Sun. Solar north may thus be at an arbitrary angle, pointing sideways in the image frame. These effects can generally be corrected for by simple affine transformations applied to the image coordinates. In a second step, the data array is then interpolated to the new image coordinates. Note that SWAP calibration software automatically detects images with a commanded off-point and does not translate the position of the Sun to the center of the image frame for these exposures (Seaton et al., 2013a).

Optical effects include distortion of the image itself and attenuation and dispersion of the incoming signal due to imperfections in the mirrors and filters in the optical system. This category thus includes several effects that are caused by the optical path of the telescope. For example, the telescope causes a small amount of distortion which results in images of a slightly elliptically instead of circularly shaped Sun. For SWAP, this distortion can be corrected for by another affine transformation.

The telescope design includes several filters and mirrors, which have imperfections that affect the recorded signal. For example, the filter support grid attenuates the signal. Attenuation can also be caused by shadowing and vignetting (this last term refers to reduction of the brightness of the image in the periphery as compared to the center). The attenuation that these imperfections in the optical path cause, can be characterized and results in the instrumental *flat field* or instrumental *gain*.

A third optical effect is dispersion: the telescope has a *point-spread-function* (PSF) which describes how much the light of a point source is spread out over more than one pixel (for example due to internal scattering, pinholes in the front filter or imperfect coating of the mirrors), resulting in so-called *stray light*. In SWAP's case the only significant source of stray light is non-specular reflection

⁴<https://wis.kuleuven.be/CHARM/images/partners/seaton-rachmeler.pdf>

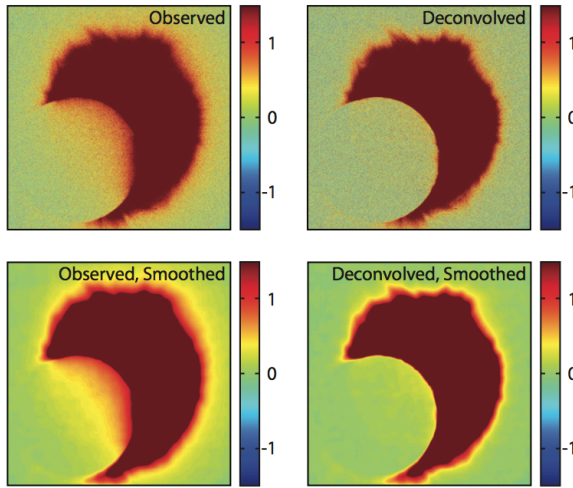


Figure 2.8 Comparison of lunar eclipse images before stray light correction (left column) and after (right column) in units of DN. The bottom row presents the same images smoothed with a 32×32 boxcar to reduce noise. (Image adapted from Seaton et al., 2013b, © AAS, reproduced with permission.)

by the multi-layer mirror coatings, which results in a PSF with an extremely narrow core and broad wings (Seaton et al., 2013b). The core is narrow enough to be entirely contained within one pixel, while the broad wings spread signal to distances as large as hundreds of pixels, far from its origin. Therefore, stray light effects are most pronounced in the dark regions near the edge of SWAP’s field-of-view. One method of stray light removal is to deconvolve the image with the estimated PSF. To estimate this PSF, eclipse images are used. The Moon and inner planets do not emit in EUV wavelengths. However, EUV images of the transit of these objects in front of the Sun do show scattered light from the Sun across their disks, which makes it possible to determine the PSF directly from solar images using a blind deconvolution process (see Seaton et al., 2013b). After a deconvolution of the eclipse images with the estimated PSF, they show a sharply defined and completely dark Moon, thereby confirming the validity of the estimated PSF (Figure 2.8; Seaton et al., 2013b).

Detector effects are dominated by *dark current*, which is temperature-dependent noise that arises from spontaneously generated electrons in the detector pixels. Note that SWAP has a passively-cooled CMOS-APS detector, which results in a relatively high detector temperature (approx. 0°). This means that dark current has a major influence on the image quality (Seaton et al.,

2013b). As is the case for all signals, the dark current has a electron shot noise, which is a random temporal noise that scales as the square root of the signal.⁵

Additionally, each pixel in the SWAP instrument has its own electronics and thus its own unique behavior, leading to a spatial noise in the SWAP images. So for each of SWAP's one million pixels a dark model was constructed, depending on temperature, to characterize this noise. These empirical dark current models have been derived from a series of calibration campaigns that were conducted throughout the PROBA2 mission. During these campaigns the noise was characterized with dark SWAP images taken at different temperatures, while the spacecraft was off-pointing to avoid any solar signal reaching the detector. Using these models it is possible to reconstruct the dark current in an image and remove it via subtraction.

The detector may also show defects in the form of, for example, *bad pixels*, which are not functioning properly and result in speckling in the image. Bad pixels can be corrected by replacing them by the median of their neighbors.

The *bias* is a precharge value of the detector, resulting from the voltage that is applied to it. The bias is constant and independent of exposure time or temperature. It can thus easily be subtracted from the measured image. In SWAP's case, however, the bias is already removed from the image due to the Correlated Double Sampling (CDS) readout mode that is routinely used for SWAP observations. In CDS mode, SWAP's pixels are read out twice, in the beginning and at the end of an exposure, and the resulting values are subtracted from each other to obtain the signal (De Groof et al., 2008). This subtraction removes the bias that is present in both images.

The recorded image is the result of the sequential application of many transformations to the incoming signal by the platform, optical system, and detector. We denote the perfect, incoming solar signal by \mathbf{S} , which is a 1024×1024 array of data values that can be represented by a 1024×1024 matrix. In the calibration process, we work backwards from the measured image \mathbf{I} to reobtain \mathbf{S} .

The effects of the spacecraft orientation and any (affine) distortions resulting from the optics of the instrument can be described by an affine transformation, $f_T : \mathbf{S} \rightarrow \mathbf{S}'$, that results in \mathbf{S}' , a transformed matrix of the solar image.

Each of the other instrumental effects described above further modifies the incoming signal. Inspired by the articles of M. V. Newberry in *CCD Astronomy*⁶,

⁵This shot noise is sometimes called *thermal noise*. However, there is no consensus on the definition of calibration terms. We therefore have attempted to be as specific as possible on the terminology used in this section.

⁶Seaton (2001), http://physics.bgsu.edu/~layden/Anim/CCD_Images/ccd_flatfield.htm

we can derive an equation to describe these other transformations in order, which can then be inverted to obtain the calibrated incoming signal.

$$\mathbf{I} = [(\mathbf{S}' \Delta t) \circ \mathbf{G}] * \mathbf{P} + \mathbf{d}(\mathbf{T}) \Delta t + \mathbf{B}_0 + \text{Error}$$

In the equation above, \mathbf{G} represents the correction needed for the detector gain and the instrumental flat field combined. \mathbf{P} is the telescope's point-spread-function, \mathbf{d} the dark current and \mathbf{B}_0 the bias. (Note that \mathbf{G} , \mathbf{P} , \mathbf{d} and \mathbf{B}_0 are all 1024×1024 matrices as well.) The dark noise and the signal are dependent on the integration time Δt (which determines how many photons are collected). The symbol \circ denotes a Hadamard product of the transformed signal $\mathbf{S}' \Delta t$ and \mathbf{G} , which is an element-wise multiplication of two matrices.

The residual error is mainly *photon and electron shot noise* (originating from the discrete nature of photon composition of light) which can be modeled by a Poisson distribution and thus scales as the square root of the recorded signal. Additional residual error results from the readout by the detector, the clipping of the signal, and the nonlinearity of the SWAP detector. The digitization process, during which the detector converts continuous photon measurements to discrete data numbers, introduces a discretization error as well. All of these are included in the *Error* term in the equation above.

This equation provides a framework that shows how one can undo the various transformations applied by the instrument, working backwards to recover the original incoming solar signal that entered the telescope (up to the limitations of instrumental error)⁷.

The calibration of level-0 files is performed by the SWAP Base Science Data Generator (SWBSDG, Figure 2.4) and results in level-1 scientific data. Level-0 FITS (Flexible Image Transport System) files contain complete image data in raw detector data numbers (DN) with all of the associated metadata needed to generate calibrated images stored as FITS keywords in an image header. Level-1 FITS files are calibrated and corrected by the P2SC software following the principles described above. These images are also time-normalized, so individual pixel values are given in units of DN s⁻¹. Images that are blurred by LARs or intended for calibration purposes are not converted into level-1 format. The level-1 SWAP FITS archive thus only contains images useful for scientific analysis, while the level-0 archive contains all images recorded by SWAP. A level-0 image and its corresponding level-1 image are shown in Figure 2.9. This figure clearly illustrates the vast improvement in image quality that is obtained by the SWAP calibration.

⁷Note that the equation above is a conceptual representation of the transformations that are applied to the incoming signal. The actual calibration process is not applied using this kind of mathematical formalism.

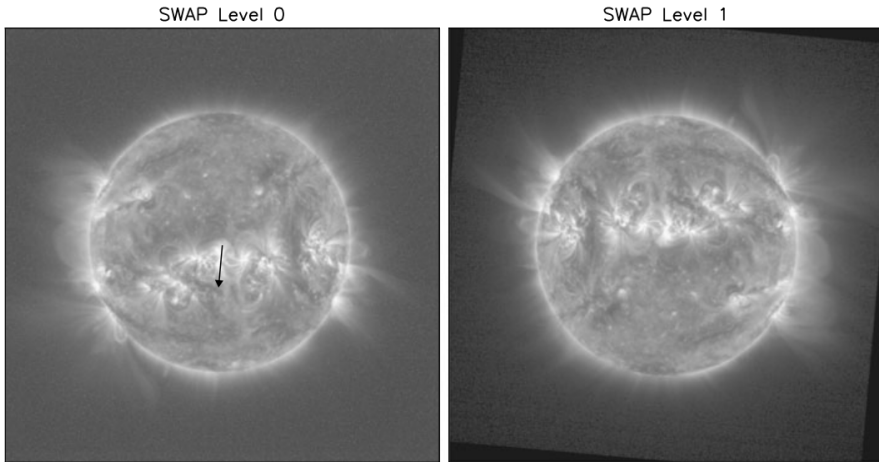


Figure 2.9 *An original SWAP image as observed on-board (that is level-0, left) and the same image after correction for spacecraft orientation, pointing, and instrumental effects such as dark current (level-1, right). The arrow in the uncorrected image indicates the direction of solar north, while north is oriented directly upwards in the level-1 image. (Image taken from Seaton et al., 2013a, reproduced with permission.)*

2.5 Personal Contribution

When I joined the PROBA2 team at ROB, my initial task was the testing and validation of the P2SC software. I first performed tests on each pipeline module separately, in collaboration with the developers. In a next step, we combined the different modules step-by-step into 3 pipelines, and I performed the software tests on these pipelines as well. This testing phase was crucial in preparation for the launch of the PROBA2 spacecraft: we needed to be able to process the incoming data as soon as the instruments on-board saw their first light.

Some pipeline modules and operator tools were still in an early development phase when I joined the P2SC. For those building blocks, I participated in the design discussions. In addition to this testing and design of the P2SC software, I performed setup and maintenance tasks for the P2SC servers.

Once the first data from the spacecraft were received, several improvements to the software modules were made. Each improvement required a reprocessing of the previously obtained data on a separate dedicated server, which I performed several times during the first year after the launch. After each of these

reprocessing efforts, I also carried out a careful integration of the reprocessed data on the nominal P2SC server.

In the early phase of the mission, I assisted the PROBA2 team with operator tasks such as monitoring the data processing pipelines and resolving reported errors. These operator tasks are performed using several tools which I tested before launch.

Once the operational part of the mission was running nominally, I turned to the scientific exploitation of the SWAP data. While performing my own research, described in this manuscript, I was a member of the SWAP science team and participated in the weekly SWAP meetings that are aimed at advancing our research through discussion. Furthermore, I contributed to the P2SC Guest Investigator Program (see Appendix A) by reviewing proposals and supporting the visitings scientists.

In addition to these software and research tasks, I dedicated a lot of time and effort to the outreach concerning PROBA2. In collaboration with ROB-colleague Petra Vanlommel, I initiated the Proba2@School project for high school students which is described in detail in Appendix A. This appendix also explains how this project evolved into a Junior College program, thereby reaching an even larger public.

2.6 Conclusions

PROBA2 is a successful technology demonstration platform, space weather monitor and solar observatory. It provides EUV images and solar irradiance measurements that are crucial for the space weather forecasting done at ROB. The unique characteristics of PROBA2's solar instruments, such as the diamond detectors on LYRA and the large field-of-view of SWAP, make these instruments a valuable addition to the existing solar instrumentation.

The SWAP images are used in near-real time in a space weather context to determine the sources of coronal mass ejections and decide whether these events are front-sided (directed towards Earth) or not. In that sense, SWAP images and detections by the SoFAST tool will be an important source of information for the identification and study of stealth CMEs, presented in Chapter 4. We also use SWAP data extensively in the analysis presented in Chapter 3, where we especially took advantage of the extended field-of-view available in SWAP images.

Chapter 3

The 2010 August 14 Rotating CME: a Forecasting Case Study

A first analysis of this solar eruption was presented in poster form at the *Sun 360: Stereo-4/SDO-2/SOHO-25 Workshop* (July 25-29, 2011 in Kiel, Germany) and during the *First European school on Fundamental processes in space weather: a challenge in numerical modeling*, organised by the SWIFF network from 4 to 9 June, 2012, in Spineto, Italy. We reported on further progress with a new poster at the *5th Solar Orbiter Workshop* in Bruges, Belgium (September 10-14, 2012). We are preparing a paper on this CME to be submitted in 2016 to the *Journal of Space Weather and Space Climate*.

This work benefitted from discussions with A. De Groof (ESA) and C. Jacobs (then CmPA). The STEREO-A in situ-data were obtained by L. Rodriguez (ROB). J. Magdalenic (ROB) assisted us with the interpretation of the radio data.

3.1 Introduction

On 2010 August 14 an unusual filament eruption occurred on the north-west solar limb. It was one of the first strong eruptions of solar cycle 24, which had just started to rise in activity at the time. This eruption was associated with a

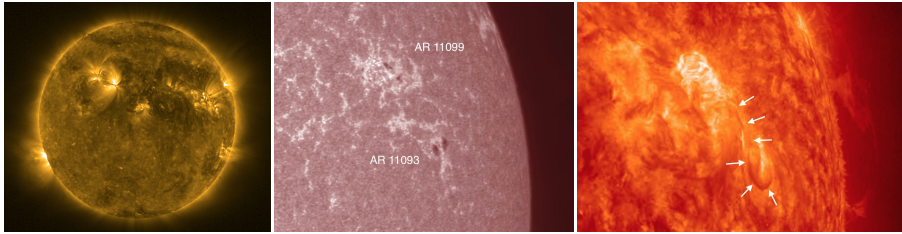


Figure 3.1 *Left Panel:* PROBA2/SWAP 174 Å image of the Sun on 2010 August 14 at 04:15 UT. The eruption studied in this chapter occurred in the upper right quadrant. *Middle Panel:* SDO/AIA 1700 Å image, taken at 05:35 UT, with annotated NOAA active region numbers. *Right Panel:* SDO/AIA 304 Å image, taken at 08:25 UT. The white arrows indicate the location of the filament that will erupt shortly after.

fast CME. However, this CME was also accompanied by only a weak solar flare. The eruption was also the source of the first proton event recorded in nearly four years¹. Moreover, the destabilized filament exhibited a notable untwisting motion as it was accelerated away from the Sun. Figure 3.1 shows the source regions for these eruptions in PROBA2/SWAP and SDO/AIA images, with annotated active region numbers provided by NOAA, the National Oceanic and Atmospheric Administration.

As this was a period with few significant solar eruptions, many authors were interested in this event. For example, Long et al. (2011) studied the kinematics and expansion rate of the associated coronal bright front (CBF, more commonly known as an *EIT wave*). Using multi-wavelength radio observations, Tun and Vourlidis (2013) derived the properties of the magnetic field within the core of the CME associated with this eruption. We took a different interest in the 2010 August 14 CME and focused on the initiation mechanism for this event. We obtained a comprehensive interpretation of this eruption combining observations made by STEREO, SDO/AIA, PROBA2/SWAP and SOHO/LASCO.

Indeed, an important question regarding solar eruptions is what mechanisms trigger such eruptions and the magnetic reconnection that drives them. Several models offer explanations for these triggers. One of the proposed mechanisms is magnetic flux emergence, which assumes that an initial flux rope equilibrium breaks down as a reaction to the injection of magnetic energy when additional flux emerges on the nearby solar surface. The flux cancellation mechanism, on the other hand, explains the loss of equilibrium by the disappearance of magnetic flux near the neutral line that separates regions of opposite magnetic polarity.

¹<http://umbra.nascom.nasa.gov/SEP/>

As we will demonstrate, SDO/HMI (Helioseismic and Magnetic Imager; Schou et al., 2012) magnetogram observations show a significant amount of change in the amount of flux observed in the eruption region, which suggests that one of these mechanisms may have been involved in facilitating the eruption on 2010 August 14.

Steed and Lapenta (2011) studied the similarities between the event on 2010 August 14 and a homologous eruption that originated from the same source regions on 2010 August 7. Both events are associated with the eruption of a reverse S-shaped filament structure, a flare, a coronal dimming and an EIT wave. The coronagraphs on-board the STEREO spacecraft observed a halo CME in both cases. Further collaborative study (Steed et al., 2012) showed that while for both eruptions similar signs of eruptions (such as the reverse S-shaped flux rope structures and EIT waves) were observed, their interplanetary evolution was rather different. These authors emphasize that minor differences between the CMEs close to the solar surface (such as small differences in velocity and propagation angle), as well as variations in the surrounding solar wind (for example, compression by a high speed solar wind stream from a coronal hole), may result in very different interplanetary propagation profiles for homologous CMEs.

The eruption on 2010 August 7 was investigated extensively by other authors as well. For example, Vemareddy et al. (2012) describe how the slow rising of a reverse S-shaped filament, lying along the polarity inversion line (PIL), resulted in a fast CME and a long-duration, two-ribbon flare of class M1.0 (the start and end times reported by GOES are 17:55 and 18:47 UT, with the flare peak at 18:24 UT). The source region was NOAA AR 11093, which had a simple magnetic β -configuration (that is, a bipolar region with a simple and distinct boundary between both polarities). The authors explain the onset of the eruption with the tether-cutting model (Moore et al., 2001). Flux emergence and cancellation are observed in different regions around the eruptive filament. Vemareddy et al. (2012) interpret these changes in the magnetic flux, in combination with localized brightenings, as signs of tether weakening. In this process, the magnetic field overlying the filament reconnects with the field to the side. This reduces the magnetic tension of the overlying field and destabilizes the filament, allowing it to rise slowly. The onset and driving of the filament eruption is then triggered by tether-cutting reconnection below the filament.

Feng et al. (2012) applied a three-dimensional mask fitting reconstruction method to observations by different coronagraphs of the 2010 August 7 eruption in order to investigate the three-dimensional evolution of the associated CME. They attribute a southward deflection of the CME to the influence of the fast solar wind emanating from a nearby coronal hole. Their 3D reconstruction allows the authors to interpret the in-situ observations from the Venus Express

spacecraft (VEX; Zhang et al., 2006), STEREO and the Advanced Composition Explorer (ACE; Stone et al., 1990). In a follow-up paper, Feng et al. (2013) compared 5 different methods for 3D CME reconstruction, using the data from the 2010 August 7 event.

Furthermore, Srivastava and Murawski (2012) studied the motions of hot and cool plasma in the post-flare loops that were observed during the decay phase of the 2010 August 7 two-ribbon flare. The EUV dimming associated with the 2010 August 7 eruption was studied by Mason et al. (2014).

3.2 Observations

3.2.1 Filament Eruption

On 2010 August 14 the EUV imagers PROBA2/SWAP, SDO/AIA and STEREO-A/EUVI observed a strong filament eruption that occurred on the north-west limb of the Sun. Two separate active regions, linked by a filament, were involved: NOAA AR 11099 (north) and NOAA AR 11093 (south). These active regions were classified according to their magnetic configuration as, respectively, a β (bipolar) and an α (unipolar) region. PROBA2/SWAP images show these regions crackling with small-scale activity until the filament finally rises, starting around 08:50 UT.

Prior to the eruption, the first signs of activity are seen in the form of flickering bright points and small plasma flows, mainly in the northern active region. Around 08:54 UT, SDO/AIA 171 Å images show the onset of the rise of the filament that connects both active regions. The filament first starts to rise in the southern region, and subsequently drags the northern part with it until equilibrium is lost. Then the southern part of the filament erupts violently and the northern part is trapped in the corona. As the filament unwinds the erupting plasma is hurled into space with a significant untwisting motion. Similarly to what is described by Vourlidis et al. (2011), this rotation may be caused by the disconnection of one of the CME footpoints, in this case the southern one, early in the eruption.

Figure 3.2 shows the evolution of the eruption in SDO/AIA 171 Å and STEREO-A/EUVI 195 Å images. Just before 09:00 UT, the filament (indicated in the top panels by a white arrow) starts to rise, becomes unstable, and finally erupts one hour later. As it is ejected into interplanetary space, the southern part of the filament unwinds (panels on second and third row), while the northern part remains confined in the corona. The post-eruptive loop system is clearly visible in the bottom panels in Figure 3.2. Note that these SDO/AIA images also show

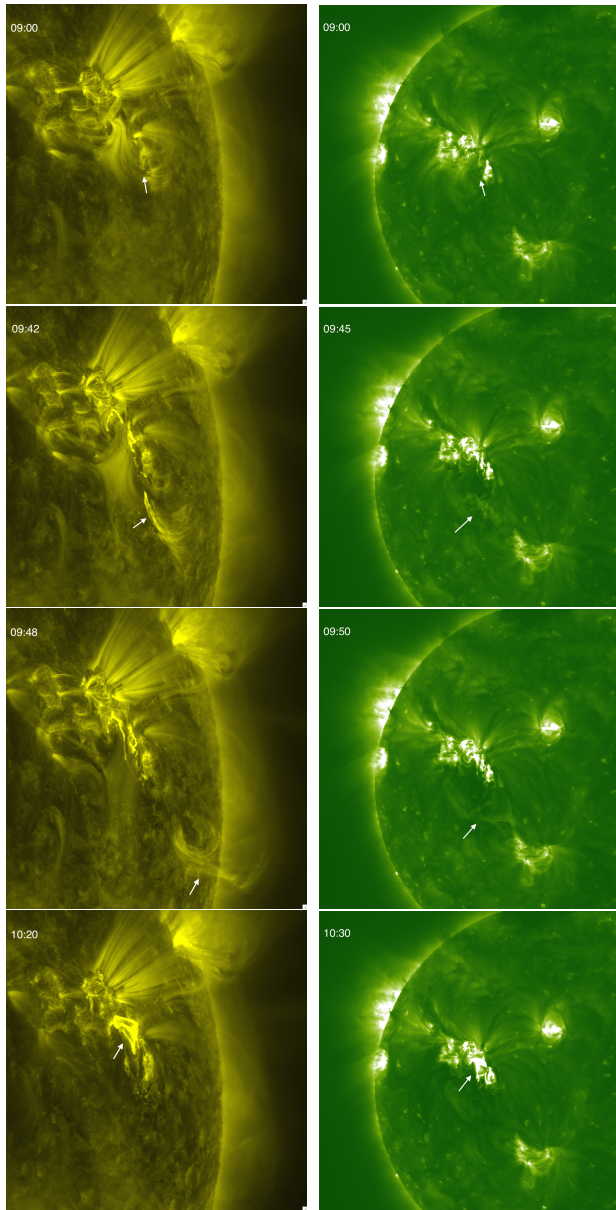


Figure 3.2 *SDO/AIA 171 Å images (left column) of the eruption on 2010 August 14, combined with STEREO-A EUVI 195 Å images (right column) taken at approximately the same time. These images show (from top to bottom and indicated by the white arrow): the rising filament, its untwisting motion as it is hurled into space, and the post-eruptive loops.*

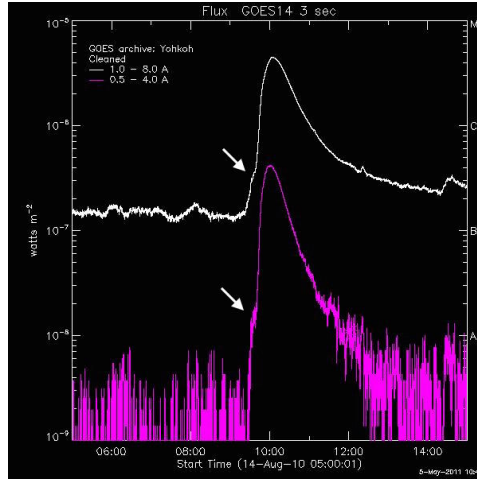


Figure 3.3 *The GOES X-ray flux measurements on 2010 August 14 show a C4.4 flare at the time of the eruption. The arrows indicate a shoulder in the rising phase around 09:30 UT, which corresponds in time to the start of the filament eruption in the southern region.*

a dark region, a transient coronal hole or dimming, to the left of the eruption site, indicating the evacuation of coronal plasma in that region. Additional discussion of the CME trajectory and onset appears below in Section 3.3.

3.2.2 Flare

Both active regions showed weak flaring activity up to B-level in the days before and after the eruption. The event itself was measured by GOES as a moderate C4.4 flare with a peak time of 10:05 UT (Figure 3.3). The rising phase of the flare in the GOES flux curve contains a shoulder (indicated by the arrows in Fig. 3.3) around 09:30 UT which appears to correspond to the start of the filament eruption in the southern region. However, the flare peak occurs only after the northern part of the filament erupts as well. GOES measured the start and end time of this flare as 09:38 UT and 10:31 UT, respectively.

Solar Demon, an automatic event detection tool for solar flares, dimmings and EIT waves (Kraaikamp and Verbeeck, 2015) identifies a flare, dimming and EIT wave associated with this eruption (see Figure 3.4 for an image of the dimming detection). The flare is classified as C7 by *Solar Demon* with peak time at 10:14 UT and it lasts from 09:44 UT to 11:24 UT, spanning 51 consecutive

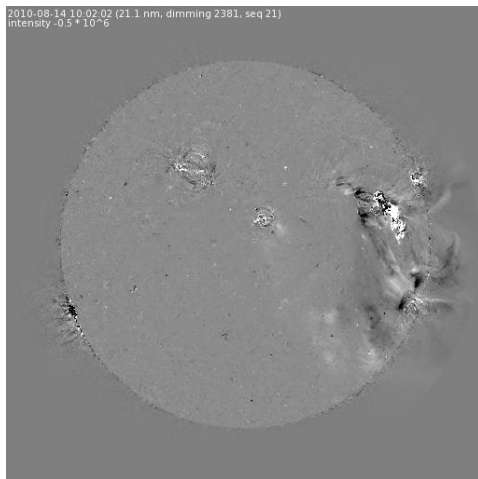


Figure 3.4 *Dimming associated with the eruption on 2010 August 14 and detected by Solar Demon in SDO/AIA 211 Å images. Image taken from <http://solardemon.oma.be/>.*

SDO/AIA 94 Å images. This discrepancy in flare classification and duration can be explained by the different wavelengths of the observations that are used to measure these quantities by Solar Demon (EUV) and GOES (X-ray).

3.2.3 EIT Wave and Coronal Dimming

As mentioned above, Solar Demon also detected an EIT wave and EUV dimming associated with this eruption in running difference images made from the SDO/AIA 211 Å observations. The observed dimming is shown in Figure 3.4.

The properties of the associated EIT wave were studied by Long et al. (2011). Using STEREO-A/EUVI 195 Å images, as well as various SDO/AIA passbands, these authors report initial velocities for the EIT wave ranging from 343 to 460 km s⁻¹, indicating that these measurements are highly dependent on the passband that is used. The accelerations for the SDO/AIA wavelengths range from -128 to -431 m s⁻². Using these results, the authors applied coronal seismology to estimate the quiet-corona magnetic field strength and found that it lies within the range of 1 to 2 G.

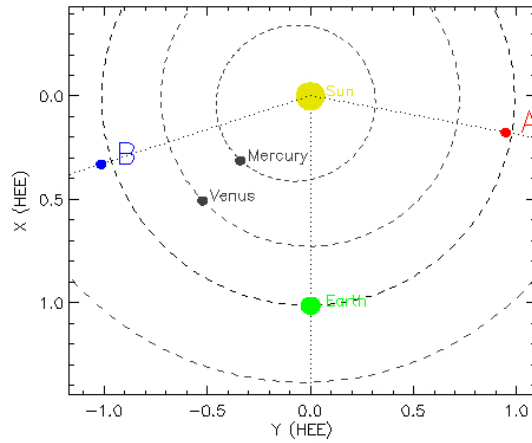


Figure 3.5 *Position of the STEREO spacecraft at 09:00 UT on 2010 August 14, with respect to the Sun and Earth. The position of planets Venus and Mercury are indicated as well.*

3.2.4 Coronal Mass Ejection

This filament eruption was associated with a strong coronal mass ejection that was observed by the coronagraphs on-board SOHO and both STEREO spacecraft as a halo CME. The location of the STEREO spacecraft with respect to planets Earth, Venus and Mercury is illustrated in Figure 3.5. The separation angle between STEREO-B and Earth was 72° on 2010 August 14, while between Earth and STEREO-A it had increased to 79.5° . The SOHO and STEREO spacecraft combined forces to observe this CME from three distinctly different viewpoints, providing us with a maximum of information on the angular extent, direction and velocity of this plasma cloud.

STEREO-A/COR2 observed the first part of this halo CME around 10:38 UT in the south-east. Its counterpart instrument on STEREO-B made the first observation of the plasma cloud at roughly the same time (10:39 UT). From this viewpoint, the CME was directed towards the west. LASCO, the coronagraph on-board SOHO, detected this event even earlier, at 10:12 UT, and from this point-of-view it was also directed towards the west. Some observations by these coronagraphs, made when the CME had fully come into view, are shown in the top row of Figure 3.6. The bottom row images depict the detections of this coronal mass ejection that were made by CACTus, an automated CME detection tool (Robbrecht et al., 2009a). CACTus also determines a number

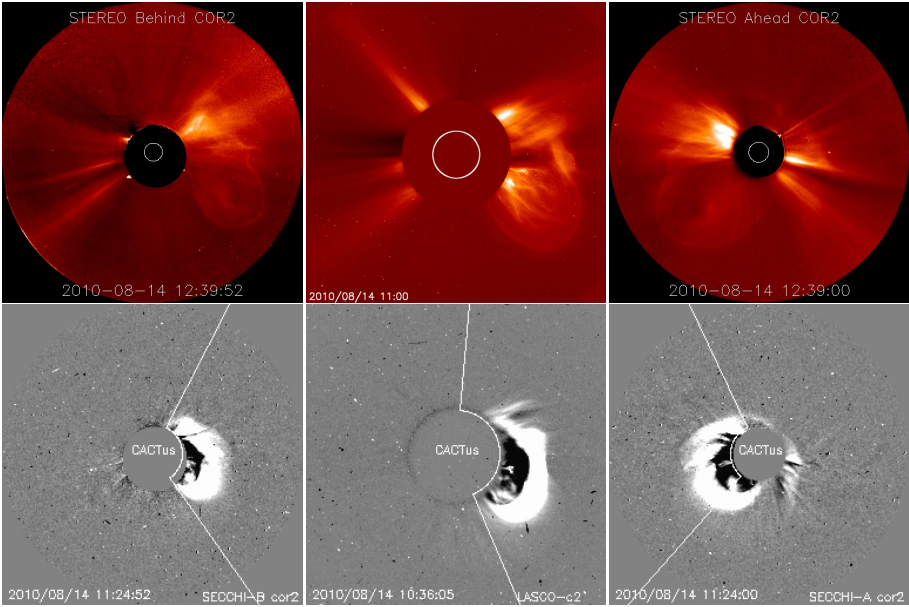


Figure 3.6 *Top panels:* CME observations of the plasma cloud associated with the filament eruption on 2010 August 14. These observations were made by STEREO-B/COR2, SOHO/LASCO, and STEREO-A/COR2 respectively (from left to right). *Bottom panels:* CACTus detections of the coronal mass ejections based on observations from the same instruments. The white lines indicate the estimated angular width of the plasma cloud. Images taken from <http://sidc.oma.be/cactus/>.

Coronagraph	Earliest detection time (UT)	Angular width (degree)	Median velocity (km s^{-1})
STEREO-B/COR2	2010/08/14 10:24	118	641 ± 221
SOHO/LASCO	2010/08/14 10:12	152	657 ± 223
STEREO-A/COR2	2010/08/14 09:54	114	568 ± 184

Table 3.1 *CME parameters for the CACTus detections of the plasma cloud in coronagraph data from the SOHO and STEREO spacecraft. Data reproduced from <http://sidc.oma.be/cactus/>.*

of parameter values for each detection, these are listed in Table 3.1 for each of the coronagraph instruments that observed the CME. The parameters based on observations by the different coronagraphs agree rather well. Note that, as the bottom right panel in Figure 3.6 clearly shows, the angular width for this CME was somewhat underestimated in the STEREO-A data because only part of the CME was detected automatically by CACTus.

The CACTus detections can be compared to what can be found in other CME detection catalogs. For example, the manual CDAW catalog is based on SOHO/LASCO images and reports this event as a halo CME with a position angle of 224° , which corresponds rather well to the 279° that CACTus finds. A linear fit to the height-time measurements results in an estimated velocity of 1205 km s^{-1} (Figure 3.7, left panel). A quadratic fit to the same measurements yields a velocity of 993 km s^{-1} (Figure 3.7, top right panel). With an estimated deceleration of 43 m s^{-2} (Figure 3.7, bottom right panel) this leads to a velocity of 989 km s^{-1} at a height of $20 R_\odot$. These velocities are much faster than what CACTus finds. However, the CACTus tool computes a median velocity over all angles within the extent of the detected CME, whereas in the CDAW catalog the speed along only one position angle is reported. Additionally, CACTus tracks the brightest feature (which is not necessarily the fastest front), while in the CDAW catalog usually the CME leading edge is traced. When we closely study the CACTus velocity distribution (Figure 3.8), we indeed find angles along which the speeds amounts to approximately 1000 km s^{-1} . Tun and Vourlidas (2013) also report that the CME front travels at 1204 km s^{-1} .

3.2.5 Radio Signatures and Solar Energetic Particles

Radio Bursts

The Observatoire de Paris maintains a radio survey in collaboration with the Artemis team, the Universities of Athens and Ioanina and the Naval Research Laboratory. These institutes provide daily surveys which combine radio spectra covering a large frequency range from various observing sites in France, China, Australia and Greece. These spectra are further complemented by spectrograph information from the WIND (Bougeret et al., 1995) and STEREO missions, Nançay Radioheliograph data and information on CME occurrence from SOHO and STEREO.

Their data demonstrate clear radio signatures for the event on 2010 August 14, as is shown in Figure 3.9. The left panel of this figure is a composite of radio observations from ground-based telescopes and WIND/WAVES, the radio and plasma wave investigation on-board the WIND spacecraft. This image

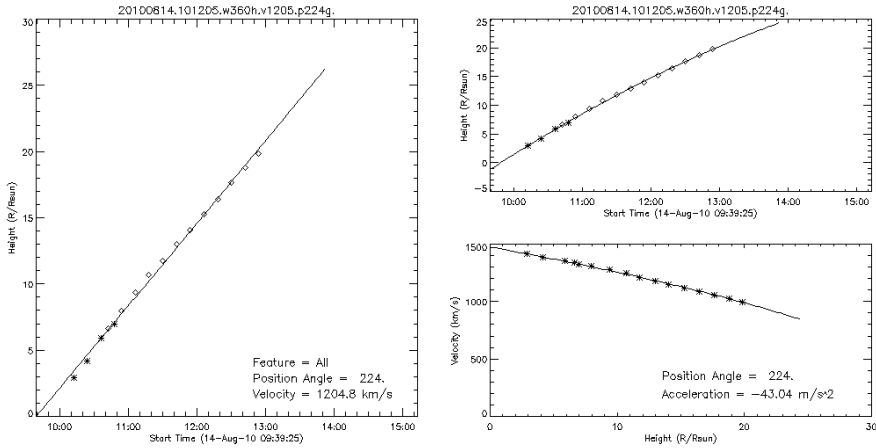


Figure 3.7 *Left Panel:* CDAW catalog height-time measurements for the CME, overplotted with a linear fit of the data, leading to a velocity value of 1205 km s^{-1} . *Right Panel:* A quadratic fit over-plotted to the same height-time measurements (top) and a plot of the CME velocity versus its height (bottom), leading to an acceleration value of -43 km s^{-2} which indicates that the CME decelerates while it travels through the SOHO/LASCO field-of-view. Image taken from http://cdaw.gsfc.nasa.gov/CME_list/.

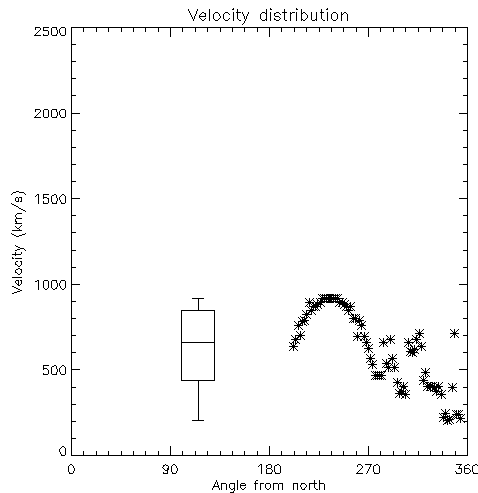


Figure 3.8 *Velocity distribution* across all angles for the CACTus detection of the CME in the SOHO/LASCO-C2 images. The median velocity for this eruption is $657 \pm 223 \text{ km s}^{-1}$. Image taken from <http://sidc.oma.be/cactus/>.

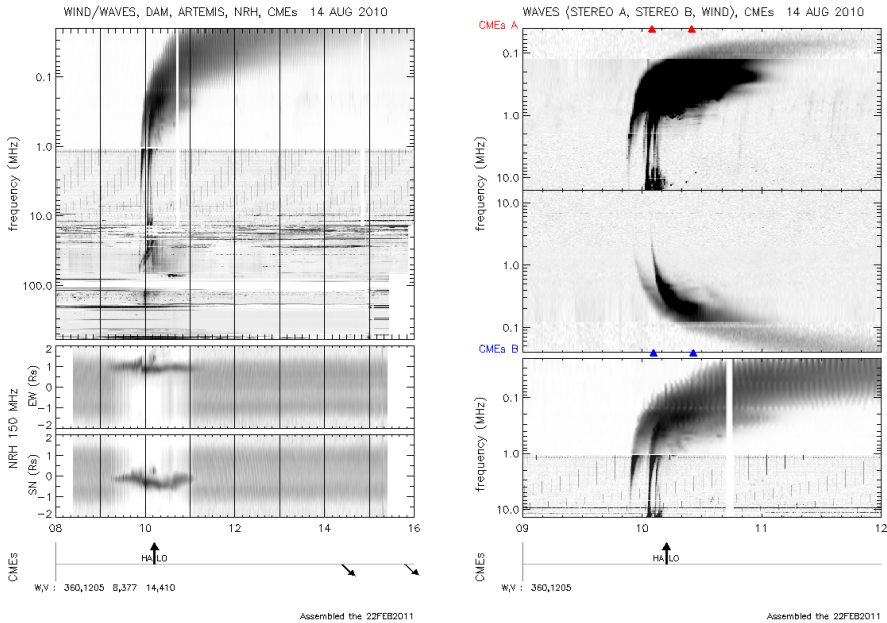


Figure 3.9 *Left Panel:* Composite radio image combining data from the WIND spacecraft and various spectrographs, showing type II and type III radio bursts. Below are the locations of the radio sources and the reported times of associated CMEs. *Right Panel:* Radio signatures measured by the STEREO spacecraft. STEREO-A measures the strongest signatures, due to the fact that the shock is propagating in the direction of that spacecraft. Images taken from <http://radio-monitoring.obspm.fr/>.

thus shows the solar radio bursts observed from the Earth's perspective. There are clear signs of a type II burst and multiple type III bursts in this graph. The fast-drifting type III bursts occur when electrons are accelerated by the propagating shock of a CME. Type II bursts originate from the shock wave as well. However, these burst generally drift more slowly and smoothly from high to low frequencies (compared to type III events). Type II bursts are mostly associated with CMEs, while type III events are linked to flares.

The right panel of Figure 3.9 shows the radio signatures measured by the SWAVES (STEREO/WAVES) instrument on-board the STEREO spacecraft. Again type III radio bursts are clearly observed. They are stronger for STEREO-A than for STEREO-B, simply because the shock is propagating in the direction of the STEREO-A spacecraft.

This CME was accompanied by diverse radio signatures, including also a moving type IV radio burst, observed by Tun and Vourlidas (2013) in Nançay Radioheliograph data. The cause of this type IV burst is believed to be the gyrosynchrotron emission from the core of the CME, which corresponds to the erupting filament itself. Tun and Vourlidas (2013) estimated the loop-top magnetic field strength along the line of sight and at $1 R_{\odot}$ above the solar surface to lie between $5 G$ and $15 G$.

Proton Event

Solar proton events are triggered when fast CME shocks accelerate charged particles in the solar atmosphere to very high velocities. A strong increase in the proton flux can have a number of space weather effects on technology in space and on Earth. For example, during a proton storm satellites' electronics may be damaged and the ionization rate of the ionosphere (a layer of Earth's atmosphere) may be locally increased, which in turn causes disturbances with HF (High Frequency) radio communication.

Figure 3.10 (left panel) clearly shows a strong increase in the proton flux measured by the GOES spacecraft. The strongest peak was measured for protons with energies > 10 MeV. The curve barely crossed the threshold of 10 proton flux units ($1 \text{ pfu} = 1 \text{ particle cm}^{-2} \text{ s}^{-1} \text{ ster}^{-1}$), which corresponds to a minor solar radiation storm of type S1. By the end of the next day, August 15, the proton levels had decreased back to normal levels. An S1 radiation storm is not expected to cause any problems with satellite operations, but minor impact on HF radio communication in the polar regions is possible. Nevertheless, some white streaks were visible in the SOHO/LASCO C3 images as a result of energetic particles hitting the coronagraph detector (visible in the left panel of Figure 1.12).

The effects of solar energetic particles at Earth were thus minimal for this event, despite the strong shock that accompanied this fast CME. Indeed, the source region for this event was located close to the solar limb when the CME erupted and the CME itself was directed mostly westward as seen from the Earth (thus directed more towards the STEREO-A spacecraft). It is likely that most of the accelerated particles travelled on magnetic field lines that were not connected to Earth and thus did not arrive at our magnetosphere. Despite its moderate strength, this proton event received a lot of attention as it was the first proton event recorded since December 2006 and the only one observed during the year 2010².

²<http://umbra.nascom.nasa.gov/SEP/>

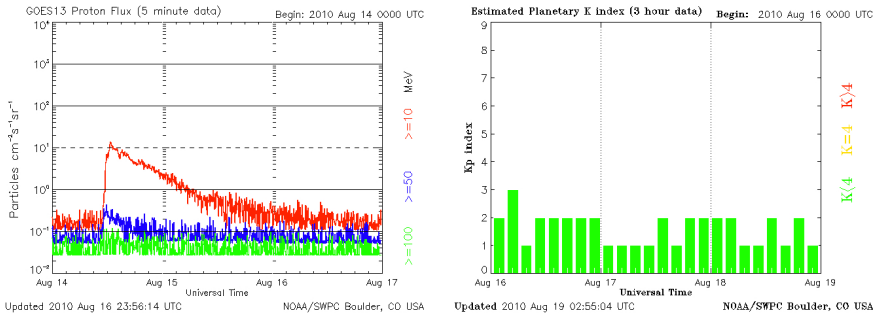


Figure 3.10 *Left Panel:* Proton fluxes measured by the *GOES* spacecraft, illustrating a clear jump in the measurements of the > 10 MeV protons, associated with the 2010 August 14 eruption. *Right Panel:* Planetary K index measured for the days after the eruption. No strong disturbance of the magnetic field is measured, resulting in quiet levels for the K_p -index ($K_p < 4$). Images provided by NOAA at <ftp://ftp.swpc.noaa.gov/pub/warehouse/>.

3.2.6 Effects on Interplanetary Space

When analyzing this plasma cloud in SIDC's daily bulletin, the space weather forecaster on duty noted that the CME was mostly southward, but partially Earth-directed. Due to the limited amount of data available at the time of the forecast, a preliminary estimate was made: the CME upper region was expected to skim the Earth on August 17. The in-situ data recorded in the days after the eruption do not show the arrival of this interplanetary CME (ICME) at Earth (Figure 3.11). Consequently, also the planetary K -index, a measure indicating how strongly the Earth's magnetic field is disturbed by space weather events, was at most $K_p = 3$ (Figure 3.10, right panel) in the days after the eruption, corresponding to quiet conditions and confirming the absence of a geomagnetical storm.

The ICME did arrive at the STEREO-A spacecraft, however, and is observed in the in-situ measurements shown in Figure 3.12. This plot shows a moderate shock in the late afternoon of 2010 August 17 in the measurements of the total magnetic field strength, the solar wind velocity, the proton density and the proton temperature (between 17.12 and 18.00 on the x-axis). Together with the decreasing velocity profile and the relatively low temperature, these are clear signs of the passing of an ICME. This shock seems rather small compared to the high velocity we derived for the CME. However, it is likely that STEREO-A only measured the flank of the CME, as it propagated between STEREO-A

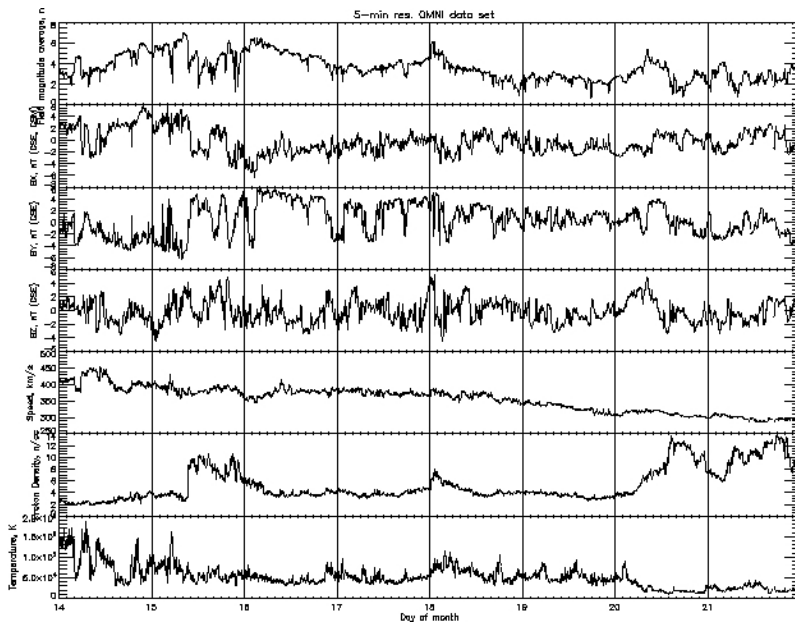
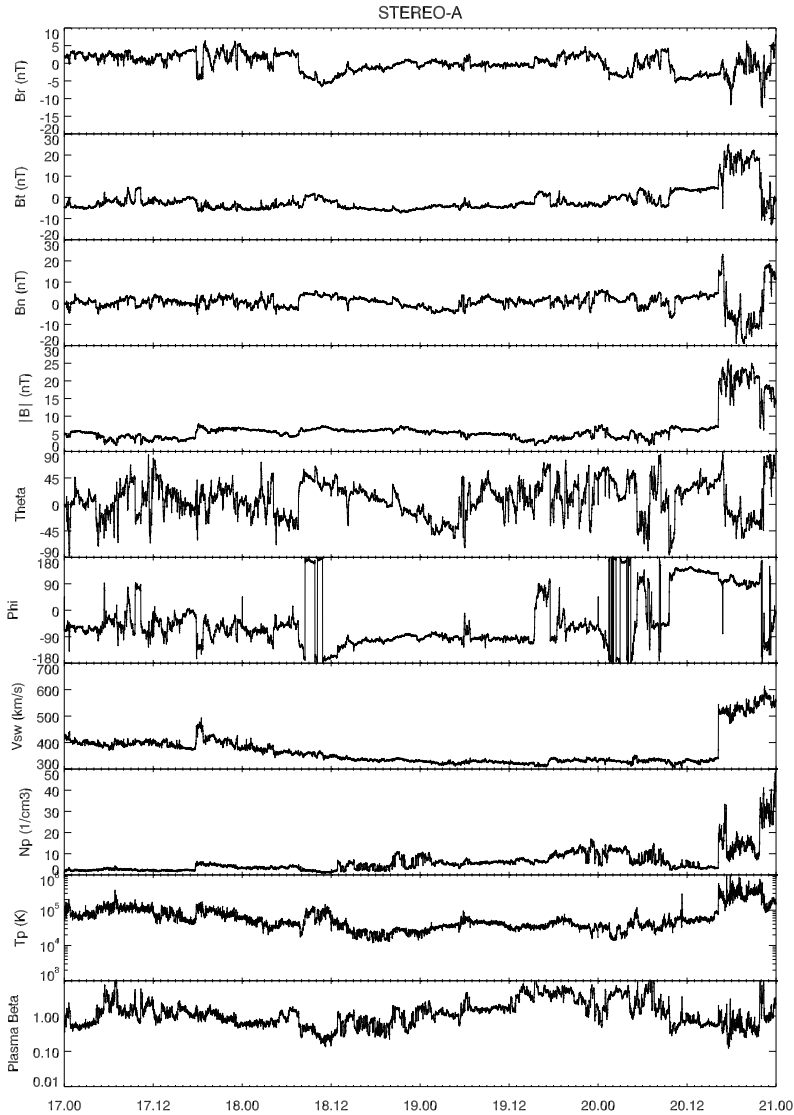


Figure 3.11 *In-situ data from the ACE satellite measuring the conditions of the solar wind close to Earth. Plotted are (from top to bottom) the total strength of the magnetic field, the B_x , B_y and B_z component of this magnetic field, the solar wind speed, the proton density and the temperature. No clear signs of the arrival of the ICME are visible in the days after 2010 August 14. Image produced with http://omniweb.gsfc.nasa.gov/form/omni_min.html .*

and Earth. The 3D reconstructions reported on below place the source location 20° east of the central meridian as seen from the STEREO-A point-of-view.

The STEREO-B spacecraft measurements did not show any indications of the passing of a magnetic cloud, which is to be expected as the CME was mostly directed towards STEREO-A, and thus propagating away from the STEREO-B spacecraft.



17 Aug 2010 (doy: 229) - 21 Aug 2010 (doy: 233)

Figure 3.12 Measurements of the solar wind obtained by the in-situ instruments on-board STEREO-A. In the afternoon of 2010 August 17 (between 17.12 and 18.00 on the x-axis), a weak shock is visible in these observations of the solar wind speed (v_{sw}), the proton temperature (T_p), the total magnetic field strength ($|B|$) and the proton density (N_p). Image provided by L. Rodriguez (ROB).

3.3 Three-dimensional Reconstructions

Three-dimensional reconstruction methods are often used to study the trajectory, kinematics and morphology of CMEs starting from their site of initiation to their propagation into interplanetary space. By exploiting the different viewpoints of various spacecraft, this type of modeling allows to mitigate projection effects and estimate the CME's evolution in interplanetary space. This information is crucial to understand how the ejected CME interacts with the surrounding solar wind and to predict whether and how the plasma cloud will affect the Earth's magnetosphere.

We explored the morphology of the CME associated with the eruption on 2010 August 14 through the `scc_measure` solarsoft program. This program is based on epipolar geometry (Inhester, 2006) and allows the user to locate the same feature on two solar images taken from different vantage points. The user first selects a feature in an image taken from the first viewpoint. The program then displays the image from the second spacecraft's vantage point with a line over-plotted that indicates the line-of-sight from the first spacecraft. The user selects a point along this line that corresponds to the same feature that was tracked in the first image. The program then computes the heliographic coordinates of this feature in three-dimensional space.

In the case of the 2010 August 14 event, the eruptive filament was clearly visible in EUV wavelengths. Various EUV instruments (PROBA2/SWAP, STEREO-A/EUVI and SDO/AIA) observed this prominence from different angles and saw the filament rise, destabilize and twist as it erupted into space. The further propagation of this filament into interplanetary space was imaged by the coronagraphs on-board SOHO and STEREO.

Ideally, a three-dimensional reconstruction would allow us to track the rise and acceleration profile of the erupting flux rope without projection effects, which, in turn could yield an accurate height-time diagram. Schrijver et al. (2008) argued that by fitting such a height-time diagram with different functions it should be possible to determine which of several eruption mechanisms was likely responsible for the onset of the eruption by comparing these fits to predictions from simulations. For example, a height-time profile with a parabolic shape matches the numerical results for the breakout model (Lynch et al., 2004). The CME rising phase in case of the catastrophe model follows a power law with exponent 2.5 (Priest and Forbes, 2002). Finally, MHD instabilities are compatible with an exponential rising phase (Török et al., 2004; Török and Kliem, 2005; Kliem and Török, 2006).

We first reconstructed the entire erupting filament using PROBA2/SWAP and STEREO-A/EUVI images. The results are shown in Figure 3.13. This

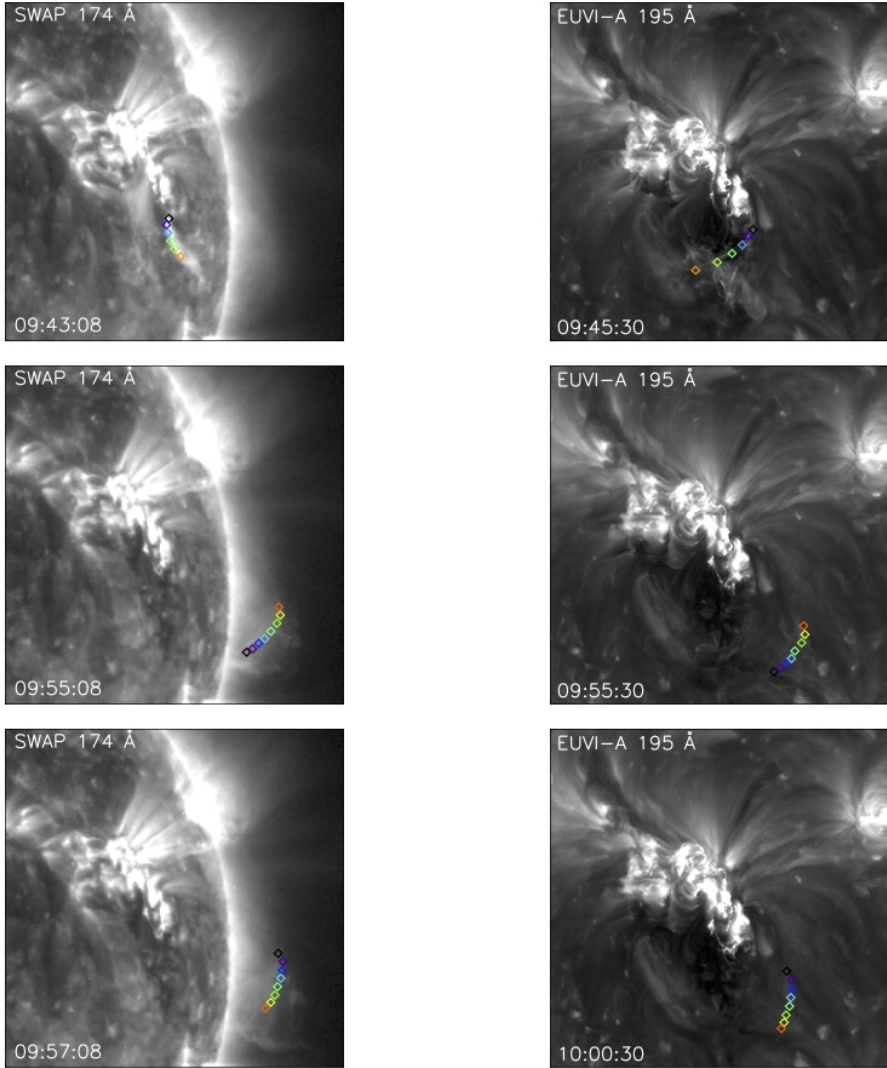


Figure 3.13 *Three-dimensional reconstruction using epipolar geometry of the erupting flux rope observed during the 2010 August 14 event. For this reconstruction, we used PROBA2/SWAP 171 Å and STEREO-A/EUVI 193 Å images, matching in time as closely as possible.*

reconstruction showed that the filament erupts close to the equator at an average longitude of 65° . Unfortunately, there were insufficient pairs of SWAP and EUVI-A images where the feature was clearly visible and the images well-matched in time. Thus only a few points could be measured, not enough to create a useful height-time diagram.

We therefore expanded our dataset with the images from SDO/AIA and obtained the 3D reconstruction of the center of the bright front by combining SDO/AIA and STEREO-A/EUVI data. The result is shown in the height-time plot in Figure 3.14. Because AIA has a limited field-of-view, these fitted points revealed the location of the eruption only in the very low corona. To extend the trajectory, we measured the plane-of-sky height of the feature in SWAP images, which have a large field-of-view. We then deprojected these measurements for the true propagation angle by assuming the erupting structure was traveling largely radially in the same direction as the three-dimensional reconstructions had indicated. Since the locations we obtained from our earlier reconstructions revealed points between 55° and 65° longitude, we assumed a propagation angle of 60° , which produced good agreement with the reconstructed trajectory using AIA and EUVI-A images. The resulting deprojected points are also shown in Figure 3.14.

To extend our plot to larger heights, we also analyzed the propagation of the eruption using coronagraphic instruments. First we tracked the eruption using images from SOHO/LASCO. Since SOHO views the Sun from roughly the same viewing angle as Earth, we applied the same deprojection correction to the plane-of-sky heights we measured using LASCO as we did for the measurements from SWAP. These corrected measurements appeared to align smoothly with the trajectory measured in SWAP images, but because the LASCO occulting disk blocks our view of the corona to relatively large heights above the surface, a gap remained between the SWAP-derived heights and the LASCO-derived heights.

To fill this gap, we turned to the COR 1 coronagraph on STEREO-A. COR 1 reveals the corona to much lower heights, low enough to produce data that nearly overlapped with SWAP observations. However, since the separation angle between the feature we were tracking and STEREO-A was only about 20° , during the whole early part of the event the center of the erupting prominence was traveling almost directly towards the COR 1 coronagraph and was thus largely obscured behind its occulting disk until it reached large heights. Thus, after tracking the eruption in the plane of the sky, we could no longer use the same deprojection technique that we employed on the SWAP and LASCO data. Instead, we assumed that as it reached larger heights the flux rope expanded, so its easternmost edge was traveling radially away from the Sun along with

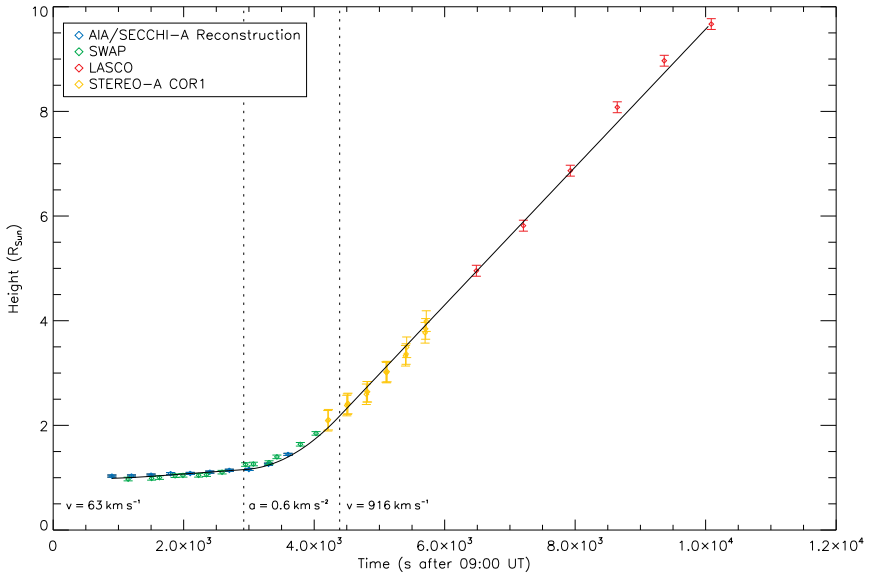


Figure 3.14 Height-time diagram for the CME on 2010 August 14, combining measurements made using observations by different EUV imagers and coronagraphs. These data points show clearly that while the flux rope initially rises with a very low velocity, it gets an extra impulse and acceleration when it erupts catastrophically and propagates with a nearly constant, but very high, velocity afterwards. The measurement errors were obtained by remeasuring the position of the flux rope several times in sample images. We then applied error propagation to the standard deviation of these measurements to obtain the error bars shown here. The COR1 datapoints (in yellow) show the largest error bars because it was harder to define the exact position of the flux rope in those images.

the rest of the CME, but at a much more eastward longitude, yielding a larger separation angle with COR 1.

Because we lacked another set of co-temporal coronagraphic images to use for three-dimensional reconstructions, we instead estimated the appropriate projection angle for this eastern CME edge by assuming that the deprojected COR 1 measurements should extend the trajectory we calculated for lower heights using AIA and SWAP. The plane-of-sky COR 1 measurements revealed an essentially linear trajectory, so we extrapolated backwards to the time of the largest height measurement we obtained with SWAP and determined the projection angle necessary to produce a point that matched the SWAP

measurements at that time. This method yielded a longitude of roughly 40° . This is roughly 20° east of the center of the eruption, not an implausible extent for a large, rapidly expanding CME. Because all of these independently deprojected points fit together to yield an essentially smooth trajectory in the plot with few outliers, we consider this validation that we have captured — at least very roughly — the dynamics of the eruption’s onset and early propagation through the corona.

We were unable to fit the points in the resulting height-time diagram with any of the functions described in Schrijver et al. (2008), which could be because those authors confined their analysis to low heights in the corona or could be an indication that another acceleration mechanism may have come into play for this eruption. In fact, we found that the points were well-fit by a piecewise-defined function with a slow, constant-velocity rise at about 63 km s^{-1} , followed by a constant acceleration of about 0.6 km s^{-2} for approximately 1500 s, followed by a high-speed constant-velocity propagation out of the corona at just over 900 km s^{-1} . This final velocity of the CME is compatible with what was measured in the CDAW CME catalog. It also fits the measurements by CACTus of the central part of the CME (Figure 3.8), which was indeed the point that we reconstructed here.

In fact, the acceleration experienced by the erupting flux rope is very likely considerably stronger. The net effect of our several assumptions and the inherent error in our measurements likely acts to smooth the acceleration phase of the eruption. Inspection of the images from SDO/AIA and PROBA2/SWAP suggests that the flux rope experienced a very impulsive acceleration phase as it began to rotate and untwist after its slow rise. We discuss this impulsive acceleration in section 3.4.2.

Figure 3.15 shows the acceleration derived from the fit in the height-time diagram (Figure 3.14), combined with the gravitational acceleration as a function of height. The gravitational acceleration is defined as $a = GM_\odot/|r|^2$, with $G = 6.67 \times 10^{-11} \text{ m}^3 \text{ kg}^{-1} \text{ s}^{-2}$ the gravitational constant, M_\odot the solar mass and r the height of the CME. This plot shows that the CME is only significantly accelerated between 1.25 and $2.25 R_\odot$, which was already clear from Figure 3.14 as well. The gravitational acceleration at $2.25 R_\odot$ is around 0.05 km s^{-2} and decreases even further as the CME travels outward. Thus as the CME is propagating at larger heights, the gravitational force acting on it is negligible. Also the drag force is small close to the Sun (Forbes et al., 2006), and is thus unable to noticeably decelerate the CME at these heights. A third force acting on the CME is the outward-directed force related to the reconfiguration of the field by magnetic reconnection. Also this force is weak, which is evident from the weak flare that is associated to this eruption. Overall, the forces acting on this CME are small, and it is thus likely that a balance can easily be achieved

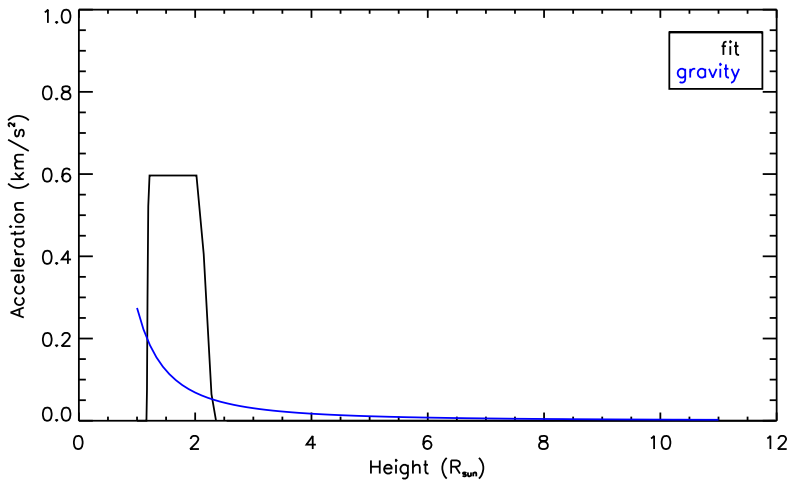


Figure 3.15 Acceleration of the CME based on the fit in the height-time diagram in Figure 3.14 (in black) compared to the gravitational acceleration (in blue). The flux rope experiences a constant acceleration of about 0.6 km s^{-2} between $1.25 R_{\odot}$ and $2.25 R_{\odot}$.

between the retarding and accelerating forces. This explains the observed linear propagation on the right hand side of the height-time diagram in Figure 3.14. Even if the CME is somewhat decelerated or accelerated in this phase, the resulting deflection of the curve in Figure 3.14 would be too small to observe by eye.

3.4 Initiation Mechanism

3.4.1 Flux Emergence versus Flux Cancellation

Zhang et al. (2008) studied the relationship between CME initiation and changes in the photospheric magnetic field. They found that for 60 % of the CME source regions an increase in the large-scale magnetic flux is observed during a period of 12 hours before the eruption, while in the other 40 % of the cases a decrease of this quantity is measured. On 2010 August 14, SDO/HMI magnetogram observations show a significant amount of flux emergence in the day and hours before the eruption, especially in the northern active region. This suggested that flux emergence played a role in triggering this eruption.

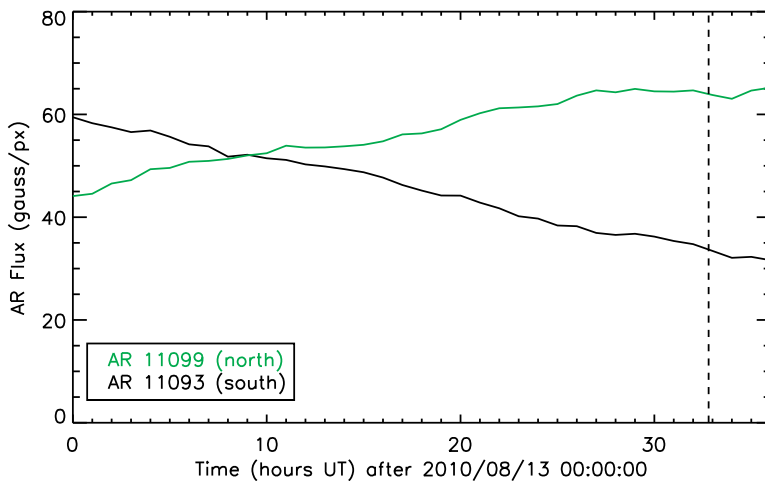


Figure 3.16 Spatially averaged flux in the northern (green) and southern (black) active region measured by SDO/HMI over time, starting on 2010 August 13 at 00:00 UT, which is more than a day before the eruption. The vertical line indicates the approximate start time of the eruption. This figure shows a clear decrease in flux for the southern region for the entire time range. The flux in the northern region increases at first, but then levels off in the hours before the eruption.

To validate this assumption, we measured the evolution of the average flux in both active regions starting on 2010 August 13 at 00:00 UT until a few hours after the eruption on August 14. The results are shown in Figure 3.16. These measurements revealed that there is indeed a clear increase in flux for the northern active region on the day before the eruption. However, the flux emergence levels off on August 14, indicating that there is no clear change in flux for this AR in the hours right before the eruption.

On the other hand, the average flux in the southern region is steadily decreasing and continues to do so in the hours before the eruption. This suggests that the destabilization of the southern end of the filament by flux cancellation may have facilitated the eruption of the entire filament. While it is difficult to conclusively say that flux cancellation was the facilitator for this eruption, the evolution of the southern spot clearly played a role in its onset. Additionally, this scenario closely matches the observations where the southern part of the filament is first seen to rise, dragging the entire magnetic structure with it as it erupts in an untwisting motion.

3.4.2 MHD Instability

The initiation scenario for this eruption may be very similar to what Vemareddy et al. (2012) describe for the homologous eruption on 2010 August 7, which had the same source regions. The cancellation of magnetic flux that we observe in the southern region may be a sign of interaction of the neighboring magnetic field with the overlying magnetic field that is restraining the filament from eruption. The ubiquitous small brightenings that we observe before the eruption also fit this scenario. Although the flux cancellation in itself is insufficient to cause the eruption, tether cutting, through a series of weak reconnection events, could assist in facilitating the onset of an eruption.

Once the equilibrium in which the filament sits is sufficiently eroded, the filament is allowed to rise slowly. This early eruption phase corresponds to the left part of the height-time diagram shown in Figure 3.14, with a steady but slow propagation. As the filament begins to reach larger heights, around 09:50 UT, it suddenly experiences a strong twisting motion. This motion, in fact, shears the filamentary flux rope apart, so the southern half of the filament is accelerated extremely rapidly and the northern half becomes trapped high in the corona. These motions are very likely the result of an ideal MHD instability, probably because the inward forces on the flux rope at large heights were no longer sufficient to balance the outward forces resulting from the toroidal field of the flux rope itself. The quasi-equilibrium that facilitated its slow rise is suddenly lost and the breakup of the flux rope yields a much stronger and more rapid eruption.

As the flux rope rises further we begin to observe some signs of magnetic reconnection in its wake, including the formation of a dim post-flare arcade and the occurrence of a relatively weak solar flare. In this case, the magnetic reconnection that accompanies the event is likely a consequence of the eruption, rather than a driver of it. That the flare is relatively weak for a fast, impulsively accelerated CME suggests that the eruption's primary energy source was the ideal MHD instability that occurred when the flux rope experienced its rapid acceleration.

3.5 Discussion

We studied the different aspects of a unusual solar eruption, occurring on 2010 August 14. Associated with this eruption, we observed all typical solar and space weather ingredients: a filament, a flare, an EIT wave, an EUV dimming, radio bursts, a proton event and an ICME; making it a prime example of a solar

eruption. We combined data from a fleet of satellites and ground instruments to get a complete picture of this event. The most striking observational feature was not the powerful CME associated with this eruption, but its untwisting motion. Our analysis made it clear that this rotation was most probably caused by the early destabilization of the southern end of the filament, which then only later dragged the northern part with it. There may also have been an influence from the fast solar wind streaming from a coronal hole to the east of the eruption site.

While the initiation mechanism for this eruption was not determined with absolute certainty, we have strong indications that flux cancellation will have played an important role in the destabilisation of the southern end of the filament, which in turn led to the eruption of the entire feature. Changes in the magnetic flux were also the trigger for the eruption on August 7, originating from the same active regions. Vemareddy et al. (2012) interpreted them as signs of tether weakening. The scenario described by these authors may also be applicable to the August 14 eruption.

We then argued that, while flux cancellation facilitates the eruption, the actual trigger was in fact an MHD instability. Only when this instability kicks in, does the flux rope accelerate significantly. This sudden acceleration is accompanied by the formation of a shock, observed in radio observations. Afterwards, the CME propagates at a high velocity into interplanetary space.

The fact that this event was accompanied by energetic protons, a relatively fast CME and an ICME signature in STEREO-A in-situ data is interesting, because the associated flare itself is quite weak. This emphasizes the need for careful inclusion of all possible information concerning a solar eruption in the analyses. Flare strength is not always a good indicator of the space weather risk of a CME, as we will explain further in Chapter 4. Space weather forecasters should therefore always consider CME properties as a whole and look at different aspects such as the presence of a flux rope, the acceleration profile, possible deflection, the presence of a shock, the source location on the Sun, etc. This is also clear from the analysis presented by Steed et al. (2012): these authors showed that the eruption on August 7 and August 14 exhibited very similar on-disk signatures, but nevertheless had widely different space weather consequences.

The 2010 August 14 CME originated from a compact, dense prominence that erupted rapidly and was clearly quite dynamical and structured, which argues that it was likely to be a fairly energetic event, despite the weak flare that was associated with this eruption. Due to the position of its source location with respect to ACE and STEREO-A, neither spacecraft experienced a head-on collision with the ICME. No strong geomagnetic effects were observed at

Earth and STEREO-A measured only a moderate ICME. Nevertheless, had the eruption taken place just a few days before, while the source regions were still facing Earth, the geomagnetic effects at Earth could have been severe.

There are various avenues for further research here. Most importantly, to investigate the possible onset of the torus instability, we can calculate the decay index for this eruption (as was done, for example, by Zuccarello et al., 2014). This decay index is a measure for how fast the external magnetic field decreases with height and it reaches a critical value for eruption within the range [1.2; 1.5] (Zuccarello et al., 2015). In order to decide whether this eruption was indeed triggered by the torus instability, we thus need to compare the height of the reconstructed filament with the height at which the decay index — based on potential magnetic field extrapolations for the eruption region — reaches this critical range. Additionally, the strong rotation that is apparent in the early stages of the eruption deserves further study.

This eruption originated from one of the first big and eruptive active regions observed during the current solar cycle. It was also associated with the first proton event recorded in nearly 4 years. Therefore, it was studied extensively by various authors, each with their own focus (See, for example, Long et al., 2011; Tun and Vourlidas, 2013). Understandably, the most spectacular eruptions attract the most attention and this example fits rather well in the traditional view of eruptions, where a flare and a CME occur together as a global response to a restructuring of the coronal magnetic field.

This eruption provided the ideal circumstances for a flare and its associated CME to occur together. However, the flare turned out to be much dimmer than we would expect from such a strong CME. This made us wonder what is then different in eruptions where we observe a strong flare with a fast CME or, alternatively, only one of these eruptive signatures instead of both. Flares without an associated CME (*confined flares*) occur frequently, especially in the case of low-energetical events. On the other hand, CMEs occurring without an observed solar flare or any other low coronal signature (such as an eruptive filament) are much more seldom. In the next chapter we investigate why these events are so rare and what the necessary conditions are for them to occur.

Chapter 4

Observational Characteristics of CMEs without Low-Coronal Signatures

In this chapter, we study coronal mass ejections without low-coronal signatures in more detail than was ever done before. We first identify 40 such events that were observed in 2012. Their observational and kinematic properties are then analyzed and compared to those of regular CMEs. To conclude, we discuss the initiation mechanisms for this type of CME.

The content of this chapter was published in D’Huys et al. (2014), © AAS, reproduced with permission. This work benefitted greatly from discussions with F.P. Zuccarello (CmPA, ROB, Obs. Paris) and the PROBA2/SWAP team. K. Bonte (ROB, then CmPA) provided the SoFAST catalog data.

4.1 Introduction

In Chapter 3 we reported on a rotating solar eruption, that showed all typical observational on-disk and low-coronal signatures (LCS) of eruption: an eruptive filament, radio bursts, an EIT wave, flux emergence, etc. The associated flare, however, was much weaker than expected from such a strong CME. In this chapter we focus on the even more extreme end of the spectrum of solar eruptions and study solar outbursts that do not leave any eruptive signs on

or close to the solar disk. The central question driving the research presented here is whether CMEs without these low-coronal signatures are fundamentally different from other CMEs. Do both classes of CMEs have different initiation and driving mechanisms or are CMEs without LCS simply at the low end of an energy spectrum, making their associated surface signatures hard to observe? Indeed, as Howard and Harrison (2013) point out, one needs to keep in mind that detections of eruption signatures are always limited by the sensitivity and bandwidth of the instrumentation used.

CMEs without low-coronal signatures, also named stealth CMEs, are not very well-studied. Nevertheless, they appear to be less uncommon than the low number of published case studies suggests. Studying the source locations of all 1078 CMEs listed in the CDAW CME catalog¹ during 1997-1998, Wang et al. (2011) found a considerable number of events ($\sim 16\%$) that were assumed to be front-sided, but lacked eruptive signatures in the EIT 19.5 nm images.

Ma et al. (2010) carried out a statistical study of CMEs without distinct low-coronal signatures. Their dataset spanned the period from 2009 January 1 to August 31, which was a time of an exceptionally low solar minimum. They report that almost one out of three CMEs in their catalog turned out to be stealth and that nearly half of the CMEs without LCS was a streamer blowout-type CME. A kinematic study of the 11 identified stealth CMEs revealed that these were slow CMEs ($v < 300 \text{ km s}^{-1}$) that were accelerated gradually and had an angular width smaller than 40° .

There is no agreement within the solar physics community on the definition of a stealth CME. Ma et al. (2010) define a CME without low-coronal signatures, where LCS means a "filament eruption, flare, post-eruptive arcade, coronal wave, coronal dimming, or jet". Alternatively, Wang et al. (2011) specify "a kind of CME that does not leave any eruptive signatures in EUV-passbands and sometimes may not even be visible in coronagraphs facing on them". Notice, however, that the prime example of a so-called stealth CME, the one studied by Robbrecht et al. (2009b), does not fit this last definition, as a careful examination of EUVI-A 17.1 nm images for this event revealed a bright structure at $0.15 R_\odot$, travelling outward to form the CME core. Thus EUV images did show an eruptive signature for this event, albeit at a very large height. This is also the case for most events studied by Ma et al. (2010). They report that 8 out of 11 identified CMEs without LCS may have been initiated by disturbances of flux ropes suspended high in the corona.

For the purpose of this study, we have defined a CME without low-coronal signatures as a *front-sided* CME (a CME occurring at a location on the Sun that is facing Earth at the time of eruption) that was detected in coronagraph

¹http://cdaw.gsfc.nasa.gov/CME_list/

images and for which no coronal signature was observed on the solar disk or in the more extended field-of-view of the EUV imagers PROBA2/SWAP (Seaton et al., 2013a), SDO/AIA (Lemen et al., 2012) and STEREO/EUVI (Howard et al., 2008a). This definition introduces a clearer distinction between stealth CMes and other events than the definitions listed above. Indeed, what makes stealth CMes stand out from other events, is exactly the fact that it is very difficult to determine their source regions. In case an eruptive signature is detected at larger height, this would be a clear indication of the origin of the CME and therefore we do not label it as a stealth event.

To classify the events in our dataset into the categories of stealth and non-stealth CMes according to our definition above, we have searched for possibly related flares and brightenings, filaments, EIT waves, jets, coronal dimmings, flows, post-flare loops, and reconfiguration of the magnetic field lines in the higher corona. Figure 4.1 illustrates the vast difference in low-coronal signatures between a stealth CME and a CME associated with a filament eruption and an M1.7 flare.

4.2 Searching for CMes without LCS

Identifying stealth CMes is not a straightforward task. In fact, we are looking for a negative association—CMes that cannot be associated with any low-coronal signature—which is much harder than proving a positive one. Our purpose was not to confirm every single candidate stealth CME in our dataset, but rather to find a number of interesting events to be used for the observational characterization of stealth CMes and for numerical modeling of specific events. Therefore we used a rather exclusive approach in determining whether a CME could be associated with low-coronal signatures or not.

To eliminate the obvious non-stealth CMes from the vast dataset we studied, we developed a procedure that combines the output of different automated tools, each one detecting a different low-coronal signature of solar eruptions. The input for this algorithm is the list of CME detections produced by CACTus (Robbrecht and Berghmans, 2004; Robbrecht et al., 2009a, www.sidc.be/cactus), a software tool that autonomously detects CMes in the SOHO/LASCO coronagraph images. For each entry, the catalog lists the CME timing information, its principal angle, angular width and median velocity. In this study we focus on the year 2012, during which CACTus detected 1596 CMes in the LASCO images. (Table 4.1)

The CACTus CME catalog for 2012 was coupled with the GOES X-ray event lists to filter out CMes with an associated X-ray flare. We associate an X-ray

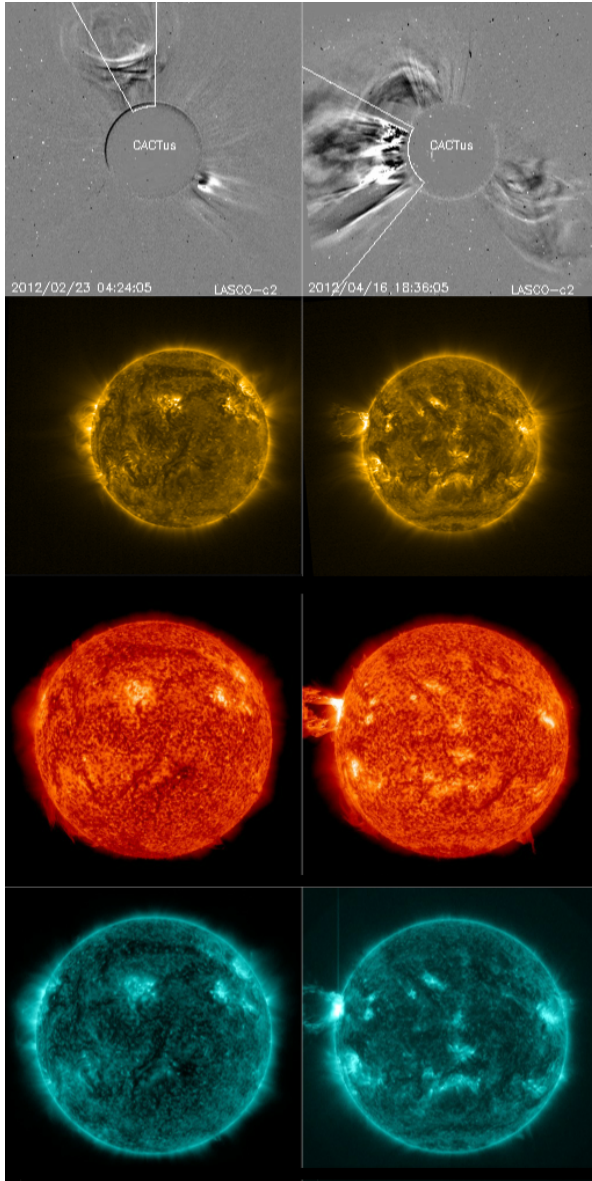


Figure 4.1 *CACTus* LASCO detections of a stealth CME (left on the top row) and of a CME associated with coronal signatures (top row, right). Subsequent rows illustrate the coronal signatures associated with these events in different wavelengths (*PROBA2/SWAP* 174 Å, *SDO/AIA* 304 Å and *SDO/AIA* 131 Å, respectively). The CME on the right was associated with an erupting filament and an M1.7 flare on the east solar limb.

CME list	Number of Events	Catalog	Number of Matches
CACTus CME list	1596	GOES event list	680
Stealth CME Candidates	481	CACTus COR2-A CME list	396
Confirmed Stealth CMEs	40	CACTus COR2-B CME list	413
		SoFAST catalog	332

Table 4.1 *Left Column* Number of CMes in the complete CACTus LASCO CME list for 2012, and in the lists of candidate and confirmed stealth CMes. *Right Column* Number of matches when comparing CACTus SOHO/LASCO CME detections to GOES flare lists, CACTus SECCHI/COR2 CME observations and SoFAST detections. Our algorithm reduced the CACTus LASCO list to a list of 481 stealth CME candidates by matching CMes to low-coronal signatures of eruption. There is a clear overlap in the matches found with different catalogs, especially between the two flaring catalogs (GOES and SoFAST) and between the catalogs based on both STEREO spacecraft. The list of candidate stealth CMes was further reduced to 40 confirmed CMes without LCS after visual inspection of all these events.

flare to a CME in cases where the flare occurred at most 4000 s before the initial detection of the CME by CACTus, or when it was observed less than 3600 s after. These are empirically derived time limits that were found to result in the best matches between CMes and associated flares. To define these limits, we have investigated the CACTus CME list for July 2012 in detail and compared the matches found by our algorithm to the observations. Initially both time ranges were set to 3600 s. However, using the July 2012 events as test cases, we found that this time interval was too narrow to find appropriate matches with the GOES and SoFAST (see below) flare catalogs in case these flares occurred before the event. We therefore increased the allowed time range to find a matching flare before the CMes detection time to 4000 s.

The permitted time interval between a flare before a CME and the CME itself was further adjusted according to the CME speed as measured by CACTus. While the CME may be accelerating or decelerating somewhat within the LASCO field-of-view, we based this adjustment on the kinematics of a particle

trajectory under constant acceleration:

$$x(t) = x_0 + \frac{v + v_0}{2}t.$$

Even though the LASCO FOV starts at $1.5 R_{\odot}$, we assumed that the average distance that a CME would have travelled before detection was $0.8 R_{\odot}$. Indeed, not all CMEs originate at the solar center, so assuming a lower average distance is appropriate. With $v_0 = 0$ the initial velocity and v the CME mean velocity calculated by CACTus, this equation then gives a transit time t , for which we set an upper limit fixed at 4000 s:

$$t = 2 \frac{0.8 R_{\odot}}{v} < 4000 \text{ s}$$

As a result of applying this algorithm, 680 out of 1596 LASCO CMEs were matched to a GOES X-ray flare. This is illustrated in Table 4.1.

Next, the algorithm compared the CACTus LASCO CME catalog to the CACTus CME detections in SECCHI/COR2 coronagraph images to exclude *back-sided* CMEs (CMEs occurring at a location on the Sun that is facing away from Earth at the time of eruption). A CACTus LASCO CME was identified as back-sided in case an associated CACTus COR2 event was found that occurred within one hour either side of the CACTus detection time in LASCO and for which the COR2 principal angle indicated the CME was propagating away from Earth. These time ranges were again based on detailed investigation of the July 2012 observations. On June 30, 2012, the midpoint in the time period that was investigated, the separation angle between STEREO A and Earth was around 119° , while the separation between STEREO-B and Earth reached 116° , implying that by combining these three viewpoints the complete solar surface could be observed. For the purpose of this study, back-sided CMEs were coarsely defined as having a principal angle (counterclockwise) in the range of 180° to 360° in the case of COR2-A, and a principal angle between 0° and 180° for COR2-B observations. Accordingly, 396 LASCO CMEs were determined to occur on the far side of the Sun based on COR2-A data, while 413 events were back-sided as seen from COR2-B. (Table 4.1)

Finally, the CACTus LASCO list was compared to the output of the Solar Flare Automated Search Tool (SoFAST, Bonte et al., 2013, www.sidc.be/sofast), based on observations from PROBA2/SWAP. SoFAST allows for the elimination of events with any associated EUV variability. Table 4.1 shows that 332 LASCO CMEs were found to be connected to variability in the SWAP images.

Each of these steps was performed independently and in the case that a specific CME from the CACTus LASCO catalog was associated with any of the detections in the other datasets, it was removed from the list of candidate

stealth CMES. Applying this procedure to the data for the year 2012 resulted in a list of 481 CMES that could not be linked automatically with flares, EUV brightenings or activity on the far side of the Sun. (Table 4.1) Visual inspection of solar images in various wavelengths using observations from PROBA2/SWAP, SDO/AIA and STEREO/SECCHI for all these events enabled us to eliminate CMES associated with filament eruptions, EIT waves. EUV dimmings, or eruptive signatures at larger heights. Some events could also be linked to flares or back-sided CMES occurring outside the time intervals that we implemented to exclude events from the CACTus LASCO CME list. This final effort resulted in a list of 40 confirmed CMES without low-coronal signatures, displayed in Table B.1 of Appendix B.

At this point it is important to emphasize once more that this procedure was not designed to extract every single CME without low-coronal signatures that occurred in 2012 directly from the input catalog. The purpose was instead to find a sufficiently large number of interesting stealth events to investigate in more detail. The algorithm was developed to eliminate as many CMES with clear observational signatures as possible following an automated procedure, thus limiting the number of events remaining for visual inspection.

Undoubtedly, during this procedure a limited number of incorrect associations was made between a CME and the detection of a flare, EUV variability or a CME on the far side of the Sun, mainly because these associations were based on timing only: information on CME principal angles and flare locations was ignored. In order to (crudely) assess the algorithm's performance, we used the location information provided in the GOES event list and in the SoFAST catalog to approximate the principal angle of propagation for CMES related to these events and the resulting principal angles were compared to those of the matching CACTus CMES. The principal angles calculated by CACTus for LASCO and COR2 CMES that were paired up by the algorithm were correlated as well. This procedure is subject to certain limitations. For example, when calculating the principal angle for SoFAST and GOES events, we are assuming that the associated CME is propagating radially outward from its source region, while in fact it may undergo a considerable deflection (see, for example, Zuccarello et al., 2012).

However, the principal angles are found to agree reasonably well, taking into account these constraints. When comparing the GOES flare locations to the principal angle of the CMES they are matched to, we find a very bad agreement (that is, a difference in principal angle larger than 90°) for only 41% of the events. When matching with the SoFAST flare catalog this percentage is even slightly lower at 38%. Comparing principal angles in the catalogs from STEREO A and B to the ones from the LASCO catalog, we observe a mismatch in 51% (respectively 61%) of the cases for STEREO A (B). The stronger

disagreement between the CME catalogs may be a consequence of the fact that the principal angles defined by CACTus are projected on the plane of the sky. Taking into account that projection effects may be very different from separate viewpoints, it is conceivable that the principal angles for the SOHO/LASCO and STEREO/COR2 observations may differ significantly.

Note also that, to get a complete view of a CME, it is important to combine all different types of observations available, as we have done here. One instrument alone can not give a comprehensive understanding of an event and even when many instruments are combined, there is often room left for interpretation. Different instruments use different physical principles to observe solar eruptions. For example, coronagraph observations are based on Thomson scattering and thus image the CME density in the line-of-sight, weighted by the scattering angle. EUV imagers, on the other hand, are based on spectral line emission and therefore depend on the temperature and velocity of the plasma. A change in temperature can cause the plasma to shift its emission in or out of the passband and sufficient velocity can cause the spectral line to doppler shift from observability. The limitations of each instrument were taken into account as much as possible during the analysis of the stealth events. For example, we searched for signatures of eruptions in many different EUV passbands to account for plasma emitting at different temperatures.

Despite its limitations, the procedure described above allowed us to sift through the large number of detections in the 2012 CACTus LASCO CME catalog in an objective, automated and reproducible manner. As a result, we were able to confirm the occurrence of 40 CMES that indisputably had no low-coronal signatures. To our knowledge, this is the largest sample of stealth CMES studied so far.

4.3 Observational Properties of CMES without Low-Coronal Signatures

We used the 40 identified CMES without low-coronal signatures and their corresponding CACTus LASCO detections listed in Table B.1 to characterize the general properties of stealth CMES. CME appearance, position angle, velocity, and angular width were studied and compared to those of CMES with LCS. We also studied the scale invariance of stealth CMES.

When interpreting these results, it is important to remember that our sample of CMES without low-coronal signatures is limited to 40 events, a low number

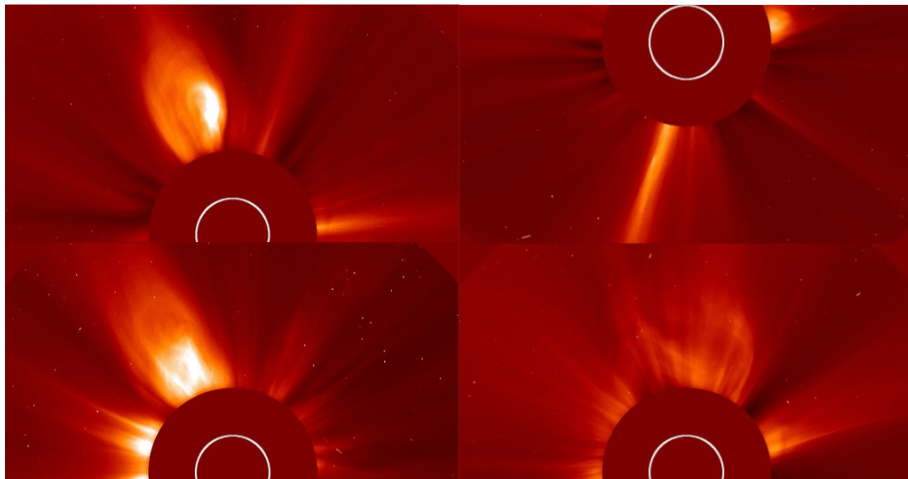


Figure 4.2 *LASCO coronagraph observations of CMEs without low-coronal signatures illustrating the variety in appearance for these events. Shown in clockwise direction, starting in the upper left corner, are a three-part CME, a narrow CME, a wide CME (angular width of 80° , measured by CACTus) and a streamer blow-out CME.*

compared to the nearly 1600 events in the complete CACTus LASCO catalog for 2012.

4.3.1 Appearance in Coronagraph Images

Observationally there is a large diversity in the appearance of CMEs without low-coronal signatures in coronagraph images. Some events are very narrow and similar to outflows while others are very wide CMEs, in some cases also showing the typical three-part structure. A few examples are shown in Figure 4.2. Seven out of 40 CMEs without low-coronal signatures were of the streamer blow-out type.

In 73% of events, the stealth CME was preceded by another nearby CME, which could conceivably have destabilized the overlying magnetic field and thus contributed to the initiation of the stealth event. Many of the stealth CMEs occurred in the vicinity of the polar coronal holes, a region of largely open magnetic field, another factor that may have contributed to facilitating a stealth eruption. Indeed, if an eruption occurs in a region where overlying field provides very little downward-directed force on the erupting structure,

that is an open field region, it may be that the eruption can unfold without a major restructuring of the magnetic field and therefore no strong low-coronal signatures of eruption are observed. For the CMEs without LCS that had a presumed source region closer to the equator, the PFSS reconstructions also showed open field lines nearby for four out of five events.

4.3.2 Position Angle

It is remarkable that many of the events in our list of CMEs without LCS have a principal angle directed towards the north. This is illustrated in Figure 4.3, where the distributions of CMEs with and without LCS are plotted as a function of the principal angle measured by CACTus. Note that, for ease of comparison and to allow for the plotting of both curves on the same axes, the number of occurrences of CMEs with coronal signatures was scaled down proportionally by a factor of $(1596 - 40)/40$. Evidently, CMEs that exhibit low-coronal signatures of an eruption are much more evenly spread across the solar disk than stealth CMEs are. The fact that many CMEs without LCS seem to originate at high northern latitudes and near the polar coronal hole, suggests that their source region is not a magnetically complex region, which is compatible with the lack of coronal signatures and the low speeds (see below) of these coronal mass ejections.

It remains important to emphasize that these findings are based on a small number of stealth events. However, when a random set of 40 events is taken from the CACTus CME list for 2012, the principal angle distribution is in a large majority of the cases randomly spread around the solar disk. Out of 1000 random samples of 40 CMEs we took, only eight (i.e. less than 1%) had at least 20 events directed towards the north, where an event towards the north was defined as having a principal angle that falls between 300° and 60° , with north corresponding to an angle of 0° . Thirty out of the 40 CMEs without low-coronal signatures studied here, fit that definition. This clearly illustrates that the predominantly northward propagation of our sample of stealth events is not just a stochastic coincidence, but an inherent property of the CMEs without low-coronal signatures studied here.

We investigated the possibility that this apparent preference for stealth CMEs to originate near the north pole was an observational effect caused by the tilt of the solar rotation axis. Indeed, when the solar north pole is directed towards Earth, possible low-coronal signatures in this region should be easier to observe and thus it should be more straightforward to determine whether a CME is stealth or not. Additionally, more stealth CMEs originating near the northern pole would be labeled as front-sided events. However, no clear relationship

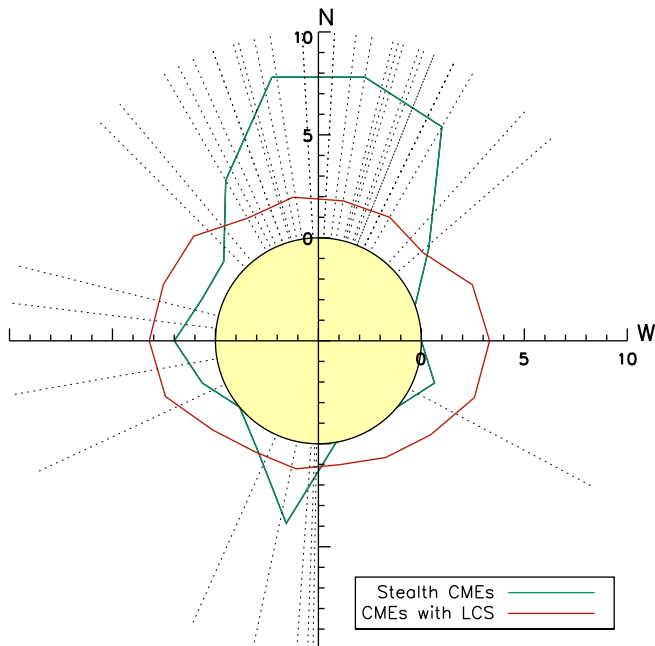
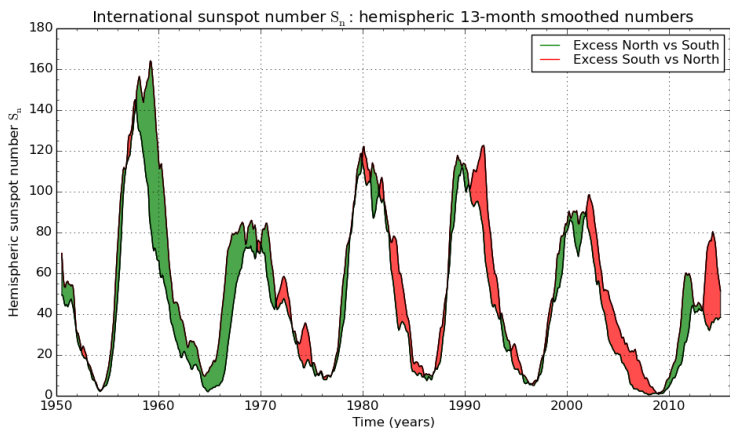


Figure 4.3 *Distribution of coronal mass ejections with (red line) and without (green line) low-coronal signatures relative to their principal angle of propagation, binned according to their principal angle with a bin size of 20° . The number of occurrences of CMEs with coronal signatures was scaled down proportionally by a factor $(1596 - 40)/40$. The dotted lines indicate the principal angle of propagation for each stealth CME as measured by CACTus.*

between the solar \mathbf{B}_0 angle, characterizing the tilt of the solar rotation axis with respect to the ecliptic north, and the number of stealth CMEs towards the north (or south) could be identified.

Another potentially contributing factor is the dominance of the northern hemisphere in solar activity during the year 2012. This can, for example, clearly be seen in Figure 4.4, that shows the hemispheric sunspot numbers during the last five cycles. Far more sunspots and active regions were observed above the solar equator than below during 2012. This explains the slight imbalance in the spread across the solar disk of the CMEs with LCS: more events were detected with a principal angle pointing towards the north. The same effect is expected for stealth CMEs. However, that observation alone



SILSO graphics (<http://sidc.be/silso>) Royal Observatory of Belgium 2015 August 7

Figure 4.4 North and south components of the monthly sunspot number (SSN) for the last five cycles (smoothed over 13 months). Green indicates when the northern sunspot number is highest, and red shows when more sunspots are counted in the southern hemisphere. (This plot is based on data from the Uccle station up to 1991 and from the World Data Center (WDC) Sunspot Number network since January 1992; SILSO data and image provided on <http://sidc.oma.be/silso/monthlyhemisphericplot> by the Royal Observatory of Belgium, used with permission.)

is probably not sufficient to explain the large discrepancy in northward and southward-directed stealth CMEs that is apparent in Figure 4.3.

4.3.3 CME Speed and Velocity Profiles

Velocity Distribution

The CACTus CME detection algorithm reports the median velocity for each observed CME. The software determines the speed of the CME in each direction within the angular span of the CME. The median of the resulting velocity profile is given as the speed of the CME. The distributions of these median velocities for CMEs with and without low-coronal signatures are shown in Figure 4.5 on a logarithmic scale. The median speeds calculated by the CACTus software tend to differ from the velocities of CMEs reported in other (manual) catalogues, mostly because the latter are usually based on measurements of the bright leading edge along one principal angle (Robbrecht and Berghmans, 2004). For

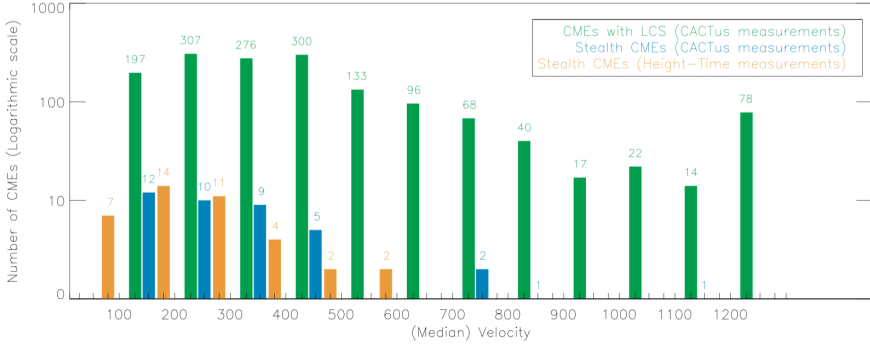


Figure 4.5 *Distribution of the median velocity for coronal mass ejections with and without low-coronal signatures as measured by the CACTus algorithm and plotted on a logarithmic scale (bin size = 100 km s^{-1}). The third distribution represents the projected CME velocities based on height-time measurements of the bright leading edge of the CME in the LASCO images.*

comparison with these catalogues, we derived the stealth CME velocity, along the principal angle and projected in the plane of the sky, from height-time profiles of the bright leading edge observed in the LASCO images. The resulting distribution is shown in Figure 4.5 as well.

Figure 4.5 illustrates that the peak of the velocity distribution occurs at lower values for stealth CMEs compared to CMEs with LCS. It follows that CMEs without low-coronal signatures are generally slow events: typically with a median velocity between 100 km s^{-1} and 500 km s^{-1} , although a few faster eruptions were also identified. This low velocity is not surprising as the lack of on-disk signatures suggest there may only be limited free energy available, not enough to drive a very fast eruption.

Our results are compatible with the distributions obtained by Ma et al. (2010). These authors found 11 stealth CMEs with velocities ranging from 100 km s^{-1} to 300 km s^{-1} . The fact that the present study also identified stealth CMEs with higher velocities could simply be linked to the larger number of stealth CMEs found here. An additional influence may come from the different phases of the solar cycle in which the CMEs in both surveys were detected. Ma et al. (2010) investigated stealth CMEs in the first half of 2009, a period of deep solar minimum, while during 2012 solar activity had increased, rising towards a new solar maximum. Indeed, Yashiro et al. (2004) studied the properties of CMEs observed in the LASCO coronagraph between 1996 and 2002, and found that

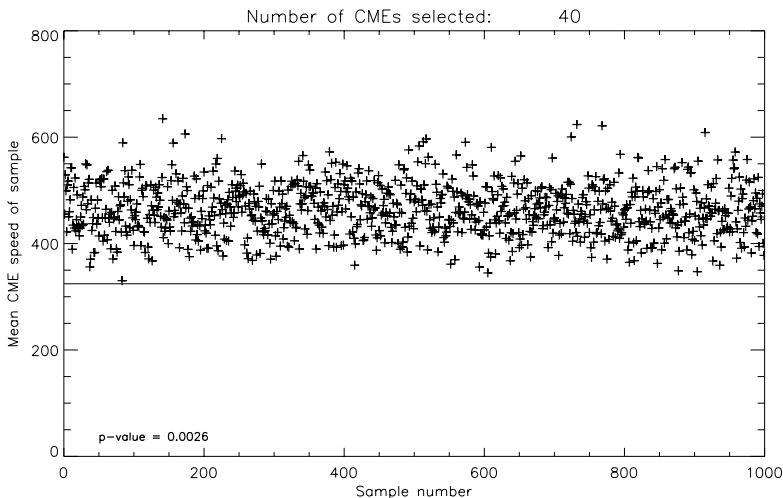


Figure 4.6 Mean CME velocity of 1000 samples of 40 randomly selected CMES. The horizontal line indicates the mean velocity of the set of CMES without low-coronal signatures.

their average speed increased from 300 km s^{-1} at solar minimum to 500 km s^{-1} at the time of solar maximum.

To assess the influence of our small sample size on the stealth CME velocity distribution, we computed the mean velocity for 1000 samples of 40 CMES, randomly selected out of the CACTus detection list for 2012. These values are shown in Figure 4.6. This figure clearly illustrates that the mean CME velocity for CMES without low-coronal signatures is much lower. The mean velocity values for the random samples are consistent with a normal distribution with mean $\mu = 461.12$ and standard deviation $\sigma = 48.80$. The mean of the stealth CME velocities is 324.48 km s^{-1} , but has a large standard deviation $\sigma = 216.47$, possibly due to the low number of events in the stealth CME sample. The probability to obtain this mean value from the gaussian distribution formed by the means of the random samples is as low as 0.3% ($p = 0.0026$), implying that the group of stealth CMES indeed stands out statistically from a random set of 40 events.

Height-time Diagrams and Velocity Profiles

We compared the height-time evolution of stealth CMEs to published results for different eruption mechanisms (see, for example, Schrijver et al., 2008). These authors compared filament rise profiles to results from numerical simulations in order to constrain the mechanisms by which the flux rope was destabilized. For example, in case of the two-dimensional catastrophe model by Priest and Forbes (2002), the height-time profile takes the form of a power law with an exponent around 2.5. An exponential rise is compatible with the kink instability (Török et al., 2004; Török and Kliem, 2005) and also with the torus instability (Kliem and Török, 2006), which in fact starts as a $\sinh(t)$ function, and thus is very similar to the exponential function. A parabolic profile is a good description for the CME rising phase in the breakout model (Lynch et al., 2004).

The best fits for our measurements are exponential and parabolic profiles, corresponding to ideal MHD instabilities and breakout, respectively. An example is shown in Figure 4.7 and the parameter values for these fits are given in Table 4.2. The lack of LCS suggests that these eruptions are indeed not driven by impulsive reconnection near the solar surface, which is consistent with the evidence from our height-time profiles.

To illustrate the spread in the best fitting parameter values for all stealth CMEs, we list the average, standard deviation and median for each of these parameters in Table 4.3. For the parabolic profile on the first row, the parameter c (which defines a shift of the profile in the y -direction) is rather well defined: the average and median are close together and the standard deviation is limited. Indeed, all profiles start at approximately the same height, defined by the inner edge of the field-of-view of the LASCO coronagraph (where the CME first comes into view). The same effect can be observed in the parameter b for the linear profiles, which has approximately the same value. Also the parameter b in the cubic function shows this effect. However, here the shift in y -values is too high: the LASCO C2 inner edge is at $2 R_{\odot}$. Visual inspection of the cubic fits indeed show that they systematically start at a too large height and are generally bad fits throughout.

Note that the other parameters for the different profiles in Table 4.3 show a large standard deviation with respect to the average value and considerable differences between the average and median values, which is indicative of a large spread in the profiles. This large variation in the height-time profiles also results in quite different velocity profiles.

These velocity profiles for all stealth events in our sample are plotted in Figure 4.8, as a function of height and for accelerating and decelerating CMEs separately. For ease of display in a single plot and to facilitate comparison

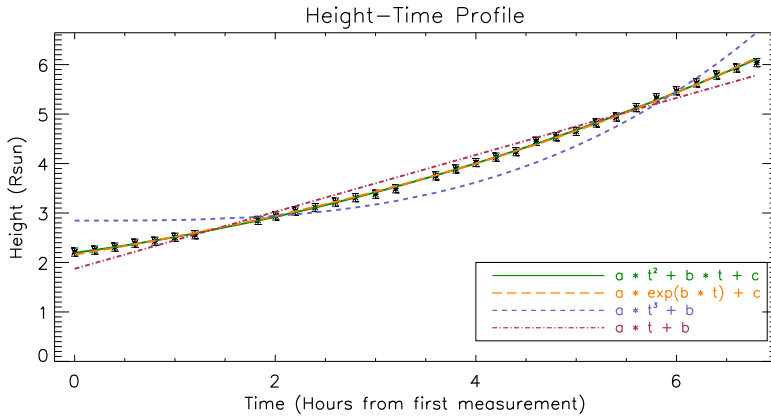


Figure 4.7 Height-time diagram for a stealth CME observed on 2012 February 22 at 23:48 UT by SOHO/LASCO. (This event is also shown in the left panels of Figure 4.1.) The height-time measurements were fitted with a parabolic, exponential, cubic and linear function (solid/green, double-dashed/orange, dashed/blue and dot-dashed/red line respectively). The best fits are found for the exponential and parabolic functions. The parameter values for these fits are given in Table 4.2.

Profile	Parameter	Value	Reduced χ^2
$at^2 + bt + c$	a	0.044	0.107
	b	0.276	
	c	2.194	
$a \exp(bt) + c$	a	2.224	0.173
	b	0.151	
	c	-0.066	
$at^3 + b$	a	0.012	18.000
	b	2.846	
$at + b$	a	0.576	4.370
	b	1.873	

Table 4.2 Parameter values for the best fits to the height-time profile of the stealth CME observed on 2012 February 22 at 23:48 UT by SOHO/LASCO. In the last column the reduced χ^2 value is given, a goodness-of-fit parameter that takes the number of datapoints into account and normalizes for the model complexity. The closer this value is to 1, the better the model fits the observations.

Profile	Parameter	Average	Standard Deviation	Median
$at^2 + bt + c$	a	0.05314	0.18258	0.02898
	b	0.95727	0.77072	0.75222
	c	2.59647	0.30235	2.54592
$a \exp(bt) + c$	a	10.59661	12.66124	4.15571
	b	0.18811	0.15499	0.13616
	c	-7.95892	12.57849	-1.74926
$at^3 + b$	a	0.28274	0.42663	0.08564
	b	3.24291	0.39725	3.28541
$at + b$	a	1.10168	0.67612	0.93854
	b	2.49901	0.39673	2.53668

Table 4.3 *Average and median parameter values for the best fits to the height-time profiles of the stealth CMES. The standard deviation on these parameter values is given as well.*

between the velocity profiles, the measurements were normalized with respect to the final CME speed for accelerating CMES, while for the decelerating ones the initial velocity was used as reference speed. The profiles were colored according to their principal angle of propagation (measured by CACTus). The color code is explained by the schematic sun drawn in the bottom right corner. This figure clearly shows that most stealth CMES are accelerating and reveals two populations in the top panel. A first group of CMES is launched at nearly their final speed and accelerates very little, while a second group of events accelerates gradually over the LASCO FOV. Additionally, the bottom panel shows that all but one of the decelerating CMES originated from the north.

Sheeley et al. (1999) distinguished two CME classes: gradual CMES that seem to originate from rising prominences and their cavities and have leading edges that accelerate gradually to a velocity in the range of 400 to 600 km s⁻¹ within 30 R_{\odot} ; and impulsive CMES, often associated with flares and having typical speeds larger than 750 km s⁻¹, decelerating as they propagate outwards. Stealth CMES fit best in the former category of gradual CMES as they are rather slow events and in most cases their velocity profiles show a moderate acceleration in the LASCO FOV. Obviously, in the case of CMES without low-coronal signatures, there is no associated prominence observed. Likewise MacQueen and Fisher (1983) reported that flare-associated events generally exhibit higher speeds and little acceleration with height, while in the case of events associated with eruptive filaments lower initial velocities and large

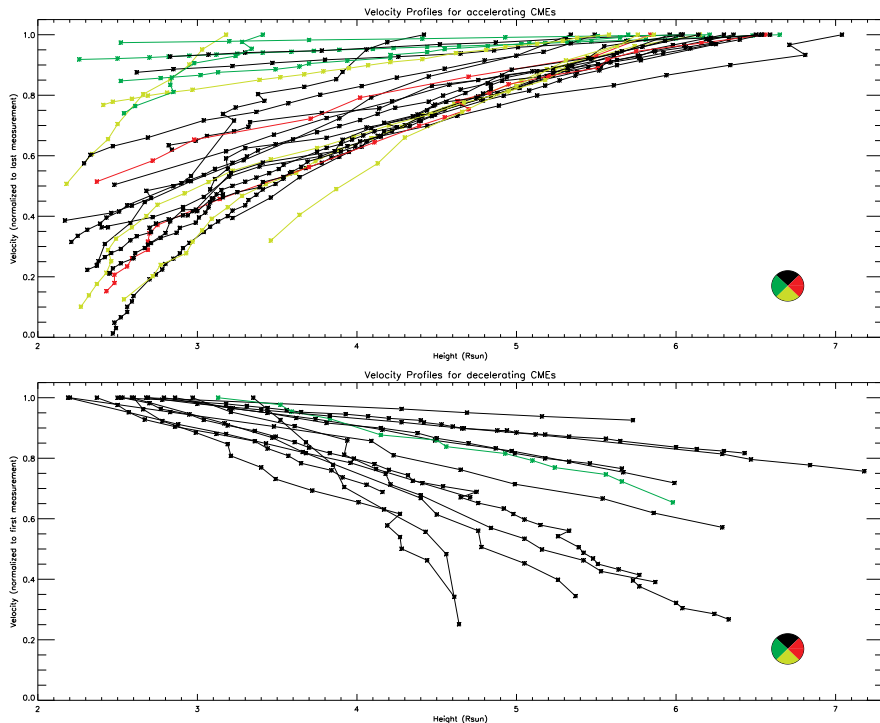


Figure 4.8 *Velocity profiles for accelerating (top) and decelerating (bottom) CMEs without low-coronal signatures, as a function of height and normalized to their final (respectively initial) velocity. All profiles are color-coded according to the principal angle of the CME as measured by CACTus.*

accelerations are observed. Unfortunately, in the case of stealth CMEs we are not able to distinguish between these two categories as we do not observe any related flares or filaments.

The height-time measurements in Figure 4.7 are based on the SOHO/LASCO data and are thus measurements of the three-dimensional CME projected onto the plane of the sky. Ideally, these data points should be corrected for projection effects using, for example, the different viewpoints from the STEREO spacecraft. Because they are derived from the height-time measurements, also the velocity profiles in Figure 4.8 suffer from these projection effects (Burkpile et al., 2004). Before the STEREO era many statistical studies of CMEs were performed with plane-of-the-sky measurements as these were the only data available. Fortunately, Howard et al. (2008b) conclude from their comparative

study between projected and deprojected CME parameters that the general trends in these parameters are preserved. The shape of our velocity profiles would therefore not change were they corrected for projection effects. Our comparison of the stealth velocity profiles to the study by Sheeley et al. (1999) and of the stealth median velocity histogram to the CDAW catalog (Figure 4.5) remains valid: in both cases plane-of-the-sky measurements are compared.

Moreover, when analyzing a sample of 1961 CMES and their associated surface signatures, Howard et al. (2008b) find that while the mean deprojected speed for these events exceeds the mean apparent (uncorrected) speed by a factor of 1.7, for the majority of the events the differences between projected and true velocities were not large: half of the corrected CME speeds were within 5% of the apparent speeds. Indeed, projection effects are especially significant when the CME source region is close to the center of the solar disk (within 45° of the Sun-Earth line; Shen et al., 2013), and much less outside this range. As most of our stealth CMES are believed to originate close to the solar poles, we expect the projection effect on the velocity for these events to remain within 5% as well. Nevertheless, the stealth CME velocities as presented here are to be considered as a lower limit for their true velocities.

4.3.4 Angular Width

The angular width distributions for stealth CMES and CMES with low-coronal signatures are shown in Figure 4.9 on a logarithmic scale. The stealth CMES show a clear peak around 20° and the distribution for CMES with LCS also indicates narrow events are more common than large-scale CMES. A maximum around 20° - 25° was reported by Robbrecht et al. (2009a) as well when studying the complete CACTus LASCO CME database for solar cycle 23. They compared their results with the manual CDAW CME catalog and noted the latter shows a flatter distribution. This can be explained by the fact that the angular width of a CME is not well defined and large discrepancies are sometimes found when comparing manual and automated measurements, especially for wide CMES. Additionally, it is known (Robbrecht and Berghmans, 2004; Yashiro et al., 2008) that CACTus detects more narrow CMES because these narrow events are sometimes regarded as outflows by operators and therefore not recorded as a CME in the CDAW catalog.

To avoid a bias due to these differences in angular width measurements in different catalogs, only the angular widths of CMES with and without low-coronal signatures as measured by CACTus are compared here. While visually both distributions do not seem to differ strongly, Figure 4.9 does suggest that stealth CMES are comparatively narrow events. The angular width of most

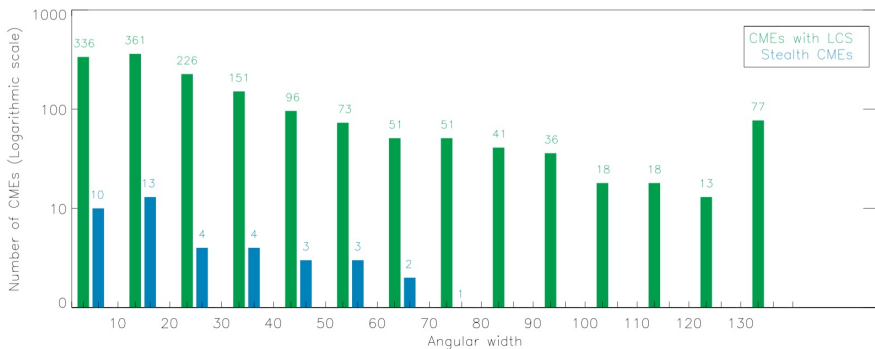


Figure 4.9 *Distribution of the angular width for coronal mass ejections with and without low-coronal signatures as measured by the CACTus algorithm and plotted on a logarithmic scale (bin size = 10°).*

stealth CMEs in our sample is below 50°, although CACTus detected some outliers with a much larger width as well. All CMEs with a width larger than 80 degrees were associated with low-coronal signatures of an eruption. Ma et al. (2010) report the angular width of their set of stealth CMEs is below 40°. As was the case for the CME velocities, this difference may be explained by their smaller sample size or by the effect of the solar cycle on CME angular width. Yashiro et al. (2004) observed an increase in the average angular CME width from 47° at the time of solar minimum (1996) to 61° in the early phase of solar maximum (1999), followed by a decrease to 53° in 2002, the late phase of solar maximum.

As before, we performed a statistical analysis to evaluate the influence of our small sample size on the angular width distribution for CMEs with low-coronal signatures. We computed the mean angular width for 1000 samples of 40 randomly selected CMEs, which resulted in a plot very similar to Figure 4.6. In this case, however, the mean widths do not form a true normal distribution. Nevertheless, we have fitted a gaussian distribution with mean $\mu = 39.40$ and standard deviation $\sigma = 7.27$ to this data. As Figure 4.10 illustrates, the actual angular width distribution is quite well reproduced by the central bell-shape of this gaussian distribution, however the tails do not fit properly. In fact, the left tail, which is of most interest to us since that is where the stealth CME mean angular width value of 25.65 is found, is overestimated by this fit. The true distribution is lower in the left tail (and higher in the right one). Because the p-value corresponds to the area below the distribution function, the p-value ($p = 0.029$) we find assuming a normal distribution is higher than the true value.

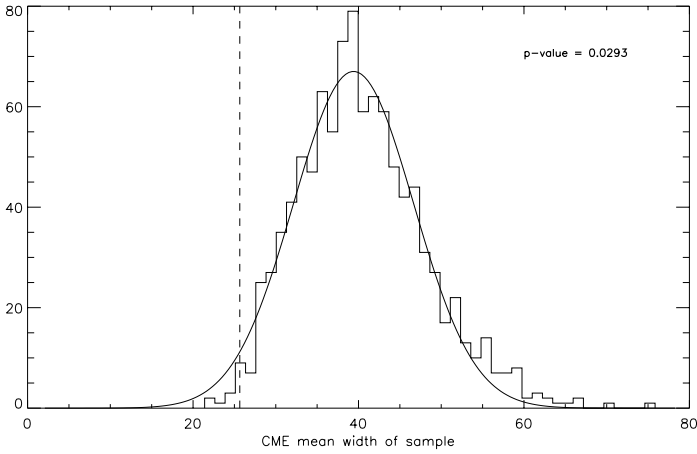


Figure 4.10 *Distribution of the mean angular width of 1000 random samples of 40 coronal mass ejections. The dashed line indicates the mean angular width that was found for the CMES without low-coronal signatures.*

Since this p-value is already very low, it is quite likely that the stealth CMES do not have the same angular width properties as a random sample of 40 events.

4.3.5 Scale Invariance²

Questioning whether small-scale outflows should be included in their CME catalog, Robbrecht et al. (2009a) studied CME width histograms for CMES detected by their CACTus algorithm on a logarithmic scale in search of a power law. They found a linear behavior over a large range of angular widths with a slope $\alpha \approx -1.66$ (see Figure 1.15). This obtained scale invariance implies that there is no characteristic size for a CME. Figure 4.11 shows the frequency distributions for CMES with and without LCS as a function of angular width. The distribution for CMES with low-coronal signatures is best described by a linear fit with a slope $\alpha \approx -1.49$, while $\alpha \approx -0.97$ was found for CMES without. To make these fits, only the events with an angular span between 5° and 120° were used. Wider CMES were excluded because, due to projection effects, their

²In this section we study the scale invariance for stealth and normal CMES and compare the scaling law parameters found for both groups of events. However, as the study in Chapter 5 will clearly illustrate, our sample of stealth CMES is too small to determine this scaling parameter reliably. We therefore revise the results from this section in Chapter 6.

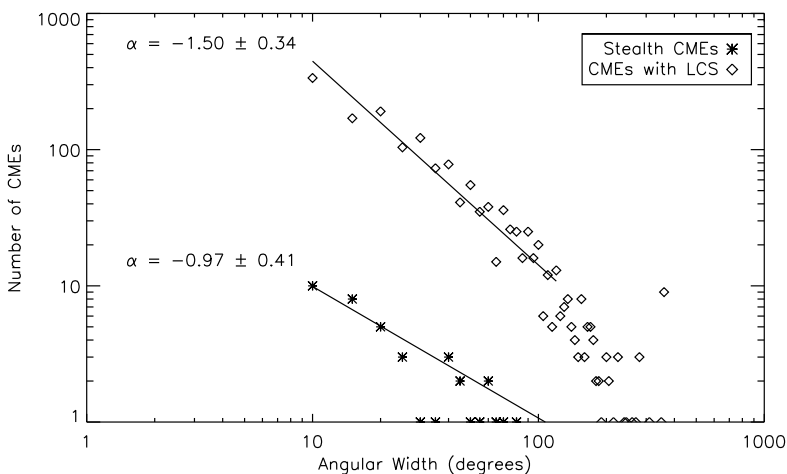


Figure 4.11 Frequency distributions for the angular width of coronal mass ejections with (diamonds) and without (asterisk) low-coronal signatures as measured by the CACTus algorithm. The linear behaviour on a logarithmic scale implies a power law that indicates the scale invariance of CMES. The stealth CME function exhibits a significantly flatter slope in comparison to CMES with LCS. The 1σ uncertainty estimate for α is based on the standard deviation of the angular width distribution.

angular width measured by CACTus may not correspond well to their true angular width.

We thus find that the angular width distributions for stealth CMES and CMES with LCS have a different slope, suggesting a different initiation mechanism may be at work for each class of events. Note that the CACTus width measurements can be an underestimation of the actual angular width, for example in case only part of the CME is detected. For nine out of 40 stealth events, the angular width was underestimated by at least 10° , implying that these CMES should be counted in a higher histogram bin and that the actual slope for the CMES without LCS could be somewhat flatter.

The difference in slope between both CME classes is significant despite the small sample size in the case of stealth CMES. It is important to note that there is indeed a clear influence of the small sample size on the slope: when 40 CMES are randomly selected from the CACTus CME list, the resulting slope value is much smaller than the one found for all normal events together, which is immediately clear from the top panel in Figure 4.12. This flatter distribution is not surprising

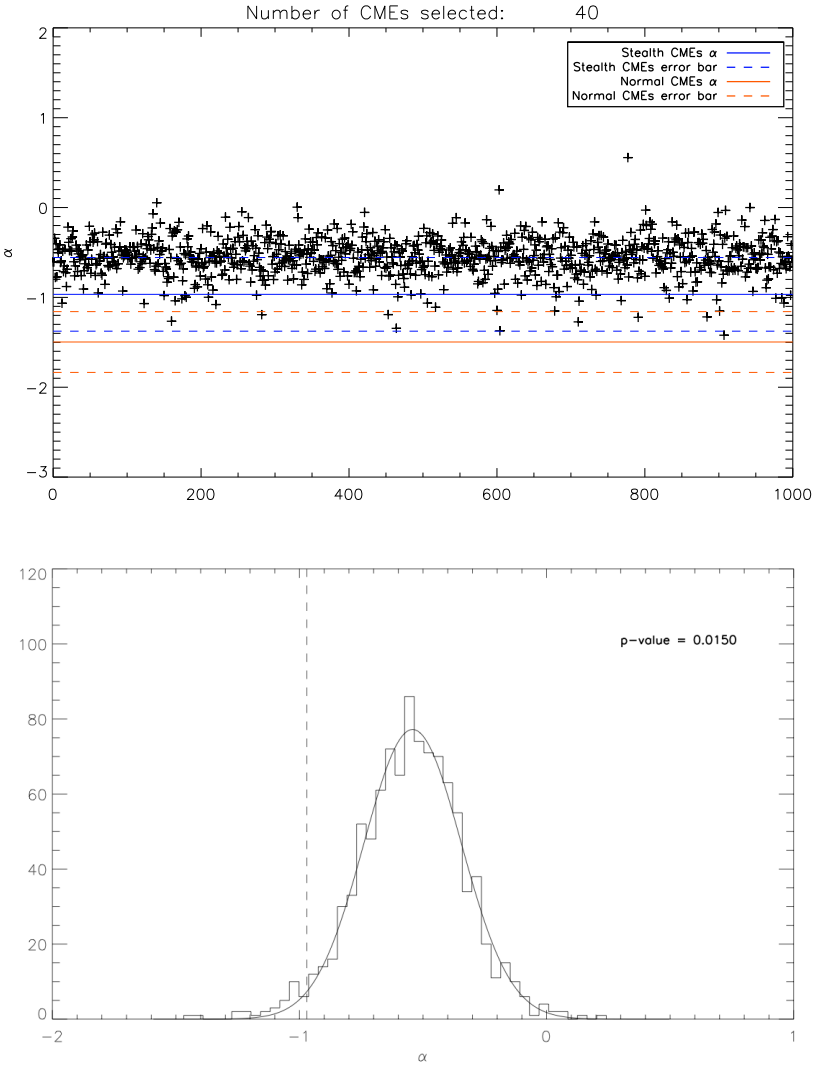


Figure 4.12 *Top Panel:* Scale invariance slope parameters for 1000 random samples of 40 coronal mass ejections. The blue (red) full line indicates the slope value that was found for the CMES without (with) low-coronal signatures. The dashed lines indicate the respective standard deviations. **Bottom Panel:** Distribution of the scale invariance slope parameter for the same samples. The dashed line indicates the slope value that was found for the stealth CME sample.

as only a small random selection is made from all CMEs and including a wide CME in such a small sample influences the slope significantly. In reality the angular width distribution of CMEs is dominated by narrow events, which becomes clear when all detections are taken into account. However, the CMEs without low-coronal signatures still stand out when compared to random small samples. Selecting 1000 random sets of 40 events yielded a normal distribution of slope values with mean $\mu = -0.55$ and standard deviation $\sigma = 0.21$ (Figure 4.12, bottom panel). For the slope value of the stealth CMEs ($\alpha = -0.97$), we find a probability less than 2% ($p = 0.015$). This implies that the linear fit is much steeper for stealth CMEs than expected for randomly selected events, indicating that there are more narrow CMEs without low-coronal signatures, compared to a random sample of 40 CMEs. This is in agreement with Section 4.3.4, where we concluded that CMEs without low-coronal signatures are generally narrow events.

4.4 Initiation Mechanisms for Stealth CMEs

This study was motivated by the question whether CMEs without low-coronal signatures are governed by different physical processes than those that do show clear signs of an eruption: do both classes of CMEs have different initiation mechanisms, or are the stealth CMEs simply at the lower energy end of a CME spectrum? In fact, based on their low velocities, gradual acceleration, limited angular width and most importantly the absence of low-coronal signatures of eruption, it is likely that stealth CMEs are not very energetic events. Presumably, all available energy goes into expelling the CME, and little is left to leave observable eruption signatures on the solar disk. Additionally, because we do not observe any signatures of magnetic reconnection close to the solar surface, it is highly likely that the crucial reconfiguration of the coronal magnetic field is occurring at higher altitudes where the low density makes the observation of plasma heating challenging.

If in fact the initiation of CMEs without low-coronal signatures occurs at larger heights, this might explain why we observe stealth CMEs to be predominantly narrow and slow. Depending on the surrounding magnetic field, CMEs usually expand and accelerate as they propagate through the corona. In the case of stealth CMEs, assuming the reconnection indeed occurs higher up in the corona, the CME would have less time to expand and speed up before entering the LASCO field-of-view and thus a more narrow and slow event would be observed by CACTus.

Pevtsov et al. (2012) suggested an explanation for the occurrence of stealth CMEs. These authors studied two erupting filament channels without filament material inside and report these eruptions produced only minor or very gradual changes in the chromosphere and corona. This points to a gradual loss of equilibrium prior to the eruption. In case of the second eruption, the authors suggest the equilibrium was eroded through flux emergence. For instance, Wang and Sheeley (1999) investigated how emerging flux can destabilize a quiescent filament by removing or opening up the magnetic field overlying the filament. They emphasize that, because the magnetic flux emergence can result in a global rearrangement of the magnetic field topology, the source region may be as much as 25° away from the erupting filament, and therefore may wrongfully appear to be unrelated to the filament eruption. This chain of events where the destabilization of an empty filament channel leads to a CME without LCS was also proposed by Robbrecht et al. (2009b) in their first case-study of a stealth event.

A different stealth CME initiation scenario takes into account that for 29 out of 40 stealth events, another CME was observed preceding the event without low-coronal signatures. These preceding eruptions may have destabilized the coronal magnetic field at higher altitude and triggered a stealth event in this way. In case of two eruptions from the same source region, the first eruption may have facilitated the initiation of the stealth event by opening up the overlying magnetic field lines and thus clearing the path for the second eruption. A similar reasoning might explain the fact that many CMEs without low-coronal signatures are observed close to coronal holes, where the open field lines might facilitate an eruption.

In the case of multiple eruptions, the first CME may create a pressure imbalance that would cause the trailing stealth CME to be "pulled" out, instead of being launched and driven from below. This chain of events would indeed not leave clear observable traces on the solar surface.

Another conceivable scenario is described in Bemporad et al. (2012), where the authors studied two consecutive CMEs, observed on 21 and 22 September 2009 and approximately 7 hours apart. The first CME was caused by a small prominence eruption towards the north, while the second CME could not be associated with a flare, dimming or erupting prominence. Numerical modeling of these events led the authors to conclude that the initiation mechanisms for both CMEs were different. While the first CME was the result of shearing motions, the second one was a mass outflow caused by the rearrangement of the coronal magnetic field after the first eruption. To obtain this second CME, the strength of the global magnetic field is decisive. In a previous simulation by Zuccarello et al. (2012) the same initial magnetic field configuration, boundary conditions and driving mechanism were used. Only the magnetic field strength

of the global dipole differed: it had a value of 1.66 G at the poles, compared to 2.2 G for the simulation by Bemporad et al. (2012). As a result, no second eruption was observed by Zuccarello et al. (2012).

All observational evidence presented here points to —at most— weak reconnection occurring close to the solar surface during the initiation of stealth CMEs. The models that best fitted their height-time profiles were the magnetic breakout model and MHD instabilities. In these models the eruption is indeed initiated by reconnection higher up in the corona. As the erupting flux rope starts to rise, a current sheet forms below. The reconnection taking place in this current sheet drives the eruption and is the source of a solar flare and other LCS that may be observed. However, in the case of stealth events, this reconnection below is most likely not very powerful, as the CME is not strongly accelerated and no LCS are detected. Some stealth events even showed a very flat velocity profile and thus experienced limited acceleration when propagating in the LASCO FOV, indicating that the driving of the CME had already stopped below $2 R_{\odot}$. An interesting question to explore might be whether populations of flaring and non-flaring CMEs that do show LCS of eruption bare any similarities to these CMEs without LCS, especially concerning their velocity profiles. However, that analysis is beyond the scope of this research.

4.5 Conclusions

In this study, 40 CMEs without low-coronal signatures (LCS), occurring in 2012, were identified. While this is a low number compared to the 1596 CMEs that CACTus detected that year, it is the largest sample of stealth CMEs studied so far. Moreover, this set of stealth CMEs is clearly distinguishable from a random set of events.

The kinematic properties of the CMEs without low-coronal signatures were analyzed and compared to those of regular CMEs. We find that the 2012 stealth CMEs are very diverse in appearance, and tend to originate in the vicinity of the solar north pole. They are generally slow events, showing a gradual propagation in the LASCO field of view, and have a limited angular width. The scale invariance for stealth CMEs reveals a different power law than for CMEs with clear low-coronal signatures of eruption, suggesting an alternative eruption mechanism may be at work for both classes of events. (*Note however that the estimation of the power-law exponent suffers strongly from the low number of data points, see Chapter 6.*) The height-time profiles for stealth eruptions fit both the breakout model and models of ideal MHD instabilities.

Most probably there is not one single initiation mechanism for stealth CMEs. However, the scenarios presented above do show some similarities. Most importantly, the prime reconnection that facilitates or triggers the stealth CME presumably occurs at higher altitude. The erupting flux rope is not expelled forcefully, but is gradually accelerated or even dragged out by the solar wind. As future work, it would be interesting to confirm these assumptions through numerical simulations of a number of CMEs without low-coronal signatures that were identified during this study.

4.6 A New Focus

While in this study we have gained significant insights in the nature of CMEs without low-coronal signatures and have taken important first steps in defining their properties, we were continually limited by the low number of stealth events we were able to identify. For each observational characteristic of stealth CMEs that we studied here, we have attempted to assess the influence of this small sample size on the results. These, somewhat rudimentary, analyses showed that concerning their angular widths and median velocities, CMEs without low-coronal signatures clearly have different properties than small samples of normal events.

However, the picture was more complicated when we focused on the scale invariance for both types of CMEs. It is clear that there is an influence of the small sample size on the slope estimate here. Nevertheless, our sample of CMEs without LCS does stand out statistically from small random samples. We conclude that our sample size is simply insufficient to decide convincingly whether or not, when it comes to their scale invariance, CMEs without LCS differ from CMEs that do show these signatures.

This difficulty triggered new research questions: what sample size do we actually need for this type of study to be conclusive? Would this require just a handful more stealth events, or would our sample size need to grow substantially? We focused specifically on the sample size needed to reliably estimate the power law for the scale invariance. To answer these questions, we undertook a statistical study on the sample sizes and methods suited to provide a valid estimate of a power-law parameter. The results of this research are presented in Chapter 5.

Chapter 5

The Effect of Limited Sample Sizes on the Accuracy of the Estimated Scaling Parameter for Power-Law-Distributed Solar Data

Studying power-law distributions over several orders of magnitudes requires large amounts of measurements and appropriate methodology. In this chapter we demonstrate the shortcomings of some popular methods in solar physics and apply them to typical sample sizes. We use synthetic data to study the effect of the sample size on the performance of different estimation methods and show that vast amounts of data are needed to obtain a reliable result with graphical methods (where the power-law exponent is estimated by a linear fit on a log-transformed histogram of the data). We demonstrate the benefits of the Maximum Likelihood Estimator (MLE) and advocate its use.

The content of this chapter is part of a submission to *Solar Physics* (D’Huys et al., 2015). The authors are grateful to V. Delouille (ROB) and the PROBA2/SWAP team for valuable input.

5.1 Introduction

For the purpose of this chapter, we define a power-law function as follows:

$$f(x) \sim x^{-\alpha}, \quad (5.1)$$

where α is called the exponent, scaling factor or scaling parameter. For power laws found in solar physics, this scaling parameter typically lies within the range $1.1 \leq \alpha \leq 3.0$ (Aschwanden et al., 2014). Often only the tail of a distribution can be described by a power law. In this case x_{min} is defined as the minimal value for which the power-law behavior is observed. Similarly, we take x_{max} as the largest x -value for which the power-law properties hold.

Power-law distributions are ubiquitous in solar physics. They have been found in studies of the flux of solar flares (in soft and hard x-ray, EUV and radio wavelengths), flare waiting times (the time between consecutive flares), abundance enhancements and waiting times for solar energetic particle events; as well as solar wind measurements. Many authors have searched for a power-law behavior in the frequency distributions of different solar parameters. For example, Yashiro et al. (2006) examined the difference in power-law index for flares with and without an associated coronal mass ejection as a function of different flare parameters (peak flux, fluence, duration). A comprehensive overview is given by Aschwanden et al. (2014).

The presence of a power law — and the deviations from it — provides important information about the underlying physics of the measured events. Parameters derived from observational power laws are compared to theoretical predictions in order to validate the theory. For example, Aschwanden et al. (2014) found a close correspondence between the power-law slopes reported for the energy and size distributions of both soft and hard X-ray solar flares, which is expected from the Neupert Effect.

Unfortunately, many authors apparently underestimate the care that must be taken when attempting to estimate power-law scaling parameters derived from data. In particular, focusing on the mathematics of power laws, Newman (2005) pointed out that a power-law index $\alpha \leq 2$ implies that the distribution has an infinite mean. This mean value of a power-law distribution $p(x) = Cx^{-\alpha}$ is given by its first moment:

$$\langle x \rangle = \int_{x_{min}}^{\infty} x p(x) dx = C \int_{x_{min}}^{\infty} x^{-\alpha+1} = \frac{C}{2-\alpha} [x^{-\alpha+2}]_{x_{min}}^{\infty}.$$

This expression is divergent in case $\alpha \leq 2$ and $x_{min} > 0$.

This divergence of the mean indicates that there may be very strong fluctuations in the means calculated for different samples taken from this distribution. The

mean calculated for a single sample may be relatively small, while very large values may occur for other samples drawn from an identical population. Any mean calculated on the basis of a limited observational sample will therefore be unreliable. Similarly, the variance (the second moment) and standard deviation are divergent in the case that $\alpha \leq 3$. These mathematical considerations are important to keep in mind when drawing conclusions about the mean and variance of any power-law-distributed sample; thus an accurate estimate of the scaling parameter is the only way to characterize the distribution.

With the vast increase in observational data volume, robust statistical analysis of large distributions is becoming an increasingly important issue in solar physics, and we will show in this chapter (and the next) that not all authors have realized this fully when characterizing the power-law-dependence of their data. While the application of inappropriate fitting techniques to power-law-dependent data may not necessarily completely undermine the analysis, such analyses can induce error in the estimated power-law parameters obtained by these authors.

One illustration of the importance of correctly estimating the scaling parameter is the argument made by Hudson (1991) that the solar flare energy distribution must have a power-law index $\alpha > 2$ in order for nanoflares to explain coronal heating. A power law this steep implies that a large number of small events with low energies occurring simultaneously would supply sufficient energy to heat the corona. Therefore, many authors have spent considerable effort trying to determine the exact scaling parameter for solar flares, resulting in a wide range of estimations of α , which left the question undecided. Additionally, Parnell (2004) pointed out that $\alpha > 2$ is not a sufficient condition for nanoflares to heat the corona: there must also be enough of these small-scale flares present at any given time in order to produce the heat needed to balance energy losses through radiation, conduction and mass loss.

In the same paper, however, Parnell highlights an example of how authors might arrive at an incorrect conclusion based on an erroneous estimate of power-law scaling parameters. Parnell explains that the estimation of this parameter for the solar flare energy distribution is subject to various influences: event detection techniques, energy computation and, of course, the method used to estimate α . These influences cause large discrepancies in the published values for α , which range from 1.5 to 2.7, spanning the critical value of $\alpha = 2$ and thus leaving the coronal heating question wide open. Parnell then re-examines the conclusion of Aschwanden and Parnell (2002), who found significantly different scaling parameters in an analysis of flares observed by both the Transition Region And Coronal Explorer (TRACE) and the Soft X-Ray Telescope (SXT) on-board Yohkoh, and attributed this difference to a temperature bias in the TRACE events. Parnell (2004) pointed out that these results were obtained by plotting the flare energy distributions on a logarithmic scale and fitting a straight line to

the part of the distribution that exhibits a power-law behavior. The re-analysis showed, using the Maximum Likelihood Method (MLE), that this graphical method yields incorrect parameter estimates; in fact, both power-law indices are consistent within the error margins and no TRACE temperature bias could be confirmed.

There are many recent reports in the literature about the power-law nature of various solar phenomena, but not all of these authors report using appropriate power-law estimation techniques, and many of the conclusions presented in these papers would benefit from a re-analysis using the methods discussed in this chapter. Among them are analyses of the properties of solar flares associated with and not associated with coronal mass ejections (Yashiro et al., 2006), analyses of the rate of active region transient brightenings observed in soft X-ray (Shimizu, 1995) and quiet-sun transient brightenings observed in extreme-ultraviolet (Berghmans et al., 1998). Even our own analysis in Chapter 4 (D’Huys et al., 2014) used a graphical method to fit a power law to the angular width of coronal mass ejections with various properties. Although the particular fitting technique these authors used is certainly not grounds to invalidate the conclusions of any of these papers, a re-analysis with more appropriate techniques would definitely improve the support for these papers’ conclusions. Moreover, using the methods discussed in the current chapter, we will re-examine several of the conclusions by these authors in Chapter 6.

We will discuss both graphical method and the Maximum Likelihood Method in more detail below. Where other authors have considered the difficulties, limitations and accuracy of these approaches in a mathematical context (See, for example, Goldstein et al., 2004; White et al., 2008; Clauset et al., 2007, v2), we will focus on the effect of the sample size on the accuracy of both estimation methods.

5.2 Estimation Methods for the Power-Law Exponent

Authors can apply various methods to estimate the scaling parameter α for their power-law distributed data. Here we discuss the most common approaches to estimate the exponent and highlight their strengths and shortcomings. It is important to note that in this work we only focus on methods to estimate this scaling parameter and assume that the data are, in fact, power-law-distributed, which may not always be the case.

In reality, it is often quite difficult to determine whether a power-law is an appropriate distribution to describe observational data. For example, log-normal or exponential behavior is hard to distinguish from a power-law, especially when only a limited range of the distribution is investigated. Additionally, turn-overs are often observed, beyond which the power-law behavior no longer holds. One should therefore carefully consider whether a power law is in fact an appropriate model for the data at hand. This aspect, however crucial, is beyond the scope of this work. Clauset et al. (2007, v2) describe how, for example, a likelihood ratio test can be used to determine whether other models fit the data better.

In this chapter, we focus on the effect of the sample size on different estimation methods for the power-law exponent. To test these methods independently from any other effects, we use perfectly power-law distributed data, while at the same time acknowledging that such perfect data are hardly ever found in real life.

5.2.1 Graphical Methods

In search of a power law, authors traditionally create a log-transformed histogram of their data. The power law then manifests itself as a straight line of data points in this graph. Frequently, authors apply a least-squares linear fit to estimate the slope of this line, which corresponds to the scaling parameter of the power law. Bins without observations are not taken into account (because $\log(0)$ is undefined) and in some cases bins with low counts are excluded as well (White et al., 2008). This technique is widely used and straightforward to apply, but is prone to errors. Most importantly, this method is very sensitive to the choice of bin width and the sample size. This is not surprising, as binning results in a loss of information about the distribution of the data points within a bin (Clauset et al., 2007, v2). Additionally, Bauke (2007) points out that graphical methods for estimating power-law parameters are unreliable because they are based on assumptions that are often not fulfilled by empirical data, such as the absence of uncertainty in x and the independency of the errors.

Improvements to this method can be made by using logarithmic binning: a larger (linear) bin size for the less dense populated tail of the distribution ensures more data points per bin and thus this approach decreases the large statistical errors that are observed in the case of linear binning where many bins are scarcely populated. It is important however to know that logarithmic binning will provide an estimate of $\alpha + 1$, not α . This has often been overlooked in previous studies and can be avoided by using normalized logarithmic binning (White et al., 2008).

Difficulties with fitting a power-law distribution using a linear fit on a log-log scale are discussed by Goldstein et al. (2004) as well. These authors conclusively show that using a graphical estimation method yields very poor results. They performed a numerical experiment drawing 10 000 random numbers from a power-law distribution and estimated the scaling factor α for this sample with different graphical approaches. An estimation bias as large as 36% is found in case the data are binned linearly. Logarithmic binning yields a bias of 29%, which is slightly better. Bauke (2007) repeated this experiment and found a bias as low as 5% for the logarithmic binning method. This large discrepancy is attributed to differences in the binning method.

Interestingly, Goldstein et al. (2004) also claim that in the case that only the first 5 points in the frequency distribution on a log-log scale are used for the estimation of the slope, the true scaling parameter is often quite well reproduced, albeit with a very large variance. Indeed, these first five bins contain most of the data and thus we may obtain an accurate estimate of the slope with this limited amount of data, while at the same time avoiding the counting problems that often occur in the tail of the distribution in the case of low sample sizes.

5.2.2 Maximum Likelihood Estimation

The method of *Maximum Likelihood* provides an accurate estimate of the scaling parameter α through a simple calculation. If we assume that our data follow a power-law distribution for $x \geq x_{min}$, the *maximum likelihood estimator* (MLE) for continuous data is given by

$$\hat{\alpha} = 1 + n \left[\sum_{i=1}^n \ln \frac{x_i}{x_{min}} \right]^{-1}, \quad (5.2)$$

where x_i , $i = 1 \dots n$ are the observed values of x such that $x_i \geq x_{min}$. The standard error on $\hat{\alpha}$ is then

$$\sigma = \frac{\hat{\alpha} - 1}{\sqrt{n}} + \mathcal{O}(1/n). \quad (5.3)$$

Equations (5.2) and (5.3) are discussed in Clauset et al. (2007, v2) and Muniruzzaman (1957).

Goldstein et al. (2004) showed that the variance of the estimates obtained with MLE is notably lower than that of the estimates using a linear fit on the first five bins in the frequency distribution. In fact, MLE has mathematically been shown to be the minimum variance unbiased estimator (White et al., 2008), that is, the maximum likelihood estimator has a lower variance than any other

unbiased estimator for all possible values of the scaling parameter. This makes MLE the most accurate and robust method to estimate the power-law scaling parameter α . In addition, this method produces a valid confidence interval for α , which is not the case for other approaches.

However, there are some drawbacks to the MLE technique. As we will discuss, MLE is sensitive to small sample sizes. Additionally, the result is heavily dependent on the choice of the parameter x_{min} , the minimal x -value for which the data exhibit a power-law behavior (see, for example, Section 6.2 and Table 6.1). Choosing x_{min} too low is especially problematic because it results in the inclusion of non-power-law-distributed data points in the calculation, which, in turn, induces erroneous results. A value for x_{min} that is chosen a bit too high is less of a problem: in this case the maximum likelihood estimator remains a good approximation for α . However, also this should be avoided because then valid data points are ignored during the calculation (Clauset et al., 2007, v2).

Note that it is also common practice to introduce a cut-off at the higher end of the x -axis, beyond which the data are no longer assumed to follow a power law. Such deviations from power-law behavior at the lower and higher x -values occur frequently and can be handled; however, this is not straightforward. White et al. (2008) provide an MLE formula for a truncated power-law distribution. Note that this equation cannot be solved analytically, and thus numerical methods are required to determine the MLE value. Despite these complications, deviations from the power-law behavior should not be ignored, especially because they may prove to be vital to understanding the underlying physical process (White et al., 2008).

The easiest and most straightforward way to determine a parameter value for x_{min} is to plot the histogram of the data on a log-log scale and visually estimate the minimal x -value at which the linear behavior starts. A slightly better option is to plot the estimation of the scaling parameter $\hat{\alpha}$ as a function of x_{min} and determine around which value for x_{min} the maximum likelihood estimator is stable. However, these are both visual methods which makes them subjective and sensitive to errors. Clauset et al. (2007, v2) advocate the more objective and statistically sound method of choosing the value of x_{min} that reduces the difference between the probability distribution of the real data and that of the best fitting power law. The distance between two probability functions is commonly measured using a Kolmogorov-Smirnov (KS) statistic. The preferred value for x_{min} is the one that minimizes the KS statistic.

5.2.3 Alternative Methods

Other strategies exist to estimate the scaling parameter for power-law-distributed data. As an alternative to graphical methods (which can be strongly influenced by the choice of the bin size, the presence of empty bins and the binning method), one may use the cumulative distribution function (CDF). This CDF represents the probability that a variable X , randomly drawn from the data, will have a value $X \geq x$ (Clauset et al., 2007, v2). Once the CDF is calculated, linear regression can be applied to the log-transformed CDF. The resulting slope corresponds to $\alpha - 1$. Note, however, that due to the way the CDF is calculated, the resulting data points are serially correlated and a linear regression should, in principle, not be applied, as it assumes independently distributed data points. Nevertheless, using the CDF does provide a better estimate of α compared to the graphical methods described above. The main advantages of using the CDF are that it is straightforward to calculate and that no binning is required, which in turn avoids a bias caused by the choice of bin width or the presence of empty bins (White et al., 2008). In addition, the CDF is more robust to fluctuations in sample size than other graphical methods (Clauset et al., 2007, v2). Nevertheless, the maximum likelihood method still outperforms this method in both accuracy and precision.

A Bayesian approach is another way to estimate the scaling parameter α of power-law-distributed data. One example of its application appears in an analysis of photon energy spectra by van Dyk et al. (2001). As Wheatland (2004) explains, estimating a power-law exponent means finding a probability function for this parameter and taking the maximum of this function as the most likely value for the exponent, while the width of the probability function is a measure for the uncertainty of this estimate. The Bayesian approach is based on *Bayes's Theorem*, which describes how to refine such a probability function based on new data or information. This theorem is iteratively applied in an *Expectation Maximization process*: an initial estimate for the scaling parameter probability (called *the prior*) is made, after which this probability function is repeatedly updated with all available data using the Bayes rule until the iterative process converges.

The drawback of Bayesian methods is that they may be less straightforward to implement and more computationally intensive than some other approaches. In the case of a power law, where the MLE can be computed as an explicit function of the data, it may be more convenient to use this last method. However, for the estimation of parameters in other types of functions no closed MLE formula may exist, and numerical optimization techniques must be applied to determine a value for the MLE. In those cases the Bayesian approach, which is very general and therefore does not depend as much on the underlying function, may be the

preferred method. In fact, MLE is a special case of the more general Bayesian approach, with the assumption of a uniform prior (Wheatland, 2004).

5.3 Sample Size Influence

To study the influence of the sample size on the estimation of the scaling parameter α , we created artificial datasets of various sizes and applied some of the techniques described above. It is easy to understand why a smaller data sample makes it more difficult to reliably estimate the slope of a power law using the graphical methods: it is simply because the histogram bins are too sparsely populated in small data sets to be well-fit by any of these methods. Clauset et al. (2007, v2) proposed a sample size $n \geq 50$ as a rule of thumb to obtain a reliable estimate with the MLE method. Bauke (2007) additionally pointed out that for the MLE method a higher value of the scaling parameter requires a larger sample size to calculate a valid estimate.

We created the random samples for this study using the technique described by Clauset et al. (2007, v2, Appendix D) and Newman (2005). Given an array r of uniformly distributed random numbers in the range $0 \leq r < 1$, we calculate a random sample x that is power-law-distributed as follows:

$$x = x_{min}(1 - r)^{-1/(\alpha-1)}. \quad (5.4)$$

Again, x_{min} is the minimal x -value for which the power law is assumed to be valid. We have arbitrarily set $x_{min} = 10$. As before, α is the power-law scaling parameter. We used values between 1.1 and 3.0 for α and evaluated the performance of the different estimation methods as a function of sample size and this scaling parameter.

Once we obtain the random samples of power-law-distributed data, we can directly apply the MLE method using Equations (5.2) and (5.3) above. For the graphical methods, we first need to create a histogram. The artificial power-law distribution described above converges to zero for large x -values. Although unlikely, it is possible that a given sample will contain a very large x -value, which would lead to a huge number of empty bins in its histogram, creating—in turn—memory issues during the calculations. To avoid this, we cut the histogram off at the higher end (we arbitrarily chose $x_{max} = 1000$). This results in slightly lower actual sample sizes because some of the data points are ignored in the calculation. However, the effect of this cutoff is limited by the fact that there are few data points above the cutoff limit, at least for large values of α . In that case, the order of magnitude for the sample sizes is always maintained.

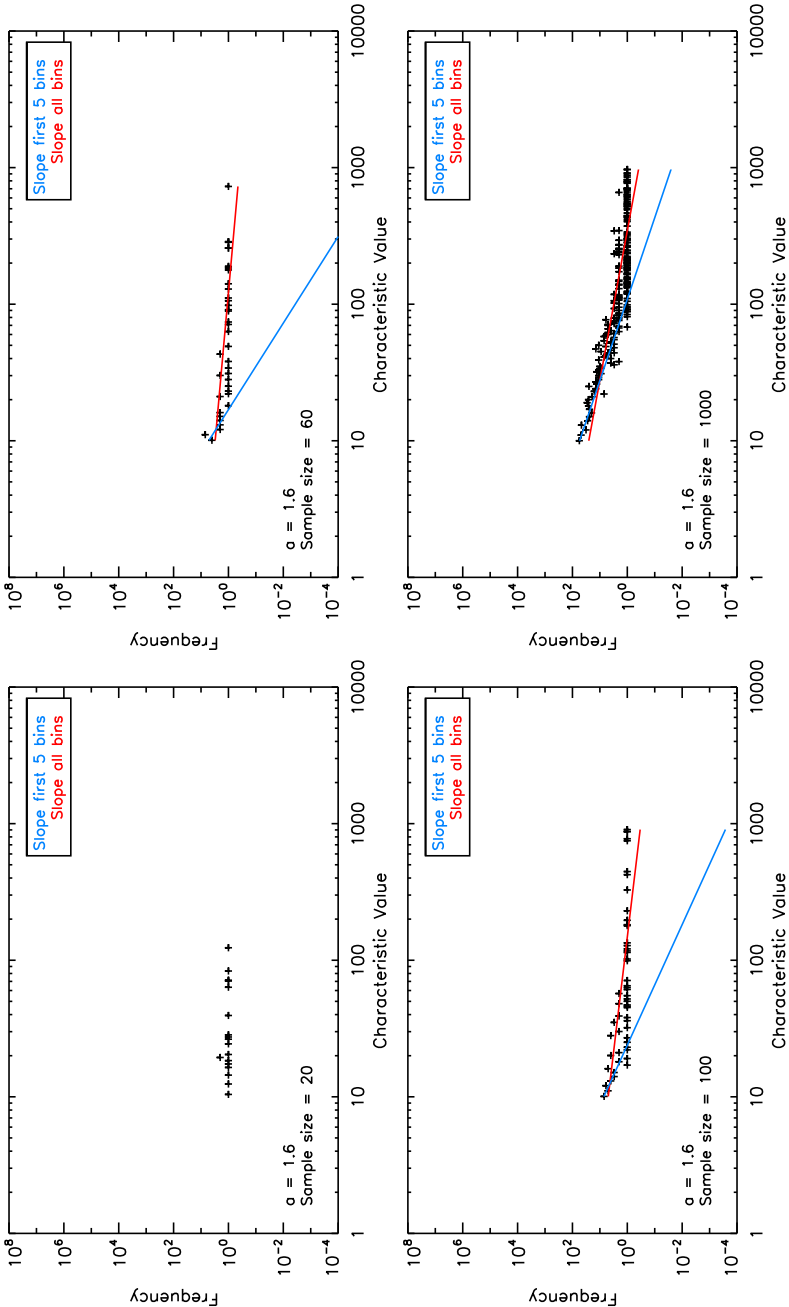


Figure 5.1 Log-transformed histograms for random samples, varying in size from 20 to 1000 elements, drawn from a power-law distribution with scaling parameter $\alpha = 1.6$. The red and blue lines are the best linear fits based on all bins and on the first 5 bins with more than one data point, respectively.

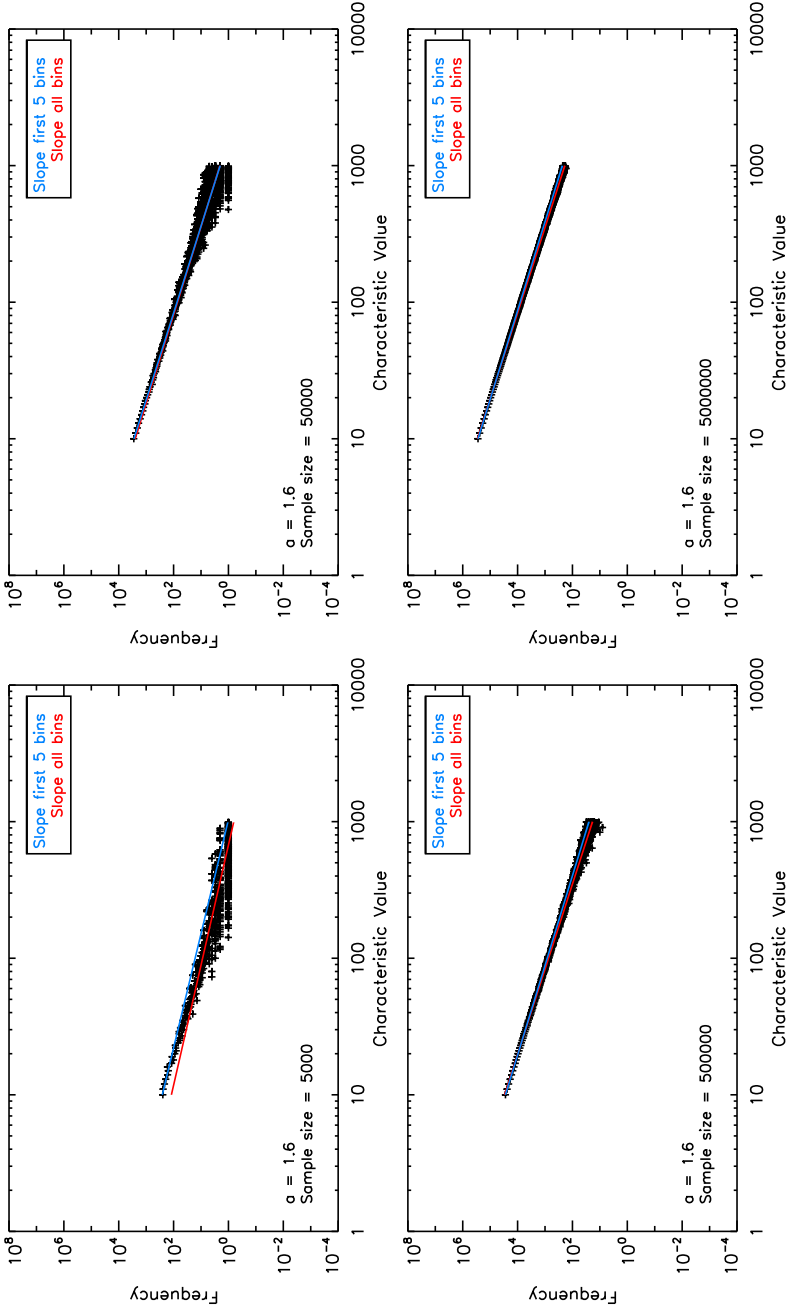


Figure 5.1 (Continued) Log-transformed histograms for random samples, varying in size from 5000 to 5 000 000 elements, drawn from a power-law distribution with scaling parameter $\alpha = 1.6$. The red and blue lines are the best linear fits based on all bins and on the first 5 bins with more than one data point, respectively.

However, when α is small, $\alpha = 1.1$ for example, the power-law distribution is quite flat, and a random sample will contain a significant number of data points above our cutoff limit. Unfortunately, increasing the cutoff value does not improve the situation, as any sample from a distribution this flat may always contain a significant number of very large values. This characteristic illustrates another limitation of using the graphical method to analyze power-law distributions.

For ease of comparison between different methods we plot the sample size for the complete sample (including $x_i \geq 1000$) in all figures throughout this chapter.

5.3.1 Graphical Methods

We first applied the most commonly used graphical method to our samples: we performed the log-log transform of the histogram of the data for each bin with more than one data point. We then calculated the slope of the line formed by the data points using a least-squares linear regression technique. This slope is our estimate for the power-law scaling parameter. As a possible improvement to this method, we repeated this calculation using only the first 5 bins of the histogram that contained more than one element. This method is apparently effective because these bins contain most of the data points, while at the same time the sparse data points in other bins are ignored to avoid a bias towards the tail of the distribution (Goldstein et al., 2004).

In Figure 5.1 we show the log-transformed histograms for power-law-distributed samples of various sizes. We obtained random samples with a lower cutoff parameter $x_{min} = 10$ and scaling parameter $\alpha = 1.6$. The red lines indicate the best fit to the data using a linear regression technique on all histogram bins with more than one data point. The blue line indicates the best fit using only the first 5 such bins. It is immediately clear that in the cases with small sample sizes the estimation of the slope is difficult due to under-sampling: too many bins are sparsely populated. We may not even have 5 bins with more than one data point. As the sample size increases, the bins for the lower values are well filled, but the higher ones are not. This heavy tail has a strong influence on the slope estimation. Only when the sample size is sufficiently large, can we resolve this problem of under-sampling in the higher bins and obtain a reliable estimate of α .

Figure 5.2 illustrates the evolution of the scaling parameter estimate as a function of the sample size. Again, we used $\alpha = 1.6$ for the underlying power law. It is immediately clear that the estimates converge towards this value (indicated by the horizontal line). When all histogram bins with more than one element are used, this convergence is gradual. Conversely, for the alternative

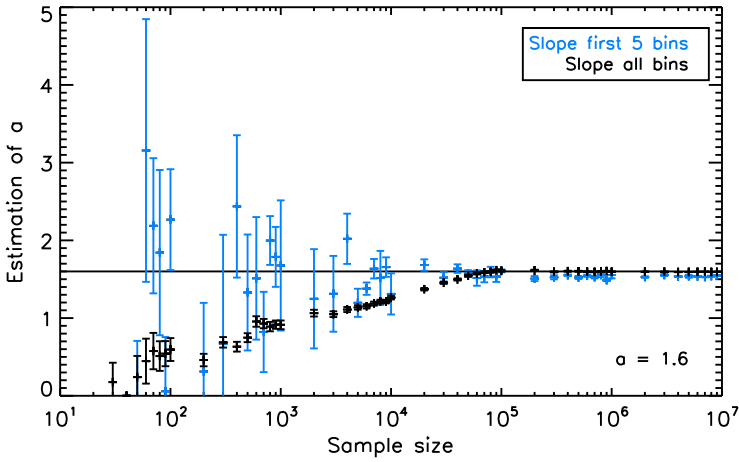


Figure 5.2 Evolution of the scaling parameter estimate as a function of sample size using the graphical method. The true value for α is 1.6 and is indicated by the horizontal line. We plot the estimates calculated using all bins with more than one element in the sample histogram (in black), as well as estimates for which only the first 5 such bins were taken into account (in blue). The error bars are defined by the 1σ uncertainty estimate for α .

graphical method where only the first five such bins are fit, the estimates are scattered around the true value of α . Nevertheless, the convergence is slightly faster in this case because the estimate is not influenced by the heavy tail of the histogram. However, the 1σ uncertainty is much larger for this alternative and, even more importantly, this method converges to a slightly lower value for α . The latter can be explained by the fact that as the sample size grows, the tail of the distribution is better sampled; however, this important information is ignored when only the first five bins are used in the estimation of the slope.

We emphasise that a large number of data points ($n \geq 10^5$) is required to reliably estimate the scaling parameter graphically. This is much more than most authors realize, and for many studies this amount of data may not be available. Moreover, this required sample size increases with the size of the scaling parameter α , as we show in Figure 5.3. The reason for this is that the distribution of data over the entire range depends on the power-law scaling. In the case of a flat power law, the data points are spread evenly over the x -range, while for a steeper slope, in contrast, there are comparatively fewer data points for the higher x -values. If, then, those higher x -values happen to be sampled, the estimated slope will be flattened by the presence of these large

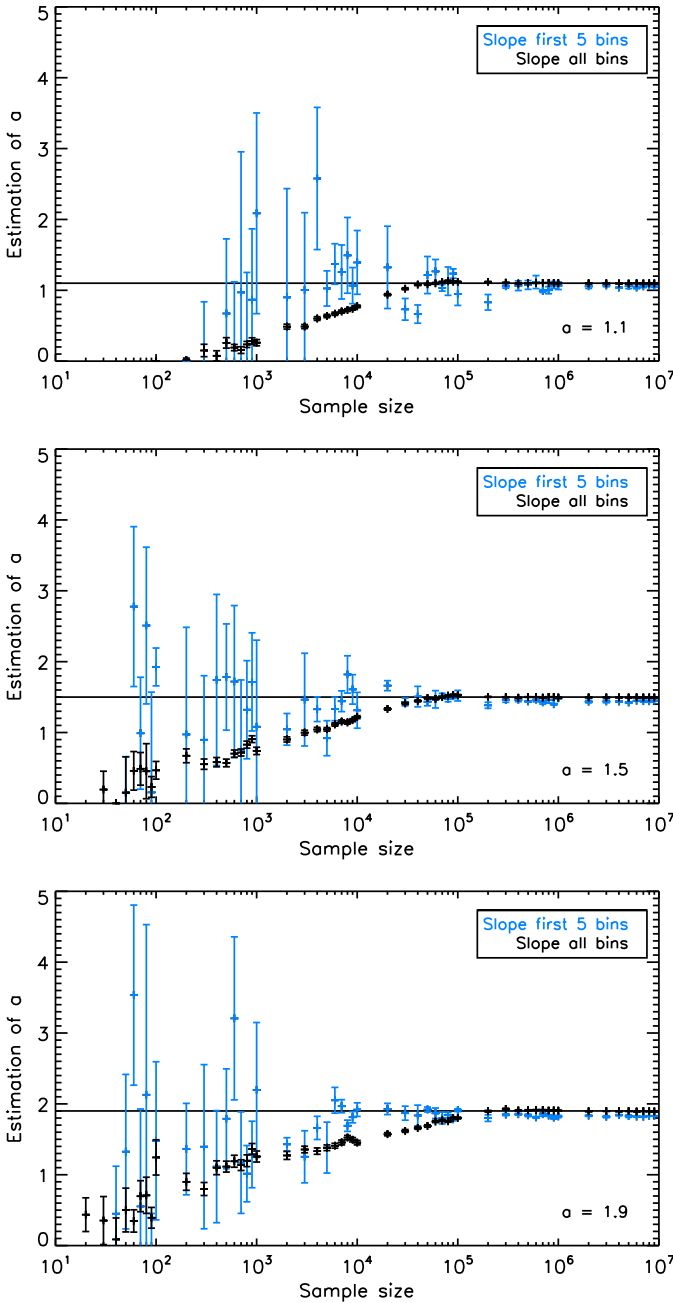


Figure 5.3 Evolution of the scaling parameter estimate as a function of sample size using the graphical method, for different values of α . This figure clearly illustrates that the required sample size to obtain a reliable estimate of the scaling parameter increases vastly as this scaling parameter itself increases.

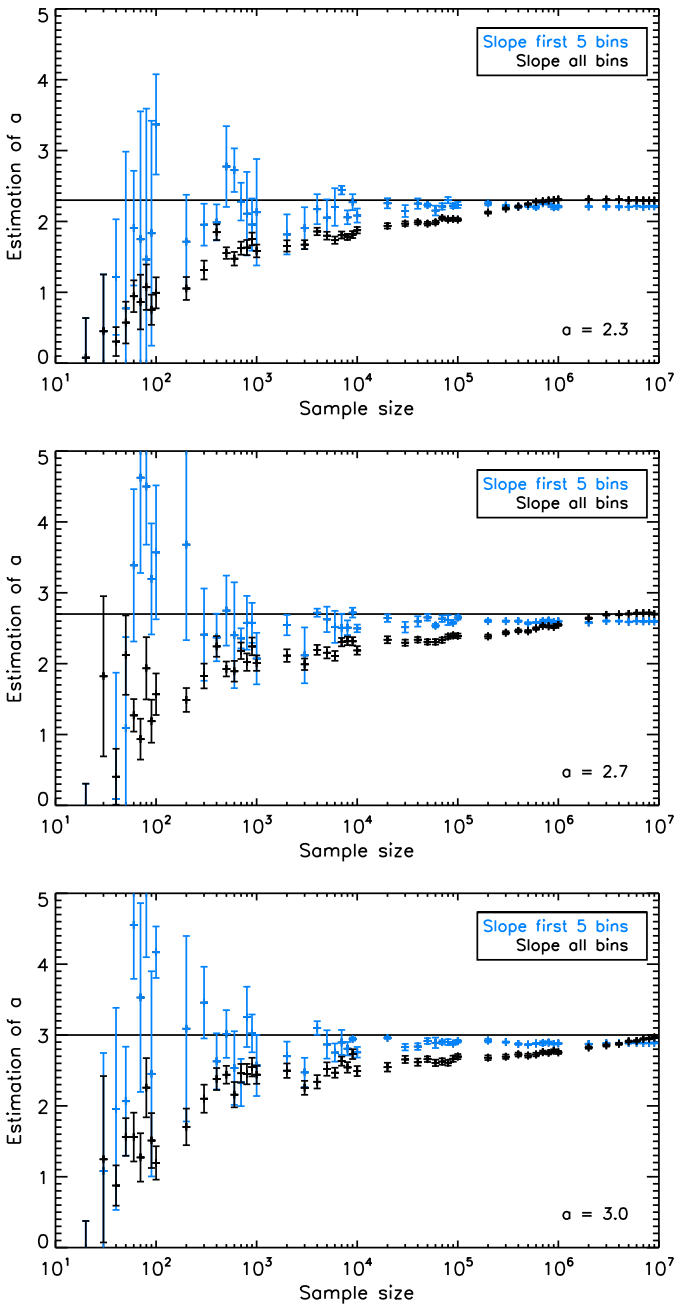


Figure 5.3 (Continued) Evolution of the scaling parameter estimate as a function of sample size using the graphical method, for different values of α . This figure clearly illustrates that the required sample size to obtain a reliable estimate of the scaling parameter increases vastly as this scaling parameter itself increases.

values. This effect is especially strong in the case of a small sample size where one high x -value has a large influence on the slope estimation. The distributions of very large samples, on the other hand, contain so many low x -values that one occasional high x -value has little effect.

Interestingly, in Figure 5.3 we observe that while the slope estimates converge continuously towards the true value for lower values of the scaling parameter, this is not the case for higher values of α . In the last panels of Figure 5.3 it is clear that the estimates fluctuate somewhat more and even appear to level off prematurely in the sample size range between $n = 10^3$ and $n = 10^5$. If the graph were to end here, an observer could erroneously conclude that the scaling parameter estimates are converging towards the true value, while in reality the slope is steeper still (which becomes clear only when even larger sample sizes are used). This once again illustrates that the scaling parameter can only be estimated accurately using graphical methods when the sample size is *very* large.

5.3.2 Maximum Likelihood Estimator

The application of the MLE method to our random samples is straightforward. Equation (5.2) provides the scaling parameter estimate and Equation (5.3) gives the standard error on this estimate. The resulting values for sample sizes varying between $n = 20$ and $n = 10^7$ are shown in Figure 5.4. When compared to Figure 5.2, this plot illustrates the power of the MLE method very convincingly: the estimates converge rapidly to the true scaling parameter value (indicated by the horizontal line). For $\alpha = 1.6$, a sample size as low as $n = 200$ is sufficient to estimate this scaling parameter reliably. Note, however, that in certain studies even this sample size cannot be reached, simply because we lack the observations (see, for example, Section 6.2).

5.3.3 Method Performance

To compare the three methods we applied above (graphical estimate using all bins in the histogram, graphical estimate using only the first five bins, and MLE), we performed a Monte Carlo-type simulation. We generated random samples of different sizes from a power-law-distributed set and studied the average of the scaling-parameter estimates over 10 000 iterations. By taking the average, we avoid misleading conclusions that could result from the large fluctuations in the estimates and their error bars in the case of small sample sizes.

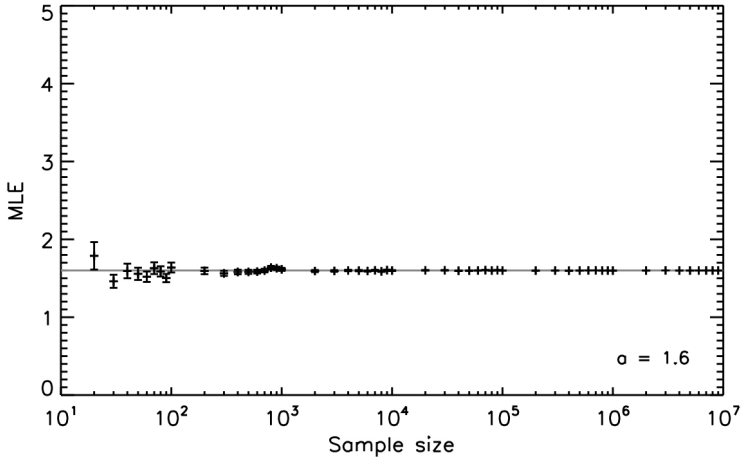


Figure 5.4 Evolution of the scaling parameter estimate as a function of sample size using the MLE method. The true value for α is 1.6 and is indicated by the horizontal line. A reasonable estimate for $\alpha = 1.6$ is obtained for a sample size as low as $n = 200$.

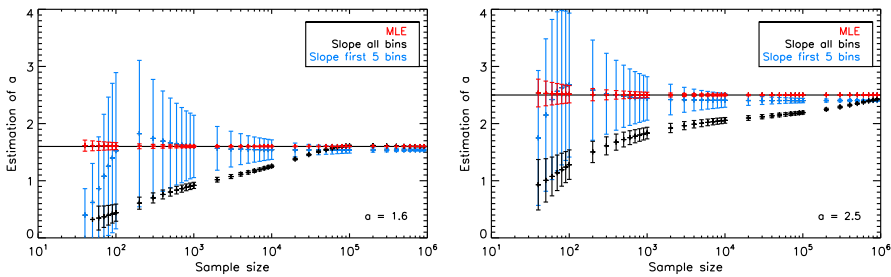


Figure 5.5 Comparison between the different estimation methods for the scaling parameter using a Monte Carlo-type simulation. Estimates (averaged over 10 000 iterations) obtained with the graphical methods are in black (all bins) and blue (first five bins). The maximum likelihood estimator is shown in red.

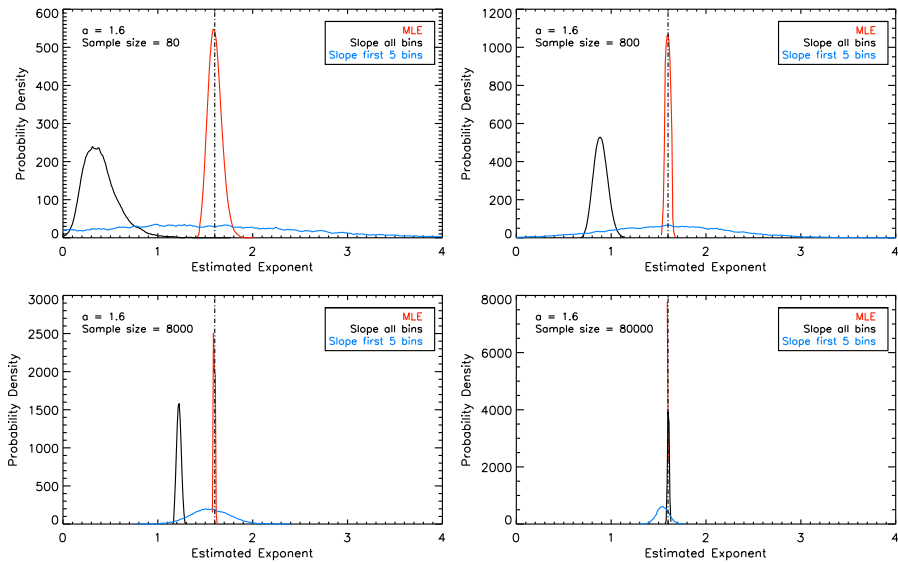


Figure 5.6 Smoothed probability density functions of the scaling parameter estimates in the Monte Carlo simulation, calculated for different sample sizes and $\alpha = 1.6$.

The results of this Monte Carlo simulation for two different values of the scaling parameter ($\alpha = 1.6$ and $\alpha = 2.5$) are shown in Figure 5.5. The average estimated slope based on all histogram bins is plotted in black. This average converges gradually towards the true scaling parameter value. Note on the right panel however that even a sample size as large as $n = 10^6$ is insufficient to obtain convergence for $\alpha = 2.5$. The slope estimate based on only the first five bins (in blue) converges much more quickly towards the true value. However, with this method none of our estimates ever reach the actual value for α because the information in the tail of the distribution is neglected, even though it becomes important as the sample size increases. Additionally, the average of the standard errors over all iterations is unacceptably large for this method. The maximum likelihood estimation method (in red) clearly stands out as the preferred approach. The average estimates converge quickly and the standard error is low, especially in the case of large sample sizes. Note that here we confirm the observation by Bauke (2007) that for the MLE method (as is the case for other methods) a higher value of the scaling parameter requires a larger sample size to obtain a reliable estimate.

The probability density functions for the estimates of the scaling parameter in the Monte Carlo simulation are shown in Figure 5.6 for different sample sizes and with the scaling parameter set to $\alpha = 1.6$. What stands out immediately is that for small sample sizes the spread of the estimates is very large when using the graphical method based on the first five histogram bins (blue curves in Figure 5.6). However, the density distribution encloses the true value for α (indicated by the vertical dotted line), which means that this method may by chance result in the right answer. The spread for the black curve (based on all the histograms bins) is much smaller. Nevertheless, this curve is shifted to the left for the small samples, indicating that the slope is underestimated (the tail of the histogram weighs too heavily in these cases). As the sample size increases, the black curve shifts towards the true value of α while simultaneously reducing its spread. This results in an accurate estimation for large sample sizes. In contrast, the MLE method (red curve) performs well for all sample sizes. The probability distribution is, even in the case of a small sample, narrow and centered around the true value of the scaling parameter. Better precision is achieved as the sample size increases, and the probability distribution narrows even further.

5.3.4 Improvements to the Graphical Methods

As discussed before, several modifications to the graphical methods are possible to improve their performance. The binning method has a large influence on the estimates obtained for the scaling parameter. When the histogram is binned linearly, as was the case before, the estimates for small sample sizes are far below the true value. Applying a least-squares method to logarithmically binned histograms for the same samples improves the estimates considerably, as is clear from Figure 5.7. In this figure, we applied a logarithmic bin size of 0.1 and normalized the histogram according to the linear bin width. Figure 5.7 shows that while the graphical method performs better with logarithmic bins, it remains unreliable for small sample sizes.

Using weights for the linear regression can improve the estimate even further. We have applied a weight w to each bin according to n , the number of data points in that bin:

$$w = \sqrt{n}.$$

Figure 5.7 illustrates the additional improvement that this weighting of the bins brings to the graphical method with logarithmic binning. Nevertheless, the MLE method outperforms also these improved graphical methods.

Many authors have indeed applied logarithmic (and sometimes even weighted) binning when analyzing their data and their estimates are thus more reliable

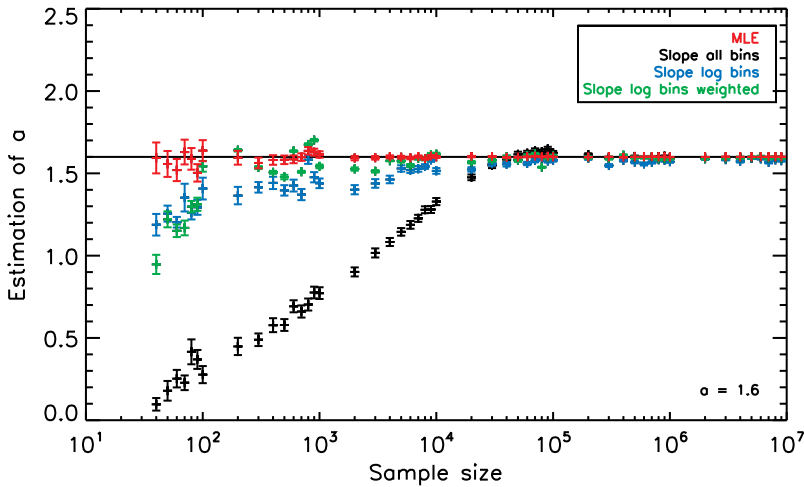


Figure 5.7 Evolution of the scaling parameter estimate as a function of sample size using the improved graphical methods. The true value for α is 1.6 and is indicated by the horizontal line. We show the estimates for α based on linear binning (in black), logarithmic binning (in blue), logarithmic binning with weights (in green) and the MLE method (in red).

than suggested by the worst-case scenario of the linearly binned graphical methods that was shown before. Nevertheless, the results may still prove different when MLE is applied to their data sets, especially if these data sets are limited in size.

5.4 Conclusions

Power-law distributions are found in various solar data sets and the accurate estimation of their scaling parameter is of great interest. For instance, these values are used to validate theoretical predictions. If small and large scale events turn out to exhibit the same power-law behavior, this may also point at a common physical process causing them. Therefore, it is vital to estimate this scaling parameter as accurately as possible.

Many authors continue to use graphical methods to obtain an estimate of the scaling parameter when they believe they have observed a power-law behavior in their data. While many of them may have found a reliable power law, some of the resulting power-law estimates need to be revisited. Indeed, we have shown

that these graphical methods often result in inaccurate estimates, especially in cases with small sample sizes. In fact, the sample sizes required in order to obtain reliable results with a graphical method are so large that they may not be achievable in certain studies. In addition to the problem of small sample sizes, the graphical estimate of the scaling parameter depends strongly on the binning method, which makes some results even less trustworthy.

As a best practice we caution other authors to avoid using graphical methods to estimate the power-law exponent. Instead, the MLE method or even more general techniques (for example a Bayesian approach) should be used. Nevertheless, the problem of sample size remains for these techniques as well: a sufficiently large sample is needed to obtain a reliable estimate. Even though this minimally required number of data points is vastly lower in the case of the MLE method than for the graphical methods, it may still be too large for some studies. In that case, we would advise authors to be extremely prudent in drawing conclusions based on any estimation, even those made using the MLE method. Likewise, previous studies in which a graphical method — or even the MLE method — was applied to a limited amount of data should be treated carefully. In that respect, we also need to revise some of our own results obtained in Chapter 4. This re-analysis is the subject of the next chapter.

Chapter 6

Power Laws in Solar Data Re-Examined

Our study on the effect of the sample size on the estimated values for power-law parameters led us to realize that we need to revisit some of our own work where we have analyzed power laws in solar data. In Chapter 4, we investigated a scaling law for the angular width of coronal mass ejections (D’Huys et al., 2014); while Berghmans et al. (1998) studied the power-law-distributed radiative losses of quiet-sun coronal brightenings. In both studies, the graphical method was applied to a log-transformed histogram of the dataset. The discussion in Chapter 5 clearly illustrates that this is not the preferred approach. We therefore repeat the earlier analyses, now applying the MLE method to these data, and discuss the differences in the results.

The content of this chapter is part of a submission to *Solar Physics* (2015). Co-author D. Berghmans provided the nanoflare dataset used in Section 6.3 by running his detection algorithm on SOHO/EIT 304 Å images.

6.1 Introduction

Based on our results in Chapter 5 and in view of our analysis of existing studies on power laws in solar physics, we strongly recommend that authors who have published scaling parameter estimates based on a graphical method review and reconsider their analyses using more appropriate estimation methods. We set

the example in this chapter by re-analysing two datasets for which a power-law parameter, obtained through a graphical method, was published.

6.2 CMEs without Low Coronal Signatures

We investigated coronal mass ejections without low coronal signatures: solar eruptions, detected as CMEs in coronagraph observations, for which no on-disk signatures such as flares or filament eruptions are observed (Chapter 4; D’Huys et al., 2014). We studied the observational characteristics of these stealth CMEs and asked how they differ from classical CMEs. One characteristic we studied in detail is the scale invariance of the CME angular widths. This property was discussed by Robbrecht et al. (2009a) in their analysis of the CACTus LASCO CME catalog. These authors found a power law with an average scaling parameter $\alpha \approx 1.66$ over 10 years of CME detections (1997 to 2006, based on the LASCO level zero images, see Figure 1.15). We repeated this analysis for the case of CMEs with and without LCS, observed in 2012, and found a notably different slope for both classes of events: $\alpha = 0.97 \pm 0.41$ for CMEs without LCS, and $\alpha = 1.50 \pm 0.34$ for classical CMEs (based on the LASCO quicklook images). To derive these parameters, we applied the graphical method based on all bins with more than one element in the linearly binned histogram, as described in Chapter 5.

In Chapter 4, we already noticed the important influence of the sample size on the derived slope. When selecting only a small sample of classical CMEs, the resulting slope was notably flatter than the slope derived for the complete set of CMEs in 2012. Selecting a wide CME in a small sample influences the slope significantly because it creates a heavy tail for the distribution, resulting in a flatter slope. In reality, however, the angular width distribution of CMEs is dominated by narrow events. This becomes clear when more detections are taken into account (D’Huys et al., 2014). The observation of the effect of the sample size on our stealth CME results was an important motivation for the work presented in Chapter 5.

Our research there suggests that applying the MLE method to the CME data set should yield far more reliable results. To calculate the MLE, we first need to select a suitable value for the lower cutoff, x_{min} . There are several candidate parameter values: the current CACTus catalog uses an angular width of 5° as the distinction criterion between an outflow and a CME and we used this limit in Chapter 4 to calculate the scaling parameter for stealth CMEs. In 2009, at the time of the analysis by Robbrecht et al. (2009a), this boundary was set at 10° . However, these authors report a scale invariance in a range of 20° to 120° .

x_{min}	MLE Stealth CMEs	MLE Classical CMEs
5°	1.735 ± 0.116	1.657 ± 0.017
10°	2.177 ± 0.202	1.984 ± 0.028
20°	2.482 ± 0.349	2.341 ± 0.047

Table 6.1 *Maximum likelihood estimators for CMEs without low coronal signatures and for classical CMEs. Different values for the parameter x_{min} were applied.*

It is unclear whether they in fact used 10° or 20° as the lower cutoff value in their analysis. We therefore tested different values for x_{min} and calculated the corresponding MLE. The results are listed in Table 6.1.

In fact, the value of the parameter x_{min} should be derived from the actual data. We thus plotted the histograms for the CMEs with and without LCS on a log-log scale. The minimal x-value for which the linear behavior becomes visible is our best graphical estimate for x_{min} . Figure 6.1 shows that the stealth CME sample is too small to provide an estimate of x_{min} . (*Note that the estimates for the slope in this figure differ from the values reported on in Chapter 4, due to the use of a different binning method.*) Based on the histogram for classical CMEs we conclude that $x_{min} = 10$ is the most appropriate graphical estimate for x_{min} .

However, this graphical estimation of the parameter x_{min} is still based on visual inspection of the dataset, which is always biased. A more objective and statistically sound method is described by Clauset et al. (2007) (v2). The idea is to choose the value for x_{min} that minimizes the difference between the probability functions for the empirical data and for the best-fit power law above this x_{min} . The distance between these two probability functions (or CDF's) is calculated by the Kolmogorov-Smirnoff (KS) statistic:

$$D = \max_{x \geq x_{min}} |S(x) - P(x)|. \quad (6.1)$$

In this equation, $P(x)$ is the CDF for the best-fitting power law, and is given by the following formula (Clauset et al., 2007, v2):

$$P(x) = \left(\frac{x}{x_{min}} \right)^{-\alpha+1}. \quad (6.2)$$

$S(x)$ denotes the CDF for the observations. Remember that the cumulative distribution function describes the probability that a variable X , randomly drawn from the data, will have a value $X \geq x$. Therefore $S(x)$ can be written as

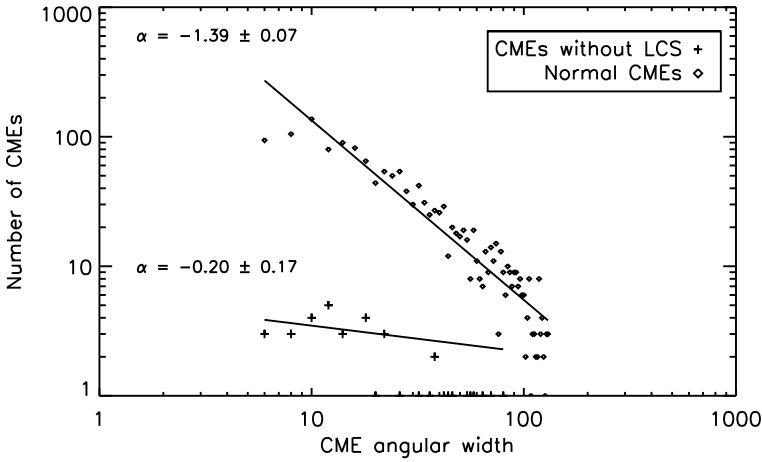


Figure 6.1 *Log-transformed histogram of the angular widths of CMEs with and without low coronal signatures. This figure does not exactly reproduce the original one shown in Chapter 4 (D’Huys et al., 2014) due to the use of a different binning method. In our previous study we included the maximum of the bin ($b_{i-1} < x \leq b_i$), while here we include the minimum ($b_{i-1} \leq x < b_i$), which is more conventional. This different binning also influences the slope estimates: the values for α shown here differ strongly from the ones reported on in Chapter 4. This illustrates once more the unreliability of the graphical methods.*

the vector $[1, \frac{n-1}{n}, \dots, \frac{2}{n}, \frac{1}{n}]^1$. We can then calculate the Kolmogorov-Smirnoff statistic for each possible value of x_{min} . The preferred value for this parameter is the one that minimizes D .

We implemented this procedure for the observations of the angular width of stealth and normal CMEs. The lowest value for x_{min} we considered was $x_{min} = 5$, as this is the lower detection limit set by the CACTus program. For CMEs without LCS we used an upper limit of $x_{min} = 55$ in order to retain at least 5 data points to construct the probability functions with. For the regular CMEs, the upper limit was set to $x_{min} = 120$, the maximal angular width for non-halo CMEs, as set by CACTus (see below). The resulting estimate for both classes of CMEs was $x_{min} = 5$ and we will therefore use this parameter value for the remainder of the discussion.

¹http://www.stat.berkeley.edu/~aldous/Research/Ugrad/Willy_Lai.pdf

<i>Method</i>	Stealth CMEs	Classical CMEs
Graphical method (binned with $b_{i-1} < x \leq b_i$)	0.97 ± 0.41	1.50 ± 0.34
Graphical method (binned with $b_{i-1} \leq x < b_i$)	0.20 ± 0.17	1.39 ± 0.07
MLE ($x_{min} = 5$)	1.735 ± 0.116	1.657 ± 0.017

Table 6.2 *Overview of the slope values and the maximum likelihood estimators for stealth and normal CMEs when different binning methods and the MLE method are applied.*

While determining this minimal value for which power-law behavior is assumed, we also set an upper limit for the angular width of CMEs to 120° . Beyond this maximal angular width CMEs are considered to be halo CMEs. Halo events are CMEs propagating towards or away from Earth. The expanding cloud is observed in coronagraph images as a halo around the Sun, seemingly with a large angular width. Because the CME is propagating close to the Sun-Earth line, the observations suffer from strong projection effects and therefore the true angular width can not be accurately determined for these halo CMEs. Accordingly, we did not take these detections into account when calculating the slopes and MLE values reported on in this section.

Table 6.2 combines all estimates for the scaling parameter α , derived from the CME angular width data using different methods. From the last line in this table we immediately see that the MLE values for both classes of CMEs are quite similar, which suggests that CMEs without low coronal signatures may not be so different from events that do show these features, at least as far as their angular width distribution is concerned (even though the results in Table 6.2 for the graphical methods would suggest differently). Note that the small number of stealth CMEs (we found only 40 events) means that even the MLE value cannot be trusted completely, although it should be more reliable than the slopes we found using the graphical method. The group of classical CMEs contained nearly 1600 events, which should be sufficient to obtain a reliable MLE value (as is also clear from the small error margins). For graphical methods, in contrast, this sample size is too small. Clearly, the slopes and error margins we determined for both classes of CMEs with the graphical methods differ significantly from the estimated values now obtained with the MLE method due to the limited sample sizes.

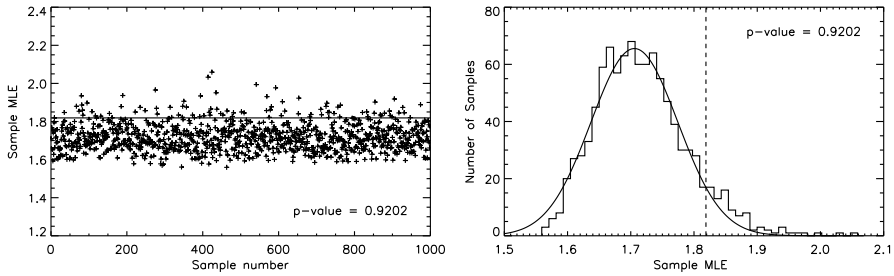


Figure 6.2 *Left Panel:* Scatterplot for the MLE values calculated for 1000 random samples of 40 classical CMEs. The horizontal line indicates the MLE found for CMEs without LCS. *Right Panel:* Distribution for these MLE values with a gaussian fit overlotted. The vertical dotted line indicates the MLE value for stealth CMEs.

Our study of CMEs without LCS was motivated by the question of whether and how this class of events differs from classical CMEs. To assess whether the angular width scaling parameter for stealth CMEs differs from that of classical CMEs while simultaneously eliminating influence from the difference in sample size for both classes of events, we have taken 1000 random samples of 40 classical CMEs and calculated the MLE for each sample with the parameter x_{min} set to 5. The left panel of Figure 6.2 shows a scatterplot of the MLE values found for these random samples. The MLE found for CMEs without LCS is indicated by the horizontal line for comparison. The right panel of Figure 6.2 displays the corresponding density function. Although this distribution is not truly gaussian, we have overlotted the best fitting gaussian curve. The vertical dotted line indicates the value we obtained for CMEs without LCS. This value is found in the wing of the distribution but does not stand out statistically, although the value is on the edge of the p-value range: the p-value we obtained for the stealth CME MLE is 0.92 while a 95% threshold is usually applied in the right wing (note that the p-value analysis depends in the assumption that our distribution is gaussian, which is not the case). We can conclude that the MLE value calculated for stealth CMEs is a quite unusual one to be found for such a small sample, however statistically not impossible to obtain.

In Chapter 4, we performed a similar analysis and calculated the scaling parameter with the graphical method for 1000 random samples of 40 classical CMEs. This resulted in a normal distribution of slope values and the stealth CME value was again found in the wing, here with a p-value as low as $p = 0.015$. This implies that the probability to select a random sample with this slope value is less than 2%. Therefore we concluded that stealth CMEs exhibit a

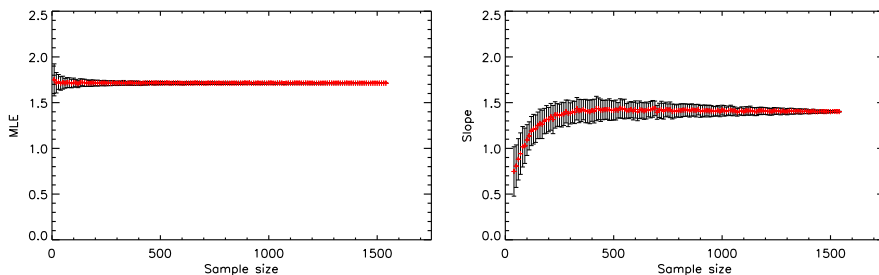


Figure 6.3 Evolution of the scaling parameter estimate as a function of sample size using the MLE method (left panel) and the graphical method on the log-transformed sample histogram (right panel) for the angular width of CMEs detected by CACTus in 2012.

steeper slope, indicating that we observe more narrow CMEs without LCS than expected in a random sample of 40 classical CMEs.

Our findings here are different: the p-value we obtained with the MLE method is within the statistical range. On this basis, we thus cannot conclude that the group of stealth CMEs exhibits a power-law behavior different from that of a random sample of classical events. However, we emphasize that the p-value still suggests that it is very unlikely to obtain, with a random sample, the MLE for CMEs without LCS that we calculated. Additionally, we are drawing conclusions based on a very small sample of stealth CMEs. A thorough answer to the question of whether stealth CMEs are physically different from classical CMEs really requires more data. Unfortunately, these stealth CMEs are not easily identified, which makes expanding our data set challenging and very time-consuming.

Figure 6.3 illustrates once more the importance of a sufficient sample size when determining the scaling parameter. We applied both the graphical method and the MLE approach to CME angular width samples of increasing sizes, drawn from CACTus LASCO CME detections for the year 2012. When randomly selecting the samples we were careful not to oversample by selecting the same event twice. For each sample size, we calculated the average of the MLE and slope estimates over 100 samples. The results are shown in Figure 6.3 (left panel). This plot illustrates the quick convergence for the MLE values. However, the slope values originating from the graphical method (right panel) do not seem to converge to the same value, instead they level off around 1.5 (while the MLE value converges to 1.7). This premature levelling off of the slope values is also seen in several panels of Figure 5.3 for sample sizes of the order of 10^3 elements. This illustrates that while there seems to be a convergence in the case

Year	Slope	Year	MLE
1997	$\alpha = 1.49$	2010	1.68 ± 0.04
1998	$\alpha = 1.64$	2011	1.70 ± 0.02
1999	$\alpha = 1.68$	2012	1.66 ± 0.02
2000	$\alpha = 1.64$	2013	1.68 ± 0.02
2001	$\alpha = 1.63$	2014	1.67 ± 0.02
2002	$\alpha = 1.67$		
2003	$\alpha = 1.97$		
2004	$\alpha = 1.83$		
2005	$\alpha = 1.71$		
2006	$\alpha = 2.04$		

Table 6.3 *Maximum likelihood estimators and slope estimates for CMEs detected by CACTus for various years. Slope parameters for the years 1997 to 2006 were calculated using a graphical method by Robbrecht et al. (2009a), reproduced with permission.*

of the graphical method, this result cannot be trusted due to the limited sample size. Unfortunately, in this case we used all the CME data that was available for the year 2012, which means that it is impossible to increase the sample size further. It is therefore even more crucial to choose the appropriate method to analyse this limited data set, in this case the MLE method, to ensure we obtain a reliable estimate for the scaling parameter α .

Finally, we can compare the yearly maximum likelihood estimator based on the CME widths in the CACTus LASCO quicklook catalog to the scaling parameters obtained by Robbrecht et al. (2009a) for the years 1997 to 2006. These values are shown in Table 6.3 for both time periods. Interestingly, the MLE estimates for the years 2010 to 2014 lie very close together, which increases our confidence in the values we obtained.

Though the results reported by Robbrecht et al. (2009a) are mostly in agreement with ours, there is quite some spread in their estimates. It is likely that, for the deviating years, they suffered somewhat from the limitations of the graphical method they applied, especially in light of the fact that their sample size was probably relatively small. (Unfortunately, Robbrecht et al. did not report exactly how many CMEs they used to determine the power-law slopes, so we can only speculate here.) It is conceivable that, especially at the time of solar minimum, the number of CMEs per year may have been small, while large sample sizes are required for the graphical method. Another influence on their estimate may come from unusual solar events. In 2003, for example, the very

strong Halloween storms were observed. Atypical CMEs like this one may have skewed the statistics. Also here the influence of one unusual event on the estimate is especially large in case of small sample sizes.

For the MLE calculations applied to the years 2010, 2011, 2012, 2013 and 2014 samples of, respectively, 221, 1057, 1289, 1381, and 1470 CMEs were used. These sample sizes should be sufficient to obtain a reliable MLE result, but not a graphical one. To increase our sample size even more, we calculated the MLE for all CMEs observed in the period starting in July 2010 to December 2014 (spanning the complete CACTus LASCO quicklook catalog) and obtained a scaling parameter estimate $\alpha = 1.677 \pm 0.008$.

6.3 Quiet-Sun EUV Brightenings

Berghmans et al. (1998) studied the radiative losses of transient brightenings in the quiet-sun regions of SOHO/EIT 304 Å images. The study of the energy distribution of solar brightenings has been a popular subject ever since Hudson (1991) proposed that a power-law exponent $\alpha = 2$ is the critical value deciding whether coronal heating can be explained by nanoflares. If the small events outnumber the larger ones sufficiently (corresponding to a steep power law: $\alpha > 2$), these nanoflares would contain enough energy to heat the solar corona, while remaining below the detection limit. Berghmans et al. (1998) reported a scaling parameter $\alpha = 1.9 \pm 0.1$ for their measurements of the radiative losses of impulsive EUV brightenings in the transition region, which suggests that the majority of the energy is provided by the larger events, although the difference between this value and the critical slope value is marginal.

We revisited the original data set, spanning a little over 3 hours, observed by SOHO/EIT on 1996 December 28 and reconstructed the event detection as described by Berghmans et al. (1998). Figure 6.4 shows one of the SOHO/EIT 304 Å images used for this detection algorithm, over-plotted with the subfield that was defined. We did not apply any pre-processing (flat-field, grid pattern correction, solar rotation compensation, etc.) as Berghmans et al. applied these in a non-standard way (that is, they did not use the `eit_prep` solar software) and this preprocessing has in any case no real effect on the statistics of event detection. More important to note is that we also chose to skip removal of cosmic ray hits as these cannot be reliably distinguished from the smallest brightenings in the solar atmosphere.

For the event detection algorithm itself we closely followed the method described in Section 4.1 of Berghmans et al. (1998), thereby taking a running-average of 1 hour to produce the reference background for each pixel. We used the $\Sigma_P = 2.5$

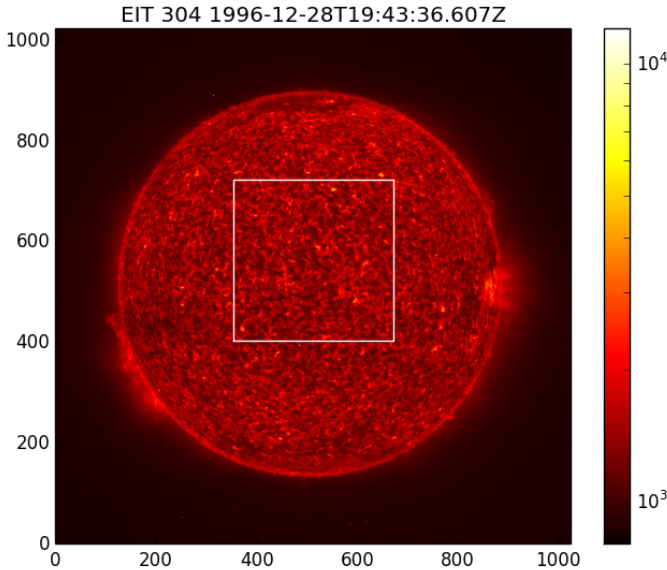


Figure 6.4 *The Sun's transition region observed by SOHO/EIT on 1996 December 28. The white box indicates the subfield used in the algorithm to detect nanoflares. The color scale indicates the intensity in this 304 Å image.*

and $\Sigma_E = 1.5$ thresholds for the peaks and their intensity to obtain 133 262 brightening detections. Figure 6.5 shows a linearly binned histogram of the radiative losses of these events, as well as a logarithmically binned one². Our new analysis finds an order of magnitude more events compared to the 13 067 events found by Berghmans et al.. Note however that in contrast to Figure 17 of Berghmans et al., our new Figure 6.5 linearly binned histogram does not bend-over for small events. We thus attribute the difference in the number of events to the class of the smallest scale brightenings which are easily confused with cosmic ray hits.

We applied a linear fit to the linearly binned histogram of the radiative losses of all detected brightenings. This graphical method, described in Chapter 5, yielded a slope value of $\alpha = 1.45$, lower than that reported by Berghmans et al. (1998). However, the right panel of Figure 6.5 clearly shows that the linear fit

²Our dataset expresses energy in data numbers (DN). Berghmans et al. (1998) report a factor of 2×10^{20} erg per DN to convert the flare energies to the physical units used in the histograms. However, we suspect a typographical error in this conversion factor. We needed to rescale our histogram by a factor of 2×10^{24} erg per DN to reproduce the results of Berghmans et al. and to obtain reasonable energies for solar flares.

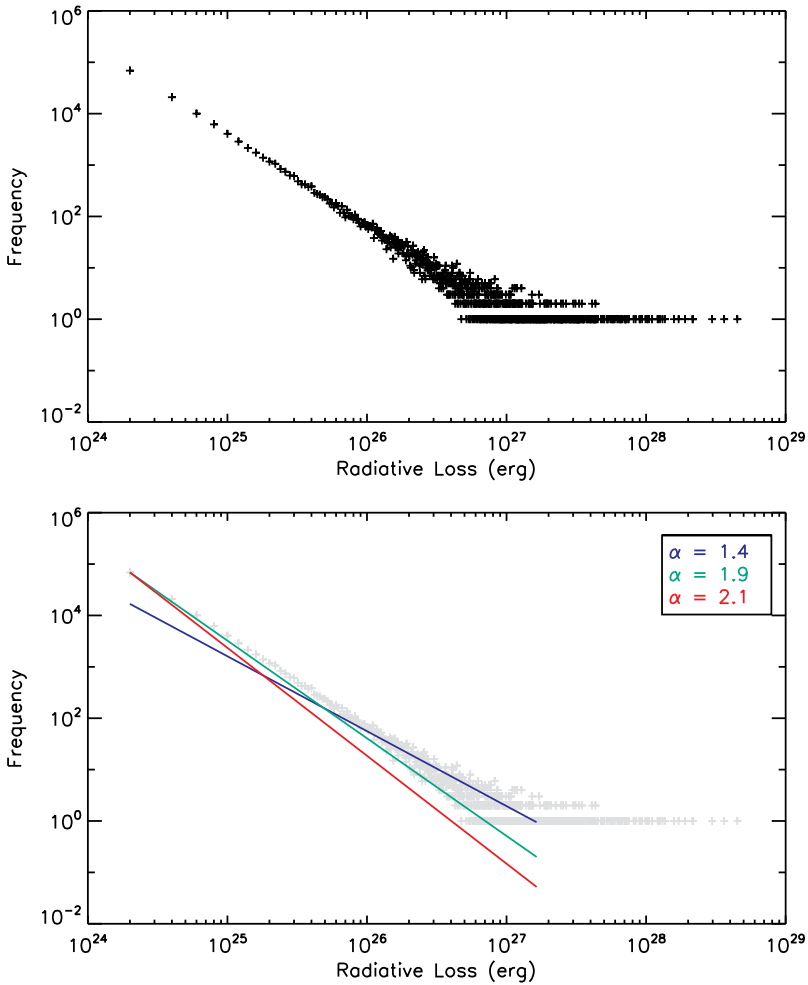


Figure 6.5 *Top Panel:* Frequency histogram for the nanoflare radiative loss, binned linearly. *Bottom Panel* The same histogram, overplotted with lines with slope $\alpha = 1.9$ (as reported by Berghmans et al. (1998), in green), $\alpha = 1.4$ (the result of a linear fit on the entire data sample, in blue) and $\alpha = 2.1$ (the maximum likelihood estimator, in red). The slope for the MLE value and the value found by Berghmans et al. are anchored in the first data point of the histogram.

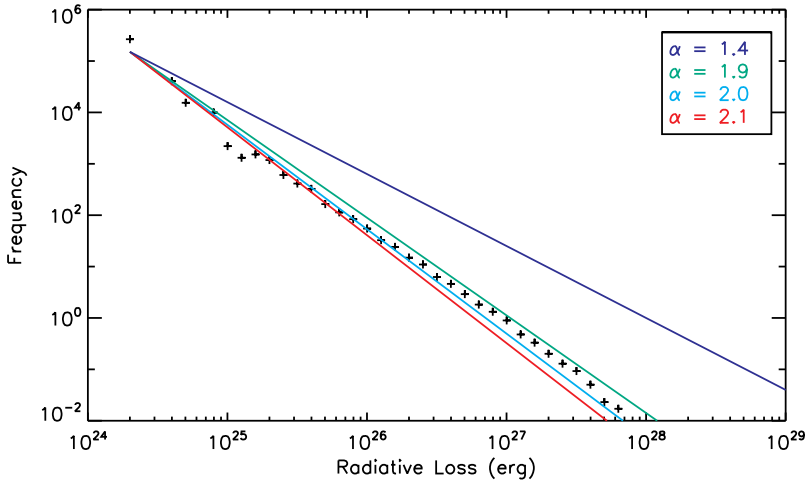


Figure 6.6 *Logarithmically binned frequency histogram for the radiative losses of nanoflares. We over-plotted the same slopes as in Figure 6.5, with the addition of $\alpha = 2.0$, the result of a linear fit on the logarithmically binned histogram (light blue). The slopes are all anchored in the starting point of the light blue fit to the logarithmic histogram (with $\alpha = 2.0$).*

is strongly influenced by the heavy tail of the histogram and that a slope value of $\alpha = 1.9$ (which was reported by Berghmans et al.) is a good fit to the linear part of the histogram.

It has been pointed out by several authors that logarithmic binning improves the estimate of α (see, for example, Goldstein et al., 2004; Milojević, 2010). In logarithmic binning, the data points are separated into bins of equal size in logarithmic space. To obtain the logarithmically binned histogram in Figure 6.6, we used a logarithmic bin width of 0.1 and normalized by dividing the number of data points in each bin by the bin width (in linear space). Figure 6.6 clearly shows that this type of histogram solves the problem of a heavy tail because more data points are combined in the larger bins at the high end. This is why logarithmic binning generally yields better estimates of α , provided that the sample size is large enough. A linear fit to the logarithmically binned histogram gives us a slope value of $\alpha = 2.0$ (Figure 6.6), which is close to the one found by Berghmans et al. (1998).

However, applying the MLE method to these data paints a different picture still. We obtain a scaling parameter value $\alpha = 2.10 \pm 0.03$, which is above the critical nanoflare heating value proposed by Hudson (1991). This value was

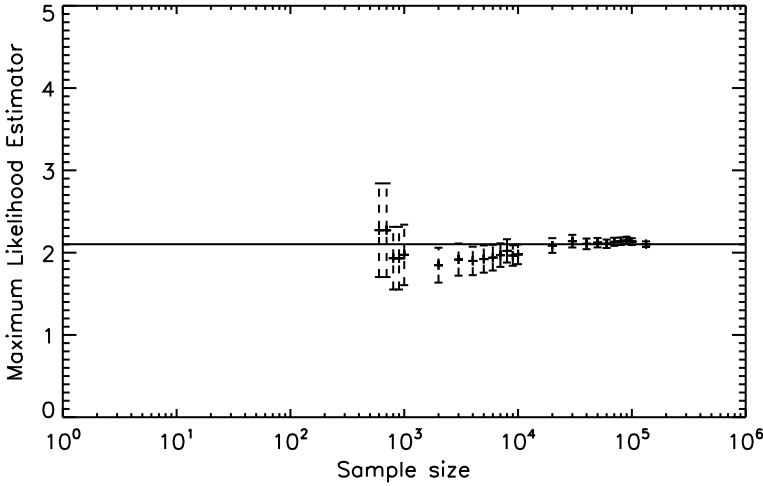


Figure 6.7 Evolution of the scaling parameter estimate as a function of sample size using the MLE method on the nanoflare detections with $x_{min} = 4.66 \times 10^{26}$ erg. The MLE value was only calculated for samples with at least 5 data points above or equal to this x_{min} . The MLE value for the complete sample is $\alpha = 2.1$ and is indicated by the horizontal line.

obtained by setting the parameter $x_{min} = 4.66 \times 10^{26}$ erg. As was the case in Section 6.2, we used the Kolmogorov-Smirnoff statistic to determine this x_{min} . As an extra condition, we made sure at least 1000 data points remained for the MLE calculation. Based on Figure 5.5, we consider this a sufficient number to estimate a scaling parameter with a value around 2 reliably. Note that this high value for x_{min} means that, for this data set, the power law does not hold for lower energies and no conclusion on nanoflare heating can be drawn, even though our MLE estimate is above the critical $\alpha = 2$ value. This is exactly the caveat pointed out by Berghmans (2002): the steepness of the power law is a necessary, but not a sufficient condition for coronal heating by nanoflares. The different behavior for lower energies may be physical, or it may be a result of the applied detection technique. It is conceivable, for example, that it is a consequence of the possible confusion between very small brightenings and cosmic rays.

Figure 6.7 illustrates once more the importance of the sample size. Here we plot the maximum likelihood estimator for different samples of detected nanoflares. Before drawing our samples, we first put the detections in a random order to avoid possible biases that may be caused by the timing of the events (consider

for example the possibility of consecutive nanoflares from the same location with similar physical properties). For each sample size n , we then calculated the MLE value using the first n events from the jumbled detection list. We set $x_{min} = 4.66 \times 10^{26}$ erg as was deduced from the entire sample using the KS statistic and use only samples for which we have at least 5 data points $x_i \geq x_{min}$. We clearly see that the MLE estimate quickly converges to the value we obtained for the entire sample: $\alpha = 2.1$.

We emphasize once more that the sample size here is of the order of $n \sim 10^5$ elements, which may seem sufficient to many authors, even when applying graphical methods. Figure 5.3 suggests, however, that for a true value of $\alpha = 2.1$ there is a levelling in the slope estimates when $10^3 \leq n \leq 10^5$, which—incorrectly—suggest convergence is reached. An even larger sample size is needed to reliably estimate the scaling parameter using a graphical method like the one applied by Berghmans et al. (1998). We suspect that had the authors used a more robust estimation method for the scaling parameter, for example the MLE method, the conclusions of their work may have differed.

6.4 Conclusions

We reviewed previously published work on power laws describing the angular width of CMEs and brightenings in quiet-sun regions. This re-analysis was required as the original studies applied a graphical method to derive an estimate of the scaling parameter. Chapter 5 has taught us this is not a valid approach. Here, instead, we calculated the maximum likelihood estimator and obtained a reliable estimate of the scaling parameter α and its error for both datasets.

Concerning the angular width of CMEs, this re-analysis did not conclusively answer the question whether or not events with and without low coronal signatures scale differently. To decide on this question we currently do not have sufficient stealth events to analyse. However, the MLE values for both classes of CMEs are much closer together than the graphical estimates were. Even more, they are compatible with each other in case the error margins are taken into account. This suggests that, while the scaling law for stealth events might be slightly steeper and these CMEs thus tend to be somewhat more narrow, the scaling for both classes of events is also not that different. This conclusion differs from our original interpretation, which was first presented in Chapter 4.

Following our re-examination, the original conclusions on the nanoflare data need to be revised as well. Where Berghmans et al. (1998) found a slope below the critical value of 2 using a graphical method, we found a value above 2 using the MLE formula. This new result favors the nanoflare hypothesis. However,

a crucial observation is that according to our new analyses, this steep power law may not hold for low-energy flares, and thus the coronal heating question remains open.

Summary and Future Prospects

We have studied atypical solar eruptions from both an observational and a statistical perspective. Instead of focusing on the most striking solar outbursts, we have put the seemingly inconspicuous stealth CMEs in the spotlight. While these coronal mass ejections are clearly observed in coronagraph data, they are not associated with significant low-coronal signs of eruption, which makes it challenging to determine their source region and predict their trajectory through interplanetary space. These events may therefore surprise space weather forecasters and present them with a real challenge to forecast the possible space weather effects of these stealth CMEs.

However, like many researchers, we started off with an observational study of a powerful solar eruption that showed all the interesting features one can expect from a strong solar eruption. On 2010 August 14, a rotating filament eruption was observed on the north-west solar limb. At that time, the new solar cycle had only just started to increase in activity. This filament eruption was one of the first major events that occurred, so it naturally drew our attention, and that of many other researchers as well. While our colleagues were focused on, for example, the properties of the associated coronal mass ejection and radio bursts, we were interested in the initiation mechanism responsible for this event.

Two separate active regions were involved, and we observed a significant decrease in magnetic flux in one of them. This led us to hypothesize the filament was at first destabilized by the flux cancellation in this active region, allowing it to rise slowly. From 3D reconstructions of the trajectory of this erupting filament as it travelled through the field-of-view of EUV imagers and coronagraphs we learned that while the flux rope was at first rising slowly, it reached a critical point and erupted rapidly around 09:50 UT. The sudden onset of an MHD instability at that time led to the observed twisting motion for the filament.

Due to the acceleration of the CME during this phase, it traveled at a high velocity into interplanetary space afterwards. As future work, a comparison of the height of the reconstructed filament to the height at which the decay index reaches its critical range may lead to the confirmation of the torus instability as onset mechanism for this eruption.

While this rotating eruption was an eye-catching event, the observations showed that the associated flare was quite weak for such an impulsive CME. Although this can be explained by the onset of an MHD instability, where the erupting flux rope is not driven by strong reconnection below, this observation prompted us to investigate the distribution of energy over the various eruptive signatures associated with CMEs. Are there events that do not show the typical tell-tale low-coronal signs of an energetic eruption? And how do they fit our current models?

Current observational research on solar eruptions is often focused on studies of spectacular events, preferably with large flares or strong CMEs. This is understandable. First of all, these events draw more attention due to their prominent nature. Second, and more importantly, many characteristics of these eruptions can more easily be deduced from the clearer observations. Third, these strong events are often seen as the eruptions with the most potential for hazardous space weather effects, which is why space weather forecasters need to keep a close eye on them. We, on the other hand, decided to study the other end of the scale: solar eruptions that are less energetic and therefore do not show clear observational signatures of eruption, but nevertheless can be of importance to space weather.

In Chapter 4 we embarked on a search for these stealth CMEs. It turned out that these events were not easily identified. Separating them from back-sided eruptions and eliminating all possible surface activity was a challenging and time-consuming task. Part of this task was performed by combining the output of different tools that automatically detect various signs of eruption. This allowed us to eliminate a large number of the events in our original dataset of CMEs detected by CACTus in the year 2012. After this initial automated step, we were left with nearly 500 eruptions to analyze in detail. By combining data from a wide range of instruments, we were able to eliminate most of the events, linking them to some sign of eruption in the observations of the low solar corona. The final result was then a list of 40 true stealth events: CMEs which we positively could not relate to any low-coronal signature or an eruption on the back-side of the Sun. Despite the apparently small number of CMEs without LCS that we identified, this is nonetheless — to our knowledge — the largest sample of stealth CMEs that has been studied so far.

These stealth eruptions then became the focus of a detailed observational study during which we identified the main characteristics of CMEs without low-coronal signatures. While there is a large diversity in the appearance of CMEs without LCS in coronagraph images, ranging from narrow outflows to large-scale CMEs with a classical three-part-structure, it is striking that in 2012 most of these stealth events originated from the northern polar region. Further, the velocity of CMEs without LCS is generally low compared to their counterparts with LCS, with a stealth CME median velocity between 100 km s^{-1} and 500 km s^{-1} , although a few faster eruptions were observed as well. A further study of the kinematics of our sample of stealth CMEs taught us that their height-time profiles are compatible with the models for MHD instabilities and the breakout mechanism and that most stealth CMEs accelerate gradually as they are traveling outwards. The angular width distribution for CMEs without low-coronal signatures shows a peak around 20° , indicating that the stealth CMEs in our sample were quite narrow.

When it comes to the eruption mechanisms responsible for stealth-type CMEs, the picture may not be so different from the models describing normal eruptions. Surely, stealth eruptions are low-energy events and probably most of the available energy is used to expel the CME and not to heat the surrounding plasma. This is, however, compatible with some of the existing models, for example the eruption of an empty filament channel at large height. Another important element is the preceding eruptions that are observed before the stealth events and that have likely cleared the path for the stealth eruptions by removing most of the overlying, and restraining, magnetic field. Similarly, the open field lines around the poles may have facilitated a polar CME without LCS.

Clearly, we are not the only ones to think along these lines. Following the publication by Robbrecht et al. (2009b), the term stealth event was introduced and other studies ensued. Ma et al. (2010) conducted an observational study rather similar to ours. Single event studies of stealth CMEs were published by Vourlidas et al. (2011) and Nieves-Chinchilla et al. (2013). Howard and Harrison (2013) wrote their perspective on the stealth CME concept, cautioning authors to classify CMEs in different groups and favouring the interpretation of stealth CMEs being at the low-energy end of a spectrum of coronal responses to the same common process. This points at a growing interest in the subject of CMEs without low-coronal signatures of eruption. While we were conducting this PhD research, stealth CMEs have become a hot topic.

From the literature and our own research, it is clear that CMEs without low-coronal signatures are generally slow and narrow CMEs that probably occur at large heights and therefore do not show signs of a powerful eruption. Why do we even bother studying them then? The pragmatic answer is that these events, despite their low speeds and narrow range, still have the capability of provoking

space weather effects when headed towards Earth. While, energetically speaking, these events may be less powerful, they can still be significant, especially in case they have a significant southward-directed component in their magnetic field. Moreover, their stealth nature may leave them undetected. Indeed, where the narrow Earth-directed stealths may not even expand to an angular extent wide enough to appear from behind the occulter, the wider stealth CMEs also suffer from strong projection effects which makes them appear very faint in coronagraph data and thus they may go unnoticed. Because these events also do not leave clear observational signatures of eruption behind, we need other criteria (for example the observation of a shock) to alert us to the possible eruption of an Earth-directed stealth event.

However, the more important argument to study CMEs without LCS is the academic need to understand this type of event. Flares and CMEs have been studied for a very long time, and while they often occur within the same eruption, they do not always do so. The question of why one sometimes occurs without the other may be crucial to advance our understanding and models of solar eruptions.

Clearly, more observations of stealth CMEs are needed to move our knowledge of these eruptions forward. While they are not easily extracted from past observations due to their inconspicuous nature, forecasters could conceivably report on their occurrence within just a few hours after onset. However, even when paying close attention, it is in itself hard to distinguish CMEs without low-coronal signatures from other low-energy events and, to add to this difficulty, there is no agreement on the definition of a stealth CME. Nevertheless, if we hope to study and understand these eruptions thoroughly, we need to find a workable way to identify more of these events and increase our sample size.

Besides more observational studies, another important line of future research is to model stealth events numerically. A good starting point would be the modeling done by Bemporad et al. (2012). These authors modeled the scenario described above: a preceding eruption destabilizes the magnetic field and causes a second, stealth-like eruption as a result of the relaxation of that field. From this study it was already clear that the strength of the global magnetic field determines whether this second CME without LCS is actually formed. A thorough parameter study using this model could reveal what the range of global magnetic field strength is that will allow stealth events, and may identify other crucial parameters as well. These values can then, in turn, be compared to what we observe for the stealth CMEs identified in this study.

Our definition of stealth CMEs is an observational one, even though one of the main arguments for Howard and Harrison (2013) to caution researchers about sorting CMEs into observational subcategories was the dependence on

the available instrumentation. Indeed, as our instruments improve, we may in the future observe the high-lying flux ropes which are likely to be the sources of stealth CMEs. It would therefore be better, for example, to define a minimal height above which a CME needs to be initiated in order to classify it as a stealth event. However, to establish that height, we first need to observe the eruption of high-lying flux ropes for a number of stealth events.

The new *Extreme Ultraviolet Imager* (EUI) on-board the Solar Orbiter spacecraft (to be launched in 2018, observations expected to start in 2021) may be able to do just that. This instrument is composed of two high-resolution imagers (HRI) which have a limited field-of-view, and a *full-sun imager* (FSI) with a large field-of-view. Solar Orbiter will take solar observations closer to the Sun than has ever been done before with an increased sensitivity in the high corona compared to current instrumentation. This may allow us to observe the high-lying flux ropes that now escape our view.

Additionally, Solar Orbiter will have an orbit that takes the spacecraft out of the ecliptic plane, allowing for observations of the poles using the EUV imagers and magnetometer on board. This out-of-the-ecliptic view is especially interesting for the study of stealth CMEs as most of the events found in 2012 seemed to originate near the north pole. Observations of this region may thus allow us to determine the source region for polar stealth events. The coronagraph onboard Solar Orbiter will also observe out of the ecliptic, which can mitigate projection effects for halo CMEs that are now difficult to assess. In the case of CMEs without low-coronal signatures, it is conceivable that we currently miss stealth events that are Earth-directed because they are less energetic and these weak halo events are difficult to observe. However, these stealth halo events could in the future be caught by the different point-of-view of the coronagraph on-board Solar Orbiter.

The PROBA3 mission will help us to investigate stealth CMEs as well. The coronagraph images from this mission will show the solar corona from $3 R_{\odot}$ down to just $1.05 R_{\odot}$, bridging the gap that currently separates EUV images and coronagraph observations and thus allowing us to track CMEs from their initiation site (even if that is high in the corona) out into the heliosphere.

In Chapter 4, we also investigated the scale invariance for CMEs without low-coronal signatures, looking for evidence that these stealth events might have a different initiation mechanism than eruptions that do show low-coronal signatures. We concluded that the power-law parameter for the angular width of stealth events is indeed likely to be different from that of normal CMEs because we observed very different slopes in the log-transformed histograms of our observations. This result seemed compatible with our finding that CMEs without LCS are generally more narrow than CMEs that do show these features.

We realized, however, that our sample of stealth events was very small, and started wondering how this would affect our results. This was our motivation for the more theoretical research presented in Chapter 5, where we investigated the influence of the sample size on the estimation of the power-law parameter using various techniques.

Chapter 5 explains clearly that enormous sample sizes are needed to estimate a power-law parameter reliably, at least when using the graphical method that we applied in Chapter 4. It immediately became clear that our results on the scale invariance for stealth CMEs were not reliable. We therefore investigated a better approach to analyze power laws: the Maximum Likelihood Method. This technique is easy to implement and performs vastly better than graphical methods, even with relatively small sample sizes.

By using highly idealized data, as we did in Chapter 5, the vast difference in performance for both approaches became abundantly clear: the graphical method to determine a power-law parameter (in which the logarithmic transform of the histogram is taken and a least-squares technique is used to determine the slope of the resulting line) needs an enormous amount of data to produce an acceptable result, while the alternative MLE method can produce a more accurate estimate with a simple calculation on a sample that is orders of magnitude smaller in size. Several modifications, such as logarithmic binning and weighing, can be made to the standard graphical method in order to ameliorate its performance. While these changes ensure a definite improvement in the estimations for α , the MLE method still performs better.

In Chapter 6 we therefore applied this preferred MLE method to the CME angular width data for stealth events and compared the results to the MLE parameter found for classical CMEs. As a result, we had to revise our previous conclusion: no difference in the power-law parameters for both classes of CMEs could be confirmed within the error margins. However, our problem of a small sample size remained: even for the MLE method, the number of CMEs without low-coronal signatures was too small to determine their scaling law parameter with sufficient certainty. To definitively answer the question whether the scaling laws for both types of CMEs differ from each other we really need more stealth CME observations.

We also re-analysed another dataset in Chapter 6. This study concerned the energy measured for nanoflares in the solar transition region. Indeed, the energy of solar flares of all sizes can be expressed with a power law. The exact value of this scaling law is subject of debate in research on coronal heating and has therefore attracted a lot of attention in the past already. The original study of this nanoflare dataset was performed by Berghmans et al. (1998) and yielded a power-law parameter just below the critical value of 2. Our re-analysis with

the MLE method led to a different scaling-law exponent, above this limit. This, however, does not mean that the coronal heating problem is now solved. Indeed, we were unable to confirm that the power law we identified, is also valid for smaller energies, which is the crucial argument for nanoflares to be a viable source of coronal heating. More research with larger samples is thus needed to decide whether nanoflares contribute significantly to the heating of the solar corona.

Our research in Chapters 5 and 6 illustrates that vast quantities of data are needed to study power laws in solar physics. Additionally, it is crucial for the reliability of the results that the proper methods are applied. These aspects were sometimes overlooked in previous studies. While the authors of these studies may indeed have found a reliable power law in their data, their analyses would benefit from a new evaluation of the observations using the appropriate methods. Indeed, as our methodology and scientific knowledge in different fields advance, we must dare to revisit some of our earlier results. It is likely that in the meantime better techniques were developed and researchers should not hesitate to re-analyze old datasets and draw more accurate conclusions. Falsification of a proposed theory is a part of the research process that is just as vital and valuable as the confirmation of one.

We have presented our research on atypical solar eruptions and their initiation mechanisms. We focused on CMEs that could not be associated with low-coronal signs of eruptions and investigated a fast eruption for which the accompanying flare was unusually weak as well. While these events still fit our existing models for CME initiation, they are clearly located towards the edge of a spectrum of possible responses to a restructuring of the coronal magnetic field. The classical view of a solar eruption focuses on the central part of this spectrum and connects strong CMEs with strong flares. However, the events studied here certainly show that during solar eruptions energy can be distributed in various ways, making some eruptive signatures more clearly observable than others. It therefore remains important to study solar eruptions as a whole and include all possible information in the analyses of CMEs in order to obtain a better understanding of their initiation.

Beknopte Samenvatting

We beschrijven hier de resultaten van een observationele en statistische studie van atypische zonne-uitbarstingen. Inderdaad, de Zon is niet zomaar een rustige ster die ons van warmte en licht voorziet, ze bulkt ook van de activiteit. Zonne-uitbarstingen vinden verschillende keren per dag plaats en indien de straling, het plasma en de energetische deeltjes die hierbij ontsnappen zich in de richting van de Aarde voortbewegen, kunnen we het slachtoffer worden van sterke ruimteweerstormen. Hierbij kan heel wat van onze technologie op Aarde en in de ruimte verstoord of beschadigd worden: denk aan communicatie en navigatie, maar ook aan het elektriciteitsnetwerk en satellieten. Het is dus van cruciaal belang dat we deze zonne-uitbarstingen nauwkeurig bestuderen.

We spitsen ons in dit onderzoek toe op zogenaamde coronale massa-uitbarstingen (CMEs), plasmawolken die van de Zon worden weggekatapulteerd en die waargenomen worden met een coronagraaf, een telescoop die een artificiële eclips creëert door met een plaatje het overheersende licht van de zonnenschijf te blokkeren. In plaats van te focussen op de meest spectaculaire zonne-uitbarstingen, brengen we hier de schijnbaar onopvallende *stealth CMEs* onder de aandacht. Hoewel deze coronale massa-uitbarstingen duidelijk zichtbaar zijn in beelden van een coronagraaf terwijl ze zich door de interplanetaire ruimte voortbewegen, verraden ze verder op geen enkele manier dat er een zonne-uitbarsting heeft plaatsgevonden: er zijn geen waarneembare aanwijzingen voor een uitbarsting te vinden in de lage corona en ook niet op het zonsoppervlak. Dit maakt het uitermate moeilijk om te bepalen waar exact op het zonsoppervlak of in de lage corona deze stealth CMEs zijn ontstaan, en ook om hun traject door de interplanetaire ruimte te voorspellen. Daardoor kunnen deze uitbarstingen ruimteweervoorspellers verrassen en is het een hele uitdaging voor deze voorspellers om de mogelijke gevolgen van stealth CMEs op het vlak van ruimteweer in te schatten.

Net als vele andere zonnefysici begonnen we dit onderzoek echter met een observationele studie, beschreven in hoofdstuk 3, van een opvallende zonne-

uitbarsting die alle interessante kenmerken vertoonde die men kan verwachten van een krachtige zonne-explosie. Op 14 augustus 2010 werd de uitbarsting van een roterende protuberans waargenomen op de noord-westelijke zonerand. De huidige zonnecyclus was toen nog maar juist begonnen aan zijn nieuwe klim naar een piek in de zonneactiviteit. De uitbarsting van deze protuberans was één van de eerste grote gebeurtenissen in de nieuwe cyclus, dus logischerwijs trok deze zonne-explosie onze aandacht, en ook die van vele andere onderzoekers. Terwijl onze collega's zich onder andere richtten op de eigenschappen van de bijbehorende CME en op de oprispingen gemeten in radiogolven, waren wij vooral geïnteresseerd in de mogelijke initiatiemechanismen voor deze uitbarsting.

Twee verschillende actieve gebieden waren betrokken bij deze zonne-uitbarsting, en we stelden een significante daling in de magnetische flux vast voor één van hen. Daarom was onze hypothese dat de protuberans in eerste instantie zijn stabiliteit verloor door het verdwijnen van flux in dit actieve gebied, waardoor hij langzaam kon opstijgen. Uit het traject van de uitbarstende protuberans dat werd waargenomen door de EUV-instrumenten en de coronagrafen, leerden we inderdaad dat de protuberans aanvankelijk langzaam steeg tot hij een kritiek punt bereikte rond 09:50 UT en met grote snelheid werd weggekatapulteerd. Waarschijnlijk zette de draaibeweging die de protuberans plots onderging een magnetohydrodynamische (MHD) instabiliteit in gang. Omwille van de versnelling die de protuberans in deze fase onderging, verplaatste de CME zich daarna met hoge snelheid door de interplanetaire ruimte. In de toekomst kunnen we nog de hoogte van de gereconstrueerde protuberans vergelijken met de hoogte waarop de *decay* index een kritieke waarde bereikt, om zo mogelijk aan te tonen dat inderdaad de torus instabiliteit deze uitbarsting aandreef.

Hoewel dit een opvallende zonne-uitbarsting was, toonden de waarnemingen aan dat de bijbehorende zonnevlam vrij zwak was in vergelijking met de snelle CME. Hoewel dit verklaard kan worden door de aanvang van een MHD-instabiliteit, waarbij de protuberans niet aangedreven wordt door sterke magnetische reconnectie onderin, vroegen we ons door deze vaststelling af hoe de beschikbare magnetische energie tijdens een zonne-uitbarsting wordt verdeeld over de verschillende tekenen van zo'n explosie. Zijn er CMEs die niet gekoppeld kunnen worden aan duidelijke signalen die de oorsprong van de uitbarsting in de lage corona verraden en hoe passen zij in onze huidige modellen?

Observationele studies van zonne-uitbarstingen zijn tegenwoordig vaak gericht op de meest spectaculaire gebeurtenissen, liefst met de helderste zonnevlammen en de snelste coronale massa-uitbarstingen. Dat is zeer begrijpelijk. Ten eerste trekt dit soort uitbarstingen meer aandacht omdat ze intrigerend zijn om naar te kijken. Bovendien, en van meer belang, kunnen de eigenschappen van deze uitbarstingen accurater bepaald worden door de duidelijkere waarnemingen ervan. Daarbij komt nog dat dit soort uitbarstingen door ruimteweersvoorspellers wordt

gezien als de belangrijkste kandidaten voor het veroorzaken van verschillende ruimtewereffecten, en daarom houden ze deze gebeurtenissen goed in het oog. Wij, daarentegen, besloten het andere uiterste van het spectrum te bestuderen: zonne-uitbarstingen die heel wat minder energetisch zijn en daardoor geen duidelijk waarneembare tekens achterlaten op het zonsoppervlak, maar die desondanks toch belangrijk kunnen zijn voor het ruimteweer.

In hoofdstuk 4 gingen we op zoek naar deze stealth coronale massa-uitbarstingen. Bleek al snel dat deze uitbarstingen niet eenvoudig te herkennen zijn. Het onderscheid maken tussen stealth CMEs en uitbarstingen aan de achterkant van de Zon en daarnaast ook nog alle mogelijk geassocieerde activiteit op het zonsoppervlak elimineren was een moeilijke en tijdrovende taak. Deze opdracht kon gedeeltelijk uitgevoerd worden door de resultaten van verschillende programma's te combineren die automatisch verschillende voorbodes en tekenen van zonne-uitbarstingen detecteren. Hierdoor konden we een groot deel van de uitbarstingen in onze oorspronkelijke dataset, die bestond uit de CACTus detecties voor het jaar 2012, elimineren. Na deze eerste geautomatiseerde stap, bleven er nog een 500-tal uitbarstingen over om in detail te bestuderen. We combineerden de gegevens van een groot aantal instrumenten en waren zo in staat om het grootste deel van deze CMEs te elimineren door ze te koppelen aan een of andere observationele indicatie dat in de lage corona een uitbarsting had plaatsgevonden. Het uiteindelijke resultaat was een lijst van 40 stealth CMEs: coronale massa-uitbarstingen waarvan we met zekerheid konden zeggen dat ze niet geassocieerd waren met signalen van een uitbarsting in de lage corona of aan de achterkant van de Zon. Hoewel dit aantal coronale massa-uitbarstingen zonder indicaties dicht bij het zonsoppervlak vrij laag lijkt, is dit —voor zover wij weten— de grootste groep van stealth CMEs die tot nu toe werd bestudeerd.

Deze stealth uitbarstingen werden vervolgens het onderwerp van een observationele studie waarin we hun belangrijkste eigenschappen ontrafelden. Hoewel er een grote diversiteit was in het uiterlijk van deze uitbarstingen, gaande van een smalle uitstroom tot grootschalige CMEs met de typische driedelige structuur, is het opvallend dat in 2012 het grootste deel van deze stealth CMEs hun oorsprong vonden in de omgeving van de noordpool van de Zon. Verder is de snelheid van CMEs zonder coronale signalen in het algemeen relatief laag, waarbij de mediaan van de snelheid tussen 100 km s^{-1} en 500 km s^{-1} ligt, al hebben we ook een aantal zeer snelle stealth uitbarstingen gevonden. Verdere studie van de kinematische eigenschappen van deze groep van stealth CMEs leerde ons dat hun hoogte-tijd-curves overeenkwamen met de modellen voor MHD-instabiliteiten en het breakout-mechanisme, en ook dat de meeste stealth CMEs gradueel versnellen wanneer ze in de richting van de interplanetaire ruimte voortbewegen. De verdeling van de hoekbreedtes voor CMEs zonder

tekenen in de lage corona vertoont een piek op 20° , wat erop wijst dat de stealth CMEs in 2012 een beperkte reikwijdte hadden.

Wat betreft de mechanismen die verantwoordelijk zijn voor het ontstaan van stealth CMEs, is het beeld eigenlijk niet zo verschillend van de modellen die gewone zonne-uitbarstingen beschrijven. Natuurlijk zijn stealth CMEs laag-energetische uitbarstingen en wordt de beschikbare energie waarschijnlijk hoofdzakelijk aangewend om de CME te lanceren en niet om het omringende plasma te verhitten. Dit is echter compatibel met een aantal van de bestaande modellen, zoals het model dat de uitbarsting van een leeg protuberanskanaal op grote hoogte beschrijft. Een belangrijk bijkomend element zijn de andere zonne-explosies die voorafgaan aan de stealth uitbarstingen en die waarschijnlijk het pad hebben vrijgemaakt voor de stealth CMEs door het grootste deel van het overkoepelende magneetveld, dat de structuur in bedwang houdt, te verwijderen. Op een gelijkaardige manier maken de open veldlijnen rond de poolgebieden het ontstaan van een polaire CME zonder coronale indicaties heel wat eenvoudiger.

Natuurlijk zijn we niet de enigen die zo redeneren. Na de eerste baanbrekende studie over stealth CMEs door Robbrecht et al. (2009b), volgden andere publicaties. Ma et al. (2010) voerden een observationele studie uit die goed te vergelijken is met de onze. Er verschenen ook papers van de hand van Vourlidas et al. (2011) en Nieves-Chinchilla et al. (2013) die telkens één specifieke stealth uitbarsting bestudeerden. Howard and Harrison (2013) schreven hun standpunt over het concept 'stealth CME' neer en waarschuwden voor de classificatie van CMEs in duidelijk gescheiden groepen. Deze auteurs steunen de interpretatie dat stealth CMEs tot het lage-energie-uiteinde behoren van een spectrum van coronal reacties op eenzelfde fysisch mechanisme. Al deze publicaties wijzen op een toenemende aandacht voor het onderwerp van CMEs zonder duidelijke signalen van een uitbarsting in de lage corona. In de periode waarin wij dit doctoraatsonderzoek voerden, zijn stealth CMEs een *hot topic* geworden.

Op basis van de literatuur en ons eigen onderzoek, is het duidelijk dat CMEs zonder indicaties in de lage corona over het algemeen trage en smalle CMEs zijn, die hoogst waarschijnlijk op grote hoogte ontstaan en daarom geen duidelijke signalen van een sterke uitbarsting vertonen. Waarom doen we dan de moeite om deze uitbarstingen te bestuderen? Het pragmatische antwoord is dat deze uitbarstingen, ondanks hun relatief lage snelheden en geringe reikwijdte, toch belangrijke ruimteweereffecten kunnen veroorzaken. Hoewel deze uitbarstingen — energetisch gezien — minder krachtig zijn, kunnen ze toch significant zijn, zeker indien hun magnetische veld een belangrijke component heeft die naar het zuiden is gericht. Bovendien maakt hun onopvallende aard stealth CMEs moeilijk te detecteren. Inderdaad, het is mogelijk dat smalle stealth CMEs die naar de Aarde zijn gericht onvoldoende uitzetten in hoekbreedte om achter de occultor van de coronograaf vandaan te komen, terwijl ook de

brederste stealth uitbarstingen door sterke projectie-effecten heel zwak lijken in coronagraafbeelden en dus mogelijk onopgemerkt blijven. Omdat deze stealth CMEs ook geen duidelijke tekenen van een uitbarsting achterlaten, moeten we op zoek naar andere criteria (zoals bijvoorbeeld een waargenomen schok) die ons kunnen waarschuwen voor de mogelijke uitbarsting van een stealth CME die naar de Aarde is gericht.

Een meer doorslaggevend argument om stealth CMEs te bestuderen, echter, is de academische noodzaak om dit soort zonne-uitbarstingen beter te begrijpen. Zonnevlammen en CMEs worden al geruime tijd bestudeerd, en ook al komen ze vaak samen voor tijdens een uitbarsting, dat is niet altijd het geval. Het antwoord op de vraag waarom het ene element soms voorkomt zonder het andere, kan cruciaal zijn om ons begrip en onze modellen van zonne-uitbarstingen te verbeteren en in die zin zijn stealth CMEs uitgelezen voorbeelden om in detail te bestuderen.

Het is overduidelijk dat er meer waarnemingen van stealth CMEs nodig zijn om onze kennis van dit soort uitbarstingen te verbeteren. Hoewel deze uitbarstingen door hun verdoken aard niet eenvoudig uit de bestaande waarnemingen te filteren zijn, is het denkbaar dat ruimteweevoorspellers voortaan stealth CMEs kunnen rapporteren binnen enkele uren na de start van de uitbarsting. Echter, zelfs wanneer er aandachtig naar gezocht wordt, is het moeilijk om stealth CMEs te onderscheiden van andere lage-energetische zonne-activiteit en bovendien is er geen consensus over de definitie van een stealth uitbarsting, wat de identificatie ervan nog moeilijker maakt. Indien we stealth CMEs echter verder willen bestuderen en beter willen begrijpen, moeten we een werkbare methode vinden om meer voorbeelden van dit type van uitbarsting te identificeren en zo onze verzameling van waarnemingen uit te breiden.

Naast meer observationele studies, is het numeriek modelleren van stealth CMEs een belangrijke onderzoekslijn voor de toekomst. Een goed startpunt zou het werk van Bemporad et al. (2012) zijn. Deze auteurs modelleerden het scenario dat hierboven al werd beschreven: een eerdere uitbarsting destabiliseert het overkoepelende magnetische veld en veroorzaakt een tweede, stealth-achtige uitbarsting als gevolg van de relaxatie van dit magneetveld. Uit deze studie bleek duidelijk dat de sterkte van het globale magneetveld bepaalt of er al dan niet een tweede CME zonder duidelijke tekenen van een uitbarsting volgt. Een gedetailleerde parameterstudie met dit model zou kunnen achterhalen welke waarden voor het magneetveld een stealth CME toelaten, en kan ook andere cruciale parameters aan het licht brengen. Deze waarden kunnen dan op hun beurt vergeleken worden met de waarnemingen van de stealth CMEs die we in deze studie hebben geïdentificeerd.

Onze definitie van stealth CME is observationeel, zelfs al was één van de belangrijkste argumenten van Howard and Harrison (2013) om onderzoekers ervoor te waarschuwen zonne-uitbarstingen niet in observationele categorieën op te delen, dat deze opdeling afhankelijk is van de huidige instrumentatie. Inderdaad, naarmate onze instrumenten verbeteren, zullen we in de toekomst mogelijk in staat zijn om de hoog-liggende lege protuberanskanalen te observeren die waarschijnlijk de bronnen zijn van stealth CMEs. Het zou daarom beter zijn om, bijvoorbeeld, een minimale hoogte te definiëren waarboven een zonne-uitbarsting moet ontstaan om geklasseerd te kunnen worden als een stealth CME. Om die hoogte vast te stellen, moeten we echter eerst het uitbarsten van een aantal van die hoog-liggende lege protuberanskanalen waarnemen.

De nieuwe *Extreme Ultraviolet Imager* (EUI) aan boord van de *Solar Orbiter* satelliet (lancering gepland voor 2018, eerste waarnemingen verwacht in 2021) zal mogelijk in staat zijn dit te doen. Dit instrument bestaat uit twee hoge-resolutie camera's (*high-resolution imagers*, HRI) die een beperkt gezichtsveld hebben, en een *full-sun imager* (FSI) die met een groot gezichtsveld de hele Zon waarneemt. *Solar Orbiter* zal de Zon van dichterbij waarnemen dan ooit gedaan. Bovendien hebben de EUV-camera's een verbeterde gevoeligheid in de hoge corona vergeleken met de huidige instrumenten. Dit stelt ons mogelijk in staat om de hoog-liggende protuberanskanalen waar te nemen die nu aan ons zicht ontsnappen.

Bovendien zal *Solar Orbiter* een baan beschrijven die de satelliet uit het ecliptische vlak laat bewegen en zo toelaat om waarnemingen te maken van de polen van de Zon met de EUV-camera's en magnetometer aan boord. Dit gezichtspunt weg van de ecliptica is zeer interessant voor de studie van stealth CMEs aangezien de meeste stealth uitbarstingen die in 2012 werden waargenomen dicht bij de polen leken te ontstaan. Waarnemingen van dit gebied kunnen ons dus mogelijk in staat stellen om de oorsprong van stealth uitbarstingen dicht bij de polen te achterhalen. De coronagraaf aan boord van *Solar Orbiter* zal ook waarnemingen maken weg van het ecliptische vlak, wat kan helpen om de projectie-effecten voor halo-CMEs te omzeilen. Deze halo CMEs zijn nu zeer moeilijk te bestuderen. In het geval van stealth CMEs is het denkbaar dat we nu deze uitbarstingen, die naar de Aarde zijn gericht, missen omdat ze minder energetisch zijn en deze zwakke halo's moeilijk te observeren zijn. Stealth halo CMEs zouden in de toekomst mogelijk wel door *Solar Orbiter* waargenomen kunnen worden vanuit een ander gezichtspunt.

De PROBA3 missie zal ook bijdragen tot de studie van stealth CMEs. De beelden van de coronagraaf aan boord zullen de zonnecorona waarnemen van $1.05 R_{\odot}$ tot $3 R_{\odot}$ en zo het gat dicht maken dat momenteel bestaat tussen waarnemingen van EUV-camera's en coronagrafen. Dit zal ons toelaten om de zonne-uitbarstingen

te volgen vanaf de plaats waar ze ontstaan (zelfs al is dat hoog in de corona) tot in de heliosfeer.

In hoofdstuk 4 onderzochten we ook de schaalinvariantie van de hoekbreedte van CMEs zonder laag-coronale tekenen van een uitbarsting, op zoek naar indicaties dat deze uitbarstingen mogelijk een ander initiatiemechanisme zouden kunnen hebben dan CMEs die wel duidelijke signalen vertonen. We besloten dat het inderdaad waarschijnlijk was dat de parameter van de machtsfunctie voor stealth CMEs anders is dan die van normale CMEs, aangezien we duidelijk verschillende hellingswaarden berekenden voor de logaritmisch getransformeerde histogrammen voor beide groepen. Dit resultaat leek ook overeen te komen met de vaststelling dat CMEs zonder laag-coronale tekenen van een uitbarsting over het algemeen een kleinere reikwijdte hebben dan CMEs die die tekenen wel vertonen. We realiseerden ons echter dat we slechts over een klein aantal stealth waarnemingen beschikten en we vroegen ons af hoe dit onze resultaten zou beïnvloeden. Dit was de motivatie voor het meer theoretische hoofdstuk 5, waarin we de invloed onderzochten van het aantal waarnemingen die in rekening worden gebracht bij de schatting van de parameter van een machtsfunctie aan de hand van verschillende methodes.

In hoofdstuk 5 bleek dat een enorm aantal waarnemingen nodig is om de parameter van een machtsfunctie betrouwbaar te schatten, ten minste wanneer we een grafische methode toepassen zoals in hoofdstuk 4. Onze eerdere resultaten in verband met de schaalinvariantie voor stealthmogelijk CME waren dus duidelijk onbetrouwbaar. Daarom onderzochten we een betere methode om machtsfuncties te bestuderen: de methode van de meest aannemelijke schatter. Deze techniek is eenvoudig te implementeren en de resultaten ervan zijn onmiskenbaar accurater vergeleken met grafische methodes, zelfs wanneer we over relatief weinig waarnemingen beschikken.

Door sterk geïdealiseerde data te gebruiken, zoals we deden in hoofdstuk 5, werd het enorme verschil in performantie van beide methodes meteen duidelijk: de grafische methode om de parameter van een machtsfunctie te berekenen (waarbij een logaritmische transformatie op het histogram wordt toegepast en de kleinste-kwadratenmethode wordt gebruikt om de helling van de resulterende rechte te bepalen) vereist een enorme hoeveelheid gegevens om een aanvaardbare schatting te bekomen, terwijl het alternatief van de meest aannemelijke schatter een accuratere schatting oplevert met een eenvoudige berekening en aanzienlijk minder gegevens. Verschillende aanpassingen aan de standaard grafische methode, zoals het logaritmisch groeperen van de data en het toekennen van gewichten aan de klassen, kunnen de grafische schattingen beduidend verbeteren. Ook ten opzichte van deze aangepaste grafische methodes levert de methode van de meest aannemelijke schatter echter nog steeds het beste resultaat.

We pasten deze voorkeursmethode van de meest aannemelijke schatter daarom in hoofdstuk 6 toe op gegevens van de hoekbreedtes van stealth CMEs en vergeleken het resultaat met de meest aannemelijke schatter voor klassieke CMEs. Het resultaat was dat we onze eerdere conclusies moesten herzien: er kon geen verschil tussen de parameterwaarden van de machtsfuncties voor stealth en gewone CMEs gevonden worden binnen de foutenmarge. Het probleem van het kleine aantal stealth CMEs was hiermee echter niet opgelost: zelfs voor de methode van de meest aannemelijke schatter was het aantal CMEs zonder signalen in de lage corona te klein om de waarde van de parameter van de machtsfunctie betrouwbaar te schatten. Om een sluitend antwoord te geven op de vraag of de schaalinvariantie voor beide groepen van CMEs verschillend is, moeten we dus over meer waarnemingen beschikken.

In hetzelfde hoofdstuk 6 bestudeerden we ook een andere dataset opnieuw. Deze gegevens beschreven de energie van zeer kleine zonnevlammen in de transitiezone van de zonne-atmosfeer. De hoeveelheid energie in kleine en grote zonnevlammen is inderdaad ook uit te drukken met behulp van een machtsfunctie. De exacte parameterwaarde voor deze machtsfunctie is het onderwerp van debat in onderzoek naar de opwarming van de corona en heeft daarom in het verleden reeds veel aandacht gekregen. Het originele onderzoek op deze dataset werd uitgevoerd door Berghmans et al. (1998) en leverde een parameterwaarde net onder de kritieke waarde 2 op. Onze nieuwe analyse van deze dataset met de methode van de meest aannemelijke schatter leverde daarentegen een andere machtsfunctie op, met een parameterwaarde boven deze grens. Dit betekent echter niet dat het probleem van de hete corona is opgelost. Inderdaad, we waren niet in staat om te bevestigen dat deze nieuwe machtsfunctie ook geldt voor kleine energiewaarden, en dat is precies het cruciale argument om zeer kleine zonnevlammen aan te duiden als warmtebron voor de corona. Verder onderzoek met meer gegevens is daarom nodig om te bepalen of zeer kleine zonnevlammen een significante bijdrage leveren tot het opwarmen van de corona.

Ons onderzoek in hoofdstukken 5 en 6 maakte duidelijk dat een aanzienlijk aantal waarnemingen nodig is om machtsfuncties in de zonnefysica te bestuderen. Bovendien is het cruciaal dat correcte methodes worden toegepast om zo betrouwbare parameterschattingen te bekomen. Deze aspecten werden soms over het hoofd gezien in vorige studies. Hoewel de auteurs ervan mogelijk een betrouwbare machtsfunctie in hun gegevens hebben gevonden, is het aangeraden om deze resultaten opnieuw te evalueren aan de hand van de gepaste methodes. Inderdaad, aangezien onze onderzoeksmethodes en wetenschappelijke kennis voortdurend evolueren, moeten onderzoekers er niet voor terugschrikken om eerdere resultaten te herbekijken. Het is aannemelijk dat in tussentijd betere technieken werden ontwikkeld en onderzoekers moeten niet twijfelen

om hun gegevens hiermee opnieuw te analyseren en accuratere conclusies te trekken. Falsificatie van een voorgestelde theorie is een onderdeel van het onderzoeksproces dat net zo belangrijk en waardevol is als het bevestigen ervan.

We bespraken hier ons onderzoek naar atypische zonne-uitbarstingen en hun initiatiemechanismen. We richtten ons op CMEs die niet in verband konden worden gebracht met een observationeel signaal in de lage corona en onderzochten ook een snelle uitbarsting waarvoor de begeleidende zonnevlam uitzonderlijk zwak was. Hoewel deze uitbarstingen nog steeds in onze huidige modellen van CME-initiatie passen, bevinden ze zich duidelijk aan het uiteinde van een spectrum van mogelijke gevolgen van veranderingen in het coronale magnetische veld. Het klassieke model van een zonne-uitbarsting focust op het centrale deel van dit spectrum en linkt sterke CMEs aan krachtige zonnevlammen. De zonne-explosies die we hier hebben bestudeerd, tonen echter duidelijk aan dat de energie op verschillende manieren kan verdeeld worden tijdens een uitbarsting, waardoor sommige observationele signalen duidelijker kunnen zijn dan andere. Daarom blijft het belangrijk om zonne-uitbarstingen in hun geheel te bestuderen en alle mogelijke informatie op te nemen in de analyse van CMEs om zo een beter begrip te krijgen van hun initiatiemechanismen.

Appendix A

PROBA2 Outreach

A.1 Scientific Outreach

The P2SC team involves the scientific community in SWAP and LYRA data exploitation through several channels. For instance, the *Science Consortium for LYRA and SWAP* was formed in 2005 and oversees the international coordination of the SWAP and LYRA science operations. In addition, a *Guest Investigator Program* allows selected researchers to spend time with the PI teams in the PROBA2 Science Center to take part in the daily instruments commanding and to set up dedicated observational campaigns. This successful program has recently selected the proposals for the sixth round of guest investigators, who are invited to visit the P2SC in the period from August 2015 to April 2016.

During the past years, much effort was put into PROBA2's visibility at scientific conferences all over the world. In Belgium, the PROBA2 full-sized model made a recurring visit to the European Space Weather Week (ESWW), organized by ROB. A fair stand and posters at the same ESWW conferences complemented this.

A.2 Reaching Out to the General Public¹

PROBA2 and its scientific instruments have always been featured prominently at ROB Open Doors through talks and posters. Visits to the P2SC are also an important part of the Open Doors program, offering the visitors the opportunity to learn about the inner workings of satellite commanding. The P2SC also hosts a full-size model of PROBA2 to show visitors how small the satellite actually is and where the most important components are located on the spacecraft. Additionally, PROBA2 is generally included in most of the outreach talks that researchers from ROB give to the general public, for example to amateur astronomy groups and teacher associations. The same goes for their popular publications. On several important occasions (such as the launch and PROBA2's birthdays) press releases were sent out as well.

Below we discuss in more detail two long-term outreach projects that were specifically inspired by the PROBA2 mission and that have been a huge success, reaching out to thousands of high school students over the last six years.

A.2.1 Proba2@School

We started the *Proba2@school* project early in 2010, shortly after the PROBA2 satellite was launched successfully and the commissioning phase had ended. The satellite was in perfect health and the solar instruments were taking valuable measurements of the Sun. While this was announced to the general public through the usual channels (website, press release), we decided to target a younger audience as well: students that are about to finish high school. By showing them the interesting world of space missions and solar physics, we hoped to broaden their perspective and motivate some of them to continue their education in science or engineering.

Petra Vanlommel (ROB) and I developed the Proba2@School project in collaboration with the *Academisch Vormingscentrum voor Leraren* (AVL, an academic educational center for high school teachers) at KU Leuven. This center offers high school teachers an opportunity to follow supplementary courses in order to keep up with new developments in the field of education and the scientific research linked to their own speciality. The first goal of the Proba2@School project was to capture the attention of high school teachers in Flanders and to give them information about space weather and the PROBA2 satellite to

¹This section is largely based on Vanlommel and 6 co-authors, including D'Huys (2014). Text reproduced with permission.



Figure A.1 *Left Panel:* Cover page of the *Proba2@School* booklet (D’Huys and Vanlommel, 2010). *Right Panel:* Impression of a *Proba2@School* workshop on the prediction of solar flares, organized at the Klein Seminarie in Hoogstraten.

incorporate in their lessons on mathematics, physics and geography (Target group: third grade of high school in Flanders, that is, 16 to 18 years old).

To accomplish this, we published a booklet for high school teachers (in Dutch) called: *Ruimteweer waarnemen met een Belgische satelliet - Observing Space Weather with a Belgian Satellite* (D’Huys and Vanlommel, 2010, left panel in Figure A.1)² containing an introduction to space weather as well as information on the PROBA2 spacecraft. (This text was also published in *Guidestar magazine* by the Astro Event Group³ and in *Science Connection*, the magazine of the Belgian Federal Science Policy Office, BELSPO⁴.) The AVL invited interested high school teachers to a seminar by representatives of the P2SC team to introduce them to these subjects. During several follow-up meetings between the teachers and the P2SC team, we extensively discussed their specific requirements as well as their wish to turn this brochure into concrete teaching material.

Following these discussions, Berdien Peeters, a master student in mathematics at the KU Leuven, developed such a course on mathematical space weather applications in the framework of her master thesis *Wiskunde achter detectie van zonnepfenomenen op basis van satellietbeelden. Projecten in de derde graad van het secundair onderwijs (Mathematics behind the detection of solar phenomena based on satellite data, projects for the third grade of high school;* Peeters, 2011).

² Available at <http://sidc.oma.be/Leerkrachten/>

³ <http://www.spacepage.be/guidestar/2010>

⁴ http://www.belspo.be/belspo/organisation/Publ/pub_ostc/sciencecon/29sc_nl.pdf

In the course of 2011, three schools asked us to organize a dedicated PROBA2@school project day for their third grade students. While we adapted the program to fit the needs of each student group and school, it typically consisted of a 10 minute introduction to space weather, followed by three parallel workshops and a 10 minute interactive quiz to conclude. For the 20 minute parallel workshops, we split the students up in smaller groups (Figure A.1, right panel). Depending on the on-site facilities and the P2SC team members available to lead a workshop, we chose between five different topics: the PROBA2 satellite (using the PROBA2 full-size model), space weather prediction, solar flare prediction, calculation of the speed of solar wind structures, and calibration and image processing (focused on SWAP data). Other schools took the opportunity to take a trip to the Royal Observatory, which allowed them to visit the P2SC, as well as the ROB space weather forecasting center and solar dome.

We maintained contact with these schools and repeated the workshops in the following years, reaching about 50 students during each visit. However, most schools and teachers preferred to switch to the Junior College project that was introduced in 2012.

A.2.2 Junior College

The second long-term outreach project in which the P2SC team participates is the Flemish interdisciplinary educational project *Junior College*, organized by KU Leuven. This project provides challenging courses for high school students in their final years. The aim is to bridge the gap between high school and university and to spark the students' interest in science.

In addition to content in a variety of sciences, Junior College provides material for courses in mathematics related to diverse themes. As a follow-up of the master thesis by Peeters (2011) and the booklet prepared by the P2SC team (D'Huys and Vanlommel, 2010), the Junior College group prepared a course book on PROBA2 and space weather (in Dutch): *Wiskunde achter Detectie en Observatie van Ruimteweer - Mathematics behind the Detection and Observation of Space Weather Phenomena* (Bonte et al., 2012, right panel in Figure A.2).

Each edition of the Junior College project typically consisted of the following elements: participating students and their teachers are invited to visit the university for an introductory seminar on space weather and the PROBA2 spacecraft given by P. Vanlommel and/or me (Figure A.2, left panel). After being immersed in the world of space weather, students and teachers then receive all educational material needed for a mathematical course, spread over 15 teaching periods of 1 hour. Towards the end of this course, the participating



Figure A.2 *Left Panel:* Screen shot from the video recording of the Junior College introductory seminar on space weather and PROBA2 in January 2015 at the KU Leuven. *Right Panel:* Cover page of the Junior College course book (Bonte et al., 2012, used with permission).

schools are once again invited to the KU Leuven for a closing seminar. This seminar then focuses on one of the applications of mathematics in the space weather context, for example numerical simulations in space weather research.

The course book prepared by the Junior College group offers a closer look at the mathematics behind the detections of coronal mass ejections and satellite data processing (the latter inspired by the calibration steps applied to SWAP images that are discussed in Section 2.4.2). These two modules discuss the transformation of coordinate systems, the Hough transform, projective geometry, and matrix transformations. Through the online Junior College platform, applets for GeoGebra (a mathematics software) are provided to the students to improve their understanding of these mathematical operations.

This Junior College project was first organized in 2012 and has been repeated every year since. As the interest in this subject grew, we reached an average of 400 high school students and their teachers per year during our introductory sessions. To accommodate schools in different regions in Flanders — and depending on the number of participants — multiple introductory sessions have been organized on several KU Leuven campuses (mainly Leuven, but also Kortrijk) in the same year.

Appendix B

Table of CMEs Without Low-Coronal Signatures of Eruption

Table B.1. CACTus detection parameters for the CMES without low-coronal signatures observed in 2012. The first four columns indicate the date and time of each event. The principal angle in the fifth column is expressed in degrees, counting counterclockwards from the north. The angular width and median velocity of the CMES are given in the last two columns.

Start Date	Start Time	End Date	End Time	Principal Angle (°)	Angular Width (°)	Median Velocity (km s ⁻¹)
07 Jan 2012	15:24:05	07 Jan 2012	17:36:05	30	6	431
07 Jan 2012	23:48:06	08 Jan 2012	01:12:06	3	12	142
19 Jan 2012	22:36:05	20 Jan 2012	00:00:06	357	12	856
20 Jan 2012	00:24:05	20 Jan 2012	02:48:05	334	22	390
20 Jan 2012	17:12:06	20 Jan 2012	18:48:07	341	8	418
26 Jan 2012	16:38:06	26 Jan 2012	18:48:05	20	46	249
28 Jan 2012	04:12:05	28 Jan 2012	05:00:06	311	12	749
04 Feb 2012	09:24:06	04 Feb 2012	14:48:05	357	80	216
22 Feb 2012	12:48:05	22 Feb 2012	12:48:05	20	10	138
22 Feb 2012	23:48:06	23 Feb 2012	02:00:05	9	44	143
23 Feb 2012	12:24:05	23 Feb 2012	14:48:06	45	12	139
29 Feb 2012	19:48:07	01 Mar 2012	01:36:22	16	58	254
21 Mar 2012	23:12:10	22 Mar 2012	04:12:05	168	42	169
19 Apr 2012	01:36:05	19 Apr 2012	01:36:05	176	14	116
16 May 2012	03:24:05	16 May 2012	08:24:05	179	64	207
03 Jun 2012	07:12:05	03 Jun 2012	12:00:07	345	36	261
09 Jun 2012	07:24:05	09 Jun 2012	08:48:05	27	20	330
17 Jun 2012	04:48:05	17 Jun 2012	07:24:05	83	12	466

Table A.1. — Continued

Start Date	Start Time	End Date	End Time	Principal Angle (°)	Angular Width (°)	Median Velocity (km s ⁻¹)
07 Jul 2012	18:00:06	07 Jul 2012	22:36:06	100	14	323
13 Jul 2012	05:05:54	13 Jul 2012	08:24:06	330	18	329
14 Jul 2012	19:24:06	14 Jul 2012	19:24:06	334	10	310
17 Jul 2012	23:24:06	18 Jul 2012	01:26:17	318	18	1117
21 Jul 2012	02:36:06	21 Jul 2012	05:00:07	76	18	771
28 Jul 2012	14:24:07	28 Jul 2012	16:12:06	338	6	330
12 Aug 2012	20:24:07	12 Aug 2012	20:48:06	338	38	197
16 Aug 2012	05:00:06	16 Aug 2012	05:48:06	40	70	137
04 Sep 2012	03:48:06	04 Sep 2012	05:24:06	344	18	443
18 Sep 2012	02:12:09	18 Sep 2012	05:12:08	3	56	469
22 Sep 2012	07:00:06	22 Sep 2012	07:12:07	178	22	136
20 Oct 2012	23:48:06	21 Oct 2012	00:36:08	15	32	138
28 Oct 2012	01:48:07	28 Oct 2012	02:24:07	115	8	336
03 Nov 2012	23:24:07	04 Nov 2012	01:48:06	346	6	257
14 Nov 2012	00:00:06	14 Nov 2012	07:00:06	242	54	231
16 Nov 2012	13:36:31	16 Nov 2012	16:00:06	353	8	292
25 Nov 2012	18:36:06	25 Nov 2012	18:36:06	24	22	136
17 Dec 2012	03:36:07	17 Dec 2012	03:36:07	156	10	312
18 Dec 2012	08:24:06	18 Dec 2012	09:12:10	334	38	262
18 Dec 2012	18:36:06	18 Dec 2012	19:12:07	340	14	138
19 Dec 2012	18:36:06	19 Dec 2012	20:48:06	350	10	364
20 Dec 2012	21:17:39	20 Dec 2012	23:48:06	12	26	277

Project, Image and Data Acknowledgements

This research was co-funded by a Supplementary Researchers Grant offered by the Belgian Science Policy Office (BELSPO) in the framework of the Scientific Exploitation of PROBA2, by the Interuniversity Attraction Poles Programme initiated by BELSPO (IAP P7/08 CHARM), by the European Union's Seventh Framework Programme for Research, Technological Development and Demonstration under grant agreement No. 284461 (Project eHeroes, www.eheroes.eu), and by the COST action ES0803. E. D'Huys and D.B. Seaton also acknowledge support from BELSPO through the ESA-PRODEX program, grant No. 4000103240.

We thank the Astrophysical Journal, the Solar Physics Journal, the Journal for Space Weather and Space Climate, the Journal of Astrophysics and Astronomy, and Wiley Books for the permission to reprint images and text excerpts in this manuscript.

Additionally, we have used images and data from a multitude of satellites and data-analyzing tools that we would like to acknowledge here:

- SOHO images are courtesy of the SOHO/EIT and SOHO/LASCO consortia. The SOHO/LASCO CME catalog (CDAW) is generated and maintained at the CDAW Data Center by NASA and The Catholic University of America in cooperation with the Naval Research Laboratory. SOHO is a project of international cooperation between ESA and NASA.
- STEREO images and data are courtesy of NASA.
- SDO images are courtesy of NASA and the AIA, EVE, and HMI science teams.

- SWAP is a project of the Centre Spatial de Liège and the Royal Observatory of Belgium funded by the Belgian Federal Science Policy Office (BELSPO).
- LYRA is a project of the Centre Spatial de Liège, the Physikalisch-Meteorologisches Observatorium Davos and the Royal Observatory of Belgium funded by BELSPO and by the Swiss Bundesamt für Bildung und Wissenschaft.
- SILSO data and images are provided by the Royal Observatory of Belgium, Brussels.
- The SoFAST EUV flare catalog, the CACTus CME catalog and the Solar Demon catalog are generated and maintained by the Solar Influences Data analysis Center (SIDC) at the Royal Observatory of Belgium.
- ACE and GOES satellite data and planetary K-indices are provided by the Space Weather Prediction Center (SWPC) at NOAA.
- The radio survey project is a joint effort of the Paris Observatory, the Yunnan Observatory, the University of Sydney, the University of Athens, the University of Ioannina and the Solar Physics Branch of the Naval Research Laboratory.

References

- S. K. Antiochos, C. R. DeVore, and J. A. Klimchuk. A Model for Solar Coronal Mass Ejections. *Astrophys. J.*, 510:485–493, January 1999. doi: 10.1086/306563.
- M. J. Aschwanden. *Physics of the Solar Corona. An Introduction*. Praxis Publishing Ltd, August 2004.
- M. J. Aschwanden and C. E. Parnell. Nanoflare Statistics from First Principles: Fractal Geometry and Temperature Synthesis. *Astrophys. J.*, 572:1048–1071, June 2002. doi: 10.1086/340385.
- M. J. Aschwanden, N. B. Crosby, M. Dimitropoulou, M. K. Georgoulis, S. Hergarten, J. McAteer, A. V. Milovanov, S. Mineshige, L. Morales, N. Nishizuka, G. Pruessner, R. Sanchez, A. S. Sharma, A. Strugarek, and V. Uritsky. 25 Years of Self-Organized Criticality: Solar and Astrophysics. *Space Sci. Rev.*, July 2014. doi: 10.1007/s11214-014-0054-6.
- G. Aulanier. The physical mechanisms that initiate and drive solar eruptions. In B. Schmieder, J.-M. Malherbe, and S. T. Wu, editors, *IAU Symposium*, volume 300 of *IAU Symposium*, pages 184–196, January 2014. doi: 10.1017/S1743921313010958.
- P. Bak, C. Tang, and K. Wiesenfeld. Self-organized criticality - An explanation of 1/f noise. *Physical Review Letters*, 59:381–384, July 1987. doi: 10.1103/PhysRevLett.59.381.
- H. M. J. Barré, B. Duesmann, and Kerr. Y. H. Smos : The mission and the system. *IEEE Transactions on Geoscience and Remote Sensing*, 46:587–593, 2008.
- H. Bauke. Parameter estimation for power-law distributions by maximum likelihood methods. *European Physical Journal B*, 58:167–173, July 2007. doi: 10.1140/epjb/e2007-00219-y.

- A. Bemporad, F. P. Zuccarello, C. Jacobs, M. Mierla, and S. Poedts. Study of Multiple Coronal Mass Ejections at Solar Minimum Conditions. *Solar Phys.*, 281:223–236, November 2012. doi: 10.1007/s11207-012-9999-3.
- D. Berghmans. Getting hot by nanoflares. In A. Wilson, editor, *Solar Variability: From Core to Outer Frontiers*, volume 506 of *ESA Special Publication*, pages 501–508, December 2002.
- D. Berghmans, F. Clette, and D. Moses. Quiet Sun EUV transient brightenings and turbulence. A panoramic view by EIT on board SOHO. *Astron. Astrophys.*, 336:1039–1055, August 1998.
- D. Berghmans, J. F. Hochedez, J. M. Defise, J. H. Lecat, B. Nicula, V. Slemzin, G. Lawrence, A. C. Katsyiannis, R. van der Linden, A. Zhukov, F. Clette, P. Rochus, E. Mazy, T. Thibert, P. Nicolosi, M.-G. Pelizzo, and U. Schühle. SWAP onboard PROBA 2, a new EUV imager for solar monitoring. *Advances in Space Research*, 38:1807–1811, January 2006. doi: 10.1016/j.asr.2005.03.070.
- D. A. Biesecker, D. C. Myers, B. J. Thompson, D. M. Hammer, and A. Vourlidas. Solar Phenomena Associated with “EIT Waves”. *Astrophys. J.*, 569:1009–1015, April 2002. doi: 10.1086/339402.
- Guido Boffetta, Vincenzo Carbone, Paolo Giuliani, Pierluigi Veltri, and Angelo Vulpiani. Power laws in solar flares: Self-organized criticality or turbulence? *Phys. Rev. Lett.*, 83:4662–4665, Nov 1999. doi: 10.1103/PhysRevLett.83.4662.
- K. Bonte, A. Vanfroyenhoven, and B. Peeters. *Wiskunde achter Detectie en Observatie van Ruimteweer*. Junior College Course, KU Leuven, 2012.
- K. Bonte, D. Berghmans, A. De Groof, K. Steed, and S. Poedts. SoFAST: Automated Flare Detection with the PROBA2/SWAP EUV Imager. *Solar Phys.*, 286:185–199, August 2013. doi: 10.1007/s11207-012-0165-8.
- J.-L. Bougeret, M. L. Kaiser, P. J. Kellogg, R. Manning, K. Goetz, S. J. Monson, N. Monge, L. Friel, C. A. Meetre, C. Perche, L. Sitruk, and S. Hoang. Waves: The Radio and Plasma Wave Investigation on the Wind Spacecraft. *Space Sci. Rev.*, 71:231–263, February 1995. doi: 10.1007/BF00751331.
- G. E. Brueckner, R. A. Howard, M. J. Koomen, C. M. Korendyke, D. J. Michels, J. D. Moses, D. G. Socker, K. P. Dere, P. L. Lamy, A. Llebaria, M. V. Bout, R. Schwenn, G. M. Simnett, D. K. Bedford, and C. J. Eyles. The Large Angle Spectroscopic Coronagraph (LASCO). *Solar Phys.*, 162:357–402, December 1995. doi: 10.1007/BF00733434.

- J. T. Burkepile, A. J. Hundhausen, A. L. Stanger, O. C. St. Cyr, and J. A. Seiden. Role of projection effects on solar coronal mass ejection properties: 1. A study of CMEs associated with limb activity. *Journal of Geophysical Research (Space Physics)*, 109:A03103, March 2004. doi: 10.1029/2003JA010149.
- H. Chen, J. Zhang, S. Ma, S. Yang, L. Li, X. Huang, and J. Xiao. Confined Flares in Solar Active Region 12192 from 2014 October 18 to 29. *Astrophys. J. Lett.*, 808:L24, July 2015. doi: 10.1088/2041-8205/808/1/L24.
- J. Chen. Effects of toroidal forces in current loops embedded in a background plasma. *Astrophys. J.*, 338:453–470, March 1989. doi: 10.1086/167211.
- P. F. Chen. Initiation and propagation of coronal mass ejections. *Journal of Astrophysics and Astronomy*, 29:179–186, March 2008. doi: 10.1007/s12036-008-0023-0.
- P. F. Chen. Coronal Mass Ejections: Models and Their Observational Basis. *Living Reviews in Solar Physics*, 8:1, April 2011. doi: 10.12942/lrsp-2011-1.
- A. Clauset, C. Rohilla Shalizi, and M. E. J. Newman. Power-law distributions in empirical data. *ArXiv e-prints*, June 2007.
- A. De Groof, D. Berghmans, B. Nicula, J.-P. Halain, J.-M. Defise, T. Thibert, and U. Schühle. CMOS-APS Detectors for Solar Physics: Lessons Learned during the SWAP Preflight Calibration. *Solar Phys.*, 249:147–163, May 2008. doi: 10.1007/s11207-008-9175-y.
- J.-P. Delaboudinière, G. E. Artzner, J. Brunaud, A. H. Gabriel, J. F. Hochedez, F. Millier, X. Y. Song, B. Au, K. P. Dere, R. A. Howard, R. Kreplin, D. J. Michels, J. D. Moses, J. M. Defise, C. Jamar, P. Rochus, J. P. Chauvineau, J. P. Marioge, R. C. Catura, J. R. Lemen, L. Shing, R. A. Stern, J. B. Gurman, W. M. Neupert, A. Maucherat, F. Clette, P. Cugnon, and E. L. van Dessel. EIT: Extreme-Ultraviolet Imaging Telescope for the SOHO Mission. *Solar Phys.*, 162:291–312, December 1995. doi: 10.1007/BF00733432.
- E. D’Huys and P. Vanlommel. Proba2 - ruimteweer waarnemen met een belgische satelliet, 2010. URL http://sidc.oma.be/Leerkrachten/PROBA2@school_20101001.pdf.
- E. D’Huys, D. B. Seaton, S. Poedts, and D. Berghmans. Observational Characteristics of Coronal Mass Ejections without Low-coronal Signatures. *Astrophys. J.*, 795:49, November 2014. doi: 10.1088/0004-637X/795/1/49.
- L. Dolla, C. Marqué, D. B. Seaton, T. Van Doorselaere, M. Dominique, D. Berghmans, C. Cabanas, A. De Groof, W. Schmutz, A. Verdini, M. J. West, J. Zender, and A. N. Zhukov. Time delays in quasi-periodic pulsations

- observed during the x2.2 solar flare on 2011 february 15. *The Astrophysical Journal Letters*, 749(1):L16, 2012.
- M. Dominique, J.-F. Hochedez, W. Schmutz, I. E. Dammasch, A. I. Shapiro, M. Kretzschmar, A. N. Zhukov, D. Gillotay, Y. Stockman, and A. BenMoussa. The LYRA Instrument Onboard PROBA2: Description and In-Flight Performance. *Solar Phys.*, 286:21–42, August 2013. doi: 10.1007/s11207-013-0252-5.
- L. T. Elkins-Tanton. The sun, mercury, and venus. *Infobase Publishing*, 2006.
- L. Feng, B. Inhester, Y. Wei, W. Q. Gan, T. L. Zhang, and M. Y. Wang. Morphological Evolution of a Three-dimensional Coronal Mass Ejection Cloud Reconstructed from Three Viewpoints. *Astrophys. J.*, 751:18, May 2012. doi: 10.1088/0004-637X/751/1/18.
- L. Feng, B. Inhester, and M. Mierla. Comparisons of CME Morphological Characteristics Derived from Five 3D Reconstruction Methods. *Solar Phys.*, 282:221–238, January 2013. doi: 10.1007/s11207-012-0143-1.
- T. G. Forbes. A review on the genesis of coronal mass ejections. *J. Geophys. Res.*, 105:23153–23166, October 2000. doi: 10.1029/2000JA000005.
- T. G. Forbes, J. A. Linker, J. Chen, C. Cid, J. Kóta, M. A. Lee, G. Mann, Z. Mikić, M. S. Potgieter, J. M. Schmidt, G. L. Siscoe, R. Vainio, S. K. Antiochos, and P. Riley. CME Theory and Models. *Space Sci. Rev.*, 123: 251–302, March 2006. doi: 10.1007/s11214-006-9019-8.
- K. Gantois, F. Teston, O. Montenbruck, P. Vuilleumier, P.V.D Braembussche, and M. Markgraf. Proba2 mission and new technologies overview. *Small Satellite Systems and Services - The 4S Symposium*, 2006.
- G. A. Gary. Plasma Beta above a Solar Active Region: Rethinking the Paradigm. *Solar Phys.*, 203:71–86, October 2001. doi: 10.1023/A:1012722021820.
- J. P. H. Goedbloed and S. Poedts. *Principles of Magnetohydrodynamics*. Cambridge University Press, August 2004.
- M. L. Goldstein, S. A. Morris, and G. G. Yen. Problems with fitting to the power-law distribution. *European Physical Journal B*, 41:255–258, September 2004. doi: 10.1140/epjb/e2004-00316-5.
- N. Gopalswamy, S. Akiyama, S. Yashiro, and P. Mäkelä. Coronal Mass Ejections from Sunspot and Non-Sunspot Regions. In S. S. Hasan and R. J. Rutten, editors, *Magnetic Coupling between the Interior and Atmosphere of the Sun*, pages 289–307, 2010. doi: 10.1007/978-3-642-02859-5_24.

- J.-P. Halain, D. Berghmans, D. B. Seaton, B. Nicula, A. De Groof, M. Mierla, A. Mazzoli, J.-M. Defise, and P. Rochus. The SWAP EUV Imaging Telescope. Part II: In-flight Performance and Calibration. *Solar Phys.*, 286:67–91, August 2013. doi: 10.1007/s11207-012-0183-6.
- B. N. Handy, L. W. Acton, C. C. Kankelborg, C. J. Wolfson, D. J. Akin, M. E. Bruner, R. Carvalho, R. C. Catura, R. Chevalier, D. W. Duncan, C. G. Edwards, C. N. Feinstein, S. L. Freeland, F. M. Friedlaender, C. H. Hoffmann, N. E. Hurlburt, B. K. Jurcevich, N. L. Katz, G. A. Kelly, J. R. Lemen, M. Levay, R. W. Lindgren, D. P. Mathur, S. B. Meyer, S. J. Morrison, M. D. Morrison, R. W. Nightingale, T. P. Pope, R. A. Rehse, C. J. Schrijver, R. A. Shine, L. Shing, K. T. Strong, T. D. Tarbell, A. M. Title, D. D. Torgerson, L. Golub, J. A. Bookbinder, D. Caldwell, P. N. Cheimets, W. N. Davis, E. E. Deluca, R. A. McMullen, H. P. Warren, D. Amato, R. Fisher, H. Maldonado, and C. Parkinson. The transition region and coronal explorer. *Solar Phys.*, 187:229–260, July 1999. doi: 10.1023/A:1005166902804.
- F. A. Hanser and F. B. Sellers. Design and calibration of the GOES-8 solar x-ray sensor: the XRS. In E. R. Washwell, editor, *GOES-8 and Beyond*, volume 2812 of *Society of Photo-Optical Instrumentation Engineers (SPIE) Conference Series*, pages 344–352, October 1996.
- D. Hercik, P. Travnicek, S. Stverak, P. Hellinger, J. Lebreton, Z. Kozacek, and J. Brinek. The DSLP Langmuir Probe Experiment Onboard Proba2: Scientific Objectives and Description. *AGU Fall Meeting Abstracts*, page B1629, December 2008.
- J.-F. Hochedez, W. Schmutz, Y. Stockman, U. Schühle, A. Benmoussa, S. Koller, K. Haenen, D. Berghmans, J.-M. Defise, J.-P. Halain, A. Theissen, V. Delouille, V. Slemzin, D. Gillotay, D. Fussen, M. Dominique, F. Vanhellemont, D. McMullin, M. Kretzschmar, A. Mitrofanov, B. Nicula, L. Wauters, H. Roth, E. Rozanov, I. Rüedi, C. Wehrli, A. Soltani, H. Amano, R. van der Linden, A. Zhukov, F. Clette, S. Koizumi, V. Mortet, Z. Remes, R. Petersen, M. Nesládek, M. D’Olieslaeger, J. Roggen, and P. Rochus. LYRA, a solar UV radiometer on Proba2. *Advances in Space Research*, 37:303–312, 2006. doi: 10.1016/j.asr.2005.10.041.
- R. A. Howard, J. D. Moses, A. Vourlidas, J. S. Newmark, D. G. Socker, S. P. Plunkett, C. M. Korendyke, J. W. Cook, A. Hurley, J. M. Davila, W. T. Thompson, O. C. St Cyr, E. Mentzell, K. Mehalick, J. R. Lemen, J. P. Wuelser, D. W. Duncan, T. D. Tarbell, C. J. Wolfson, A. Moore, R. A. Harrison, N. R. Waltham, J. Lang, C. J. Davis, C. J. Eyles, H. Mapson-Menard, G. M. Simnett, J. P. Halain, J. M. Defise, E. Mazy, P. Rochus, R. Mercier, M. F. Ravet, F. Delmotte, F. Auchere, J. P. Delaboudiniere, V. Bothmer,

- W. Deutsch, D. Wang, N. Rich, S. Cooper, V. Stephens, G. Maahs, R. Baugh, D. McMullin, and T. Carter. Sun Earth Connection Coronal and Heliospheric Investigation (SECCHI). *Space Sci. Rev.*, 136:67–115, April 2008a. doi: 10.1007/s11214-008-9341-4.
- T. A. Howard and R. A. Harrison. Stealth Coronal Mass Ejections: A Perspective. *Solar Phys.*, 285:269–280, July 2013. doi: 10.1007/s11207-012-0217-0.
- T. A. Howard, D. Nandy, and A. C. Koepke. Kinematic properties of solar coronal mass ejections: Correction for projection effects in spacecraft coronagraph measurements. *Journal of Geophysical Research (Space Physics)*, 113:A01104, January 2008b. doi: 10.1029/2007JA012500.
- H. S. Hudson. Solar flares, microflares, nanoflares, and coronal heating. *Solar Phys.*, 133:357–369, June 1991. doi: 10.1007/BF00149894.
- A. J. Hundhausen. Coronal Expansion and Solar Wind. *Physics and Chemistry in Space*, 5, 1972. doi: 10.1007/978-3-642-65414-5.
- B. Inhester. Stereoscopy basics for the STEREO mission. *ArXiv Astrophysics e-prints*, December 2006.
- C. Jacobs, S. Poedts, and B. van der Holst. The effect of the solar wind on CME triggering by magnetic foot point shearing. *Astron. Astrophys.*, 450: 793–803, May 2006. doi: 10.1051/0004-6361:20054670.
- J. Jing, Y. Xu, J. Lee, N. V. Nitta, C. Liu, S.-H. Park, T. Wiegmann, and H. Wang. Comparison between the eruptive X2.2 flare on 2011 February 15 and confined X3.1 flare on 2014 October 24. *Research in Astronomy and Astrophysics*, 15:1537, September 2015. doi: 10.1088/1674-4527/15/9/010.
- M. L. Kaiser, T. A. Kucera, J. M. Davila, O. C. St. Cyr, M. Guhathakurta, and E. Christian. The STEREO Mission: An Introduction. *Space Sci. Rev.*, 136:5–16, April 2008. doi: 10.1007/s11214-007-9277-0.
- J. T. Karpen, S. K. Antiochos, and C. R. DeVore. The Mechanisms for the Onset and Explosive Eruption of Coronal Mass Ejections and Eruptive Flares. *Astrophys. J.*, 760:81, November 2012. doi: 10.1088/0004-637X/760/1/81.
- B. Kliem and T. Török. Torus Instability. *Physical Review Letters*, 96(25): 255002, June 2006. doi: 10.1103/PhysRevLett.96.255002.
- J. A. Klimchuk. Theory of Coronal Mass Ejections, in Space Weather (eds P. Song, H. J. Singer and G. L. Siscoe). *American Geophysical Union, Washington, D. C.*, 125:143, 2001.

- E. Kraaikamp and C. Verbeek. Solar Demon - an approach to detecting flares, dimmings, and EUV waves on SDO/AIA images. *Journal of Space Weather and Space Climate*, 5(27):A18, June 2015. doi: 10.1051/swsc/2015019.
- J. R. Lemen, A. M. Title, D. J. Akin, P. F. Boerner, C. Chou, J. F. Drake, D. W. Duncan, C. G. Edwards, F. M. Friedlaender, G. F. Heyman, N. E. Hurlburt, N. L. Katz, G. D. Kushner, M. Levay, R. W. Lindgren, D. P. Mathur, E. L. McFeaters, S. Mitchell, R. A. Rehse, C. J. Schrijver, L. A. Springer, R. A. Stern, T. D. Tarbell, J.-P. Wuelser, C. J. Wolfson, C. Yanari, J. A. Bookbinder, P. N. Cheimets, D. Caldwell, E. E. DeLuca, R. Gates, L. Golub, S. Park, W. A. Podgorski, R. I. Bush, P. H. Scherrer, M. A. Gummin, P. Smith, G. Aufer, P. Jerram, P. Pool, R. Soufli, D. L. Windt, S. Beardsley, M. Clapp, J. Lang, and N. Waltham. The Atmospheric Imaging Assembly (AIA) on the Solar Dynamics Observatory (SDO). *Solar Phys.*, 275:17–40, January 2012. doi: 10.1007/s11207-011-9776-8.
- J. Lin and T. G. Forbes. Effects of reconnection on the coronal mass ejection process. *J. Geophys. Res.*, 105:2375–2392, February 2000. doi: 10.1029/1999JA900477.
- J. Lin, Y.-K. Ko, L. Sui, J. C. Raymond, G. A. Stenborg, Y. Jiang, S. Zhao, and S. Mancuso. Direct Observations of the Magnetic Reconnection Site of an Eruption on 2003 November 18. *Astrophys. J.*, 622:1251–1264, April 2005. doi: 10.1086/428110.
- D. M. Long, E. E. DeLuca, and P. T. Gallagher. The Wave Properties of Coronal Bright Fronts Observed Using SDO/AIA. *Astrophys. J. Lett.*, 741:L21, November 2011. doi: 10.1088/2041-8205/741/1/L21.
- B. C. Low. Solar Activity and the Corona. *Solar Phys.*, 167:217–265, August 1996. doi: 10.1007/BF00146338.
- E. T. Lu and R. J. Hamilton. Avalanches and the distribution of solar flares. *Astrophys. J. Lett.*, 380:L89–L92, October 1991. doi: 10.1086/186180.
- B. J. Lynch, S. K. Antiochos, P. J. MacNeice, T. H. Zurbuchen, and L. A. Fisk. Observable Properties of the Breakout Model for Coronal Mass Ejections. *Astrophys. J.*, 617:589–599, December 2004. doi: 10.1086/424564.
- S. Ma, G. D. R. Attrill, L. Golub, and J. Lin. Statistical Study of Coronal Mass Ejections With and Without Distinct Low Coronal Signatures. *Astrophys. J.*, 722:289–301, October 2010. doi: 10.1088/0004-637X/722/1/289.
- R. M. MacQueen and R. R. Fisher. The kinematics of solar inner coronal transients. *Solar Phys.*, 89:89–102, November 1983. doi: 10.1007/BF00211955.

- J. P. Mason, T. N. Woods, A. Caspi, B. J. Thompson, and R. A. Hock. Mechanisms and Observations of Coronal Dimming for the 2010 August 7 Event. *Astrophys. J.*, 789:61, July 2014. doi: 10.1088/0004-637X/789/1/61.
- S. Milojević. Power-law Distributions in Information Science - Making the Case for Logarithmic Binning. *ArXiv e-prints*, November 2010.
- R. L. Moore, A. C. Sterling, H. S. Hudson, and J. R. Lemen. Onset of the Magnetic Explosion in Solar Flares and Coronal Mass Ejections. *Astrophys. J.*, 552:833–848, May 2001. doi: 10.1086/320559.
- A. N. M. Muniruzzaman. On measures of location and dispersion and tests of hypotheses on a pareto population. *Bulletin of the Calcutta Statistical Association*, 7:115–123, 1957.
- P. Murdin. *Encyclopedia of astronomy and astrophysics*. Bristol: IOP Publishing and London: Nature Publishing, 2001.
- National Research Council. *Severe Space Weather Events—Understanding Societal and Economic Impacts: A Workshop Report*. The National Academies Press, doi:10.17226/12507, 2008.
- M. Newman. Power laws, Pareto distributions and Zipf’s law. *Contemporary Physics*, 46:323–351, September 2005. doi: 10.1080/00107510500052444.
- T. Nieves-Chinchilla, A. Vourlidis, G. Stenborg, N. P. Savani, A. Koval, A. Szabo, and L. K. Jian. Inner Heliospheric Evolution of a ”Stealth” CME Derived from Multi-view Imaging and Multipoint in Situ observations. I. Propagation to 1 AU. *Astrophys. J.*, 779:55, December 2013. doi: 10.1088/0004-637X/779/1/55.
- C. E. Parnell. The Role of Dynamic Brightenings in Coronal Heating. In R. W. Walsh, J. Ireland, D. Danesy, and B. Fleck, editors, *SOHO 15 Coronal Heating*, volume 575 of *ESA Special Publication*, page 227, December 2004.
- C. E. Parnell. Solar theory (mt4510). 2010. URL http://www-solar.mcs.st-andrews.ac.uk/~clare/Lectures/sol_theory/solar2010.pdf.
- B. Peeters. Wiskunde achter detectie van zonnepfenomenen op basis van satellietbeelden. *Master Thesis, K.U.Leuven. Faculteit Wetenschappen*, 2011.
- A. A. Pevtsov, O. Panasenco, and S. F. Martin. Coronal Mass Ejections from Magnetic Systems Encompassing Filament Channels Without Filaments. *Solar Phys.*, 277:185–201, March 2012. doi: 10.1007/s11207-011-9881-8.
- E. Priest. *Magnetohydrodynamics of the Sun*. Cambridge University Press, May 2014.

- E. R. Priest and T. G. Forbes. The magnetic nature of solar flares. *Astron. Astrophys. Rev.*, 10:313–377, 2002. doi: 10.1007/s001590100013.
- T. Pulkkinen. Space Weather: Terrestrial Perspective. *Living Reviews in Solar Physics*, 4:1, May 2007. doi: 10.12942/lrsp-2007-1.
- C. L. Raftery, D. S. Bloomfield, P. T. Gallagher, D. B. Seaton, D. Berghmans, and A. De Groof. Temperature Response of the 171 Å Passband of the SWAP Imager on PROBA2, with a Comparison to TRACE, SOHO, STEREO, and SDO. *Solar Phys.*, 286:111–124, August 2013. doi: 10.1007/s11207-013-0266-z.
- E. Robbrecht and D. Berghmans. Automated recognition of coronal mass ejections (CMEs) in near-real-time data. *Astron. Astrophys.*, 425:1097–1106, October 2004. doi: 10.1051/0004-6361:20041302.
- E. Robbrecht, D. Berghmans, and R. A. M. Van der Linden. Automated LASCO CME Catalog for Solar Cycle 23: Are CMEs Scale Invariant? *Astrophys. J.*, 691:1222–1234, February 2009a. doi: 10.1088/0004-637X/691/2/1222.
- E. Robbrecht, S. Patsourakos, and A. Vourlidas. No Trace Left Behind: STEREO Observation of a Coronal Mass Ejection Without Low Coronal Signatures. *Astrophys. J.*, 701:283–291, August 2009b. doi: 10.1088/0004-637X/701/1/283.
- D. F. Ryan, M. Dominique, D. B. Seaton, and A. White. The effects of flare definitions on the statistics of derived flare distributions. *In Preparation*, 2016.
- S. Santandrea, K. Gantois, K. Strauch, F. Teston, E. Tilmans, C. Baijot, D. Gerrits, A. De Groof, G. Schwehm, and J. Zender. PROBA2: Mission and Spacecraft Overview. *Solar Phys.*, 286:5–19, August 2013. doi: 10.1007/s11207-013-0289-5.
- B. Schmieder, P. Démoulin, and G. Aulanier. Solar filament eruptions and their physical role in triggering coronal mass ejections. *Advances in Space Research*, 51:1967–1980, June 2013. doi: 10.1016/j.asr.2012.12.026.
- J. Schou, P. H. Scherrer, R. I. Bush, R. Wachter, S. Couvidat, M. C. Rabello-Soares, R. S. Bogart, J. T. Hoeksema, Y. Liu, T. L. Duvall, D. J. Akin, B. A. Allard, J. W. Miles, R. Rairden, R. A. Shine, T. D. Tarbell, A. M. Title, C. J. Wolfson, D. F. Elmore, A. A. Norton, and S. Tomczyk. Design and Ground Calibration of the Helioseismic and Magnetic Imager (HMI) Instrument on the Solar Dynamics Observatory (SDO). *Solar Phys.*, 275:229–259, January 2012. doi: 10.1007/s11207-011-9842-2.

- C. J. Schrijver and G. L. Siscoe. *Heliophysics: Plasma Physics of the Local Cosmos*. Cambridge University Press, July 2009.
- C. J. Schrijver, C. Elmore, B. Kliem, T. Török, and A. M. Title. Observations and Modeling of the Early Acceleration Phase of Erupting Filaments Involved in Coronal Mass Ejections. *Astrophys. J.*, 674:586–595, February 2008. doi: 10.1086/524294.
- R. Schwenn. Space Weather: The Solar Perspective. *Living Reviews in Solar Physics*, 3:2, August 2006. doi: 10.12942/lrsp-2006-2.
- D. B. Seaton. Continuing science from the 1998 and 1999 eclipses: high frequency oscillations, general structure, and correlation with space based observations. *Undergraduate Thesis, Williams College*, 2001.
- D. B. Seaton, M. Mierla, D. Berghmans, A. N. Zhukov, and L. Dolla. SWAP-SECCHI Observations of a Mass-loading Type Solar Eruption. *Astrophys. J. Lett.*, 727:L10, January 2011. doi: 10.1088/2041-8205/727/1/L10.
- D. B. Seaton, D. Berghmans, B. Nicula, J.-P. Halain, A. De Groof, T. Thibert, D. S. Bloomfield, C. L. Raftery, P. T. Gallagher, F. Auchère, J.-M. Defise, E. D’Huys, J.-H. Lecat, E. Mazy, P. Rochus, L. Rossi, U. Schühle, V. Slemzin, M. S. Yalim, and J. Zender. The SWAP EUV Imaging Telescope Part I: Instrument Overview and Pre-Flight Testing. *Solar Phys.*, 286:43–65, August 2013a. doi: 10.1007/s11207-012-0114-6.
- D. B. Seaton, A. De Groof, P. Shearer, D. Berghmans, and B. Nicula. SWAP Observations of the Long-term, Large-scale Evolution of the Extreme-ultraviolet Solar Corona. *Astrophys. J.*, 777:72, November 2013b. doi: 10.1088/0004-637X/777/1/72.
- N. R. Sheeley, J. H. Walters, Y.-M. Wang, and R. A. Howard. Continuous tracking of coronal outflows: Two kinds of coronal mass ejections. *J. Geophys. Res.*, 104:24739–24768, November 1999. doi: 10.1029/1999JA900308.
- C. Shen, Y. Wang, Z. Pan, M. Zhang, P. Ye, and S. Wang. Full halo coronal mass ejections: Do we need to correct the projection effect in terms of velocity? *Journal of Geophysical Research (Space Physics)*, 118:6858–6865, November 2013. doi: 10.1002/2013JA018872.
- T. Shimizu. Energetics and Occurrence Rate of Active-Region Transient Brightenings and Implications for the Heating of the Active-Region Corona. *Pub. Astron. Soc. Japan*, 47:251–263, April 1995.
- A. K. Srivastava and K. Murawski. Observations of Post-flare Plasma Dynamics during an M1.0 Flare in AR11093 by the Solar Dynamics

- Observatory/Atmospheric Imaging Assembly. *Astrophys. J.*, 744:173, January 2012. doi: 10.1088/0004-637X/744/2/173.
- K. Steed and G. Lapenta. Investigating the Origins and Heliospheric Evolution of Homologous CMEs Originating from NOAA AR11093 on 7 and 14 August 2010. *AGU Fall Meeting Abstracts*, page C1974, December 2011.
- K. Steed, D. M. Long, J. A. Davies, A. P. Walsh, and G. Lapenta. The origins and heliospheric evolution of cmes on 7 and 14 august 2010 originating from the same solar source region. *Poster at Solar Orbiter 5 Workshop*, <http://www.spaceweather.eu/en/repository/show?id=328>, 2012.
- E. C. Stone, L. F. Burlaga, A. C. Cummings, W. C. Feldman, W. E. Frain, J. Geiss, G. Gloeckler, R. E. Gold, D. Hovestadt, S. M. Krimigis, G. M. Mason, D. McComas, R. A. Mewaldt, J. A. Simpson, T. T. von Rosenvinge, and M. E. Wiedenbeck. The advanced composition explorer. In W. V. Jones, F. J. Kerr, and J. F. Ormes, editors, *Particle Astrophysics - The NASA Cosmic Ray Program for the 1990s and Beyond*, volume 203 of *American Institute of Physics Conference Series*, pages 48–57, March 1990. doi: 10.1063/1.39173.
- X. Sun, M. G. Bobra, J. T. Hoeksema, Y. Liu, Y. Li, C. Shen, S. Couvidat, A. A. Norton, and G. H. Fisher. Why Is the Great Solar Active Region 12192 Flare-rich but CME-poor? *Astrophys. J. Lett.*, 804:L28, May 2015. doi: 10.1088/2041-8205/804/2/L28.
- J. K. Thalmann, Y. Su, M. Temmer, and A. M. Veronig. The Confined X-class Flares of Solar Active Region 2192. *Astrophys. J. Lett.*, 801:L23, March 2015. doi: 10.1088/2041-8205/801/2/L23.
- T. Török and B. Kliem. Confined and Ejective Eruptions of Kink-unstable Flux Ropes. *Astrophys. J. Lett.*, 630:L97–L100, September 2005. doi: 10.1086/462412.
- T. Török, B. Kliem, and V. S. Titov. Ideal kink instability of a magnetic loop equilibrium. *Astron. Astrophys.*, 413:L27–L30, January 2004. doi: 10.1051/0004-6361:20031691.
- S. D. Tun and A. Vourlidis. Derivation of the Magnetic Field in a Coronal Mass Ejection Core via Multi-frequency Radio Imaging. *Astrophys. J.*, 766: 130, April 2013. doi: 10.1088/0004-637X/766/2/130.
- T. Van Doorselaere, A. De Groof, J. Zender, D. Berghmans, and M. Goossens. Lyra observations of two oscillation modes in a single flare. *The Astrophysical Journal*, 740(2):90, 2011.

- D. A. van Dyk, A. Connors, V. L. Kashyap, and A. Siemiginowska. Analysis of Energy Spectra with Low Photon Counts via Bayesian Posterior Simulation. *Astrophys. J.*, 548:224–243, February 2001. doi: 10.1086/318656.
- P. Vanlommel, M. Messerotti, J. Liliensten, S. Calders, K. Bonte, E. D’Huys, and V. Žigman. Exploitation, dissemination, education and outreach in the frame of the COST action ES0803 ”developing space weather products and services in Europe”. *Journal of Space Weather and Space Climate*, 4(27):A05, January 2014. doi: 10.1051/swsc/2014002.
- P. Vemareddy, R. A. Maurya, and A. Ambastha. Filament Eruption in NOAA 11093 Leading to a Two-Ribbon M1.0 Class Flare and CME. *Solar Phys.*, 277:337–354, April 2012. doi: 10.1007/s11207-011-9903-6.
- A. Vourlidas, R. A. Howard, E. Esfandiari, S. Patsourakos, S. Yashiro, and G. Michalek. Comprehensive Analysis of Coronal Mass Ejection Mass and Energy Properties Over a Full Solar Cycle. *Astrophys. J.*, 722:1522, October 2010. doi: 10.1088/0004-637X/722/2/1522.
- A. Vourlidas, R. Colaninno, T. Nieves-Chinchilla, and G. Stenborg. The First Observation of a Rapidly Rotating Coronal Mass Ejection in the Middle Corona. *Astrophys. J. Lett.*, 733:L23, June 2011. doi: 10.1088/2041-8205/733/2/L23.
- B. Vršnak, D. Sudar, and D. Ruždjak. The CME-flare relationship: Are there really two types of CMEs? *Astron. Astrophys.*, 435:1149–1157, June 2005. doi: 10.1051/0004-6361:20042166.
- Y. Wang, C. Chen, B. Gui, C. Shen, P. Ye, and S. Wang. Statistical study of coronal mass ejection source locations: Understanding CMEs viewed in coronagraphs. *Journal of Geophysical Research (Space Physics)*, 116:A04104, April 2011. doi: 10.1029/2010JA016101.
- Y.-M. Wang and N. R. Sheeley, Jr. Filament Eruptions near Emerging Bipoles. *Astrophys. J. Lett.*, 510:L157–L160, January 1999. doi: 10.1086/311815.
- D. F. Webb and T. A. Howard. Coronal Mass Ejections: Observations. *Living Reviews in Solar Physics*, 9:3, June 2012. doi: 10.12942/lrsp-2012-3.
- M. S. Wheatland. A Bayesian Approach to Solar Flare Prediction. *Astrophys. J.*, 609:1134–1139, July 2004. doi: 10.1086/421261.
- Ethan P. White, Brian J. Enquist, and Jessica L. Green. On estimating the exponent of power-law frequency distributions. *Ecology*, 89(4):905–912, 2014/10/31 2008. doi: 10.1890/07-1288.1.

- T. Wiegmann and T. Sakurai. Solar Force-free Magnetic Fields. *Living Reviews in Solar Physics*, 9:5, September 2012. doi: 10.12942/lrsp-2012-5.
- T. N. Woods, F. G. Eparvier, R. Hock, A. R. Jones, D. Woodraska, D. Judge, L. Didkovsky, J. Lean, J. Mariska, H. Warren, D. McMullin, P. Chamberlin, G. Berthiaume, S. Bailey, T. Fuller-Rowell, J. Sojka, W. K. Tobiska, and R. Viereck. Extreme Ultraviolet Variability Experiment (EVE) on the Solar Dynamics Observatory (SDO): Overview of Science Objectives, Instrument Design, Data Products, and Model Developments. *Solar Phys.*, 275:115–143, January 2012. doi: 10.1007/s11207-009-9487-6.
- S. Yashiro, N. Gopalswamy, G. Michalek, O. C. St. Cyr, S. P. Plunkett, N. B. Rich, and R. A. Howard. A catalog of white light coronal mass ejections observed by the SOHO spacecraft. *Journal of Geophysical Research (Space Physics)*, 109:A07105, July 2004. doi: 10.1029/2003JA010282.
- S. Yashiro, N. Gopalswamy, S. Akiyama, G. Michalek, and R. A. Howard. Visibility of coronal mass ejections as a function of flare location and intensity. *Journal of Geophysical Research (Space Physics)*, 110:A12S05, December 2005. doi: 10.1029/2005JA011151.
- S. Yashiro, S. Akiyama, N. Gopalswamy, and R. A. Howard. Different Power-Law Indices in the Frequency Distributions of Flares with and without Coronal Mass Ejections. *Astrophys. J. Lett.*, 650:L143–L146, October 2006. doi: 10.1086/508876.
- S. Yashiro, G. Michalek, and N. Gopalswamy. A comparison of coronal mass ejections identified by manual and automatic methods. *Annales Geophysicae*, 26:3103–3112, October 2008. doi: 10.5194/angeo-26-3103-2008.
- J. Zender, D. Berghmans, D. S. Bloomfield, C. Cabanas Parada, I. Dammasch, A. De Groof, E. D’Huys, M. Dominique, P. Gallagher, B. Giordanengo, P. A. Higgins, J.-F. Hochedez, M. S. Yalim, B. Nicula, E. Pylyser, L. Sanchez-Duarte, G. Schwehm, D. B. Seaton, A. Stanger, K. Stegen, and S. Willems. The Projects for Onboard Autonomy (PROBA2) Science Centre: Sun Watcher Using APS Detectors and Image Processing (SWAP) and Large-Yield Radiometer (LYRA) Science Operations and Data Products. *Solar Phys.*, 286:93–110, August 2013. doi: 10.1007/s11207-012-0033-6.
- T. L. Zhang, W. Baumjohann, M. Delva, H.-U. Auster, A. Balogh, C. T. Russell, S. Barabash, M. Balikhin, G. Berghofer, H. K. Biernat, H. Lammer, H. Lichtenegger, W. Magnes, R. Nakamura, T. Penz, K. Schwingenschuh, Z. Vörös, W. Zambelli, K.-H. Fornacon, K.-H. Glassmeier, I. Richter, C. Carr, K. Kudela, J. K. Shi, H. Zhao, U. Motschmann, and J.-P. Lebreton. Magnetic field investigation of the Venus plasma environment: Expected new results

- from Venus Express. , 54:1336–1343, November 2006. doi: 10.1016/j.pss.2006.04.018.
- Y. Zhang, M. Zhang, and H. Zhang. On the Relationship between Flux Emergence and CME Initiation. *Solar Phys.*, 250:75–88, July 2008. doi: 10.1007/s11207-008-9150-7.
- F. P. Zuccarello, A. Bemporad, C. Jacobs, M. Mierla, S. Poedts, and F. Zuccarello. The Role of Streamers in the Deflection of Coronal Mass Ejections: Comparison between STEREO Three-dimensional Reconstructions and Numerical Simulations. *Astrophys. J.*, 744:66, January 2012. doi: 10.1088/0004-637X/744/1/66.
- F. P. Zuccarello, D. B. Seaton, M. Mierla, S. Poedts, L. A. Rachmeler, P. Romano, and F. Zuccarello. Observational Evidence of Torus Instability as Trigger Mechanism for Coronal Mass Ejections: The 2011 August 4 Filament Eruption. *Astrophys. J.*, 785:88, April 2014. doi: 10.1088/0004-637X/785/2/88.
- F. P. Zuccarello, G. Aulanier, and S. A. Gilchrist. Critical Decay Index at the Onset of Solar Eruptions. *Astrophys. J.*, 814:126, December 2015. doi: 10.1088/0004-637X/814/2/126.

Curriculum Vitae

Elke D’Huys

Royal Observatory of Belgium
Solar Physics and Space Weather Operational Directorate

Ringlaan 3, 1180 Brussel (Ukkel), Belgium
+32 2 / 890 9 845
Email: elke.dhuys@observatory.be

Education

2001 - 2006	Master in Mathematics and Astronomy Graduated with distinction from KU Leuven Thesis Title: <i>Search for a magnetic field and study of pulsations in the slowly pulsating B-star 3 Vulpeculae</i> Promotors: Dr. M. Briquet and Dr. C. Neiner
2003 - 2007	Teaching degree in Mathematics Graduated with high distinction from KU Leuven
2006 - 2007	Master in Business Economics Graduated with distinction from KU Leuven

Professional Experience

Since December 1, 2015	SWAP Instrument Scientist
October 2011 - October 2014	Researcher for the scientific exploitation of the Belgian solar mission PROBA2 at the Royal Observatory of Belgium (ROB)
Since January 2009	Space Weather Forecaster at ROB
Since October 2008	Researcher at ROB
2007 - 2008	High school teacher in mathematics and physics at the Sint-Albertus-College, Haasrode (Belgium)
July 2006	Summer student at ROB
July 2005	Summer student at ROB

Grants

October 2011 - October 2012	Supplementary Researcher grant from the Belgian Science Policy Office (BELSPO) in the framework of the scientific exploitation of the Belgian solar mission PROBA2
October 2012 - October 2013	Renewed supplementary researcher grant from BELSPO
October 2013 - October 2014	Renewed supplementary researcher grant from BELSPO

Peer-Reviewed Publications

1. **E. D'Huys**, D. B. Seaton, D. Berghmans, and S. Poedts
The 2010 August 14 Rotating CME: a Forecasting Case Study
 In preparation, to be submitted to *Journal of Space Weather and Space Climate*, 2016

2. **E. D’Huys**, D. Berghmans, D. B. Seaton, and S. Poedts
The effect of limited sample sizes on the accuracy of the estimated scaling parameter for power-law-distributed solar data
Submitted to *Solar Phys.*, 2015
3. **E. D’Huys**, D. B. Seaton, S. Poedts, and D. Berghmans
Observational Characteristics of Coronal Mass Ejections without Low-coronal Signatures
Astrophys. J., 795, 49, 2014. doi:doi: 10.1088/0004-637X/795/1/49
4. P. Vanlommel, M. Messerotti, J. Lilensten, S. Calders, K. Bonte, **E. D’Huys**, V. Zigman
Exploitation, dissemination, education and outreach in the frame of the COST action ES0803 "developing space weather products and services in Europe"
Journal of Space Weather and Space Climate, 4, A05, 2014.
5. D. B. Seaton, D. Berghmans, B. Nicula, J.-P. Halain, A. De Groof, T. Thibert, D. S. Bloomfield, C. L. Raftery, P. T. Gallagher, F. Auchère, J.-M. Defise, **E. D’Huys**, J.-H. Lecat, E. Mazy, P. Rochus, L. Rossi, U. Schühle, V. Slemzin, M. S. Yalim, and J. Zender
The SWAP EUV Imaging Telescope Part I: Instrument Overview and Pre-Flight Testing
Solar Phys., 286, 43-65, 2013. doi:doi: 10.1088/0004-637X/795/1/49
6. J. Zender, D. Berghmans, D. S. Bloomfield, C. Cabanas Parada, I. Dammasch, A. De Groof, **E. D’Huys**, M. Dominique, P. Gallagher, B. Giordanengo, P. A. Higgins, J.-F. Hochedez, M. S. Yalim, B. Nicula, E. Pylyser, L. Sanchez-Duarte, G. Schwehm, D. B. Seaton, A. Stanger, K. Stegen, S. Willems
The Projects for Onboard Autonomy (PROBA2) Science Centre: Sun Watcher Using APS Detectors and Image Processing (SWAP) and Large-Yield Radiometer (LYRA) Science Operations and Data Products
Solar Phys., 286, 93-110, 2013
7. M. Kretzschmar, I. E. Dammasch, M. Dominique, J. Zender, G. Cessateur, **E. D’Huys**
Extreme ultraviolet solar irradiance during the rising phase of solar cycle 24 observed by PROBA2/LYRA
Journal of Space Weather and Space Climate, 2, A14, 2012

Popular Publications

- **E. D’Huys**, P. Vanlommel
Ruimteweer waarnemen met een Belgische Satelliet
Observing Space Weather with a Belgian Satellite.
 Information brochure for high school teachers on PROBA2, the Sun and Space Weather
 Published by Vliebergh-Senciecentrum (KU Leuven), 2010,
http://sidc.oma.be/Leerkrachten/PROBA2@school_20101001.pdf
- **E. D’Huys**, P. Vanlommel
Ruimteweer waarnemen met een Belgische Satelliet
Observing Space Weather with a Belgian Satellite
 Series (5 episodes) in Guidestar (Newsletter Astro Event Group Oostende),
 August to December 2010, p 38, <http://www.spacepage.be/guidestar>
- **E. D’Huys**, P. Vanlommel
De Koninklijke Sterrenwacht aan boord van PROBA2
The Royal Observatory of Belgium on board PROBA2
 Guidestar (Newsletter Astro Event Group Oostende), July 2010, p 38,
<http://www.spacepage.be/guidestar>
- **E. D’Huys**, P. Vanlommel
De Koninklijke Sterrenwacht aan boord van PROBA2 - een blik op de toekomst
The Royal Observatory of Belgium on board PROBA2 - looking into the future.
 Science Connection (Belgian Science Policy magazine), April 2010, p 24,
http://www.belspo.be/belspo/organisation/publ_science_en.stm

Conference Talks and Posters

- 2015 PROBA2 Science Working Team at the 12th European Space Weather Week, November 23-27, 2015, Oostende, Belgium
Oral presentation: *SWAP Status Update*
D’Huys E., Seaton D.B., and the SWAP team
- 2014 11th European Space Weather Week, November 17-21, 2014, Liège, Belgium
Oral presentation: *Observational Characteristics of CMEs without low coronal signatures*
D’Huys E., Seaton D.B., Poedts S., Berghmans, D.

Third annual CHARM meeting, 18-19 September, 2014, Brussels, Belgium
Oral presentation: *Observational Characteristics of CMEs without low coronal signatures*

D’Huys E., Seaton D.B., Poedts S., Berghmans, D.

14th European Solar Physics Meeting, 8-12 September 2014, Dublin, Ireland

Oral Presentation: *Observational characteristics of CMEs without low coronal signatures*

D’Huys E., Seaton D.B., Poedts S.

Seventh Solar Information Processing Workshop, 18-21 August, 2014, La Roche-en-Ardenne, Belgium

Poster Presentation: *The influence of small sample sizes on the determination of power laws. - How large does your sample need to be before you can publish a power law?*

D’Huys E., Seaton D.B., Berghmans D.

40th COSPAR Scientific Assembly, 2-10 August 2014, Moscow, Russia

Oral Presentation: *Study of stealth flux-rope CMEs arriving at the Earth in 2009*

Mierla M., Kilpua E., Zhukov A., Rodriguez L., **D’Huys E.**, Zuccarello F.P., Seaton D.B.

eHeroes 3rd General Meeting, 10-12 March 2014, Davos, Switzerland

Oral Presentation: *Properties and Initiation Mechanisms for CMEs without distinct coronal signatures*

D’Huys E., Seaton D. B., Poedts S.

Second annual CHARM meeting, 30-31 January, 2014, Ghent, Belgium

Oral Presentation: *Properties and Initiation Mechanisms for CMEs without distinct coronal signatures*

D’Huys E., Seaton D. B., Poedts S.

2013 Tenth European Space Weather Week, November 18-22, 2013, Antwerp, Belgium

Poster Presentation: *Properties and Initiation Mechanisms for CMEs without distinct coronal signatures*

D’Huys E., Seaton D. B., Bonte K., Poedts S.

Tenth European Space Weather Week, November 18-22, 2013, Antwerp, Belgium

Oral Presentation: *Study of stealth CMEs arriving at Earth in the period 2009-2010*

Mierla M., Kilpua E., Rodriguez L., **D’Huys E.**, Zuccarello F.P., Zhukov A.N., Seaton D.B.

- 2012 Ninth European Space Weather Week, November 5-9, 2012, Brussels, Belgium
Poster Presentation: *Initiation Mechanisms for CMEs without distinct coronal signatures*
D’Huys E., Seaton D.B., Bonte K., Berghmans D., Poedts S.
- CHARM kickoff meeting, October 8-9, 2012, KULeuven, Leuven
Oral Presentation: *Combining Observations and Models of Magnetic Reconnection During Solar Coronal Eruptions*
D’Huys E., Seaton D.B., Poedts S., Berghmans D.
- Fifth Solar Orbiter Workshop, September 10-14, 2012, Brugge, Belgium
Poster Presentation: *Multi-spacecraft Analysis and modeling of a solar eruption on August 14, 2010*
D’Huys E., Seaton D., Jacobs C., De Groof A. and Poedts S.
- First European school on Fundamental processes in space weather: a challenge in numerical modeling, SWIFF network, June 4-9, 2012. Spineto, Italy
Poster Presentation: *Multi-spacecraft Analysis and modeling of a solar eruption on August 14, 2010*
D’Huys E., Seaton D., Jacobs C., De Groof A. and Poedts S.
- 2011 The Sun 360 (Stereo-4/SDO-2/SOHO-25 Workshop), July 25-29, 2011, Christian-Albrechts-Universit Kiel, Germany
Poster Presentation: *Multi- spacecraft analysis and modeling of a solar eruption on August 14, 2010*
D’Huys E., Seaton D., Jacobs C., De Groof A. and Poedts S.
- 3rd SOTERIA General Meeting, May 30 - June 1, 2011, Leuven, Belgium
Oral Presentation: *Studying Reconnection During Solar Eruptions Using AIA and SWAP: Observations and Modeling*
Seaton D.B., Reeves K., Savage S., Forbes T., **D’Huys E.**,
- First LWS/SDO Workshop, May 1-5, 2011, Squaw Valley, CA
Oral Presentation: *Joint AIA-SWAP Observations of Reconnection-Related Processes During Coronal Eruptions*
Seaton D.B., **D’Huys E.**, Reeves K., Forbes T., Savage S.
- 2010 38th COSPAR Scientific Assembly, 18-15 July 2010, Bremen, Germany
Poster Presentation: *Space Weather data and services at SIDC/RWC Belgium*
Van der Linden, R. et al., including **D’Huys E.**

PROBA2 Science Working Team Workshop, June 14-16, 2010, La Roche-en-Ardenne, Belgium

Oral Presentation: *The PROBA2 Science Center*

D’Huys E. and the P2SC team

SOTERIA General Meeting, January 18-20, 2010, Davos, Switzerland

Poster Presentation: *The PROBA2 Science Center*

D’Huys E. and the P2SC team

2009 Sixth European Space Weather Week, 16-20 November 2009, Brugge, Belgium

Poster Presentation: *Visualization of distributed solar data and metadata with the Solar Weather Browser*

D’Huys E., Nicula B., Marqué C., Berghmans D.

Space Weather Workshop, 27-30 April 2009, Boulder, Colorado

Poster Presentation and Live Demonstration: *Visualization of distributed solar data and metadata with the Solar Weather Browser*

D’Huys E., Nicula B., Marqué C., Berghmans D.

Space Climate Symposium 3, 18-22 March 2009, Saariselkä, Finland

Poster Presentation: *Visualization of distributed solar data and metadata with the Solar Weather Browser*

D’Huys E., Nicula B., Marqué C., Berghmans D.

Space Climate Symposium 3, 18-22 March 2009, Saariselkä, Finland

Poster Presentation: *Solar Sub-cycles*

Wauters L., Van der Linden R., Berghmans D., Willems S., Vanlommel P., **D’Huys E.**

SOTERIA Workshop, 23-24 March 2009, Saariselkä, Finland

Oral Presentation: *Status of the WP6 Document Repository*

D’Huys E., Berghmans D.

SOTERIA Workshop, 23-24 March 2009, Saariselkä, Finland

Oral Presentation: *Virtual Observatory Action Plan*

Berghmans D., Otruba W., Abourdarham J., Clette F., Nicula B., Calebout C., **D’Huys E.**

Seminars

- Observational Characteristics of CMEs without low coronal signatures in 2012
Department 4 Seminar, May 21, 2014, Meridian Room, ROB
E. D’Huys, D.B. Seaton, S. Poedts, D. Berghmans
- Observational Characteristics of CMEs without low coronal signatures in 2012
CmPA/ KU Leuven Seminar, June 24, 2014
E. D’Huys, D.B. Seaton, S. Poedts, D. Berghmans
- The effect of limited sample sizes on the accuracy of the estimated scaling parameter for power law distributed solar data
Department 4 Seminar, December 2, 2015, TV Room, ROB
E. D’Huys, D. Berghmans, D.B. Seaton, S. Poedts

Outreach Presentations

- Space Weather and PROBA2
Junior College sessions at KU Leuven for high school students (2012, 2013, 2014, 2015)
E. D’Huys, P. Vanlommel and the P2SC team
- PROBA2: Ontwikkeling, lancering en exploitatie
PROBA2@school sessions in various high schools (2011, 2012, 2013, 2014)
E. D’Huys, P. Vanlommel, and the P2SC team
- De Zon bestuderen met PROBA2 - Hoe ontwerp en lanceer je een satelliet?
Open Doors Royal Observatory of Belgium, October 10-12, 2014, Brussels, Belgium
E. D’Huys, and the P2SC team
- Running Presentation: PROBA2
Paris Air Show at Le Bourget, STCE stand, June 20 - 26, 2011, Paris, France
E. D’Huys and the P2SC team
- De Zon, Ruimteweer en PROBA2
Stedelijk Humaniora Dilsen visits ROB, November 23, 2010
E. D’Huys, A. De Groof, and P. Vanlommel

- Running Presentation at the Science Fair: PROBA2
Seventh European Space Weather Week, November 15-19, 2010, Bruges, Belgium
E. D’Huys and the P2SC team
- PROBA2: Eerste gegevens van SWAP en LYRA
Werkgroep Aardrijkskunde Brabant, Heilig Hart Instituut, Leuven, Belgium, September 28, 2010
E. D’Huys

International Schools and Training

2013 September 16-19 • Space Science Training Week 2013: Data Driven Modeling and Forecasting, Leuven, Belgium

2012 June 4-9 • SWIFF First European School on Fundamental Processes in Space Weather: A Challenge in Numerical Modelling, Spineto, Italy

2012 May 3-4 • STCE Workshop on on-orbit degradation and PROBA2 Science Days Brussels, Belgium

2012 Februari 20-24 • CmPA Workshop: SWIFF1-CPA20, Plasma Astrophysics, acquired knowledge and future perspectives, Leuven, Belgium

2011 May 23 • STCE Workshop: Accessing and exploiting SDO data, Brussels, Belgium

2011 February 17-18 • PROBA2 Science Workshop, Brussels, Belgium

2011 February 15-16 • SOTERIA Capacity Building Workshop, Brussels, Belgium

2010 June 15-19 • CESRA (Community of European Solar Radio Astronomers) Workshop 2010, La Roche-en-Ardenne, Belgium

2010 September 12-16 • Solar Image Processing Workshop, Les Diablerets, Switzerland

2010 October 18-29 • SOTERIA International Advanced School on Space Weather Modelling and Applications, Trieste, Italy

2009 April 22-24 • All Clear Workshop, Boulder, Colorado

2009 March 15-18 • Space Climate School, Saariselkä, Finland

Calvin and Hobbes by Bill Watterson



FACULTY OF SCIENCE
DEPARTMENT OF MATHEMATICS
CENTRE FOR MATHEMATICAL PLASMA-ASTROPHYSICS
Celestijnenlaan 200B, bus 2400
B-3001 Heverlee

